3D simulations of oxygenated rocky planetary climates and observational predictions

Gregory James Cooke

School of Physics and Astronomy

University of Leeds

Submitted in accordance with the requirements for the degree of

Doctor of Philosophy

May 2023

The candidate confirms that the work submitted is his own, except where work which has formed part of jointly authored publications has been included. The contribution of the candidate and the other authors to this work has been explicitly indicated. The candidate confirms that appropriate credit has been given within the thesis where reference has been made to the work of others.

For Mum and Dad.

"I don't pretend we have all the answers. But the questions are certainly worth thinking about." - Arthur C. Clarke

Preface

The chapters in this thesis are based on work presented in the following publications:

I. Cooke GJ, Marsh DR, Walsh C, Black B, & Lamarque J-F. 2022. A revised lower estimate of ozone columns during Earth's oxygenated history. *Royal Society Open Science*. 9: 211165.

II. Cooke GJ, Marsh DR, Walsh C, Rugheimer S, & Villanueva GL. 2023. Variability due to climate and chemistry in observations of oxygenated Earth-analogue exoplanets. *Monthly Notices of the Royal Astronomical Society*. 518(1). pp. 206–219

III. Ji A, Kasting J, Cooke GJ, Marsh DR, & Tsigaridis K. 2023. Comparison Between Ozone Column Depths and Methane Lifetimes Computed by 1-D and 3-D Models at Different Atmospheric O_2 Levels. *Royal Society Open Science*. 10: 230056.

IV. Cooke GJ, Marsh DR, Walsh C, Youngblood A. 2023. Degenerate interpretations of O_3 spectral features in exoplanet atmosphere observations due to stellar UV uncertainties: a 3D case study with TRAPPIST-1e, *The Astrophysical Journal*. Accepted.

Papers I, II, and IV form the basis of Chapters 4, 5, and 7, respectively.

For Papers I, II, and IV, the simulations and analysis were all performed by G. J. Cooke. Setup of the WACCM6 model and adapting it for different simulations was done jointly with D. R. Marsh. For Paper II, advice on setting up the Planetary Spectrum Generator was

provided by G. L. Villanueva. G. J. Cooke performed all Planetary Spectrum Generator simulations in Papers II and IV. G. J. Cooke wrote the drafts for Papers I, II, and IV. Subsequent drafts were iterated with D. R. Marsh and C. Walsh, with final drafts in advance of submission for publication iterated with other co-authors.

Paper III forms a small proportion of Chapter 4, with G. J. Cooke providing simulations, data, analysis and comments. A. Ji wrote the manuscript.

Acknowledgements

In 2019, when I joined the University of Leeds, I knew the forthcoming years would usher in unfamiliar territory. But looking back at the bizarre path I have taken since then, to arrive at the final stage of my PhD, it is an understatement to say the journey went as expected; the covid pandemic was brutal for countless reasons. I am happy to have had several opportunities since then to talk to many amazing people, to travel, and to learn about cutting-edge exoplanet and climate research. It has been a pleasure to be able to disseminate my own explorations into the exciting topic of rocky planetary climates.

Supporting me through it all, I am grateful to Dan and Catherine, my two wonderful supervisors. They have both made this entire project possible through fascinating discussions, helpful feedback, and valuable insights. I am fortunate to have collaborated and authored papers with several brilliant scientists. Additionally, I appreciate the funding from STFC for this PhD opportunity.

I am ineffably indebted to my parents. There is no way I would have made it this far if it wasn't for their constant dedication, support, and love. Thank you to Ash, for inspiring me to be a better person in every sense, and for taking the mick out of me whenever she gets the opportunity.

Eve, Rob, and I were welcomed with open arms by Alice B, Miguel, Abi, James, John, and Alice P, all the way back in 2019. The Fenton will not be forgotten. I must give a special mention to Eve, Rob, Jacob, Julia, and Hannah, for putting up with my complaints about

science, the world, and the soaring price of bread. The countless hours Daniel and I sunk into creating the world's best football team were an essential distraction. Furthermore, I am beholden to the brightness of the large lamp that stopped me going blind in the darkest of days during the latter two lockdowns. I am grateful for Huw, Lucy, Nick, Harry, and Rowan, who I do not see enough but they have always been there for me during the strange 3.5 years that have just transpired. I am thankful for Claire, Ali, Ellie, Lily, Bernadett, Dante, Emma, Binghan, Isaac, Maisie, Marcin, Marie, Sam, Jake, Nelson, Phoebe, Ashleigh, Annie, Elle, Dom, and Brendan. Thanks to Steph, for her motivational spirit, remarkable intuition, and for bringing the revelation I needed.

The multiple lockdowns took from me my sense of optimism, which, by virtue of all of my friends and family, I have managed to regain. I thank them all for keeping me sane, grounded, human, and entertained.

Abstract

There are now hundreds of known terrestrial exoplanets (rocky planets orbiting other stars), with ~ 60 considered potentially habitable worlds. In the next two decades, several state-of-the art observatories will observe these exoplanets with unprecedented sensitivity, requiring the parallel use of computational models to constrain their climates. Using Earth's inhabited paleoclimates as templates may elucidate which exoplanets could host life.

I use WACCM6, a three-dimensional (3D) Earth System Model, to simulate Earth's oxygenated paleoclimates, as well as the climates of Earth-like terrestrial exoplanets. I use these simulations as input to the Planetary Spectrum Generator, a radiative transfer suite, to predict spectroscopic telescope transmission spectra and direct imaging spectra observations of exoplanets.

Earth's atmosphere has been oxygenated for the past 2.4 billion years. I find that different amounts of O_2 alters the 3D distribution of temperature, clouds, dynamics, and composition, with reduced ozone (O_3) concentrations between 0.1 – 50% the present atmospheric level of O_2 compared to previous 1D and 3D modelling. Considering these scenarios as Earth-analogue exoplanets, I predict their transmission and direct imaging spectra with next generation telescopes, finding that annual variability in reflected light, which depends on both clouds and composition, could be observable through state-of-the-art high-contrast imaging.

I perform simulations of TRAPPIST-1e and Proxima Centauri b, two potentially tidally locked habitable zone exoplanets. Three distinct

layers of atmospheric super rotation are resolved in the data. Furthermore, uncertainty in the incident ultraviolet (UV) radiation may lead to ambiguities when interpreting observations and inferring atmospheric oxygenation scenarios. This can be partially resolved with a dedicated, sensitive UV observatory.

This thesis demonstrates the requirement for model development to better estimate the O_2-O_3 relationship across a variety of (exo)planets. Such advances are important for reconstructing Earth's paleoclimates, and are crucial for efforts to determine if any exoplanets host Earth-like biospheres.

Contents

List of Figures

LIST OF FIGURES

List of Tables

Chapter 1

Introduction

Discovering extraterrestrial life on another world would be a momentous revelation. There are eight planets that orbit the Sun, and now there are $\sim$ 5300 known exoplanets[1,2] (planets that orbit other stars). One major objective for astronomers is to find habitable exoplanets: exoplanets that are able to host life. Around 200 of the detected exoplanets are thought to be terrestrial exoplanets, with $\sim$ 60 suggested to be potentially habitable[3]. As it is currently the only known inhabited planet, Earth serves as the foundation in the search for habitable exoplanets.

This thesis uses an Earth System Model (ESM), known as WACCM6, to investigate various different climates scenarios which all include oxygenated atmospheres, where free oxygen (O_2) exceeds 0.2 parts per million by volume (ppmv). Such O_2 levels have been present since $\sim$ 2.4 Gyr ago, the point at which Earth's atmosphere is generally considered to have transitioned to an oxygenated state (Catling & Zahnle, 2020). An ESM simulates Earth's atmosphere, ocean, cryosphere (ice and snow), and land (including rivers, lakes, and vegetation). These models build upon Global Climate Models (GCMs) which typically

[1] https://exoplanetarchive.ipac.caltech.edu/
[2] http://www.exoplanet.eu/
[3] https://phl.upr.edu/projects/habitable-exoplanets-catalog

simulate the ocean-atmosphere system alone (Edwards, 2011). My work leverages the coupled chemistry and physics of the ESM to calculate how molecular oxygen (O_2) and the radiation incident on the planetary atmosphere affect the spatial distribution of chemical species, the temperature structure, and cloud distribution. As I will demonstrate, these factors each have a significant effect on how an exoplanet's atmosphere will appear through telescopes.

In this thesis I will use the terms 'Earth-like' and 'Earth-analogue' to describe exoplanets. Hereafter, Earth-analogues refer to exoplanets that orbit a Sun-like star at 1 astronomical unit (AU; the mean Earth-Sun distance), have an atmospheric surface pressure of 1 bar (1,000 hPa), and a radius of 1 $R_{\oplus}$. Subscripts of $\oplus$ refer to Earth units, whilst subscripts with $\odot$ refer to solar units. Sun-like stars are G dwarf stars (stars between 0.83 – 1.09 solar masses and an effective stellar temperature between 5,370 – 6,150 K; Habets & Heintze, 1981) which have approximately the same size and luminosity as the Sun. Earth-like exoplanets refer to exoplanets that are roughly Earth-sized $\approx 0.5 - 1.6\ R_{\oplus}$ (although note that this is not a strict limit; Rogers, 2015; Demory *et al.*, 2016; Chen & Kipping, 2017; Fulton *et al.*, 2017) and that orbit any stellar type with planetary and orbital parameters that theoretically enable liquid water to exist upon its surface.

This Chapter provides a synopsis on exoplanets, their potentially habitability, and how their composition might be used to determine if extraterrestrial life is present outside the solar system. Planetary climate modelling is introduced, in addition to synthetic exoplanet observations produced from these numerical simulations. Because the Earth has been continuously inhabited for at least 3 billion years, Earth's atmospheric history and its importance for exoplanetary science is summarised. Finally, this Chapter discusses the prospect of future observations linked to terrestrial exoplanet climate research.

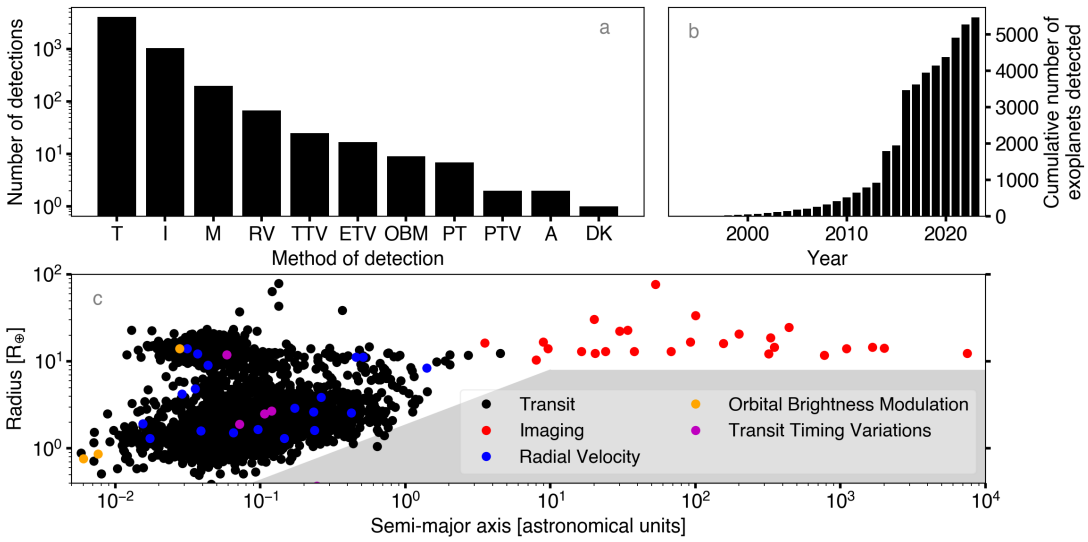

Figure 1.1: (a) The number of detection methods is plotted versus the method of detection. From left to right: transit (T), radial velocity (RV), Microlensing (M), direct imaging (I), transit timing variations (TTV), eclipse timing variations (ETV), orbital brightness modulation (OBM), pulsar timing (PT), pulsation timing variations (PTV), astrometry (A), and disk kinematics (DK). (b) The cumulative number of detected exoplanets versus calendar year is plotted, from 1992 to 2023. (c) The semi-major axis of exoplanets (in astronomical units) is plotted against their measured radius (in units of Earth radii, $R_\oplus$), with only T (black), RV (red), I (orange), and OBM (blue) detections in this parameter space. The grey region shows where measuring the semi-major axis and radius of exoplanets is currently impractical.

1.1 The exoplanet population

The study of exoplanets is relatively new. In 1992, the first confirmed exoplanet was found orbiting a pulsar (Wolszczan & Frail, 1992), a neutron star that emits electromagnetic radiation from its poles. The first exoplanet orbiting a main sequence star (a dwarf star that fuses hydrogen into helium) was located around the G dwarf 51 Pegasi in 1995 (Mayor & Queloz, 1995). Since then, there have been another $\sim$ 5300 more exoplanets discovered using several different detection techniques.

1. INTRODUCTION

The majority of exoplanets have been discovered with the 'primary transit method' ($\sim$ 4000 discovered exoplanets). A primary transit is where an exoplanet orbits its star and periodically causes a dip in starlight reaching an observer due to line of sight blocking. The 'radial velocity method', where Doppler shifts in the host star's spectral lines are used to find exoplanets, has been used to discover $\sim$ 1000 exoplanets. Fig. 1.1a shows the number of exoplanets found for every detection method according to the NASA Exoplanet Archive, whilst Fig. 1.1b shows the cumulative number of exoplanets discovered so far with respect to the year of discovery. For many exoplanets, several important properties, such as mass ($\approx$ 46.7% have their mass measured), or the radius ($\approx$ 76.0% have their radius measured), are not known due to the fact that a single detection method may only yield one of these parameters. As observational capabilities improve, more exoplanets are likely to be discovered beyond the current detection limits. Such detection bias is indicated in Fig. 1.1c, which shows the orbital semi-major axis and radius parameter space for exoplanets. The grey portion in this figure shows a region where exoplanets are expected to exist, but currently they are too small or too far away from their host star to be detected.

No exoplanet that resembles Earth has yet been found. Occurrence rate estimates for Earth-analogue planets around G-type stars (usually denoted as $\eta_{\oplus}$) in the literature have various definitions (Catanzarite & Shao, 2011; Traub, 2012; Fressin *et al.*, 2013; Zink & Hansen, 2019; Bryson *et al.*, 2021), and the calculated rates typically vary between 0.01 – 2 per star (Petigura *et al.*, 2013; Traub, 2012; Burke *et al.*, 2015; Bryson *et al.*, 2021). 2 exoplanets per star is a high-end estimate, indicating that the majority stars have exoplanets, whilst 0.01 would indicate most stars don't host any. Data from Gaia (Brown *et al.*, 2018) and the Transiting Exoplanet Survey Satellite (TESS; Ricker *et al.*, 2009), as well as ongoing ground-based surveys (Mayor *et al.*, 2003; Pollacco *et al.*, 2006) and fu-

ture missions such as the PLAnetary Transits and Oscillations of stars (PLATO) spacecraft (Rauer *et al.*, 2016), will add thousands of exoplanets to the list. In the next two decades, potentially more than 20,000 exoplanets will have been discovered (Perryman *et al.*, 2014; Barclay *et al.*, 2018). Upcoming transit and radial velocity surveys will characterise terrestrial exoplanets in greater detail by making more precise measurements of their mass and radius, thus enabling confident estimates of their density and surface gravity. Establishing the properties of their climates is the next step towards understanding these faraway worlds.

With current telescopes, determining the climates of Earth-sized exoplanets around Sun-like stars remains out of reach because the atmospheric spectroscopic signal is drowned out by the much more luminous host star. However, many (~ 100[1]) terrestrial exoplanets have been located around M dwarfs, which are the most common type of main sequence star ($\sim 75\%$ of the stellar population; Segura *et al.*, 2005). These stars have masses < 0.454 solar masses and effective temperatures < 3700 K (Habets & Heintze, 1981). A selection of M dwarf terrestrial exoplanets that are in their star's habitable zone (HZ), the orbital region around a given star where an exoplanet could be habitable, include: LHS 1140b (Dittmann *et al.*, 2017); Ross 128 b (Souto *et al.*, 2018), TRAPPIST-1e (Gillon *et al.*, 2017); and Proxima Centauri b (Anglada-Escudé *et al.*, 2016). These systems provide easier routes to characterisation resulting from the smaller size ratio between the host star and its exoplanets. For example, the transit depth, which measures the reduction in starlight during a primary transit, is $(0.91R_{\oplus}/0.1192R_{\odot})^2$ for TRAPPIST-1e. This is a factor of 58 times greater than for the Earth-Sun system. Furthermore, the relatively fast orbital periods of HZ M dwarf exoplanets (e.g. 6.1 days for TRAPPIST-1e) allow several orbits to be observed in a relatively short time frame. Due to their proximity to their hot

[1] https://exoplanetarchive.ipac.caltech.edu/

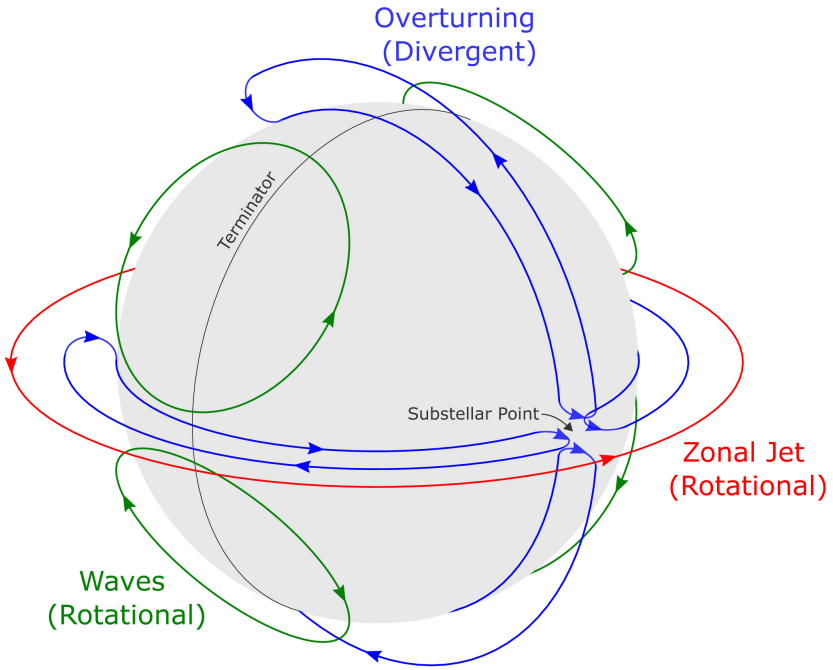

Figure 1.2: Figure from Hammond & Lewis (2021), who used a Helmholtz decomposition (where a 3D vector field is separated into divergence-free and curl-free components) to isolate the rotational and divergent components of atmospheric circulation for tidally locked exoplanets. The figure shows the various parts of the circulation: the overturning circulation (blue), the tropospheric equatorial jet (red), and planetary-scale stationary waves (green).

stars (e.g TRAPPIST-1e has a semi-major axis of 0.03 AU), these exoplanets experience significant tidal forces and may have the same side always facing their host star (i.e. they could be 'tidally locked').

1.2 Tidally locked exoplanets

Terrestrial exoplanets orbiting M dwarf stars have received a lot of attention (e.g. Turbet *et al.*, 2016; Meadows *et al.*, 2018a; Yang *et al.*, 2013; Checlair *et al.*, 2017), in part because M dwarfs are the most abundant main sequence star, and there is no equivalent in the solar system. As M dwarf stars are much less luminous than G dwarf stars, their HZs are much closer to their host star in comparison to

that of the solar system (e.g $\sim 0.03 - 0.09$ AU for Proxima Centauri; Ribas *et al.*, 2016), and this is expected to result in exoplanets that are rotating synchronously (Pierrehumbert & Hammond, 2019).

Synchronously rotating exoplanets, commonly known as tidally locked exoplanets, are exoplanets that rotate around their axis with the same period they orbit their star (Barnes, 2017). The tidally locked exoplanet will have a permanent day side and a permanent night side because the substellar point is static (Pierrehumbert & Hammond, 2019). This is only the case if the exoplanet has zero obliquity (no axial tilt) and zero eccentricity ($\epsilon = 0$ for a circular orbit), thus removing the effects that these parameters have on seasons. Examples of M dwarf exoplanets already found exhibit low eccentricities, including the seven terrestrial exoplanets orbiting TRAPPIST-1 which are constrained to have $\epsilon < 0.015$ (Grimm *et al.*, 2018) through variations in transit times due to inter-planetary gravitational interactions. Many tidally locked exoplanet simulations assume a fixed substellar point (Proedrou & Hocke, 2016; Proedrou *et al.*, 2016; Chen *et al.*, 2019; Sergeev *et al.*, 2020; Chen *et al.*, 2021). However, it is possible that asynchronous spin-orbit rotation may apply to exoplanets with an atmospheric density of 1 bar or more around stars with a mass greater than $\sim 0.3\ M_{\odot}$ (Leconte *et al.*, 2015) emerging from a torque applied via atmospheric thermal tides. Asynchronous spin-orbit rotation will cause exoplanets to evolve to alternative climate states when compared to synchronous rotation (Boutle *et al.*, 2017).

Joshi *et al.* (1997) performed the first simulation of a tidally locked terrestrial planet using a three-dimensional global atmospheric circulation model, finding that heat transported by winds can prevent the atmosphere from condensing and eventually collapsing on the nightside. Since then, many different models have been used to simulate the climates of a variety of tidally locked terrestrial planets, varying the planets in radius, stellar insolation, rotation rate, atmospheric

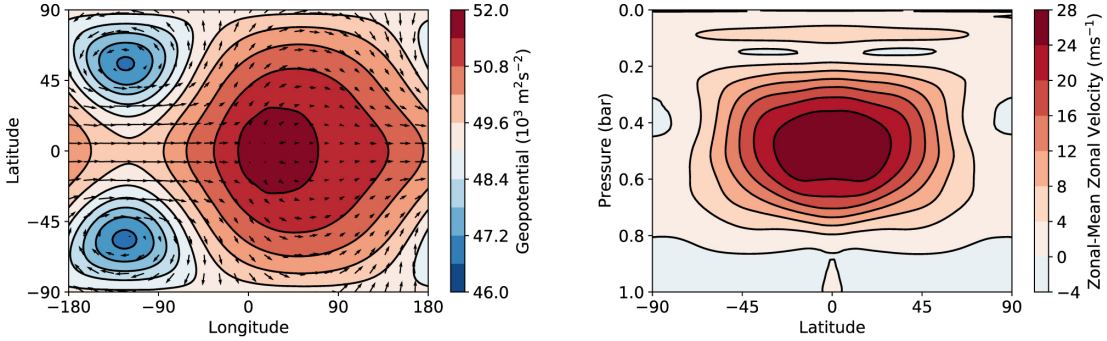

(a) Geopotential and velocity fields at the 390 mbar level

(b) Zonal-mean zonal velocity

Figure 1.3: Hammond *et al.* (2020) used a 3D GCM known as Exo-FMS to simulate a terrestrial tidally locked exoplanet with a radius of 0.942 $R_{\oplus}$, a substellar point receiving 300 W m^{-2} of instellation, and a rotation period of 10 days. Panel a shows the geopotential and horizontal wind vectors at 390 hPa, whilst panel b shows the zonal mean of the zonal wind velocity, where the equatorial jet (which is super rotating) is centred at 500 hPa. Winds flowing eastward are indicated in red, whilst westward winds are indicated in blue. Figure from Hammond *et al.* (2020).

composition, and surface composition (Yang *et al.*, 2013; Wolf, 2017; Yang *et al.*, 2020). Simulations often predict a circulation with characteristics similar to those shown in Fig. 1.2: a fast eastward flowing jet stream at the equator (Showman & Polvani, 2011) and an overturning divergent circulation (heat redistribution from the day side to the night side) due to the temperature difference between the day side and night side (Hammond & Lewis, 2021). When the jet's axial angular momentum is greater than that of the solid planet, the winds are considered to be super rotating (Pierrehumbert & Hammond, 2019), an example of which is displayed in Fig. 1.3. Even though these reported climates are drastically different from Earth's, it is possible that tidally locked exoplanets harbour conditions suitable for life.

1.3 Habitability

A habitable environment is one in which a single living organism can endure. Liquid water is a solvent which enables many vital chemical reactions to occur in cells, such that liquid water is required for all life on Earth to survive and reproduce (Cockell *et al.*, 2016). Therefore, it is common to adopt liquid water availability as the condition for life's survival. This habitability metric is biased by what is known about life on Earth (Kasting *et al.*, 1993; Wordsworth & Kreidberg, 2022). Habitability can be defined instantaneously for an exoplanet, where an exoplanet is habitable based on its current state, or in terms of continuous planetary habitability (Kasting *et al.*, 1993; Rushby *et al.*, 2013; Cockell *et al.*, 2016), where an exoplanet can sustain life for geological periods of time. This is possible on a body which has permanent surface liquid water, or subsurface liquid water only. An example of the latter can be given by Enceladus and Europa (Cockell *et al.*, 2016), which have cold, icy surfaces, but subsurface liquid water oceans.

The habitable zone (Hart, 1979; Kasting *et al.*, 1993; Kopparapu *et al.*, 2013; Kopparapu *et al.*, 2016) is depicted in Fig. 1.4. Stars with greater luminosity have HZs which are further away from them, whilst dimmer stars are able to host HZ exoplanets much closer in. The HZ will be pushed to greater orbital distances with increasing stellar age because the luminosity of main sequence stars increase with age (Hart, 1979; Cockell *et al.*, 2016).

HZs are not just dependent on the received irradiation. The HZ is dependent on several factors including: the planetary mass; if an atmosphere exists; the atmospheric composition and how strong the greenhouse effect is (Pierrehumbert & Gaidos, 2011); the planetary albedo which measures the reflectivity of the planet (Barnes *et al.*, 2015; Del Genio *et al.*, 2019a); geological activity (e.g. plate tectonics; Lammer *et al.*, 2009); the total water inventory (Lammer *et al.*,

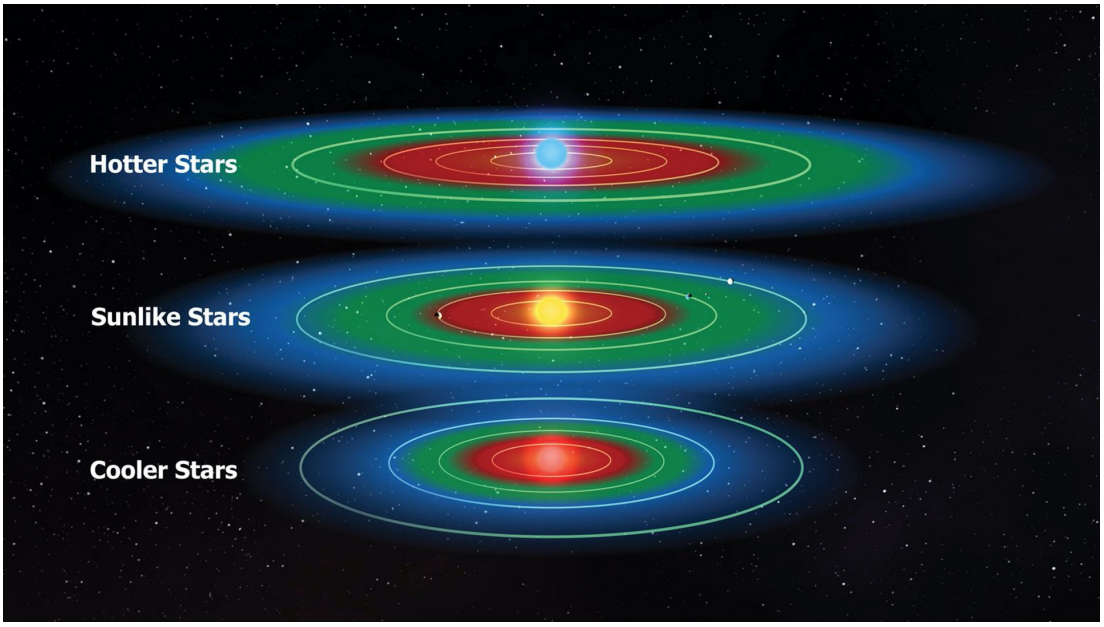

Figure 1.4: The habitable zone is the region around a star where liquid water can persist on a planetary surface, depicted here in green. In the red region the planet receives a relatively high amount of irradiation from the host star, becomes too hot, and any liquid water present boils into water vapour. In the blue region there is less irradiation because the planet is further away. Accordingly, any water present freezes into ice because the planet is too cold. Earth is in the Sun's habitable zone and retains liquid water on its surface. Compared to the Sun, cooler stars (such as M dwarfs) have a lower luminosity, so the area around the star at which exoplanets can retain liquid water on their surface is relatively close in when compared to Sun-like stars systems (G dwarfs). Larger and hotter stars emit more radiation compared to the Sun, and this pushes their habitable zones to be further away from the star. Image credit: Kepler mission/Ames Research Center/NASA.

2009); the orbital eccentricity (Williams & Pollard, 2002) and axial tilt, which affect how heat is distributed across the planet. The simulated width of the HZ around a star depends on whether a 1D or 3D model is used due to horizontal atmospheric heat transport and cloud feedback (reflection of incoming energy and trapping of outgoing terrestrial energy) within 3D models (Yang *et al.*, 2013).

Terrestrial exoplanets may have climates that differ considerably from Earth's.

For example, revealing comparisons can be made in the solar system with Venus and Mars (Lammer *et al.*, 2018; Kasting & Catling, 2003), the climates of which are inhospitable for two major contrasting reasons that prohibit liquid water persistence: Mars is too cold (despite early Mars being in the HZ; Kasting *et al.*, 2014), whilst Venus is too hot, with global mean surface temperatures of 210 K and 737 K, respectively (Krasnopolsky & Lefèvre, 2013).

There are other sources of energy, such as internal heating from tidal effects (Scharf, 2006), that will enable exoplanets, or indeed exomoons (moons of exoplanets; Heller & Barnes, 2013; Dobos *et al.*, 2017), to be habitable further beyond the region defined by the traditional stellar HZ. Once a potentially habitable exoplanet has been located, confirming whether it is inhabited by life will require multiple indicators, such as confirmation of H_2O in the atmosphere, and observed biosignatures.

1.4 Composition and biosignatures

Biosignatures, in the context of astrobiology, are signs that indicate that life is present on an astronomical body, such as an exoplanet (Grenfell, 2017; Schwieterman *et al.*, 2018b). Some examples of proposed remotely detectable signs of life include biologically produced gases (such as O_2, CH_4, and N_2O), the vegetation red edge (the large change in reflectance in the near infrared region due to vegetation; Seager *et al.*, 2005), seasonal variations in gases caused by life (Earth's CO_2 concentration periodically changes with the seasons – see Olson *et al.*, 2018b), and technosignatures (evidence of technology; Berdyugina & Kuhn, 2019; Socas-Navarro *et al.*, 2021). In terms of gases, many are of interest: Seager *et al.* (2016) compiled a list of approximately 14,000 molecules and determined that hundreds of them are produced by life on Earth and therefore could be considered potential biosignatures.

If a biosignature is detected in an exoplanet's atmosphere, there is the potential for it to be a false-positive (Harman & Domagal-Goldman, 2018; Krissansen-Totton *et al.*, 2021). In other words, the signature observed could have been produced by an abiogenic process, such as photochemical production (e.g. CO_2 or H_2O photolysis producing O_2; Domagal-Goldman *et al.*, 2014), or geological processes like magmatic outgassing of CH_4 (Wogan *et al.*, 2020; Thompson *et al.*, 2022).

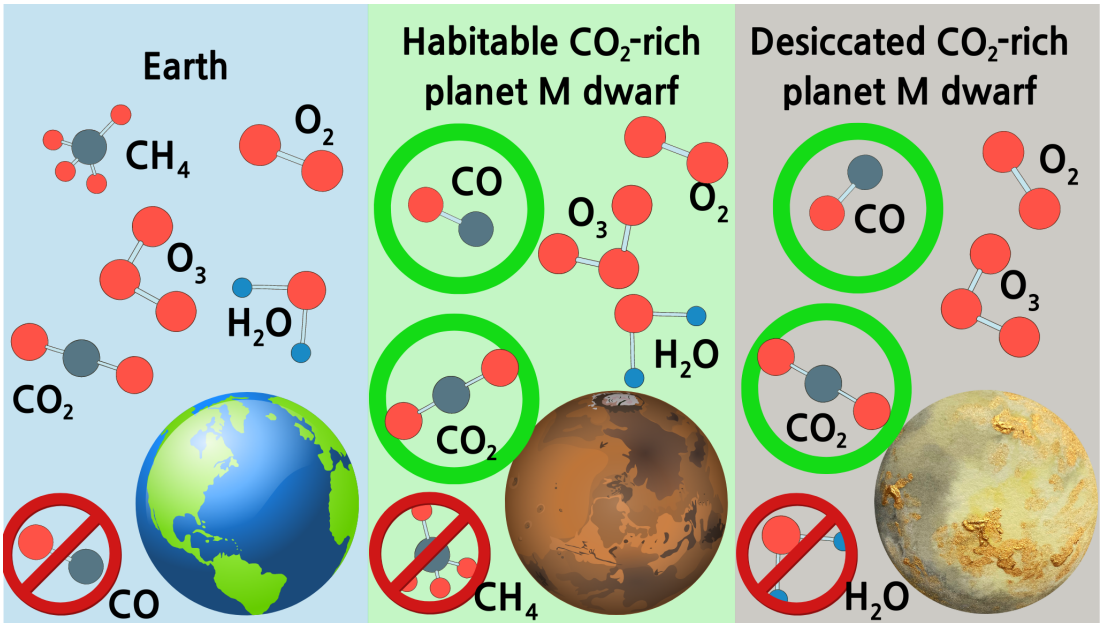

Figure 1.5: Two possible biosignature false positives mechanisms by which O_2 can form at high abundances through abiogenic sources on terrestrial exoplanets are shown. For Earth (left), observing O_2, O_3, CH_4, CO_2, and H_2O without CO, indicates that Earth's O_2 has a biological source. In the other two panels, if the molecules that are circled are detected in the atmosphere then the false positive mechanism could be determined. Similarly, if the molecules that are crossed out at the bottom of the figure are not detected, then this can be used to discriminate between biogenic and abiogenic O_2. The right hand panel provides an example of this for a desiccated CO_2-rich exoplanet orbiting an M dwarf star. If the CO_2 and CO have been detected, but H_2O has not, then it is a sign that the O_2 in the atmosphere has been produced from CO_2 photodissociation, rather than life. Figure adapted from Meadows *et al.* (2018b).

The credibility of a potential biosignature being attributed to life can be evaluated through characterisation of exoplanet properties, evaluating the environmental context of the biosignature, and ruling out false positives (Catling *et al.*, 2018; Lisse *et al.*, 2020), as well as demonstrating chemical disequilibrium on the exoplanet (Krissansen-Totton *et al.*, 2016). For example, on Earth, atmospheric O_2 and CH_4 are in chemical disequilibrium and should quickly react to form CO_2 and H_2O, implying a biological source for these gases (Schwieterman *et al.*, 2018b). Fig. 1.5 shows examples of how the detection and non-detection of various molecules can be used to infer a false positive biosignature mechanism (Meadows *et al.*, 2018a). In the case of a desiccated M dwarf exoplanet, the detection of CO and CO_2 without detecting water would indicate that the detected O_2 arises from an abiogenic source.

1.5 Exoplanet observations

Establishing the composition of an exoplanet's atmosphere will require either transmission spectra or direct imaging spectra observations, or a combination of both. These measurements can also extract information regarding the atmospheric pressure and temperature.

Transmission spectra are derived from spectroscopy measurements of a star whilst the exoplanet transits. If an exoplanet has an atmosphere, then that atmosphere will block out starlight to a level depending on the chemical species present in the atmosphere, their abundance with altitude, and their absorption strength which varies with a wavelength dependence.

Throughout the orbit, the exoplanet will show varying fractions of its illuminated face. Direct imaging spectra are integrated flux measurements from the exoplanet's observable disk, where typically the stellar light needs to be subtracted to find the contribution from the exoplanet alone, and this can be achieved

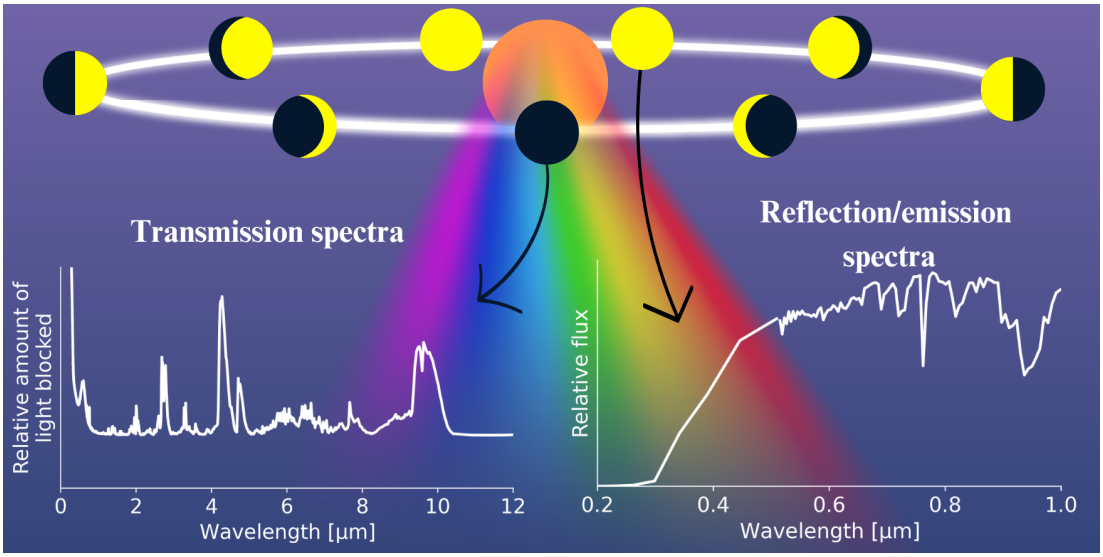

Figure 1.6: A cartoon of an exoplanet in an edge-on orbit around a star is shown. An example transmission spectrum (left) and a direct imaging spectrum (right), based on the pre-industrial Earth, are shown. Depending on the wavelength range, direct imaging spectra will be comprised of reflection or emission spectra, or both. A transmission spectrum (which can only be taken during a primary transit) probes the terminator of the exoplanet's atmosphere, whilst direct imaging spectra (which can be taken throughout the orbit) probes the observable disk of the exoplanet. As the exoplanet orbits the star, varying fractions of the illuminated face are observable, changing the amount of light seen by the observer.

through the use of a coronagraph that blocks out the starlight. For a terrestrial exoplanet like the Earth, at ultraviolet (UV), visible (VIS), and near-infrared (NIR) wavelengths, reflection spectra can be observed because reflection dominates the total received flux over emission, which begins to dominate in the mid-infrared. Examples of transmission spectra and direct imaging spectra are shown in Fig. 1.6.

The first exoplanet to have its atmosphere observed was HD 209458 b (Charbonneau *et al.*, 2002), a 'hot-Jupiter'. Hot Jupiters are exoplanets with a mass similar to Jupiter and an orbital period < 10 days. More recently, observers have tried to find terrestrial exoplanets with atmospheres. For example, Demory

et al. (2016) observed the super-Earth 55 Cancri e and found evidence of a 'hot spot shift' (where the warmest part of the surface is not located at the substellar point, the region with maximum irradiance) which was potentially due to atmospheric rotation or low-viscosity magma flows. Water vapour was found in the atmosphere of an 8 Earth mass (8 $M_{\oplus}$) exoplanet (Tsiaras *et al.*, 2019; Benneke *et al.*, 2019), but whether the interior is rocky is uncertain (Madhusudhan *et al.*, 2020). Kreidberg *et al.* (2019) found no evidence of a thick atmosphere on LHS 3844b, a terrestrial exoplanet in an 11-hour orbit around the red dwarf LHS 3844, which is at a distance of 15 parsecs from Earth. Additionally, de Wit *et al.* (2018) used Hubble Space Telescope (HST) observations to determine that the terrestrial exoplanets TRAPPIST-1 d, e and f do not have cloud-free hydrogen-dominated atmospheres, but could not rule it out for TRAPPIST-1 g.

The James Webb Space Telescope (JWST) is scheduled to observe terrestrial exoplanet atmospheres around M dwarfs, particularly in the TRAPPIST-1 system in the near future (e.g. TRAPPIST-1e between June 16$^{\text{th}}$ - October 28$^{\text{th}}$, 2023), improving on the sensitivity when compared to previous measurements (Lustig-Yaeger *et al.*, 2019). When these observations are taken, the exoplanet community will need to use computational models (such as retrieval models and 1D and 3D climate models) to characterise the atmospheres and climates of such exoplanets.

1.6 Climate and atmospheric modelling

Observatories, such as JWST and the extremely large telescopes (ELTs), will eventually return precise transmission spectra and direct imaging spectra observations of terrestrial exoplanets. Until then, the exoplanet community has the solar system terrestrial planets to benchmark against, as well as computational studies through a variety of numerical models to better understand planetary climates and atmospheres. The models used range in complexity from energy

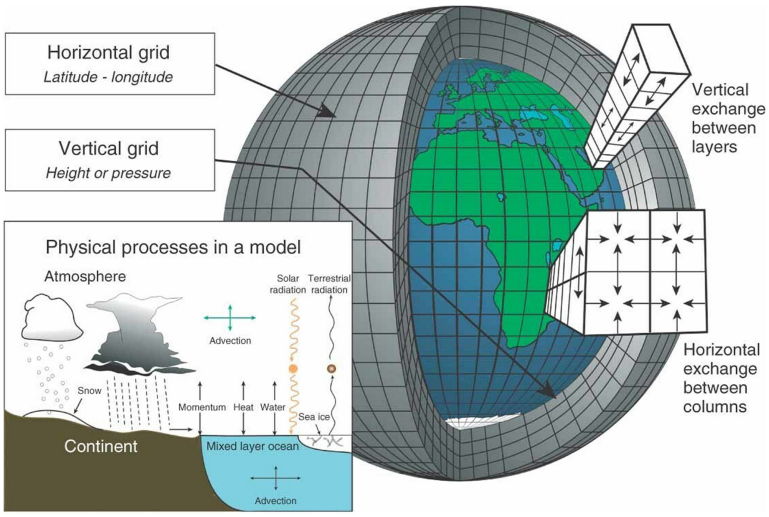

Figure 1.7: The figure shows a schematic representing a 3D Global Climate Model (GCM). 3D GCMs split up the surface and atmosphere of a planet into a 3D grid, with longitude, latitude, and pressure or height coordinates. Various physical processes can be accounted for, and these include, but are not limited to: radiative transfer; the flow of air parcels; evaporation, cloud formation and precipitation; chemistry. Figure from Edwards (2011).

balance models (EBMs), to the more computationally expensive, 3D GCMs and 3D chemistry-climate models. 1D and 2D models of various types are of intermediate complexity.

EBMs treat the planet as if it has a single surface temperature (Edwards, 2011), as shown in Eq. 2.3. They are useful for studying the effect of individual parameters, like stellar effective temperature, on climate (Shields, 2019). 1D models usually have a vertical coordinate in terms of altitude or pressure above the surface. These models can simulate chemical reactions, vertical motion, and heating rates. Examples include VULCAN (Tsai *et al.*, 2017) and the Kasting 1D model and its derivatives (Kasting & Donahue, 1980; Pavlov *et al.*, 2003; Kaltenegger & Sasselov, 2010; Arney *et al.*, 2016). There is also a 1D version of the 3D Laboratoire de Météorologie Dynamique Generic Climate Model (LMD-g; Yassin Jaziri *et al.*, 2022). In comparison to 1D and 3D models, 2D models (lon-

gitude–height coordinates) have been sparsely used in exoplanet science (Baeyens *et al.*, 2021; Song *et al.*, 2022).

Typically, a 3D GCM is a time-dependent three-dimensional (coordinates for each grid cell consist of longitude, latitude, height or pressure) model of a planet which calculates physical processes occurring in the atmosphere-ocean system (Shields, 2019). In the atmosphere, GCMs calculate fluid motions, radiative transfer, and in some cases, chemistry, outputting the average physical attributes of each grid cell (Shields, 2019). GCMs include a 'dynamical core' which predicts the motion of air parcels in the atmospheric grid and include sub-grid scale processes (e.g. cloud formation) through 'parameterisations' that use mathematical formulae to represent the physical processes rather than resolving them explicitly (Edwards, 2011). A schematic representing a 3D GCM is shown in Fig. 1.7. Commonly used 3D models in the field of exoplanets include the Community Atmosphere Model (CAM; Wolf *et al.*, 2017), the Exo-Flexible Modelling System (Exo-FMS; Hammond *et al.*, 2020), ExoCAM (Wolf *et al.*, 2022), Laboratoire de Météorologie Dynamique Generic Climate Model (LMD-g; Yassin Jaziri *et al.*, 2022), Resolving Orbital and Climate Keys of Earth and Extraterrestrial Environments with Dynamics (ROCKE-3D; Way *et al.*, 2017), the Unified Model (UM; Sergeev *et al.*, 2020), and the Whole Atmosphere Community Climate Model (WACCM; Chen *et al.*, 2019; Cooke *et al.*, 2023). Many 3D GCMs that are used to simulate exoplanets (e.g. ROCKE-3D, ExoCAM, and UM) have been adapted from models originally designed to model Earth, whilst some have been built from first principles (e.g. THOR; Mendonça *et al.*, 2016).

1D, 2D, and 3D models that resolve the vertical structure of the exoplanet's atmosphere can be used to predict possible atmospheric observables, such as broadband emission phase curves and transmission spectra, with radiative transfer forward models employed for this purpose. If these radiative transfer mod-

els use data from climate models which resolve horizontal dimensions (latitude-longitude), then the influence of spatial inhomogeneities can be estimated. Furthermore, as I will show in this thesis, ingesting time-dependent data can help to evaluate how climate variability will impact spectra at different observational epochs.

1.7 Forward modelling of exoplanet observations

Forward modelling of exoplanet spectra is used for interpreting observations, the planning of future telescope missions (The LUVOIR Team, 2019; Gaudi *et al.*, 2020), and determining how detectable gases such as O_3 and CO_2 will be for Earth-analogues (Alei *et al.*, 2022). Forward models are also used in retrieval models (Konrad *et al.*, 2022), which are models that aim to place limits on atmospheric pressure-temperature and abundance profiles based on observations (Madhusudhan & Seager, 2009).

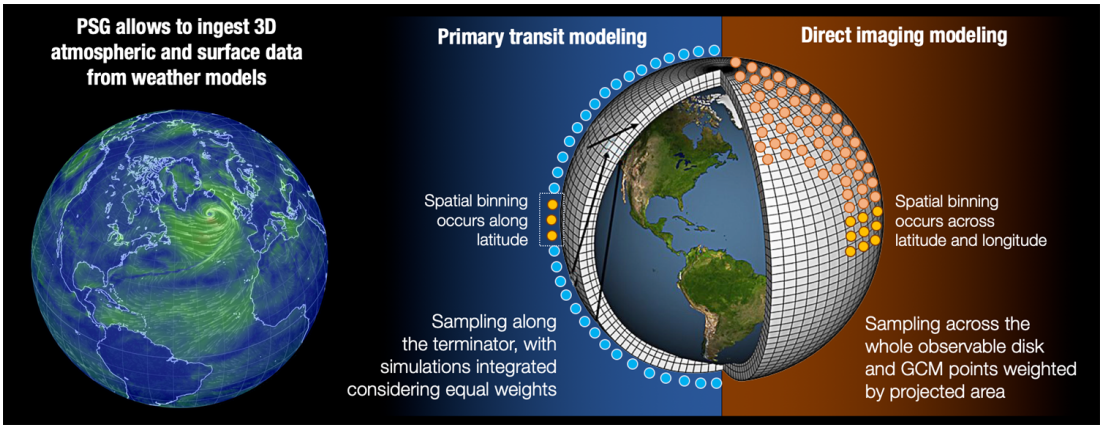

Figure 1.8: The forward modelling capabilities of the Planetary Spectrum Generator (PSG; Villanueva *et al.*, 2018) are displayed. 3D GCM data can be uploaded to the Global Emission Spectra application (GlobES) in PSG to compute transmission spectra (calculated from profiles at the terminator) or direct imaging spectra (calculated by integrating across the observable disk). Image credit: NASA.

Forward models take as input the temperature and pressure profile of the atmosphere, the chemical composition, and any surface features. They consider telescope properties such as wavelength coverage, spectral resolving power, diameter, and sources of noise. A schematic of the forward modelling capabilities of the Planetary Spectrum Generator (PSG), which is used in this thesis, is shown in Fig. 1.8.

In the coming decades, comprehensive climate models, forward models, and retrieval software, will be vital for the analysis of exoplanet atmospheric observations (Shields, 2019). The combination of climate modelling and observational forward modelling has been used extensively in the exoplanet community to investigate Earth-analogue, Earth-like, and Venus-like exoplanets (Lustig-Yaeger *et al.*, 2019). This methodology has been implemented to study Earth's past climates (4 billion years ago - present day). Earth spent billions of years with atmospheric states very different from the one we breathe today, so these periods are relevant templates to be considered in the search for habitable worlds.

1.8 Earth's atmospheric history

Atmospheres in the solar system are continuously evolving and Earth's atmosphere is no exception; geological evidence shows that the the chemical composition of Earth's atmosphere has changed since its formation. From an anoxic (oxygen deficient) atmosphere at the start of the Archean eon (4 – 2.4 Gyr ago), Earth's atmospheric oxygenation has varied through time, with O_2 now the second most abundant constituent of the atmosphere (21% by volume, which is uniquely high amongst the known atmospheres) after N_2. The Archean eon was mostly an anoxic atmosphere with oxidised gases (dubbed a 'weakly reducing' atmosphere; Catling & Zahnle, 2020), like CO_2, and reducing chemical species, such as CH_4. Reducing chemical species donate electrons to oxidising species

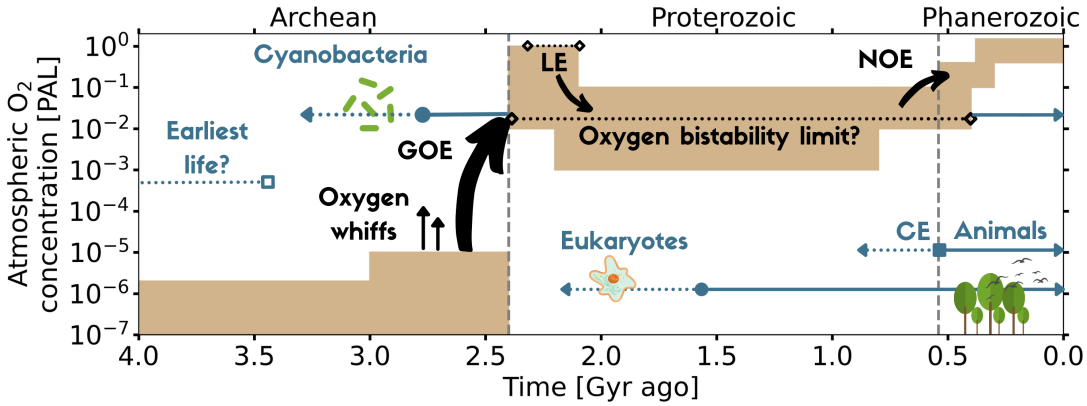

Figure 1.9: Geochemical evidence and modelling constraints place approximate limits on the concentration of O_2 against time in the past, shown by the brown boxes. Grey-blue lines show approximate timelines for the appearance of the earliest life forms (Dodd *et al.*, 2017; Schopf *et al.*, 2018), the evolution of cyanobacteria (Sánchez-Baracaldo & Cardona, 2020), eukaryotes (Han & Runnegar, 1992; Retallack *et al.*, 2013), and the origin of animals (Sperling *et al.*, 2010; Bobrovskiy *et al.*, 2018), with dotted lines showing a period of estimated emergence, and solid lines showing generally accepted presence. The grey-blue square symbol marks the Cambrian explosion (CE). Black arrows show changes in atmospheric oxygenation, with major geological episodes of increasing atmospheric oxygenation indicated: the Great Oxidation Event (GOE) and the Neoproterozoic Oxidation Event (NOE). Black dotted lines show the Lomagundi Event (LE) and a proposed oxygen bistability limit at 1% PAL (Gregory *et al.*, 2021). The LE was the largest carbon isotope excursion in Earth's history, resulting in major carbon burial during this period (Bachan & Kump, 2015). Dates and magnitude curves are not exact.

which accept electrons. In the latter stages of the Archean, temporary periods of increased oxygenation existed, and these are known as 'oxygen whiffs' (Anbar *et al.*, 2007; Kaufman *et al.*, 2007; Kendall *et al.*, 2015; Catling & Zahnle, 2020).

When cyanobacteria evolved around ~ 2.8 Ga (1 Ga = 1 billion years ago) and produced O_2 through photosynthesis (Godfrey & Falkowski, 2009), the Earth's atmosphere and ocean became progressively more oxygenated. A major shift towards higher atmospheric O_2 occurred at the end of the Archean ~ 2.4 Ga: the Great Oxidation Event (Warke *et al.*, 2020). During the Proterozoic eon (2.40 –

0.541 Gyr ago), O_2 values are estimated to have been between 0.001% and 100% the present atmospheric level (PAL; e.g. see Steadman *et al.*, 2020; Lyons *et al.*, 2021). A second rise in atmospheric oxygen to near-modern levels took place at the close of the Precambrian (Lyons *et al.*, 2021), known as the Neoproterozoic Oxidation Event (NOE). These rises in oxygen set the scene for an oxygenated biosphere and the eventual evolution of oxygen-dependent animals (Cole *et al.*, 2020). Fig. 1.9 shows this oxygenation timeline.

Ultimately, Earth's history is one possible trajectory that habitable zone exoplanets could take if they hosted life. Given the vast parameter space of exoplanets already discovered, habitable conditions may be present on a wide variety of exoplanets. Future observations will strive to not only locate potentially habitable exoplanets, but to characterise their atmospheres and surface conditions.

1.9 Future outlook and upcoming observations

The hunt for new rocky worlds will expand as more observatories join the quest for their discovery. The PLAnetary Transits and Oscillation of stars (PLATO) mission aims to observe exoplanetary transits around bright stars (visual magnitudes brighter than 10) in order to find more HZ terrestrial exoplanets (Rauer *et al.*, 2016) which will be targets for current and planned observatories. PLATO is expected to launch in 2026[1]. The James Webb Space Telescope (JWST), which launched in 2021, is set to observe terrestrial exoplanets, including the TRAPPIST-1 system. There is a new class of ground-based extremely large telescopes being constructed, and these will be able to observe terrestrial exoplanets. In 2026, construction of the the 39.1 m diameter ground based Extremely Large Telescope (ELT; Gilmozzi & Spyromilio, 2007) is due to be completed. In addition, the Giant Magellan Telescope (equivalent resolving power of a 24.5 m

[1] https://www.esa.int/Science_Exploration/Space_Science/Plato_factsheet

telescope; Fanson *et al.*, 2020) is scheduled to be built, and although the timeline is unconfirmed[2], the Thirty Metre Telescope (30 m diameter) is also planned. Additionally, the proposed space-based 6 m IR/O/UV telescope, recently prioritized by the 2020 Astrophysics Decadal Survey (National Academies of Sciences & Medicine, 2021), and informed by the LUVOIR and HabEx concepts, will be used to search for and characterise Earth-like exoplanets. The Large Interferometer for Exoplanets (LIFE) mission concept, if selected, will use mid-infrared observations to do the same. These upcoming observatories make the next few decades a very exciting time to be involved in exoplanetary science.

1.10 This thesis

The Earth is the only known example of both a habitable and inhabited planet, and it has successfully hosted life for billions of years. This thesis uses WACCM6 to simulate a variety of different (exo)planetary climates, each motivated by Earth's past. Whilst each simulation is different, all the atmospheres considered are oxygenated. Fluctuations in O_2 have shaped Earth's history, and now O_2 is of critical importance to the modern atmosphere, giving life energy, and shielding life from UV radiation through the photochemically generated O_3 layer. This thesis explores the connection between O_2 and (exo)planetary climates through different scenarios based on Earth's history, and habitable zone terrestrial exoplanets that have been located around M dwarf stars.

The next Chapter introduces important concepts regarding planetary atmospheres and their chemistry, in addition to describing the theory behind direct imaging and transmission spectra observations. A description of numerical methods can be found in Chapter 3.

Inspired by Earth's geological history, I present 3D chemistry-climate sim-

[2] https://www.nature.com/articles/d41586-022-01926-2

ulations for the first time over various O_2 concentrations (0.1% – 150% PAL) using WACCM6 (see Chapter 4). I describe the effects these O_2 changes have on the O_3 layer and various atmospheric constituents, including CH_4, an important greenhouse gas. The results challenge previously held assumptions in the Earth science and astrobiology communities. I briefly discuss a model intercomparison which aims to locate where discrepancies between 1D and 3D models that simulate oxygenated planets arise.

Assuming these simulated states are Earth-analogue exoplanets around Sun-like stars, I use PSG to compute transmission spectra for scenarios between 0.1% – 150% PAL of O_2 (see Chapter 5). Additionally, I present direct imaging predictions for the following telescope concepts: LUVOIR A, LUVOIR B, and HabEx with a starshade. I investigate how atmospheric composition, clouds, and surface albedo affect the annual and seasonal variability in synthetic high-contrast imaging observations.

Several exoplanets have now been proposed to be potentially habitable. I introduce simulations of the exoplanets TRAPPIST-1e and Proxima Centauri b in Chapter 6. They are both supposedly situated in the habitable zones of the M dwarf stars they orbit, and due to their relatively close proximity with their host stars, I assume the exoplanets are tidally locked. I vary the position of the substellar point as well as the composition. Furthermore, I utilise two different predicted spectral energy distributions for the M dwarf star TRAPPIST-1, where the UV fluxes vary by up to a factor of 5000 in specific wavelength bins. The composition and dynamics of these exoplanet simulations are analysed and compared to previous work.

Transmission, reflection, and emission spectra observations for TRAPPIST-1e are computed in Chapter 7, demonstrating how different compositions can result in ambiguous interpretations of observations when the UV portion of the

stellar spectrum is uncertain. I estimate the time variability that may be found in both transmission spectra and direct imaging spectra observations, examining the possible impact such climate changes could have on future observations that JWST will make of TRAPPIST-1e.

Finally, in Chapter 8, I summarise the thesis and suggest avenues for future work to improve both modelling efforts and the interpretation of future observations.

Chapter 2

(Exo)planetary atmospheres

The physical theories underlying atmospheric science are utilised to develop climate models, which are applied to predicting the properties of exoplanets. Light propagating through an exoplanet's atmosphere can be used to determine the atmospheric pressure-temperature profile, constrain surface features (e.g. oceans, land, ice), and to detect the presence of various gases, such as H_2O and O_3. As astronomers move towards characterising terrestrial exoplanets, insights into the formation history of the the diverse range of exoplanetary systems discovered so far, and their potential for hosting habitable environments, will be sought through these atmospheric measurements; in this process we may find answers to fundamental questions about life in the universe.

2.1 Gases

When modelling planetary atmospheres, it is common to assume that they exist in a state of hydrostatic equilibrium, with the gases comprising them obeying the principles of the ideal gas law. The hydrostatic approximation assumes that only the gravitational and pressure-gradient forces are important for vertical displacements of air parcels in atmospheres (Brasseur & Solomon, 2005). The ideal gas law is an approximation which can be successfully used to describe how gases

behave in planetary atmospheres. This universal law assumes each gas molecule behaves as a hard sphere and that the particles do not interact, such that the law is independent of the chemical species in the gas. It is given by

$$pV = Nk_BT, \tag{2.1}$$

where the total volume occupied by the gas is V, N is the total number of particles in the gas at pressure p and temperature T, and k_B is the Boltzmann constant. Provided the temperature is approximately constant with altitude z, the pressure $p(z)$ can be shown to vary with altitude such that

$$p(z) \approx p_0 \exp^{\frac{-z}{H}}, \tag{2.2}$$

where p_0 is the surface pressure at $z = 0$, and H is the scale height given by $H = k_BT/\mu g$, where μ is the mean molecular mass of the atmosphere. Eq. 2.2 assumes that atmospheric temperature is approximately constant with height. The temperature is controlled by the incoming stellar radiation, radiative transfer, transport of heat, and the composition of the atmosphere.

2.2 Stellar radiation

The simplest estimation of a planetary surface temperature is the calculation of its equilibrium temperature ($T_{\rm eq}$) through consideration of a planet in orbit around a star. Assuming that the star and its orbiting planet are blackbodies, then $T_{\rm eq}$ for the planet is given by

$$T_{\rm eq} = T_* \sqrt{\frac{R_*}{2a}} (1 - A)^{1/4}, \tag{2.3}$$

where T_* is the stellar effective temperature, R_* is the stellar radius, A is the Bond

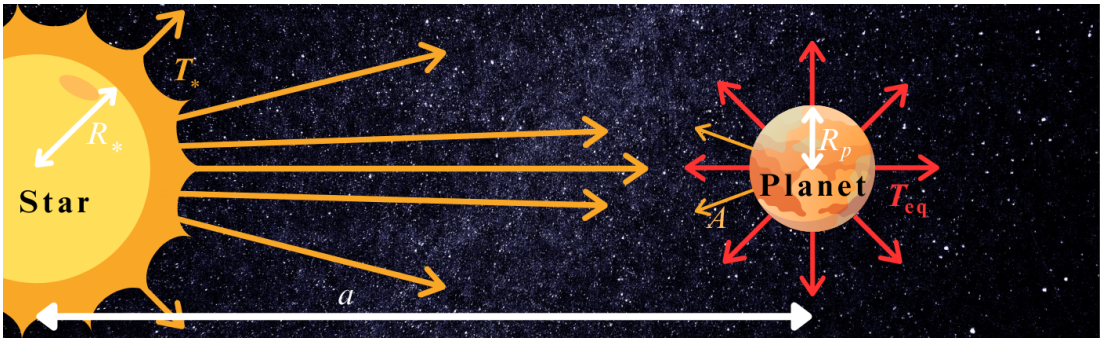

Figure 2.1: A cartoon of a planet with radius R_p, which orbits a star with stellar effective temperature T_*, is shown. The semi-major axis (half of the major axis of an ellipse, which is the longest diameter that passes through the two foci of the ellipse) of the orbit is denoted by a. Due to the irradiation from the star, the intensity of which decreases via the inverse square law, the planet heats up to an equilibrium temperature, $T_{\rm eq}$. Additionally, the planet reflects a fraction of incident energy, A (the Bond albedo). $T_{\rm eq}$ is calculated via Eq. 2.3.

albedo of the planet (the fraction of reflected light to incoming light), and a is the semi-major axis of the planet's orbit. Such a situation is depicted in Fig. 2.1. The intensity of the Sun's radiation peaks in the visible, whilst for cooler stars, the peak will be shifted to longer wavelengths, as shown in Fig. 2.2. The spectral radiance of blackbodies is given by the Planck function $B(\lambda, T)$, such that

$$B(\lambda, T) = \frac{2hc^2}{\lambda^5} \frac{1}{\exp(\frac{hc}{\lambda k_B T}) - 1}, \tag{2.4}$$

where h is Planck's constant, c is the speed of light, and λ is the wavelength. Whilst Eq. 2.3 gives a rough estimate for the mean temperature of a planet, in reality, neither the star, nor the planet, behave as true blackbodies.

The incident flux in each wavelength interval will be deposited at different points in the planetary system (e.g. surface, oceans, and atmosphere) or reflected and scattered away back into space. The transmission of electromagnetic radiation through a medium (known as radiative transfer), in this case the atmosphere, regulates atmospheric and surface temperatures, as well as chemistry

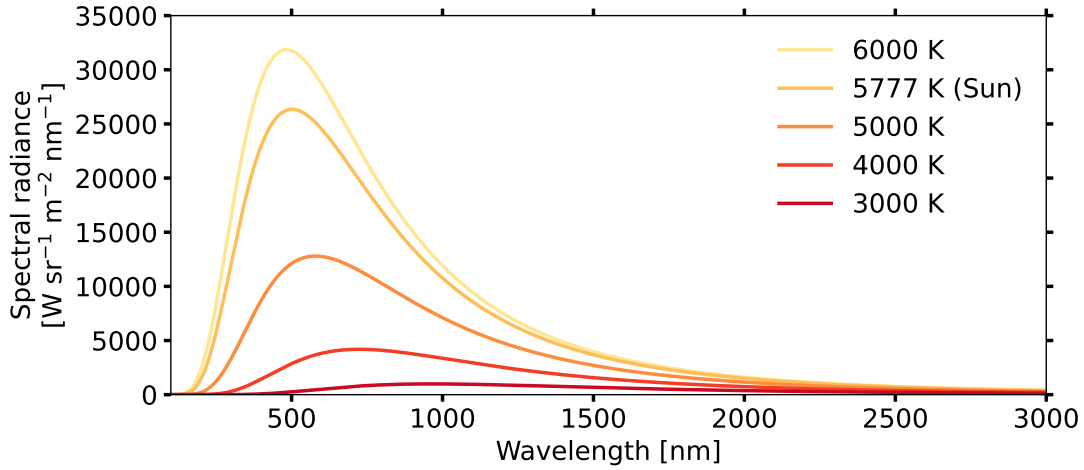

Figure 2.2: The spectral radiance of stars is shown (in units of W sr^{-1} m^{-2} nm^{-1}), assuming they behave as blackbodies (they emit radiation as given by the Planck function: e.g. Eq. 2.4). The Sun, which has a stellar effective temperature of 5777 K, is shown alongside stars with a stellar effective temperature of 3000 K, 4000 K, 5000 K, and 6000 K. Cooler stars are redder and have a lower luminosity, with their peak emission shifting to longer wavelengths.

and dynamical behaviour. Therefore, accurate radiative transfer calculations are crucial for robust modelling of planetary atmospheres.

2.3 Radiative transfer

Incoming energy in the form of a photons can result in photoionisation, photodissociation, or absorption. Photoionisation results in the ejection of an electron, whilst photodissociation splits a molecule into two species through the breaking of a chemical bond. When a photon is absorbed, the chemical species can be excited through rotational, vibrational or electronic transitions which are quantised (Caballero, 2014), with molecular motion in a gas categorised as translational, rotational, and vibrational (Brasseur & Solomon, 2005). Vibrational transitions are where the atoms in the molecule oscillate periodically, rotational transitions occur when the molecule rotates around an axis, and translational transitions

correspond to movement of the molecule in three-dimensional space (Visconti, 2016). An excited molecule can emit a photon, or collide with other molecules in the gas at which point its kinetic energy is transformed into heat, such that the temperature of the gas increases (Caballero, 2014).

The energy needed for the occurrence of electronic transitions is relatively large ($\sim 1 - 10$ eV), requiring photons in the UV and visible wavelength regions (Brasseur & Solomon, 2005). Vibrational transitions transpire in the near infrared ($\sim 10\,\mu$m, ~ 0.1 eV) and rotational transitions in the far infrared (~ 10 mm, $\sim 10^{-4}$ eV). Therefore, the energy levels of molecules, and the abundance and spatial distribution of those molecules, affect where energy is deposited in the Earth system.

Suppose a beam of monochromatic radiation with intensity I_λ and wavelength λ is propagating through a gas with mass density ρ and absorption coefficient k_λ, along a path with length s. The intensity change of the absorbed radiation dI_λ, travelling a distance ds, is given by

$$dI_\lambda = -I_\lambda \rho k_\lambda ds. \tag{2.5}$$

We can rearrange this and integrate between 0 and s to get

$$I_\lambda = I_0 \exp^{-\tau}, \tag{2.6}$$

where I_0 is the initial intensity of the beam, and $\tau = \rho k_\lambda s$ is the optical depth. Eq. 2.6 is known as the Beer-Lambert law (Beer, 1852), and it only accounts for absorption. If we now consider thermal emission from the gas too, then

$$dI_\lambda = B_\lambda(T)\rho k_\lambda ds - I_\lambda(s)\rho k_\lambda ds. \tag{2.7}$$

Thus, one can write the radiative transfer equation as

$$\frac{dI_\lambda}{d\tau} = B_\lambda(T) - I_\lambda. \tag{2.8}$$

To understand the propagation of radiation in the atmosphere, once must also account for scattering. Mie scattering assumes the scattering particles are homogeneous spheres (Mie, 1908) and depends on the refractive index of the medium, which is the ratio of the speed of light in a vacuum to the phase velocity of light in that specific medium. Mie scattering is used to define scattering where the wavelength of light is comparable to the particle size, and can therefore be used to express how visible light propagates through liquid water clouds, for instance. Rayleigh scattering is a specific solution to Mie theory, and describes the scattering of light when the radius of the particles causing scattering is much smaller than the wavelength of the incident photons (Rayleigh, 1899). The Rayleigh scattering cross section is proportional to r^6/λ^4, where r is the radius of the particle. This means that the gas molecules (predominantly O_2 and N_2 in Earth's modern atmosphere) will scatter incident stellar light at shorter wavelengths in greater proportion to longer wavelengths.

2.4 The greenhouse effect

When a terrestrial planet absorbs radiation, primarily in the UV, visible, and near-infrared ($\lesssim 4\,\mu m$), it heats up and radiates infrared energy in all directions. Greenhouse gases such as H_2O, CO_2, CH_4, O_3, and N_2O, absorb and emit in the infrared. At wavelengths longer than $4\,\mu m$, the quantity of Earth's emitted radiation exceeds the incident solar radiation (Mitchell, 1989). On Earth, spectral windows, such as between $8\,\mu m$ and $14\,\mu m$, allow for the infrared fluxes from the warm surface to be emitted to space, whilst at wavelengths where atmospheric

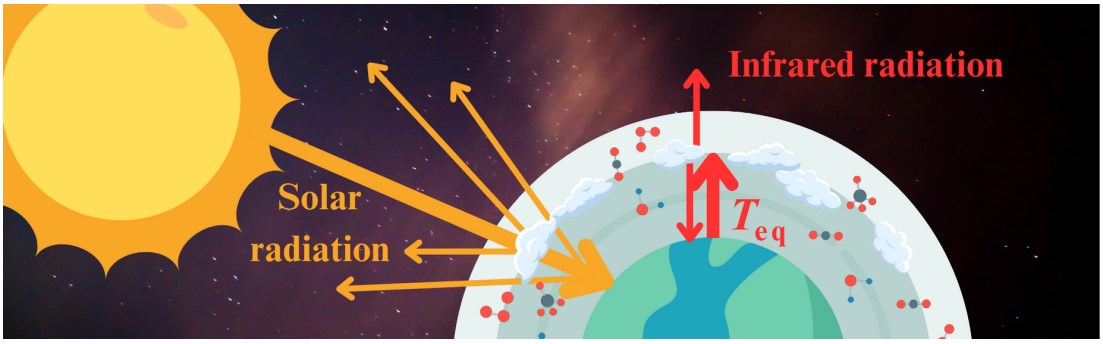

Figure 2.3: A cartoon of solar radiation (orange) incident onto a planet is displayed. Some of the solar radiation is scattered and reflected away from the surface, air, and clouds, reducing the amount of incident energy that warms the planet. The planet heats up to an equilibrium temperature ($T_{\rm eq}$) which is much lower than the stellar effective temperature (T_*) and radiates infrared radiation (red) back out into space. This infrared energy is absorbed by molecules in the atmosphere ('trapping' the outgoing radiation), so-called greenhouse gases like CO_2 and H_2O, which re-emit this radiation to space and back to the surface. The radiation that is emitted back to the surface warms the planet above $T_{\rm eq}$. This is known as the greenhouse effect.

molecules strongly absorb (e.g. CO_2 at 15 µm), the observed radiation emanates from the upper troposphere where the atmosphere is colder than the surface (Brasseur & Solomon, 2005). The radiation that travels downwards towards the planet further warms the surface. This mechanism is known as the greenhouse effect, an illustration of which is shown in Fig. 2.3.

2.5 Dynamics

Atmospheric dynamics exert a control over weather patterns, cloud formation and distribution, and the transport of chemical constituents. The movement of air parcels in the atmosphere is set by the balance of forces acting on them, including the centrifugal force, the Coriolis force, and the pressure gradient force, in addition to atmospheric waves.

Differential stellar heating, which depends on the obliquity and eccentricity

of a planet, occurs across its atmosphere and surface (Read *et al.*, 2018). For instance, meridional (south-north) circulation occurs because the poles are colder than the equator, giving rise to a pressure gradient. Atmospheric circulation then distributes heat from hotter to colder regions.

The Coriolis force is a fictitious force that results from the Earth's rotation and the fact that the Earth's surface is used as a reference frame, acting to deflect the path of air parcels and restrict meridional circulation (Brasseur & Solomon, 2005). Geostrophic balance, where Coriolis accelerations equal the horizontal pressure gradient force, is expected for planets that rotate relatively quickly (e.g. Earth; Read *et al.*, 2018). Zonal (east-west) winds result from the conservation of angular momentum when the Coriolis effect acts on meridional circulation because the planet's surface rotates at a lower velocity at higher latitudes (Read *et al.*, 2018). When the planet rotates relatively slowly, centrifugal accelerations dominate over the Coriolis force (e.g. Venus; Read *et al.*, 2018).

Atmospheric waves are a significant source of dynamical variability, including planetary scale waves (Rossby waves) and gravity waves. Rossby waves are a consequence of latitudinal gradients in potential vorticity (Baldwin *et al.*, 2001), a quantity that represents the vertical component of angular momentum (Brasseur & Solomon, 2005). Gravity waves, which are produced when air parcels are vertically perturbed in a stratified fluid and opposed by buoyancy (Plougonven & Zhang, 2014), generate dynamical variability on Earth, as described in section 2.7.2.

2.6 Chemistry

A chemical reaction is a process where a chemical species is transformed to another. It can involve a single reactant or multiple. The rate of reaction depends on the rate coefficient k (a constant which quantifies how quickly the reaction

proceeds) and the concentration of each species involved in the reaction. Homogeneous reactions involve chemical species in the same phase (e.g. all reactants are in the gas phase), whereas heterogeneous reactions occur between reactants that are in different phases (e.g. gas and liquid). The majority of gas phase reactions that take place in atmospheres can be described by three types: photolysis, bimolecular, and three-body reactions (Visconti, 2016). Considering a gas molecule X, with concentration [X], the rate of change of its concentration is given by

$$\frac{d[\mathrm{X}]}{dt} = \begin{cases} -J_{\mathrm{X}}[\mathrm{X}], & \text{(photolysis)}, \\ -k_{\mathrm{XY}}[\mathrm{X}][\mathrm{Y}], & \text{(bimolecular)}, \\ -k_{\mathrm{XYM}}[\mathrm{X}][\mathrm{Y}][\mathrm{M}], & \text{(three-body)}, \end{cases} \tag{2.9}$$

where t is time, [Y] is the concentration of species Y, [M] is the concentration of any third body gas molecule, J_{X} is the photodissociation frequency, k_{XY} is the bimolecular rate constant, and k_{XYM} is the three-body rate constant. Many reactions have a temperature dependent rate constant, given by the Arrhenius equation

$$k = C \exp^{(-E_a/k_B T)}, \tag{2.10}$$

where C is a constant (which is experimentally determined, but approximately represents the collision rate constant, and can vary depending on temperature; Brasseur & Solomon, 2005), and E_a is the activation energy, the minimum energy input required for a reaction to take place. Note that not all rate coefficients follow this formulation.

Atmospheric photodissociation is an endothermic chemical reaction that breaks chemical bonds (North & Erukhimova, 2009). It is triggered by the absorption of a photon by a particular species XY, and this results in that constituent entering

an electronically excited state, XY^* (Brasseur & Solomon, 2005). XY^* is typically unstable, and can lead to ionisation (loss of an electron), fluorescence (emission of a photon), or dissociation, the latter of which will be considered here. The photodissociation coefficient can be calculated in a wavelength region $(\lambda_1 - \lambda_2)$ by considering the wavelength dependence of the cross section σ_{XY} (the cross section describes the probability that a photon of wavelength λ will photodissociate that molecule) and the photon flux I at an altitude z in the atmosphere (Chipperfield & Arnold, 2015), such that

$$J_{XY}(z) = \int_{\lambda_1}^{\lambda_2} \sigma_{XY}(\lambda) I(z, \lambda) d\lambda. \tag{2.11}$$

The distribution of chemical species and their abundances are set by chemical reactions and atmospheric dynamics. To understand the relative importance of chemistry and transport for a chemical species, it is useful to think of a chemical lifetime τ_{chem} (the time for the concentration of a species to decrease to $1/e$ of its starting concentration) and a transport lifetime τ_{tspt} (the rate at which a chemical species concentration changes due to transport). When $\tau_{\text{chem}} \ll \tau_{\text{tspt}}$, then the chemical species is in photochemical equilibrium and production and loss depend only on local concentration and reaction rate coefficients. On the other hand, if $\tau_{\text{chem}} \gg \tau_{\text{dyn}}$, then transport impacts the spatial distribution of chemical compounds, with atmospheric fluid motion reducing any spatial gradients in mixing ratios for that particular species (Brasseur & Solomon, 2005).

2.7 Earth's atmosphere

2.7.1 Structure

The vertical pressure-temperature profile of an atmosphere controls many processes in the atmosphere, including weather and cloud formation. It also influ-

ences how exoplanets will appear through telescopes (see section 2.9)

Earth's atmosphere has multiple layers (see Fig. 2.4), with the troposphere closest to the surface, and also the most dense (80% of its mass is in the troposphere), followed by the stratosphere, mesosphere, thermosphere, the exosphere and magnetosphere as the final atmospheric layer before interplanetary space. In the troposphere, the temperature decreases with increasing altitude until the

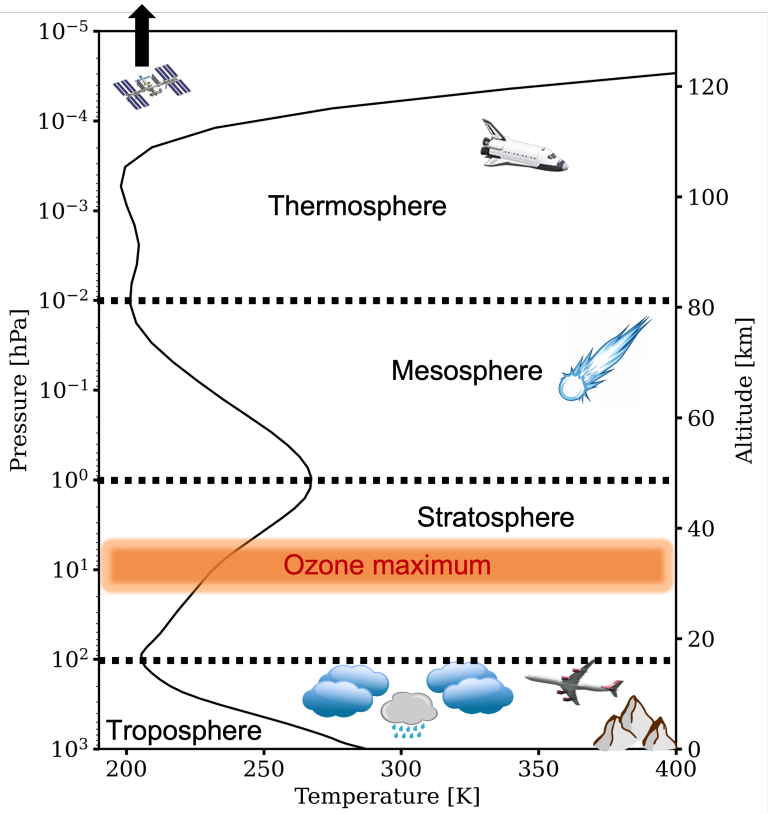

Figure 2.4: The atmospheric structure of the Earth is depicted, with altitude above the surface (in km) and atmospheric pressure (in hPa) plotted on the vertical axis against temperature in kelvin. Separated by temperature inversions, four atmospheric layers are shown: the troposphere (the densest region which contains around 80% of the atmospheric mass), the stratosphere (containing approximately 90% of atmospheric O_3), mesosphere, and thermosphere. The horizontal dotted lines approximately mark the tropopause, stratopause, and mesopause, from bottom to top, respectively.

tropopause, because rising air parcels expand and cool adiabatically (no heat transfer). The temperature decreases at a lapse rate Γ, given by

$$\Gamma = -\frac{dT}{dz}. \tag{2.12}$$

The height of the tropopause at the equator is $\approx$ 16 km, whilst it is only $\approx$ 8 km at the poles (Brasseur & Solomon, 2005). The tropical regions near the equator receive the largest amount of irradiation, whilst the poles receive the lowest amount due to the angle of the Sun and the longer path length through the atmosphere that the light travels through, which increases the optical depth and reduces the intensity of light reaching the surface, as in Eq. 2.6. In the stratosphere, temperature increases with altitude as a consequence of heating from the absorption of UV radiation by O_3 up until the stratopause. Another thermal inversion occurs here, giving rise to the mesosphere, where the coldest atmospheric temperatures exist (Lübken *et al.*, 1999). Heating in the thermosphere comes from solar extreme ultraviolet radiation (EUV; wavelengths between 10 – 100 nm) and UV radiation absorption by O_2, O_3, and CO_2 (Beig *et al.*, 2008). The exobase, which is the pressure in the atmosphere where the mean free path of molecules is approximately equal to the scale height H, marks the start of the exosphere (Johnson *et al.*, 2008). In the exosphere, planetary gases can escape to space if their radial velocity (set by the Maxwell-Boltzmann distribution which depends on mass and temperature) away from the planet is greater than the escape velocity (Johnson *et al.*, 2008), which is set by the mass of the planet and the distance from the centre of mass.

2.7.2 Circulation

On Earth, the meridional tropospheric circulation is distinguished by the Hadley, Ferrel, and polar cells, with one cell of each type in either hemisphere. The

Hadley cell consists of hot rising air in the tropics which proceeds poleward before descending at $\sim 30°$ latitude and returning to the equator. The polar cell carries warmer rising air from 60° which falls at the poles, whilst the Ferrel cell sits in-between at midlatitudes ($\sim 30° - 60°$) and its circulation proceeds counter to that of the Hadley and polar cells (Schneider, 2006). The zonal (east-west) tropospheric circulation is characterised by the trade winds in the tropics and westerlies at mid-latitudes, including a subtropical jet and a polar jet (Read

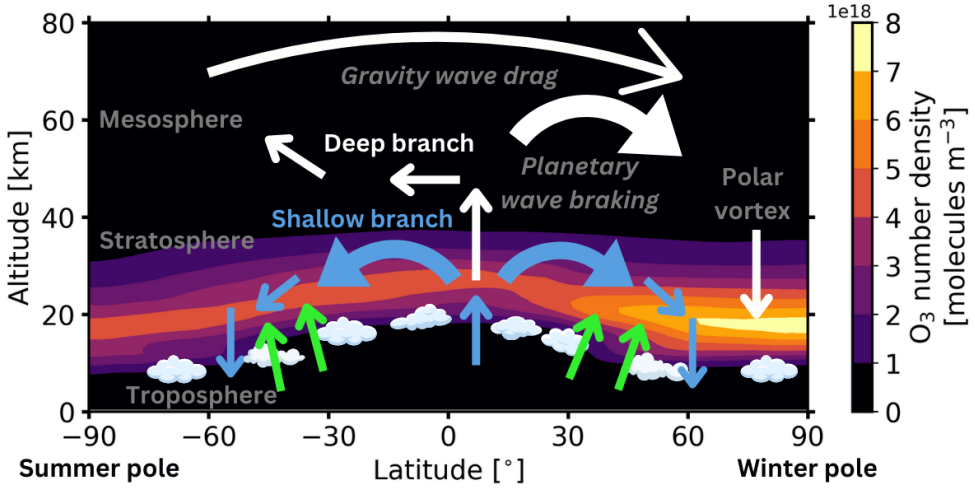

Figure 2.5: The time-averaged O_3 number density is plotted (in molecules m^{-3}) for January in a WACCM6 pre-industrial simulation, with the highest concentrations indicated in yellow and orange. The Brewer-Dobson circulation (BDC), denoted by blue ('shallow' branch) and white ('deep' branch) arrows, plays a critical role in transporting air from the tropics to both hemispheres in the lower stratosphere, followed by a downward movement through the tropopause. During the winter hemisphere (the northern hemisphere in January), the BDC exhibits a downward flow towards the poles in the middle and upper stratosphere, where planetary wave breaking takes place. In contrast, the summer hemisphere (the southern hemisphere in January) shows an upward and poleward flow in the upper stratosphere. In the mesosphere, gravity waves contribute the majority of wave energy, with the mesosopheric pole-to-pole circulation depicted by the arrow at the top of the figure. The green arrows indicate waves propagating from the troposphere into the stratosphere. This figure is adapted from North *et al.* (2014).

et al., 2018).

The zonal winds in the stratosphere typically blow westwards during summer time and eastwards in the winter (Brasseur & Solomon, 2005). The meridional circulation in the stratosphere is characterised by the Brewer-Dobson circulation, which can be generalised as rising air in the tropical stratosphere moving to higher latitudes and subsiding in the polar regions, with the the circulation depending on season, and what is referred to as a 'deep' (above $\sim$ 50 hPa) and 'shallow' (below $\sim$ 50 hPa) branch (Birner & Bönisch, 2011; Butchart, 2014). The deep branch has a transport time of several years, and is caused by planetary-scale Rossby waves breaking in the middle to upper stratosphere, whilst the shallow branch results from synoptic- ($\sim 1,000$ km) and planetary-scale Rossby waves breaking in the subtropical lower stratosphere, with transport times closer to a single year (Plumb, 2002; Birner & Bönisch, 2011). The mesospheric circulation is from the summer pole to the winter pole as a consequence of gravity wave drag (Murgatroyd & Singleton, 1961; Alexander *et al.*, 2010). There is more O_3 at higher latitudes resulting from the Brewer-Dobson circulation. A depiction of the Brewer-Dobson circulation is shown in Fig. 2.5.

Gravity, Kelvin (westward equatorial waves), and Rossby-gravity waves travel upwards at the equator and get absorbed in the stratosphere and mesosphere, dissipating their energy (Baldwin *et al.*, 2001; Maruyama, 1994). The interaction of these waves with the mean flow is what causes the quasi-biennial oscillation (QBO), a $\sim$ 28 month wind disturbance where equatorial easterly and westerly winds move downward in altitude (Dunkerton, 1997). This periodically results in anomalies of the equatorial mean abundances of trace gases, such as column changes of $\pm$10 Dobson Units (1 DU $= 2.687 \times 10^{20}$ molecules m^{-2}) for O_3 and mixing ratio variations of $\pm$0.4 ppmv for H_2O (Baldwin *et al.*, 2001).

2.7.3 Water

The behaviour of an atmosphere is altered when it contains a condensable gas, such as H_2O. H_2O is of profound interest in the search for potentially habitable exoplanets (see section 1.3). It can affect the propagation of radiation in exoplanetary atmospheres through absorption, but also through cloud formation, with clouds scattering and absorbing light.

On Earth, $\approx 70\%$ of the surface is covered in liquid water. Water evaporates and reduces the surface temperature of the ocean. Much of this evaporation occurs in the tropics, where heating from solar radiation is relatively large, leading to a disruption in tropospheric static stability (resistance to vertical displacements), which produces convection (Brasseur & Solomon, 2005). Convection results in parcels of air (often containing H_2O) rising swiftly before cooling. The H_2O eventually condenses and releases latent heat, which is an important source of atmospheric heating (Aubert, 1957; Rosenfeld, 2006).

The tropical tropopause layer (TTL) between the tropical troposphere and stratosphere is a region which is a few km thick. Atmospheric tracers (including H_2O) predominantly enter the stratosphere through the TTL (Fueglistaler *et al.*, 2009). As tropospheric water vapour passes into the colder stratosphere, it condenses into liquid water and ice. As a consequence of seasonal changes in TTL temperatures (colder in the boreal winter and warmer in boreal summer; Fueglistaler *et al.*, 2009), there is an 'atmospheric tape recorder' characterised by periodic variations in stratospheric H_2O concentrations of ± 1 ppmv (Mote *et al.*, 1996).

To condense into liquid or ice clouds, H_2O requires the presence of cloud condensation nuclei (CCN; Farmer *et al.*, 2015; Visconti, 2016). These particles come from sources such as dust, volcanic emissions, sea spray, and biomass burning (Farmer *et al.*, 2015). Various types of clouds exist, including low altitude

stratocumulus clouds, thin altostratus clouds, and high altitude cirrus clouds (Chen *et al.*, 2000), each of them important for the total radiative balance in the Earth system through reflection of shortwave radiation, or trapping of longwave radiation (Hartmann & Doelling, 1991; Chen *et al.*, 2000).

2.7.4 Atmospheric escape

The escape of gases from a planetary atmosphere is an irreversible process that leads to permanent atmospheric evolution. To escape to space, atmospheric gases first have to get to the exosphere. Lighter elements and compounds escape to space faster than heavier ones because the velocity distribution of lighter constituents means that they are more likely to travel at higher speeds, thus exceeding escape velocity more often. Hydrogen is the lightest element and escapes to space relatively easily. Many constituents that contain hydrogen (e.g. H_2O, CH_4) are broken down by photodissociation into H by the time they reach the exosphere. Assuming that upward diffusion is slow compared to the loss from the exosphere, then the hydrogen escape rate on Earth is given by the diffusion limiting rate (Kasting & Catling, 2003; Hunten, 1973), $\Phi_{\rm esc}$, such that

$$\Phi_{\rm esc} \propto f_{\rm T}({\rm H}), \tag{2.13}$$

where $f_{\rm T}({\rm H})$ is the total mixing ratio of hydrogen components at the homopause. $f_{\rm T}({\rm H})$ is weighted by the number of H atoms the hydrogen bearing molecules contain, given as

$$f_{\rm T}({\rm H}) = f({\rm H}) + 2f({\rm H_2}) + 2f({\rm H_2O}) + 4f({\rm CH_4})..., \tag{2.14}$$

where $f({\rm H})$ is the volume mixing ratio of H, and so forth for the other species.

In Earth's modern atmosphere, $f_{\rm T}({\rm H})$ doesn't decrease above the homopause.

Thus, hydrogen escape is limited because it escapes faster than the upward diffusion rate (Φ_{esc}) populates the exosphere with H atoms (Catling *et al.*, 2001), creating a 'hydrogen bottleneck' in the upper atmosphere.

The coldest parts of the TTL, known as the 'cold trap', freeze-out water as it propagates upwards (Fueglistaler *et al.*, 2009). Consequently, the H_2O mixing ratio entering the stratosphere is reduced from tropospheric levels: $f(H_2O)$ goes from $\sim$ 10,000 ppmv at the surface to $\sim$ 1 ppmv. This limits the entry value of $f_T(H)$ into the lower stratosphere, causing a lower atmospheric hydrogen bottleneck. Note that CH_4 is not halted by the 'cold trap' due to its low boiling point, but it is oxidised to produce H_2O in the lower stratosphere primarily through reaction with OH.

2.7.5 Oxygen chemistry

Alongside H_2O, O_2 is of vital importance to the existence of animal life. An oxygenated atmosphere enables the photochemical production of O_3, which is primarily produced in the tropical stratosphere, where incoming sunlight photodissociates O_2 and produces an oxygen atom (O). O combines with O_2 and any third body (M) to form O_3. This O_3 molecule can absorb ultraviolet (UV) radiation, dissociating into O and O_2. O_3 can also react with O to produce two O_2 molecules. This is known as the Chapman cycle (Chapman, 1930):

$$O_2 + h\nu \longrightarrow O + O, \tag{2.15}$$

$$O + O_2 + M \longrightarrow O_3 + M, \tag{2.16}$$

$$O_3 + h\nu \longrightarrow O_2 + O, \tag{2.17}$$

$$O + O_3 \longrightarrow 2\,O_2, \tag{2.18}$$

where $h\nu$ represents a photon and ν is the frequency of the photon (the energy

of the photon is equal to $h\nu$). Eq. 2.16 is the only known mechanism by which O_3 is produced in the Earth's atmosphere. Cross sections between 100 and 200 nm are shown for O_2, O_3, H_2O, and CO_2 in Fig. 2.6. The Schumann-Runge (S-R) continuum ($130 - 175$ nm), Schumann-Runge bands ($175 - 205$ nm), and Herzberg Continuum ($205 - 250$ nm) are regions where O_2 is photodissociated, with O_3 photodissociated in the Hartley ($200 - 310$ nm), Huggins ($310 - 340$ nm), and Chappuis ($400 - 650$ nm) bands.

However, the chemistry of O_3 is more complicated than this, as catalytic cycles involving nitrogen ($NOx = NO + NO_2$), hydrogen ($HOx = H + OH + HO_2 + H_2O_2$), and halogen ($ClOx = Cl + ClO$ and $BrOx = Br + BrO$) species play an important role in destroying O_3 molecules (Lary, 1997; Grenfell *et al.*, 2006). Some examples

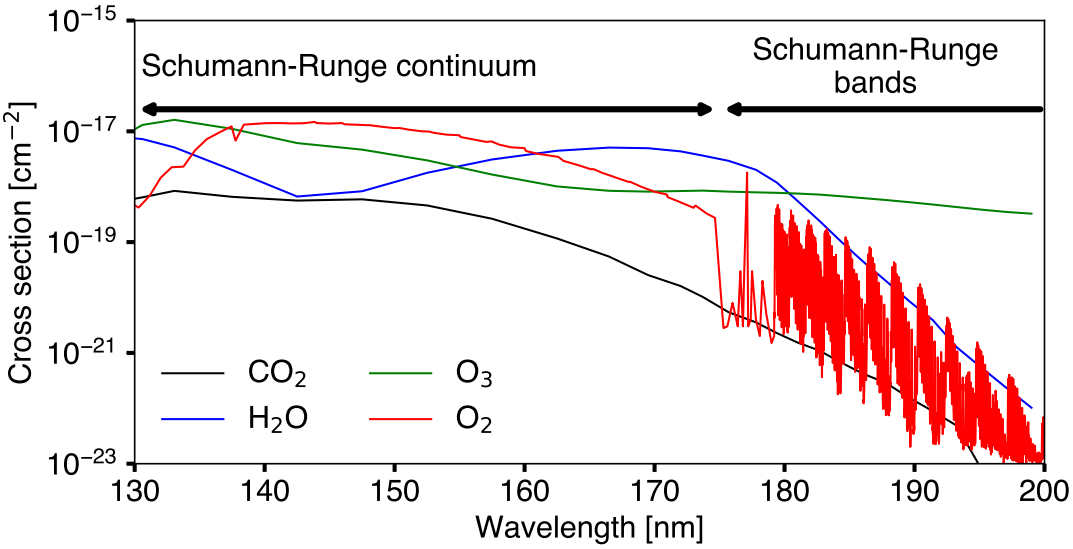

Figure 2.6: Molecular photodissoication cross sections represent the probability of a molecule undergoing photodissociation with a photon of a specific wavelength. Molecular cross sections for O_3 (green), O_2 (red), CO_2 (black), and H_2O (blue) are shown between 130 nm and 200 nm. The Schumann-Runge (S-R) continuum ($130 - 175$ nm) and Schumann-Runge bands ($175 - 205$ nm) are indicated by black arrows. Data from PHIDRATES[1] (Huebner & Carpenter, 1979; Huebner *et al.*, 1992; Huebner & Mukherjee, 2015)

include the following catalytic cycles:

$$\begin{aligned} \mathrm{NO} + \mathrm{O_3} &\longrightarrow \mathrm{NO_2} + \mathrm{O_2}, \\ \mathrm{NO_2} + \mathrm{O} &\longrightarrow \mathrm{NO} + \mathrm{O_2}, \end{aligned} \tag{2.19}$$

$$\begin{aligned} \mathrm{Cl} + \mathrm{O_3} &\longrightarrow \mathrm{ClO} + \mathrm{O_2}, \\ \mathrm{ClO} + \mathrm{O} &\longrightarrow \mathrm{O_2} + \mathrm{Cl}, \end{aligned} \tag{2.20}$$

$$\begin{aligned} \mathrm{Br} + \mathrm{O_3} &\longrightarrow \mathrm{BrO} + \mathrm{O_2}, \\ \mathrm{BrO} + \mathrm{O} &\longrightarrow \mathrm{O_2} + \mathrm{Br}. \end{aligned} \tag{2.21}$$

In each of these cases, the net reaction is $\mathrm{O} + \mathrm{O_3} \longrightarrow 2\,\mathrm{O_2}$, so the catalysts are not used up in the reaction. With heightened UV irradiation, $\mathrm{O_3}$ production increases as there are more O atoms available for reaction 2.16. Under larger temperatures, catalytic loss cycles proceed faster so $\mathrm{O_3}$ loss is accelerated. The distribution of $\mathrm{O_3}$ is set by this production and loss, as well as atmospheric dynamics which move $\mathrm{O_3}$ from the tropics to higher latitudes (via the Brewer-Dobson circulation as described in section 2.7.2). Finally, heterogeneous reactions between $\mathrm{ClONO_2}$ and HCl on polar stratospheric clouds can liberate $\mathrm{Cl_2}$, which after a series of further reactions, causes $\mathrm{O_3}$ loss at the poles via reaction cycle 2.20 (Brasseur & Solomon, 2005).

2.8 Tidally locked exoplanets

For exoplanets close enough to their host star, significant tidal stresses occur because of the balance between the gravitational pull from the star and the centrifugal force due to planetary rotation, thus warping the planet into an ellipsoid

(Pierrehumbert & Hammond, 2019). The torque applied to the exoplanet slows its rotation until it equals that of the orbital period; the exoplanet has become tidally locked. By calculating the tidal force which depends on stellar mass and distance, and considering the planetary properties (its density and the effectiveness of the tidal forces on the rotation of the planet), the timescale upon which tidal locking occurs is given by

$$t_{\mathrm{TL}} = 3.01 \times 10^{8} \cdot \frac{\Omega_{\oplus} \rho a^{6} Q}{M_{*}^{2} k_{2}}, \tag{2.22}$$

where a is the semi-major axis in AU, M_* is the mass if the star in solar masses, ρ is the mean density of the planet in terms of Earth's density, and $\Omega_\oplus$ is the angular rotation rate in terms of Earth's current rotation rate. Q is the effective specific tidal dissipation function, a measure of how efficiently the planet will dissipate the frictional energy from tidal torques (MacDonald, 1964; Barnes, 2017). k_2 is the Love number which quantifies the rigidity of the planet (Pierrehumbert & Hammond, 2019). Note that Q and k_2 are uncertain but their ratio for terrestrial planets is estimated to be ~ 1000 (Pierrehumbert & Hammond, 2019). Thus, it can be shown using Eq. 2.22 that many habitable zone tidally locked exoplanets should be tidally locked, provided the planetary system is old enough.

Compared to Earth, tidally locked exoplanets exhibit different circulation regimes, which depend on their incoming stellar energy distribution, the planetary rotation rate, and the propagation of atmospheric waves. Terrestrial planets with a rotation period faster than ~ 25 days exhibit atmospheric super rotation, whereas those slower than ~ 25 days distribute heat through radial flow from the warmer day side to the colder night side. This will be discussed in more detail in Chapter 6.

2.9 Observations of exoplanetary atmospheres

Exoplanet detection methods can provide information about the orbital period, mass (radial velocity method), or radius (transit method) of the exoplanet. Because the atmospheric composition affects radiative transfer (section 2.3) and sets the importance of the greenhouse effect (section 2.4), atmospheric observations must be made to determine the climate and surface conditions on an exoplanet, which can theoretically be done through direct imaging spectra. Transmission spectra are instead used for probing the atmospheric composition around the terminator and in the middle to upper atmosphere, but do not generally probe the surface owing to refraction (Bétrémieux & Kaltenegger, 2014).

For simplicity whilst discussing observations of exoplanets in this section, it will be assumed the exoplanet in question is transiting its star and orbits at an inclination of 90° (edge-on orbit), has a solid surface which is spherical with no distortions, and is the only exoplanet to orbit its host star.

2.9.1 Transmission spectra

When a terrestrial exoplanet passes in front of its host star from the line of sight of the observing telescope, the light reaching the telescope is attenuated by the opaque surface, and to an additional extent, the atmosphere. Wavelength dependent transmission spectra are derived from the amount of absorption in each wavelength bin. The wavelength binning depends on the spectral resolving power of the telescope's instrument, whilst the absorption depends on atmospheric pressure, temperature, and composition. The shape of the light curve results from ingress (beginning of transit), egress (end of transit), and limb darkening, which is where the 'edges' of the star appear dimmer than the centre of the star. This effect is caused by optical depth variations from where the emission originates, and the temperature of the star increasing towards the centre. The overall result

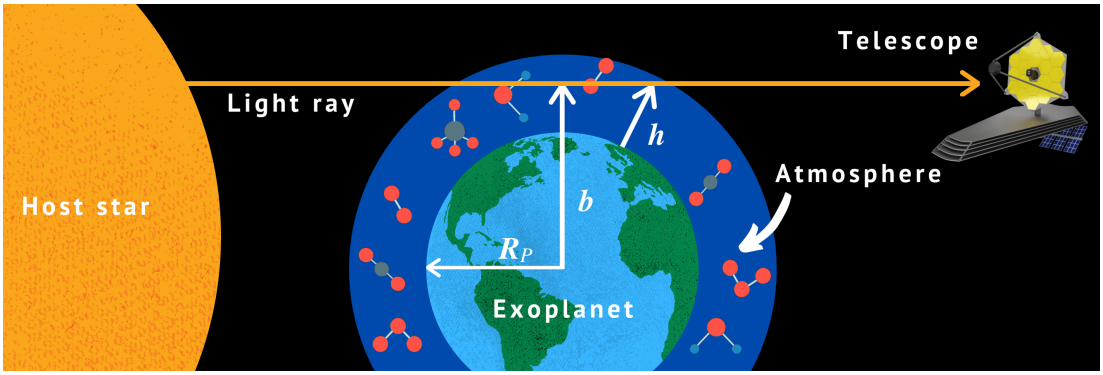

Figure 2.7: A cartoon of the geometry (not to scale) inherent in deriving transmission spectra from model atmospheres is shown. A light ray passes through the atmosphere of an exoplanet with radius R_p, height h, and impact parameter b. Light is blocked out by the solid disk, and this is revealed as a dip in the observed starlight. Additional light is absorbed and scattered in the atmosphere, and this has a wavelength dependence that depends on the composition of the atmosphere around the terminator, which is the portion of the atmosphere that transmission spectra probes. Figure adapted from Ehrenreich *et al.* (2006).

from limb darkening is that the observer sees the brightest stellar emission at the centre of the stellar disk (Espinoza & Jordán, 2015). If the exoplanet had no atmosphere, then the photon flux ($F_{\rm tel}$) seen by the telescope at maximum transit depth would be equal to

$$F_{\rm tel} = F_* \left(1 - \frac{\pi R_P^2}{\pi R_*^2}\right), \tag{2.23}$$

where R_p and R_* are the radii of the exoplanet and host star, respectively, and the incident flux from the star is F_*. Including atmospheric absorption, this expression becomes

$$F_{\rm tel} = F_* \left(1 - \frac{\Sigma_\lambda + \pi R_P^2}{\pi R_*^2}\right), \tag{2.24}$$

where Σ_λ is the equivalent disk surface area of absorption as a result of atmospheric opacity (Ehrenreich *et al.*, 2006). Σ_λ is given as

$$\Sigma_\lambda = 2\pi \int_{R_P}^{b_{\max}} b(1 - e^{[-\tau(b)]})db, \tag{2.25}$$

where b is the impact parameter, $\tau(b)$ is the optical depth as a function of b, and $b_{\max}$ is the maximum impact parameter. Σ_λ will be set by the atmospheric pressure, temperature, and chemical composition. For example, a denser atmosphere with molecules that strongly absorb at the observed wavelength will increase Σ_λ. See Fig. 2.7 for an illustration of the geometry involved in transmission spectra.

Transmission spectra for terrestrial exoplanets are usually expressed in terms of the contrast ratio (with respect to the star in parts per million), or effective altitude, which signifies the amount of absorption by the atmosphere as if it was an extension to the opaque disk (Robinson, 2017).

2.9.2 Direct imaging spectra

Direct imaging spectra can consist of reflection spectra and thermal emission spectra. Reflection spectra occur at shorter wavelengths (e.g. UV, visible), whilst thermal emission spectra occur at longer wavelengths (infrared), although depending on the stellar energy distribution of the host star and the temperature of the exoplanet, the wavelength at which these two regimes crossover may shift. For a transiting system, direct imaging spectra are best observed before the exoplanet passes into secondary eclipse (Madhusudhan, 2018) because that is when the full illuminated face of the exoplanet is in view. If observations of the flux originating from the planetary system are taken just before secondary eclipse (F_{out}), and during secondary eclipse (F_{in}), the direct imaging spectra can be given in terms of a planet-star flux ratio, F_p/F_* (Madhusudhan, 2018), such that

$$\frac{F_p}{F_*} = \frac{F_{\text{out}} - F_{\text{in}}}{F_{\text{out}}}. \tag{2.26}$$

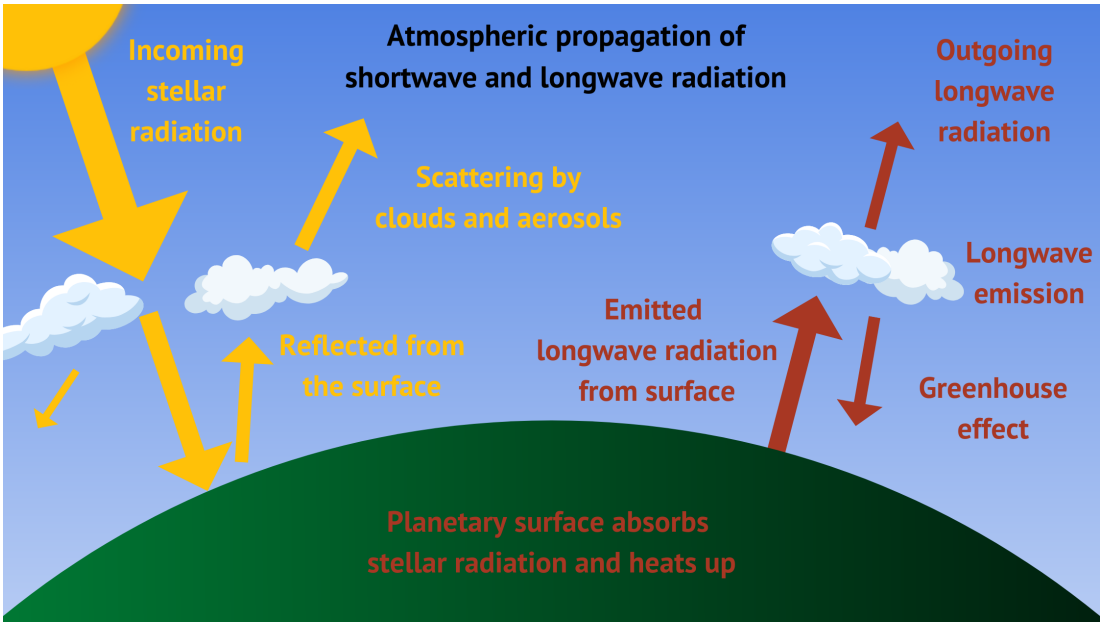

Figure 2.8: Shown are the physical processes that must be accounted for to calculate reflection and emission spectra of planetary surfaces and atmospheres. Incoming solar radiation is scattered, absorbed, and reflected by clouds, molecules, and the surface of the planet. The planet radiates energy in the infrared, and this is absorbed and remitted by clouds and greenhouse gases. Surface reflection and emission depends on the surface properties of the planet. For instance, ice is more reflective than ocean. The light collected by the telescope will depend on the phase of the orbit (e.g. see Fig. 1.6). Figure adapted from the PSG website.

Fig. 2.8 shows some of the atmospheric parameters that affect direct imaging spectra. As a ray of light passes through the planetary atmosphere and reflects back to the observer, the outgoing intensity is influenced by atmospheric scattering, clouds, surface reflection, and the absorption of gases, such that an observed reflection spectrum probes the albedo and composition of the exoplanet's surface and atmosphere. For emission spectra, consider a monochromatic ray that is emitted from the exoplanet's warm surface and passes through a gas that absorbs at the wavelength of the ray. If the temperatures of the layers above are colder, then the spectra seen by an observer will contain absorption features. Conversely, if the temperature increases with altitude, then those layers contribute to the in-

tensity of the outgoing ray and emission features are observed (Encrenaz, 2014). As a result, in addition to composition, emission spectra can be used to provide constraints on the pressure-temperature profile of the observed exoplanet (Kaltenegger *et al.*, 2010).

2.10 Summary

This Chapter discussed the important physical links between electromagnetic radiation and gases in planetary atmospheres. Throughout this thesis there is a particular focus on how light and chemical species in the modelled atmospheres interact to produce the eventual climate state predicted by the WACCM6 simulations. In the next Chapter I describe the numerical methods used to simulate (exo)planetary climates and predict observations of the predicted atmospheres.

Chapter 3

Modelling tools

In this thesis I make use of three numerical models to simulate planetary climates and predict possible observations of exoplanet atmospheres. The majority of climate simulations are performed using WACCM6, with three simulations performed with WACCM-X. Both of these models are part of the CESM2 modelling framework. The third model is PSG, which I use to predict telescope spectroscopic observations from the WACCM6 climate simulations. In this section I describe the models. In Chapters 4, 5, 6, and 7, I provide more information regarding their implementation.

3.1 CESM2

The Community Earth System Model Version 2 (CESM2) is a suite of open-source coupled models developed at the National Center for Atmospheric Research (NCAR), with input from the scientific community (Danabasoglu *et al.*, 2020). The models coupled together include: sea-ice (Hunke *et al.*, 2015), land-ice (Lipscomb *et al.*, 2019), land (Lawrence *et al.*, 2019), river transport (Li *et al.*, 2013), ocean (Smith *et al.*, 2010; Long *et al.*, 2021) and atmosphere models.

The model therefore simulates vegetation, soils, fire, lakes, snow, glaciers, ice sheets on land, river transport, sea ice sheets, the oceans (including bio-

geochemistry), and the atmosphere. The ocean can have specified sea surface temperatures, or it can be fully interactive with the atmosphere and respond to any changes. The coupler passes information between the land, atmosphere, and sea-ice components at each atmospheric time step, which is 30 model minutes, whereas the ocean receives atmospheric flux information every hour, and the coupler interacts with the land-ice model once per day (Danabasoglu *et al.*, 2020). The atmosphere component can either be the Community Atmosphere Model (CAM6), a higher-top version known as the Whole Atmosphere Community Climate Model version 6 (WACCM6; Gettelman *et al.*, 2019b) which extends CAM6 from a model top of $\sim$ 40 km to $\sim$ 140 km, or the Whole Atmosphere Community Climate Model with thermosphere and ionosphere extension (WACCM-X; Liu *et al.*, 2018). The focus of my work is on the atmosphere, and my simulations were primarily conducted with WACCM6, with some simulations using WACCM-X.

3.2 WACCM6

WACCM6 is a three-dimensional Earth System Model configuration of CESM2. The simulations in this thesis used CESM2.1.3[1]. The WACCM6 configuration used is a BWma1850 'compset' which includes the chemistry necessary to simulate the middle atmosphere[2] (stratosphere, mesosphere, and lower thermosphere). A schematic representation of the model's capabilities is shown in Fig. 3.1. Using a finite volume dynamical core (see section 3.2.3 Lin & Rood, 1997), the atmospheric resolution was 1.875° in latitude by 2.5° in longitude. This means there was 144 longitudinal grid cells and 96 latitudinal grid cells. Latitude (ϕ) is defined north-south, between $-90° \leq \phi \leq 90°$ with the equator at 0°. North-

[1] http://www.cesm.ucar.edu/models/cesm2/
[2] https://www.cesm.ucar.edu/models/cesm2/config/2.1.3/compsets.html

ern latitudes are positive and southern latitudes are negative. Longitude (Λ) is defined eastward of the prime meridian between $0° \leq \Lambda \leq 360°$. The vertical coordinate is defined in terms of hybrid sigma-pressure, where hybrid coefficients at layer interfaces (α and β) are used to evaluate the pressure coordinates. In order to achieve efficiency and maintain model stability, this coordinate system provides better atmospheric representation near the surface, where the pressure varies depending on topography (sigma coordinate), whereas the middle atmosphere uses pressure coordinate levels only. The pressure (p) in each grid cell can be calculated via

$$p = (\alpha P_0) + (\beta P_S), \tag{3.1}$$

where P_S is the surface pressure and P_0 is the reference pressure (10^5 Pa). There are 70 levels in the vertical from the surface to a pressure of 6×10^{-6} hPa ($\approx$ 140 km; Gettelman *et al.*, 2019b).

Previous versions of WACCM have been used for a variety of purposes, such as simulating climate change between the industrial revolution and the 21st cen-

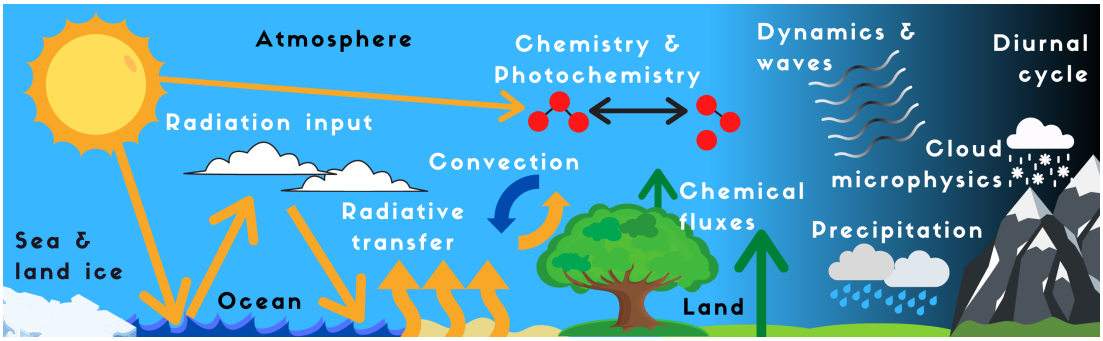

Figure 3.1: A cartoon depicts the WACCM6 Earth System Model. In this thesis, all simulations use WACCM6 with a fully interactive ocean model, as well as land-ice, sea-ice, land, and atmosphere models. WACCM6 has fully-coupled chemistry and physics in the atmosphere, includes a state-of-the art moist physics scheme, and simulates up to roughly 140 km in altitude in the pre-industrial atmosphere.

tury (Marsh *et al.*, 2013), as well as investigating the effects of solar flares on the middle atmosphere (Pettit *et al.*, 2018). This same model version has also previously been used in the context of exoplanets to simulate tidally locked exoplanets around GKM dwarf stars (Proedrou & Hocke, 2016; Proedrou *et al.*, 2016; Chen *et al.*, 2019), and to evaluate the precipitation of energetic particles through the atmospheres of exoplanets (Chen *et al.*, 2021).

3.2.1 Stellar input

Solar data was specified between 10 – 100,000 nm, with a total solar insolation of 1361.0 ± 0.5 W m^{-2}. This wavelength range includes the extreme ultraviolet, ultraviolet, visible, and infrared regions of the electromagnetic spectrum. Matthes *et al.* (2017) recommended solar forcing data for use within climate models participating in the Coupled Model Intercomparison Project phase 6 (CMIP6). The solar file which specifies the incoming irradiation in WACCM6 used this recommendation. The incoming solar radiation affects atmospheric and surface temperatures, as well as chemistry and dynamics. This solar data was changed in order to simulate the early Earth orbiting a younger Sun (see Chapter 4), or exoplanets orbiting M dwarf stars (see Chapter 6).

3.2.2 Radiative transfer

The most accurate way to represent radiative transfer in models is to use the line-by-line approach, solving the radiative transfer (RT) equation for each spectral line (Price *et al.*, 2014). This is a robust but relatively computationally expensive procedure used to calculate the spectral radiance in model atmospheres. Radiative transfer models, such as the Rapid Radiative Transfer Model for General circulation models (RRTMG; Iacono *et al.*, 2008) which is used in WACCM6, are often benchmarked against line-by-line calculations (Hogan & Matricardi, 2020).

RRTMG is a modified version of the Rapid Radiative Transfer Model (Mlawer *et al.*, 1997), made computationally more efficient so it can be incorporated into GCM models, whilst maintaining acceptable levels of accuracy. RRTMG applies the correlated-k method, splitting up the calculations into shortwave (fluxes and heating rates between 200 – 12195 nm) and longwave (fluxes and cooling rates between 3.1 – 1000 µm). The correlated-k method uses a precomputed set of correlated absorption coefficients (Leconte, 2021), enabling faster calculations of radiative transfer, with the correlated-k distribution in RRTMG based on the Line-by-Line Radiative Transfer Model (LBLRTM; Clough *et al.*, 1992, 2005). RRTMG includes multiple-scattering (where scattered photons are re-scattered) calculations in the shortwave (Clough *et al.*, 2005) through utilisation of a two-stream radiative transfer solver (Oreopoulos & Barker, 1999; Iacono *et al.*, 2008), which considers light propagating in two directions only.

3.2.3 Dynamics

The Navier-Stokes equations apply Newton's laws of motion to viscous fluids to describe the way fluids move through space and time (Foias *et al.*, 2001). In simplified form, they are known as the primitive equations, which describe atmospheric conservation of momentum (the momentum equation), the conservation of mass (the continuity equation), and the conservation of energy (the first law of thermodynamics). The finite volume dynamical core used in WACCM6 (Lin & Rood, 1997) splits up a sphere to represent the planet in real space, and solves the primitive equations (Neale *et al.*, 2010). WACCM6 incorporates orographic (Beljaars Anton *et al.*, 2004; Scinocca & McFarlane, 2000) and nonorographic (Richter *et al.*, 2010) gravity wave drag parameterisations. Orographic gravity waves originate from topography, such as mountains (Beljaars Anton *et al.*, 2004), whilst nonorgraphic gravity wave sources consist of frontal and baroclinic

systems, as well as convection (Richter *et al.*, 2010). Gravity waves generated at the equator propagate upwards and produce a forcing of the stratospheric winds that creates a downward propagating oscillation known as the quasi-biennial oscillation (QBO). However, at the resolutions simulated in this thesis, an imposed dynamical forcing that modifies the wind field is required in WACCM6 to produce the QBO, although this forcing can be turned off (Neale *et al.*, 2010). The QBO forms at higher resolutions in WACCM6 without this forcing, but computational speed is reduced.

3.2.4 Moist physics

In many climate models, the role of moist physics (e.g. water vapour microphysics and cloud processes) occurs on a sub-grid scale, meaning parameterisations must be used in order to adequately represent the influence of moisture in the atmosphere. Vertical turbulent mixing is generally described by shallow and deep convection. Shallow convection moves heat and water upward in the lower part of the troposphere, forming low-altitude clouds (e.g. cumulus), whereas deep convection consists of rapid ascending air motion into the upper troposphere. In WACCM6, the Morrison-Gettelman cloud microphysics scheme (Gettelman & Morrison, 2015) is used to forecast the precipitation amounts for snow and rain (Danabasoglu *et al.*, 2020). Additionally, a unified turbulence scheme known as Cloud Layers Unified By Binormals (CLUBB; Golaz *et al.*, 2002; Larson, 2017) is used in WACCM6. CLUBB is a parameterisation of turbulence and moist physics which unifies what previously would have been separate parameterisations for shallow convection, transitions between cloud types, and the planetary boundary layer (Bogenschutz *et al.*, 2013), which is the region of the atmosphere which is heavily governed by interactions with the surface. Finally, the Zhang-McFarlane deep convection scheme is used to parameterise deep convection (Zhang & Mc-

Farlane, 1995).

3.2.5 Chemistry

In Earth's atmosphere the chemical system is 'stiff' because the chemical lifetimes between the many chemical species vary over multiple orders of magnitude, such that numerical methods must be employed to solve the continuity equation (Garfinkel *et al.*, 1977). Chemical solvers employ a timestep Δt between each calculation. The fully explicit scheme is used to solve for long-lived species and evaluates the chemical system at a later time $t + \Delta t$ by considering the current system at time t (Brasseur & Solomon, 2005). The fully implicit scheme considers the system at time t and $t + \Delta t$ to calculate the system at the future time step $t + \Delta t$ (Sandu *et al.*, 1997). It is more computationally stable than the fully explicit scheme but may require iteration to solve for each species. Each method needs to consider the trade-off between computational efficiency, stability and accuracy (Brasseur & Solomon, 2005).

The coupled-chemistry used in WACCM6 is based on the Model for Ozone and Related chemical Tracers version 4 (MOZART-4; Emmons *et al.*, 2020, 2010; Kinnison *et al.*, 2007; Horowitz *et al.*, 2003). The specific WACCM6 setup used in this thesis includes 98 chemical species, 208 chemical reactions, and 90 photolysis reactions. The concentrations of 22 long-lived species were calculated explicitly and those of 75 species were computed using the implicit method (Horowitz *et al.*, 2003), with N_2 considered invariant. For O_3, the Chapman cycle was included, as well as the HOx, NOx, SOx, BrOx, and ClOx species which are involved in catalytic cycles that destroy O_3. Instead of using a 'family' approach where photochemical equilibrium conditions are assumed for a group of chemicals (e.g. the Ox family, comprised of O and O_3) which quickly cycle among each other (Brasseur & Solomon, 2005), the concentrations of chemical species

were determined in WACCM6 individually through separate calculations for each constituent. To calculate the rate of photochemical reactions in the lower atmosphere, WACCM6 utilises the fast-TUV (fast Tropospheric Ultraviolet-Visible) scheme (Tie *et al.*, 2003; Emmons *et al.*, 2010) and accounts for various aerosols (which scatter and absorb light), including dust and sea salt (Liu *et al.*, 2016). Above the homopause in the heterosphere, molecular diffusion dominates over turbulent mixing. As altitude increases, the abundance of gases change according to their masses. This process, where the atmospheric constituents with lower masses increase in abundance relative to the species with higher masses, is also included (Banks & Kockarts, 1973; Garcia *et al.*, 2007).

3.3 WACCM-X

WACCM-X simulates the Earth's atmosphere up to approximately 700 km in altitude (Liu *et al.*, 2018). Such an upper atmospheric model permits numerical investigations into how upper atmospheric changes influence the weather and climate at the surface of Earth (Liu *et al.*, 2018). WACCM-X accounts for physics and chemistry relevant to the ionosphere (e.g. ion-neutral reactions, 7 ions, electrons), with 74 neutral species, 289 reactions which include gas phase, heterogeneous, photolysis, and photoionization reactions, as well as calculating atomic oxygen ion transport (Liu *et al.*, 2018). The model simulates ionospheric responses that are specific to solar storms, such as Joule heating, where an electric current passes through and heats a medium (Liu *et al.*, 2018). WACCM-X is used for a limited number of simulations in Chapter. 4.

3.4 Planetary Spectrum Generator

The Planetary Spectrum Generator (PSG; Villanueva *et al.*, 2018, 2022) is an online spectroscopic suite of tools that can be used to simulate observations of

various astronomical objects, including exoplanets, with different telescopes and their associated noise sources. PSG is used in this thesis in Chapters 5 and 7 to compute theoretical reflection/emission spectra from the WACCM6 atmospheric simulation output.

PSG utilises the Planetary and Universal Model of Atmospheric Scattering (PUMAS) radiative transfer code to calculate spectra for planetary atmospheres which are in hydrostatic equilibrium (Villanueva *et al.*, 2018). It takes a layer-by-layer approach using the correlated-k method, or the line-by-line method at high spectral resolutions, and accounts for Rayleigh scattering, aerosols, and collision-induced absorption (Villanueva *et al.*, 2018). PSG accounts for background (e.g. exozodiacal) and imaging charge-coupled device (CCD) noise sources, including read noise and dark noise, using Poisson statistics (Villanueva *et al.*, 2022).

Chapter 4

Earth's oxygenated history

4.1 Introduction

Ozone (O_3), despite only making up a tiny proportion of Earth's atmosphere by weight, is one of the most important molecules for life on Earth. Without the presence of a substantial stratospheric O_3 layer, the surface would receive higher amounts of biologically harmful ultraviolet (UV) radiation. However, this modern day O_3 layer would not exist without abundant molecular oxygen (O_2), and the Earth's atmosphere has not always been O_2-rich.

Fig. 4.1 gives an overview of the current picture of Earth's oxygenation history. A large rise in oxygen concentrations occurred approximately 2.5 – 2.4 billion years ago during the Great Oxidation Event (GOE; Lyons *et al.*, 2021; Poulton *et al.*, 2021). Isotope fractionation is a measure of the relative abundance of stable isotopes of the same element, and mass-independent fractionation of sulphur isotopes in the geological record indicate that O_2 quantities fluctuated for a further $\sim$ 200 million years (Farquhar *et al.*, 2000; Gumsley *et al.*, 2017; Poulton *et al.*, 2021) before an oxygenated atmosphere was permanently established following the GOE (Bekker *et al.*, 2004; Lyons *et al.*, 2014; Luo *et al.*, 2016; Warke *et al.*, 2020). Afterwards, O_2 concentrations dropped again (Bekker & Holland, 2012; Canfield *et al.*, 2013), with O_2 concentrations likely between 10^{-3} and 10^{-1} the

present atmospheric level (PAL) for the rest of the Proterozoic (Lyons *et al.*, 2014, 2021). Some literature estimates suggest a larger range between 10^{-5} and 10^{-1} PAL (Cole *et al.*, 2020; Olson *et al.*, 2018a; Holland, 2006). However, recent one-dimensional (1D) atmospheric photochemical modelling of Earth's oxygenation history suggests geologically persistent Proterozoic oxygen levels could have been limited to values greater than or equal to 10^{-2} PAL. This is based on predictions of an atmospheric bistability (Goldblatt *et al.*, 2006; Gregory *et al.*, 2021), where there are two stable simulated (steady-state, converged simulations) regions of high- and trace-oxygen solutions, separated by a region where equilibrium solutions rarely exist. For instance, Gregory *et al.* (2021) reported a small proportion ($< 5\%$ of the high and trace-O_2 simulations) of stable solutions to exist between $3 \times 10^{-4}\%$ (0.6 ppmv) and 1% PAL of O_2.

Towards the end of the Proterozoic, there was a further episode of increasing oxygenation known as the Neoproterozoic Oxidation Event (Campbell & Squire, 2010; Lyons *et al.*, 2014; Och & Shields-Zhou, 2012), leading into the current Phanerozoic geological eon where oxygen levels have generally been estimated to have varied between 10% PAL and 150% PAL (Holland, 2006; Lyons *et al.*, 2014; Large *et al.*, 2019; Kump, 2008; Schachat *et al.*, 2018; Brand *et al.*, 2021) for the past 0.541 billion years, reaching approximate modern day concentrations during the Paleozoic (541 – 252 Myr ago; Sperling *et al.*, 2015; Wallace *et al.*, 2017; Lyons *et al.*, 2021).

The earliest fossilised animals date back $\sim$ 575 Myr ago (Narbonne, 2005; Bobrovskiy *et al.*, 2018), roughly 1.7 Gyr after the GOE. Biomarkers imply that demosponges may have emerged before this, perhaps as far back as 660 Myr ago (Zumberge *et al.*, 2018), although this has been disputed (Nettersheim *et al.*, 2019) and the debate continues (Love *et al.*, 2020; Hallmann *et al.*, 2020; Bobrovskiy *et al.*, 2021). Furthermore, analysis of biomolecular clocks (where rates

of mutation are analysed to determine the past divergence of species and biological functionalities in lieu of alternative evidence, such as fossils) indicates possible animal life 200 Myr prior to the emergence of animal fossils (Sperling *et al.*, 2010; Erwin, 2020). It has been suggested that Phanerozoic-like oxygen levels were required for complex animal life (metazoans) to diversify (Chen *et al.*, 2015; Zhang & Cui, 2016; Zhao *et al.*, 2018), but not necessarily needed for metazoans to evolve (Lenton *et al.*, 2014), because the emergence of animals may not have coincided with a rise in O_2 (Mills *et al.*, 2014; Mills & Canfield, 2014). Thus, how changing oxygen levels have influenced the evolution of life through time is uncertain (Mills & Canfield, 2014; Lenton *et al.*, 2014; Cole *et al.*, 2020) because of early-evolving animals such as sponges that can survive at very low O_2 concentrations (Mills *et al.*, 2014).

In summary, dramatic changes in atmospheric O_2 levels took place during the period between $\sim$ 2.4 and 0.4 Gyr ago, with uncertainties still covering a large O_2 range (Lyons *et al.*, 2021). Previous 1D atmospheric modelling has found that these changes in O_2 strongly impact atmospheric O_3 levels (Levine *et al.*, 1979; Kasting & Donahue, 1980; Segura *et al.*, 2003). In the modern atmosphere, the O_3 layer protects animal and plant life from harmful UV radiation, but the O_3 layer has not always been present. Rising oxygen levels above 10^{-4} PAL likely formed and increased the UV-protective O_3 column (e.g. see Kasting & Donahue, 1980; Segura *et al.*, 2003), where the column is the total number of molecules above the surface per unit area. Fluctuations in the O_3 column potentially affected the evolution of animal and plant life. For example, relatively rapid past reductions in the O_3 layer could have resulted in increased fluxes of biologically harmful UV-B radiation (280 – 315 nm) at the surface, possibly causing more than one mass extinction event during the Phanerozoic (Melott *et al.*, 2004; Benca *et al.*, 2018; Marshall *et al.*, 2020; Black *et al.*, 2014). On the other hand, because

Phanerozoic-like oxygen concentrations could have been present for $\sim$ 200 Myr during the GOE (Lyons *et al.*, 2014), the protective effect of O_3 on animal life's origin have been argued to be temporally irrelevant (Margulis *et al.*, 1976; Mills & Canfield, 2014).

It is not just O_2 and O_3 concentrations that have changed since the dawn of Earth's atmosphere. The Sun's luminosity has been steadily increasing through time (see Fig. 4.1). The increased luminosity is due to the Sun fusing hydrogen into helium, which causes the central temperature and density of the Sun to increase (Bahcall *et al.*, 2001), quickening the rate of fusion. The Sun's luminosity is estimated to have been 74% and 86% of today's solar luminosity, 4 Gyr ago and 2 Gyr ago, respectively (Bahcall *et al.*, 2001).

The Mesoproterozoic (1.8 – 0.8 Gyr ago), often referred to as the 'Boring Billion', was reportedly free of widespread glaciation (Fiorella & Sheldon, 2017; Young, 2013). This is paradoxical, because a fainter Sun during this period would result in increased ice coverage, all other atmospheric properties being equal. This problem is the 'Proterozoic Faint Young Sun Paradox'. To mitigate the fainter Sun during various geological periods, prior research has suggested that a larger greenhouse effect is required (Sagan & Mullen, 1972; Kasting, 2010; Feulner, 2012; Charnay *et al.*, 2020). Specifically for the Mesoproterozoic, elevated levels of CO_2 and CH_4 have been proposed to provide the necessary warming to avoid enhanced glaciation (Pavlov *et al.*, 2003). Whilst higher Mesoproterozoic CO_2 is consistent with geological records (Fiorella & Sheldon, 2017), recent research has cast doubt on elevated CH_4 concentrations during the Mesoproterozoic due to predicted fluxes into the atmosphere that are similar to present day fluxes or lower (Olson *et al.*, 2016; Laakso & Schrag, 2019; Daines & Lenton, 2016). Disregarding anthropogenic emissions, methane (CH_4) is currently produced on Earth primarily through biological pathways (Laakso & Schrag, 2019). However,

there are no direct indicators of CH_4 levels before the Pleistocene (> 2.580 Myr ago; Laakso & Schrag, 2019), so its concentration through geological time has generally been inferred through modelling. Laakso & Schrag (2019) suggested Proterozoic methane levels no greater than 1 ppmv, and Olson *et al.* (2016) suggested CH_4 concentrations were unlikely to exceed 10 ppmv, as did Daines & Lenton (2016). This is in contrast with the suggestion of 100 – 300 ppmv by Pavlov *et al.* (2003), which was proposed to solve this Proterozoic Faint Young Sun Paradox.

Finally, atmospheric escape of hydrogen is likely to have played a role in oxidising the Earth's surface. In the middle and upper atmosphere, H_2O is photodissociated. The liberated hydrogen (H) can escape to space, and the oxygen left behind oxidises the Earth (Catling *et al.*, 2001). Alongside photosynthetic production of O_2 from cyanobacteria, this process is thought to have contributed to the GOE (Zahnle *et al.*, 2013, 2019).

Compared to solar or chondritic xenon (Xe) and Xe trapped in Archean rocks (Avice *et al.*, 2018), the modern Xe in Earth's atmosphere has a higher fractionation by 30 – 40‰ u^{-1} (where u is the atomic mass unit and ‰ is per 1000). Xe is more easily ionised compared to the other noble gases which do not show the same fractionation (the so-called Xenon paradox; Anders & Owen, 1977; Zhu *et al.*, 2013). Thus, the escape of Xe^+ propelled by H^+ ion escape has been shown to be a feasible physical process (Zahnle *et al.*, 2019) and as a result Xe fractionation may trace high levels of atmospheric hydrogen escape. There has been relatively small changes in Xe fractionation since the GOE (Zahnle *et al.*, 2019), suggesting most historical hydrogen escape occurred prior to the GOE.

Much of the work regarding the temporal variation of the O_3 layer and any influence on biological habitats has been achieved through 1D atmosphere modelling studies (Levine *et al.*, 1979; Kasting & Donahue, 1980; Segura *et al.*, 2003;

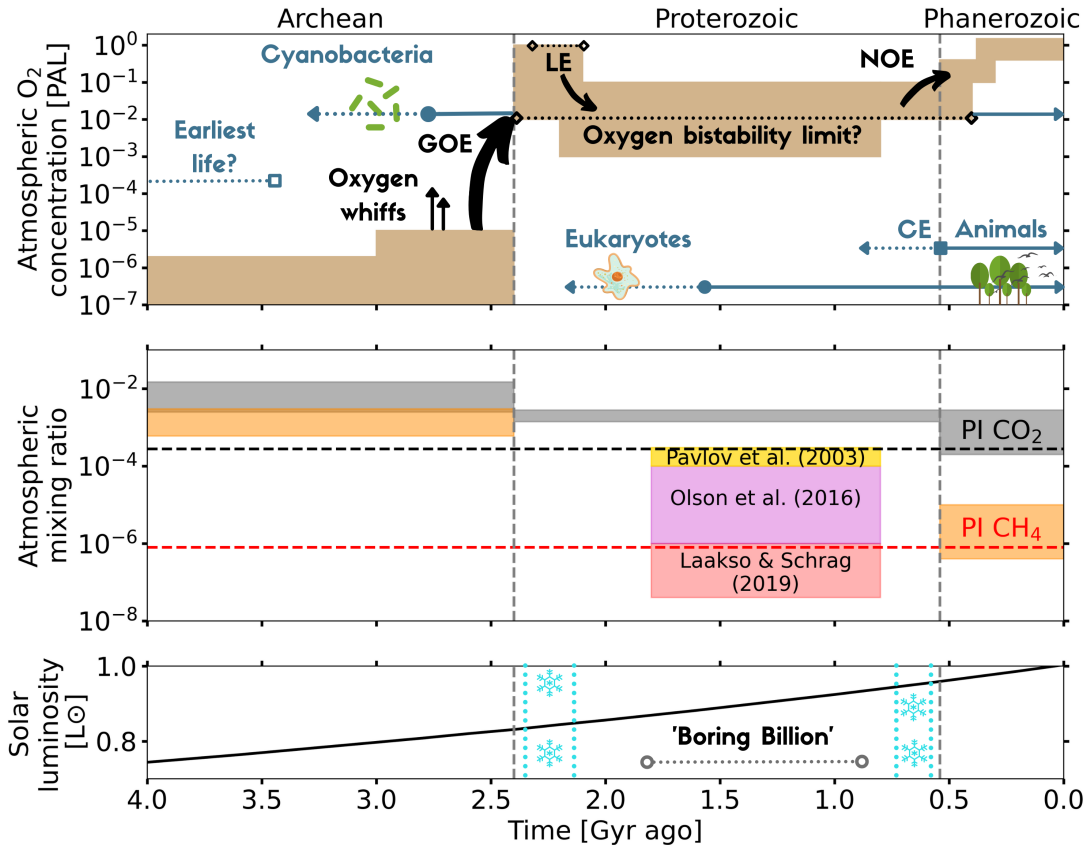

Fig. 4.1: (*Top*), same as Fig. 1.9. (*Middle*), The estimated ranges for CO_2 (grey) and CH_4 (orange) through geological time are given. Conflicting predictions in the Proterozoic are given by Pavlov *et al.* (2003) (yellow), Olson *et al.* (2016) (magenta) and Laakso & Schrag (2019) (light red). The CH_4 (orange) and CO_2 (grey) ranges in the Phanerozoic and Archean are 'preferred' ranges from Olson *et al.* (2018a), and references therein. The black dotted and red dotted lines are the pre-industrial values for CO_2 and CH_4, respectively, that were used in the simulations. (*Bottom*), The estimated luminosity of the Sun is shown with respect to time (Bahcall *et al.*, 2001). The 'Boring Billion' (1.8 – 0.8 Gyr ago) and periods of low-latitude glaciation are indicated (Young, 2013; Warke *et al.*, 2020).

Kasting & Catling, 2003). For the first time, a whole atmosphere chemistry-climate model is used to simulate 3D O_3 variations responding to changing O_2 concentrations under Proterozoic and Phanerozoic conditions applicable to Earth. Due to the uncertainty in O_2 concentrations during these geological eons, a range

Table 4.1: The twelve different simulations utilised for this work. There is a pre-industrial (PI) case and seven cases with varied O_2 levels. There are variations on the 1% PAL simulation, two with methane emissions (CH_4 em1 and CH_4 em0.1), and two with a 2 Gyr younger Sun, one of these with pre-industrial CO_2 concentrations and one with 4 times the pre-industrial CO_2 level, named YS and YS 4×CO_2, respectively. The volume mixing ratio for O_2, $f(O_2)$, is given in terms of the present atmospheric level (PAL). The volume mixing ratio for N_2, $f(N_2)$, is listed. The lower boundary condition (LBC) for CH_4 is shown, as well as the fixed lower boundary condition for CO_2. The CH_4 LBC is either a fixed mixing ratio or a fixed flux in terms of grams per year. The flux of solar radiation at the top of the atmosphere, relative to today's solar constant ($S_\odot$), is given as S.

Simulation	$f(O_2)$ [PAL]	$f(N_2)$	CH_4 LBC	$f(CO_2)$	S [$S_\odot$]
PI	1.000	0.78	fixed 0.8 ppmv	280 ppmv	1.00
150% PAL	1.500	0.68	fixed 0.8 ppmv	280 ppmv	1.00
50% PAL	0.500	0.89	fixed 0.8 ppmv	280 ppmv	1.00
10% PAL	0.100	0.97	fixed 0.8 ppmv	280 ppmv	1.00
5% PAL	0.050	0.98	fixed 0.8 ppmv	280 ppmv	1.00
1% PAL	0.010	0.98	fixed 0.8 ppmv	280 ppmv	1.00
CH_4 em1	0.010	0.98	5×10^{14} g yr^{-1} flux	280 ppmv	1.00
CH_4 em0.1	0.010	0.98	5×10^{13} g yr^{-1} flux	280 ppmv	1.00
YS	0.010	0.98	fixed 0.8 ppmv	280 ppmv	0.86
YS 4×CO_2	0.010	0.98	fixed 0.8 ppmv	1120 ppmv	0.86
0.5% PAL	0.005	0.98	fixed 0.8 ppmv	280 ppmv	1.00
0.1% PAL	0.001	0.98	fixed 0.8 ppmv	280 ppmv	1.00

of possible O_2 levels (0.1% PAL to a maximum of 150% PAL) since the beginning of the Proterozoic to the pre-industrial atmosphere is simulated. This Chapter demonstrates oxygen's 3D influence on the O_3 layer (its magnitude and spatial variation) and discusses how this affects habitability estimates. A significant reduction in O_3 provides less atmospheric heating, and the cooler tropopause that emerges restricts the total hydrogen in the upper atmosphere. This result allows an estimate of hydrogen escape rates as controlled by O_2. The effects that lower O_2 and O_3 quantities have on the chemical lifetime of CH_4 is determined, and it is found that the Proterozoic Faint Young Sun Paradox may be more difficult

to solve. The differences that arise when using a 3D chemistry-climate model for modelling paleoclimates compared to 1D modelling studies are also discussed.

4.2 Atmospheric modelling using WACCM6

This Chapter uses the most recent version of the Whole Atmosphere Community Climate Model (WACCM6; Gettelman *et al.*, 2019b), which is a specific model configuration of the Community Earth System Model version 2 (CESM2)[1]. A schematic representation of the model's capabilities is shown in Chapter 3 (Fig. 3.1). The simulations presented in this Chapter are the first time the WACCM configuration of CESM has been used to model the Proterozoic Earth and calculate how the O_3 column varies with O_2 concentration, although it is noted that Chen *et al.* (2021) did simulate Proterozoic-like O_2 concentrations for Earth-analogue exoplanets with WACCM4.

Twelve different simulations were ran for this work (see Table 4.1 for a summary). The control simulation is a pre-industrial atmosphere (hereafter PI) in which pollutants and greenhouse gas concentrations approximate those of the year 1850. This simulation starts following a 300 year control simulation with fixed 1850 conditions. The mixing ratio of O_2 is varied over the range of possible values during the last 2.4 billion years following the Great Oxidation Event. The various simulations include 150%, 50%, 10%, 5%, 1%, 0.5%, and 0.1% PAL of O_2. The standard WACCM6 pre-industrial baseline simulation initial conditions were altered to produce each of these simulations, where the only variable change is the oxygen mixing ratio at the lower boundary (see Fig. 4.3 for the O_2 mixing ratio profiles). For each of these simulations, the mixing ratios of the following chemical species were held constant at the surface: O_2 (varied as in Table 4.1), CH_4 (800 ppbv), CO_2 (280 ppmv), N_2O (270 ppbv), H_2 (500 ppbv), CH_3Cl (457

[1] http://www.cesm.ucar.edu/models/cesm2/

pptv), and $CHBr_3$ (1.2 pptv). The simulated atmospheres have a surface pressure of 1000 hPa, and in each simulation in which the mixing ratio of O_2 is decreased, N_2 is increased to maintain a 1000 hPa surface pressure. Each of these simulations utilises a modern day solar spectrum (see Fig. 4.2).

Recent work on the bistability of oxygen in Earth's atmosphere suggests that oxygen levels between 3×10^{-4}% and 1% the present atmospheric level of O_2 are unstable on geological timescales (Gregory *et al.*, 2021). The lowest O_2 concentration simulated is 0.1% PAL. The 0.5% PAL and 0.1% PAL concentrations may not be relevant for long periods of time (that is, geologically speaking), however, this depends on oxygen's relative atmospheric flux and destruction. It is noted that such mixing ratios could be relevant for shorter periods of time, and such concentrations could be stable on possible exoplanet atmospheres, so the 0.1%

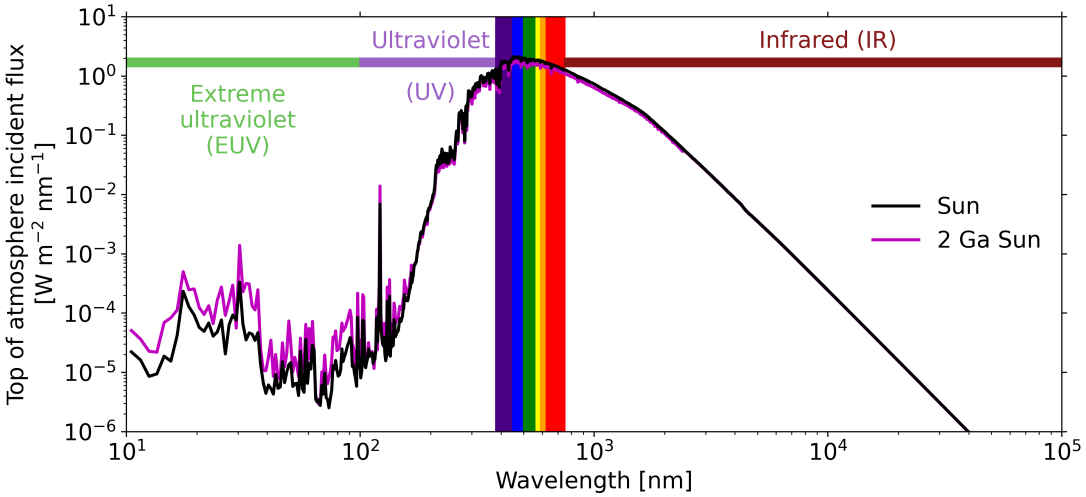

Fig. 4.2: The top of atmosphere incident flux (given in W m^{-2} nm^{-1}) is plotted against wavelength for the two solar spectra used in this Chapter, from the extreme ultraviolet (EUV) wavelengths starting at 10 nm, all the way to the infrared (IR) wavelengths. The visible wavelength region is shown by the various colours (violet, indigo, blue, green, yellow, orange, red). The present day Sun is shown in black and the 2 Gyr younger Sun shown in magenta. For wavelengths longer 175 nm, the present day Sun emits a larger flux.

PAL and 0.5% PAL simulations are included for this reason.

Variations on the 1% PAL simulation were also run. Whilst some research has advocated for a methane greenhouse during the Proterozoic (Pavlov *et al.*, 2003; Roberson *et al.*, 2011), recent research has argued that CH_4 in the Proterozoic atmosphere was lower, with mixing ratios similar to or lower than present day due to aqueous oxidation (Olson *et al.*, 2016; Daines & Lenton, 2016) or due to a low efficiency in converting organic carbon to CH_4 (Laakso & Schrag, 2019). To test the impact of variable CH_4 concentrations, two simulations were run: a case with 1% PAL of O_2 with CH_4 emissions where the flux of CH_4 to the atmosphere is the approximate modern day flux of 5×10^{14} g yr^{-1} (CH_4 em1), and a simulation with a reduced CH_4 flux of 5×10^{13} g yr^{-1} (CH_4 em0.1), which is based on suggested lower fluxes of CH_4 to the atmosphere during the Proterozoic by Laakso & Schrag (2019). Additionally, two simulations using a theoretical spectrum of the Sun 2 billion years ago (Claire *et al.*, 2012) are run to investigate the impact of a less luminous younger Sun. An existing solar evolution model (Claire *et al.*, 2012) is used to produce the solar spectrum at 2 Gyr before present (this is compared to the present day solar data in Fig 4.2). The solar evolution model can produce theoretical spectra for the Sun between 4.4 Gyr in the past and 3.6 Gyr in the future. It is valid between 0.1 nm and 160 µm, and is extended further in this Chapter into the far infrared by modelling the Sun in this region as a blackbody. The spectrum from the solar evolution model was rebinned[1] whilst conserving flux, to ensure that the new spectrum was interpolated onto the WACCM6 spectral irradiance grid. This young Sun's modelled total energy output was 13% less than the present Sun, with a weaker ultraviolet flux (the UV range was assumed to be between 100 nm and 400 nm) by a factor of 1.19, and a stronger extreme ultraviolet flux (the extreme ultraviolet wavelength range was

[1] using a Python tool called SpectRes (Carnall, 2017)

assumed to be between 10 nm and 91 nm) by a factor of 2.98. This younger Solar spectrum was used as input to the YS simulation and the YS 4×CO_2 simulation. The YS simulation has a surface mixing ratio of 280 ppmv of CO_2 (the same as the PI simulation), whilst the YS 4× CO_2 simulation has a surface mixing ratio of 1120 ppmv of CO_2, to offset the fainter Sun.

In each simulation other than the PI case, new minimum mixing ratios for O_3 and CH_4, both set at 10^{-12} by default, were set to 10^{-17} and 10^{-25}, respectively. A constant mixing ratio condition for O_2 at the lower boundary was imposed for the 0.5% and 0.1% PAL simulations because surface O_2 decreases below these scaled values without the imposed boundary condition. At 1% PAL and above, this does not occur on the time scales simulated.

The upper boundary conditions at 4.5×10^{-6} hPa are even more uncertain than the lower boundary conditions because there are fewer geological proxies for the upper atmosphere. Micrometeorites have been used to constrain the composition of the lower and upper atmosphere in the Neoarchean 2.7 Gyr ago (Tomkins *et al.*, 2016; Rimmer *et al.*, 2019; Payne *et al.*, 2020; Lehmer *et al.*, 2020). For example, Tomkins *et al.* (2016) and Rimmer *et al.* (2019) estimated high ($\sim$ 0.21) upper atmospheric O_2 concentrations, and Payne *et al.* (2020) and Lehmer *et al.* (2020) argued instead for high (possibly with mixing ratios of > 0.23) atmospheric CO_2 concentrations up to the homopause. Pack *et al.* (2017) used micrometeorites to show that Earth's modern atmospheric O_2 is isotopically homogeneous below the thermosphere. Nonetheless, there are no known upper atmospheric constraints for the Proterozoic. Therefore, many perturbation experiments were run to select upper boundary conditions in each simulation for H_2, H, H_2O, CH_4, O, O_2, and N that created smooth, consistent profiles in the thermosphere. It was found that the chosen upper boundary condition does not affect the atmosphere below 5×10^{-5} hPa, as long as the upper boundary condition is not unreasonably large

(for example, using a mixing ratio of 0.1 for water vapour would be unrealistic - see Fig. 4.3). The minimum pressure in the figures is thus truncated to 5×10^{-5} hPa. It is important to note that the choice of upper boundary conditions do not impact the conclusions.

Simulations were run until the annual cycle in total hydrogen repeats for 4 years, and there were no significant surface temperature trends in the simulations where only oxygen was changed. All results presented are time-averaged means that were from the last 4 years of each simulation. Zonal means and global means are area weighted due to grid box area coverage changing with latitude.

4.3 Results

4.3.1 The oxygen-ozone relationship

An oxygenated atmosphere enables the photochemical production of O_3, which is primarily produced in the tropical stratosphere, where incoming sunlight photodissociates O_2 and produces oxygen atoms (O). O_3 is produced and destroyed through the Chapman cycle. However, the chemistry of O_3 is more complicated than this (see Section 2.7.5), with catalytic cycles involving nitrogen, hydrogen, and halogen species playing an important role in destroying O_3 molecules (Lary, 1997; Grenfell *et al.*, 2006). WACCM6 includes such chemical reactions (Emmons *et al.*, 2020; Kinnison *et al.*, 2007).

Fig. 4.3 shows how imposing Proterozoic O_2 levels in simulations leads to striking changes in the chemical structure of the atmosphere. The maximum O_3 volume mixing ratio in the 0.1% PAL simulation (0.24 ppmv) is ≈ 40 times lower than the maximum in the PI simulation (9.99 ppmv). A decrease in O_2 concentration results in a reduction in O_3 column density, which then enables increased ultraviolet flux in the lower atmosphere and increased photolysis rates. This reduces the mixing ratios of important greenhouse gases such as H_2O, CH_4,

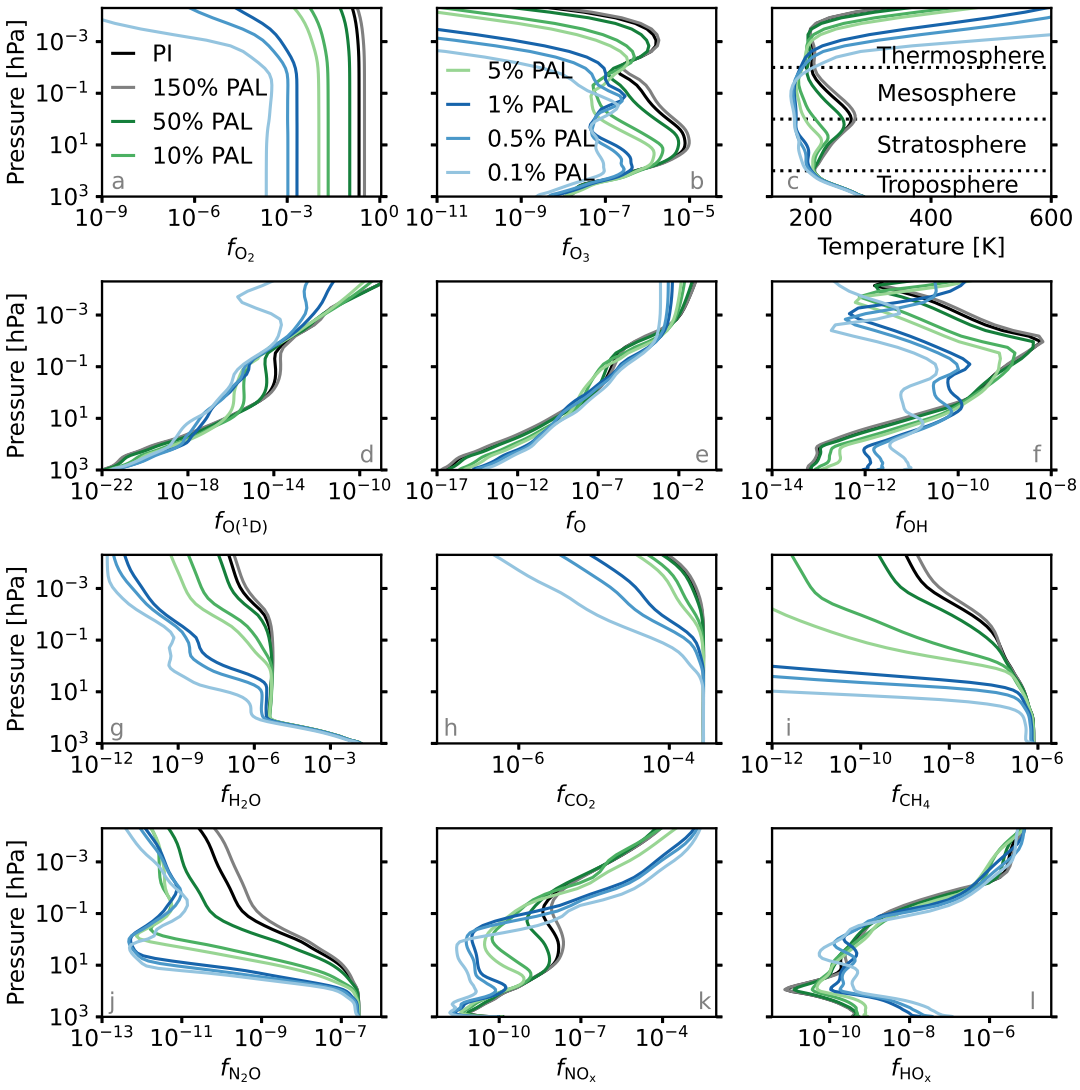

Fig. 4.3: Selected time-averaged global mean atmospheric profiles from the WACCM6 simulations are plotted against pressure in hPa. The PI (black), 150% PAL (grey), 50% PAL (dark green), 10% PAL (green), 5% PAL (light green), 1% PAL (dark blue), 0.5% PAL (blue), and 0.1% PAL (light blue) simulations are shown. PAL means relative to the present atmospheric level of O_2, which is 21% by volume. Mixing ratios for atmospheric constituents are shown for O_2 (*a*), O_3 (*b*), $O(^1D)$ (*d*), O (*e*), OH (*f*), H_2O (*g*), CO_2 (*h*), CH_4 (*i*), N_2O (*j*), NOx (*k*), and HOx (*l*). The PI atmospheric layers are indicated by black dotted lines alongside the temperature profiles in panel *c*.

N_2O, and CO_2: from the PI to the 0.1% PAL, at 0.1 hPa, the time-averaged mean volume mixing ratios for these species have been reduced by factors of 8.4×10^3, $\sim 10^{18}$, 51, and 3.5 respectively.

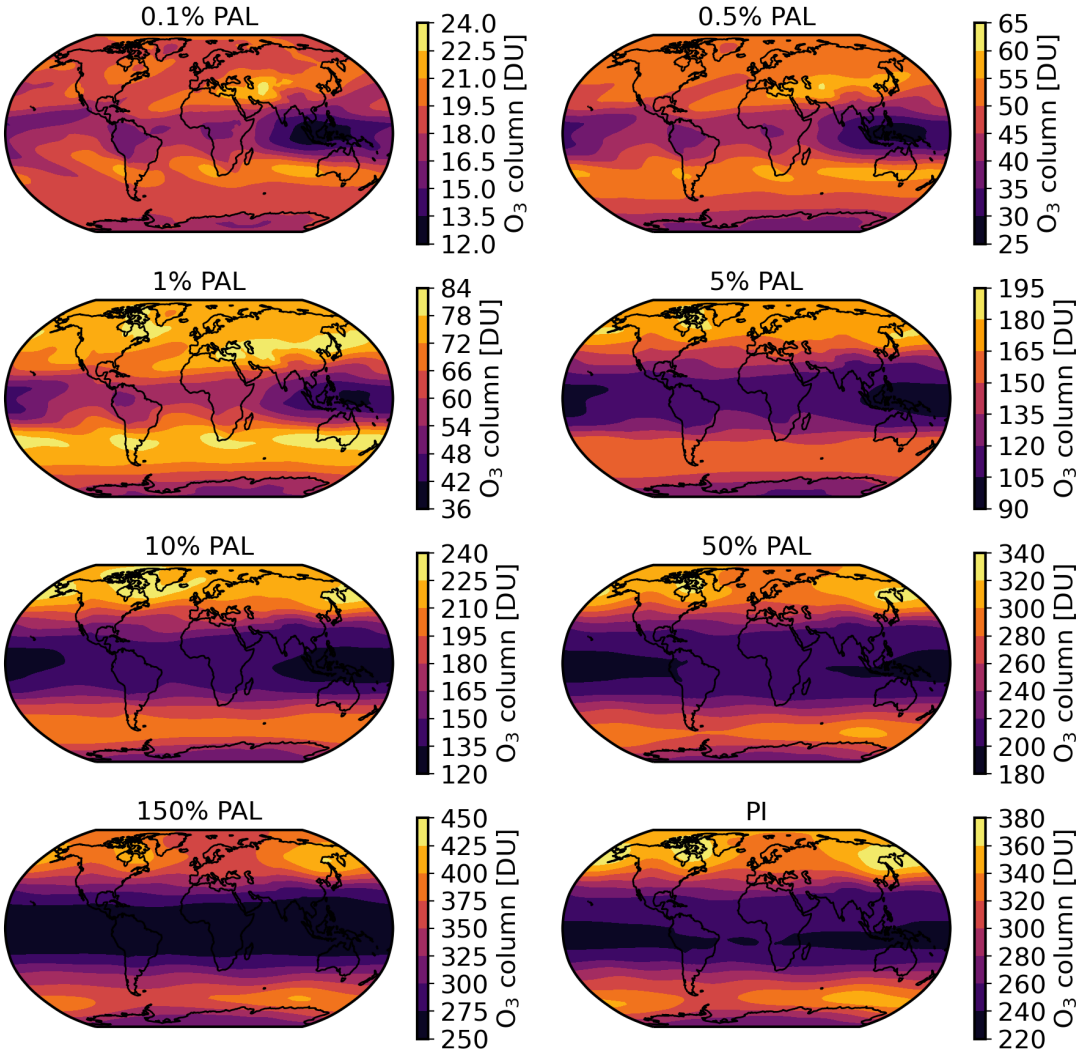

Fig. 4.4: The O_3 column is superimposed on Earth's surface and given in Dobson Units (1 DU = 2.687×10^{20} molecules m^{-2}) for the PI atmosphere and all the atmospheres where only oxygen concentrations were changed. Note the different scales on the colour bars. The tropics straddle either side of the equator, with the poles at the top and bottom of the 2D maps, and the extratropics at intermediate latitudes.

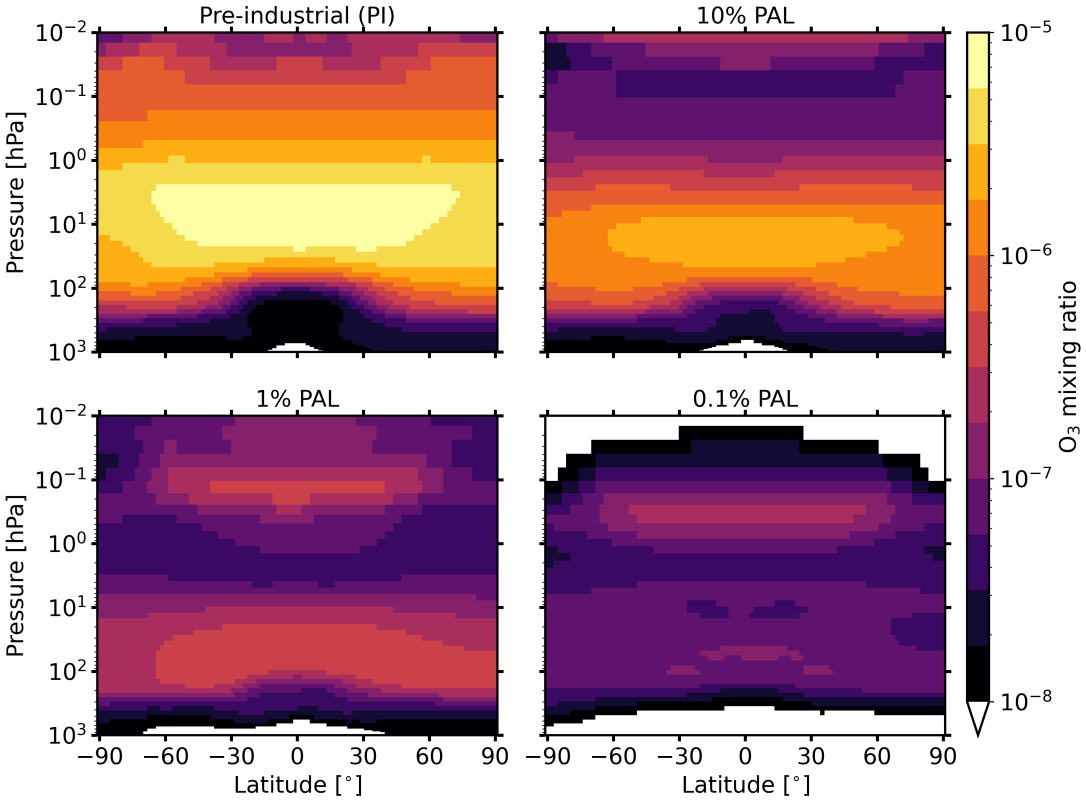

Fig. 4.5: The four panels show the O_3 mixing ratio structure in the zonal mean (longitudinal mean) between the surface and 0.01 hPa, for the PI, 10% PAL, 1% PAL, and 0.1% PAL atmospheres. The North Pole is at 90° latitude, the equator at 0°, with the South Pole at −90° latitude. The secondary night-time O_3 peak can be seen in the bottom two panels, but it is not visible for the PI and 10% PAL atmospheres as it lies above 10^{-2} hPa.

For an atmosphere with a surface pressure of 1000 hPa, where O_2 has been replaced by N_2 to maintain the surface pressure, a greater wavelength range shortward of the visible continuum can penetrate the lower atmospheric levels. For instance, the Lyman-α line (121.6 nm) which is primarily absorbed by O_2 and usually only reaches $\sim$ 80 km, can now photolyse H_2O and CH_4 at lower altitudes.

Increased tropospheric photolysis of H_2O, given by the reaction

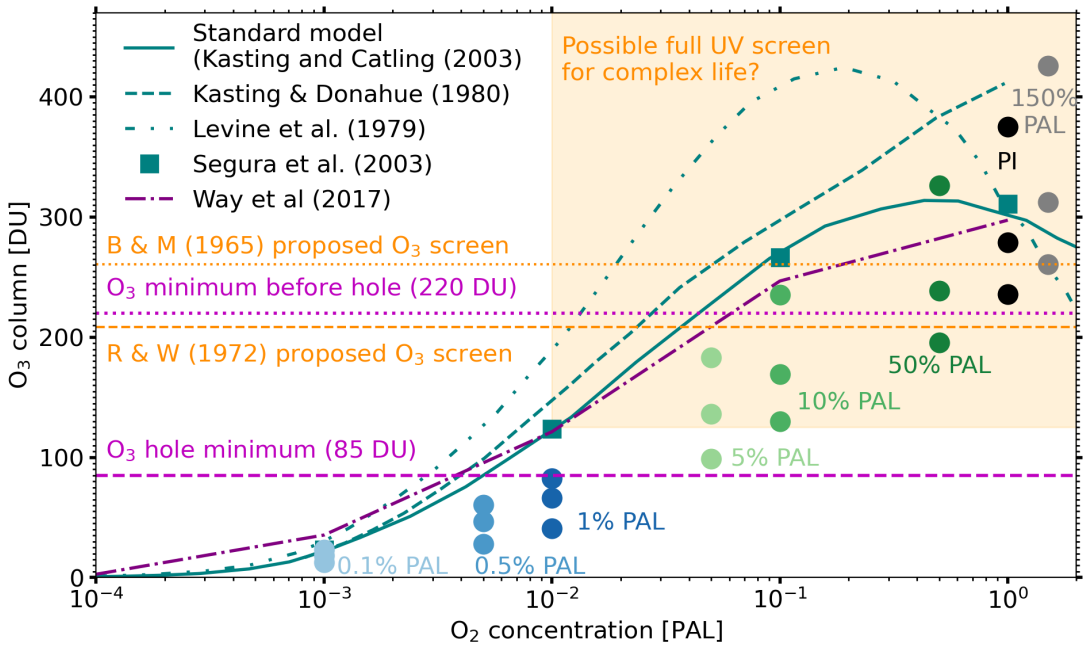

Fig. 4.6: Shown by the circles (in the same colour scheme as Fig. 4.3) are the maximum, mean, and minimum time-averaged O_3 columns from the varied O_2 simulations using WACCM6. These are compared to the mean values from previous 1D (Kasting & Donahue, 1980; Levine *et al.*, 1979; Segura *et al.*, 2003; Kasting & Catling, 2003) modelling in teal, and 3D (Way *et al.*, 2017) modelling in purple. Note that the data by Segura *et al.* (2003) is indicated by the square points with no associated line. Indicated in orange shading is a proposed full UV screen, when taking into account literature assumptions (see discussion Section 4.4.1) that levels of O_2 at 1% PAL or higher form a fully-shielding O_3 layer. Also indicated by the orange dashed and orange dotted lines are the full UV shielding O_3 screens proposed by Berkner & Marshall (1965) and Ratner & Walker (1972), respectively. The magenta dotted line shows the Antarctic O_3 minimum before the O_3 hole developed, and the magenta dashed line shows the minimum O_3 column over Antarctica after the O_3 hole developed in the 20$^{\text{th}}$ century.

$$H_2O + h\nu \longrightarrow OH + H, \tag{4.1}$$

and increased photolysis of O_3, represented by the reaction

$$O_3 + h\nu \longrightarrow O(^1D) + O_2(^1\Delta g), \tag{4.2}$$

result in the production of more OH and $O(^1D)$, which are key drivers of atmospheric chemistry. OH is increased at the surface from a volume mixing ratio of 6.2×10^{-14} to 6.9×10^{-12} between the PI case and the 0.1% PAL case. As a result of oxidation by OH and $O(^1D)$, the loss rate of CH_4 from the troposphere is increased by the following two reactions:

$$CH_4 + OH \longrightarrow CH_3 + H_2O, \tag{4.3}$$

and

$$CH_4 + O(^1D) \longrightarrow CH_3 + OH. \tag{4.4}$$

There is more stratospheric HOx ($HOx = H + OH + HO_2 + 2 \cdot H_2O_2$) as O_2 decreases which leads to further O_3 destruction. In the troposphere and lower stratosphere, each component of HOx is increased because reaction 4.1 leads to reactions that then produce more HO_2 and H_2O_2.

In contrast, NOx ($N + NO + NO_2$) is generally lower in the troposphere and stratosphere as O_2 is decreased. Usually, stratospheric N_2O gives rise to more NOx through the reaction

$$O(^1D) + N_2O \longrightarrow 2\,NO \tag{4.5}$$

(Brasseur & Solomon, 2005). When O_2 is reduced, tropospheric and stratospheric photolysis of N_2O instead produces $O(^1D)$ and N_2, and the path to NOx creation becomes increasingly limited with increasing photolysis.

The Earth's present-day O_3 column varies geographically depending on incident sunlight and the Brewer-Dobson circulation (Butchart, 2014). The Brewer-Dobson circulation is characterised by upwelling (rising fluid motion) in the tropical stratosphere, followed by poleward movement of air parcels, then downwelling (descending fluid motion) in the extratropical stratosphere, and distributes O_3 to higher latitudes (Butchart, 2014; Cohen *et al.*, 2014). The O_3 layer thus provides varying levels of UV protection across the Earth's surface which varies with season and latitude. Fig. 4.4 shows the annual mean geographical variation across Earth's longitudinal and latitudinal grid. The simulated global mean total O_3 column for the PI atmosphere case is 279 DU, decreasing to O_3 columns of 169 DU, 66 DU and 18 DU for the 10% PAL, 1% PAL and 0.1% PAL simulations, respectively. As O_2 decreases, there is a clear disruption in the pre-industrial O_3 distribution. Instead of the thick equatorial band of low O_3 levels in the PI atmosphere, the simulations which have oxygen levels $\leq$ 5% PAL have annual mean equatorial O_3 holes over the Pacific ocean and the Indian ocean.

Fig. 4.5 shows the zonal mean O_3 mixing ratio for the PI, 10% PAL, 1% PAL, and 0.1% PAL simulations. The stratospheric O_3 layer shifts in terms of altitude, shape and latitudinal variation, as does the secondary night-time O_3 layer. O_3 can be seen to trace the pressure-varying tropopause in the PI atmosphere. This is less apparent as oxygen decreases.

Displayed in Fig. 4.6 is the variation of the total O_3 column (and thus the modulation of surface UV fluxes) with atmospheric O_2 mixing ratio. The PI simulation recovers the pre-industrial O_3 column in both magnitude and latitudinal variation. At several O_2 concentrations, lower total O_3 columns are reported compared to previous 1D and 3D work (Levine *et al.*, 1979; Kasting & Donahue, 1980; Segura *et al.*, 2003; Kasting & Catling, 2003; Way *et al.*, 2017). In the 10% PAL case, the mean column is approximately 1.46, 1.57, 1.76, and 2.43 times

smaller when compared to Way *et al.* (2017), Segura *et al.* (2003), Kasting & Donahue (1980), and Levine *et al.* (1979), respectively. For the 1% PAL case, the mean O_3 column is approximately 1.83, 1.87, 2.24, and 2.89 times smaller when compared to Way *et al.* (2017), Segura *et al.* (2003), Kasting & Donahue (1980), and Levine *et al.* (1979), respectively. Also for the 1% PAL case, if the minimum time-averaged values are included (likely at the equator where UV irradiation is highest), then the discrepancy is worse and the minimum O_3 column is 2.97, 3.04, 3.63, and 4.68 times smaller compared to mean O_3 columns from to Way *et al.* (2017), Segura *et al.* (2003), Kasting & Donahue (1980), and Levine *et al.* (1979), respectively. Also shown, along with the previous 1D result from Kasting & Donahue (1980) and the 3D result from Way *et al.* (2017), is that O_3 levels consistently rise with increasing O_2 levels, rather than plateauing and decreasing between 10% PAL and 100% PAL, which previous 1D models have reported (Kasting & Catling, 2003).

The O_3 column is not just determined by O_2. It depends on many factors, including other chemical species present in the atmosphere, the flux of incoming solar radiation, and atmospheric circulation. Fig. 4.7 shows how varying the CH_4 flux (and thus its mixing ratio), the solar spectrum, and CO_2 concentrations, affects the O_3 column. Using a spectrum of a younger Sun, which has a lower total incident flux by 13%, the O_3 column is increased by $\approx$ 10 DU. Relative to the YS simulation, the O_3 column in the YS $4\times CO_2$ case is greater by $\approx$ 5 DU. This is because a younger Sun and increased CO_2 concentrations cool the stratosphere and mesosphere, with O_3 production and loss being temperature dependent (i.e. cooler temperatures result in faster O_3 production and reduced catalytic destruction). Lower CH_4 mixing ratios act to reduce the O_3 column by $\approx$ 5 DU because there is more $O(^1D)$ and OH available to destroy O_3 that would otherwise have reacted with CH_4 molecules. In all scenarios with 1% PAL of O_2,

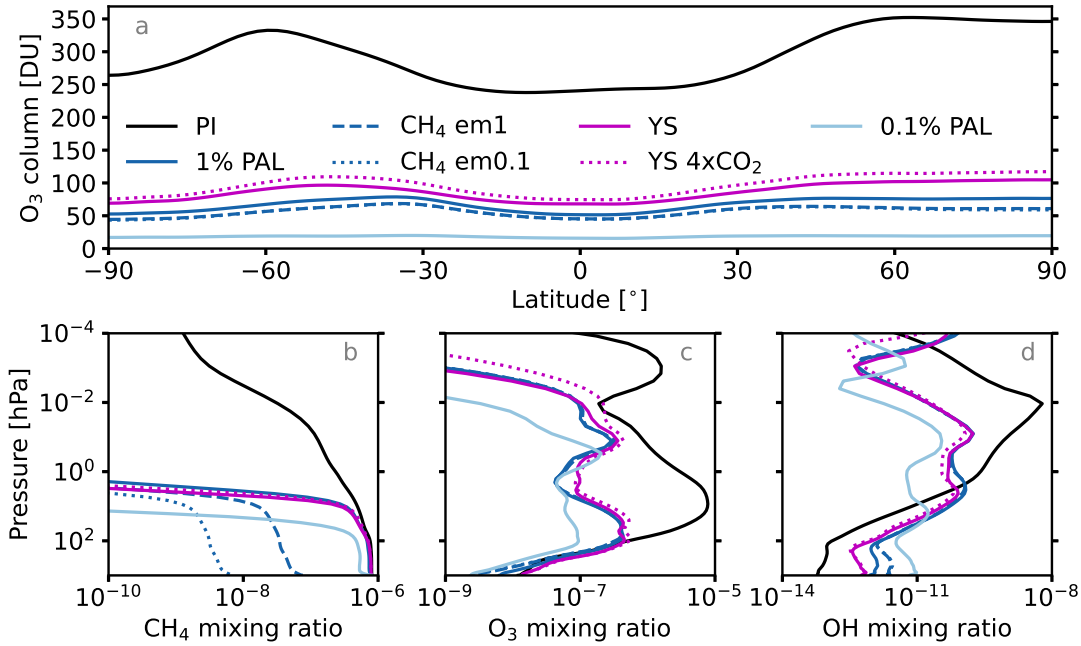

Fig. 4.7: In all panels, the PI (black), 1% PAL (dark blue), 0.1% PAL (light blue), CH_4 em1 (dark blue dashed), CH_4 em0.1 (dark blue dotted), YS (magenta) and YS $4\times CO_2$ (magenta dashed) simulations are shown. The latitudinal variation of the O_3 column is shown in panel *a*. The CH_4, O_3, and OH mixing ratio profiles are shown in panels *b*, *c* and *d*, respectively.

the mean simulated O_3 column values are lower than previous predictions.

4.3.2 Oxygen as a control on hydrogen escape

Hydrogen can be lost from planetary atmospheres through a variety of mechanisms (Gronoff *et al.*, 2020). Photolytic loss of CH_4 and H_2O, and subsequent irreversible loss of hydrogen, can abiotically increase the oxidation state of the Earth (Catling *et al.*, 2001).

The current hydrogen escape rate is $\approx 3 \times 10^{10}$ mol of H yr^{-1}, corresponding to the production of 0.1 bar of O_2 and 1 metre of water loss per 1 billion years (Zahnle *et al.*, 2013). From isotopic evidence and computational modelling, since its formation, the Earth may have lost between 0.26 and 2 times the present ocean

volume (Pope *et al.*, 2012; Kurokawa *et al.*, 2018), although such estimates depend on the water transfer between the Earth's oceans and its interior (Korenaga *et al.*, 2017).

Fig. 4.8 presents the total hydrogen mixing ratio profile, $f_{\mathrm{T}}(\mathrm{H})$, which is calculated by Eq. 2.13, from several WACCM6 simulations. For the PI simulation, the mixing ratio of total hydrogen entering the stratosphere is $f_{\mathrm{T}}(\mathrm{H}) = 12$ ppmv. Above the cold trap in the tropical tropopause layer (TTL), the H_2O mixing ratio increases until it reaches a maximum mesospheric value (≈ 5 ppmv) due to CH_4 reacting with OH. Turbulent mixing causes $f_{\mathrm{T}}(\mathrm{H})$ to remain roughly constant between the lower stratosphere and homopause. Above the homopause, through diffusive separation, the lighter atmospheric constituents increase in relative abundance with decreasing pressure (increasing altitude).

The low oxygen cases present rather different scenarios because the cold trap mechanism is sensitive to O_2 concentrations, thus affecting hydrogen escape. As the TTL cools when O_2 and simultaneously O_3 decrease, a lower amount of water is able to enter the stratosphere. Due to the ≈ 5 K difference in time-averaged zonal mean TTL temperatures between the PI and 0.1% PAL simulations, more H_2O is frozen out in the form of ice and ice clouds before the temperature inversion in the PI atmosphere at ≈ 100 hPa (Wang & Dessler, 2012). For example, there is ≈ 2 ppmv less H_2O at 100 hPa (lower stratosphere) for the 0.1% PAL case. Consequently, a reduced amount of water propagates into the stratosphere in the low oxygen cases compared to the PI atmosphere, contributing less to $f_{\mathrm{T}}(\mathrm{H})$.

The $f_{\mathrm{T}}(\mathrm{H})$ profile shows that for the lower oxygen cases the rate of hydrogen escape is lower than that of present day escape ($\Phi_{\mathrm{esc,PI}}$). The rates for the lower oxygen simulations are: $0.39\Phi_{\mathrm{esc,PI}}$, $0.64\Phi_{\mathrm{esc,PI}}$, and $0.77\Phi_{\mathrm{esc,PI}}$, for the 0.1% PAL, 0.5% PAL, and 1% PAL simulations, respectively. Therefore, O_2 levels during the Proterozoic may have partially controlled the limiting flux for hydrogen escape.

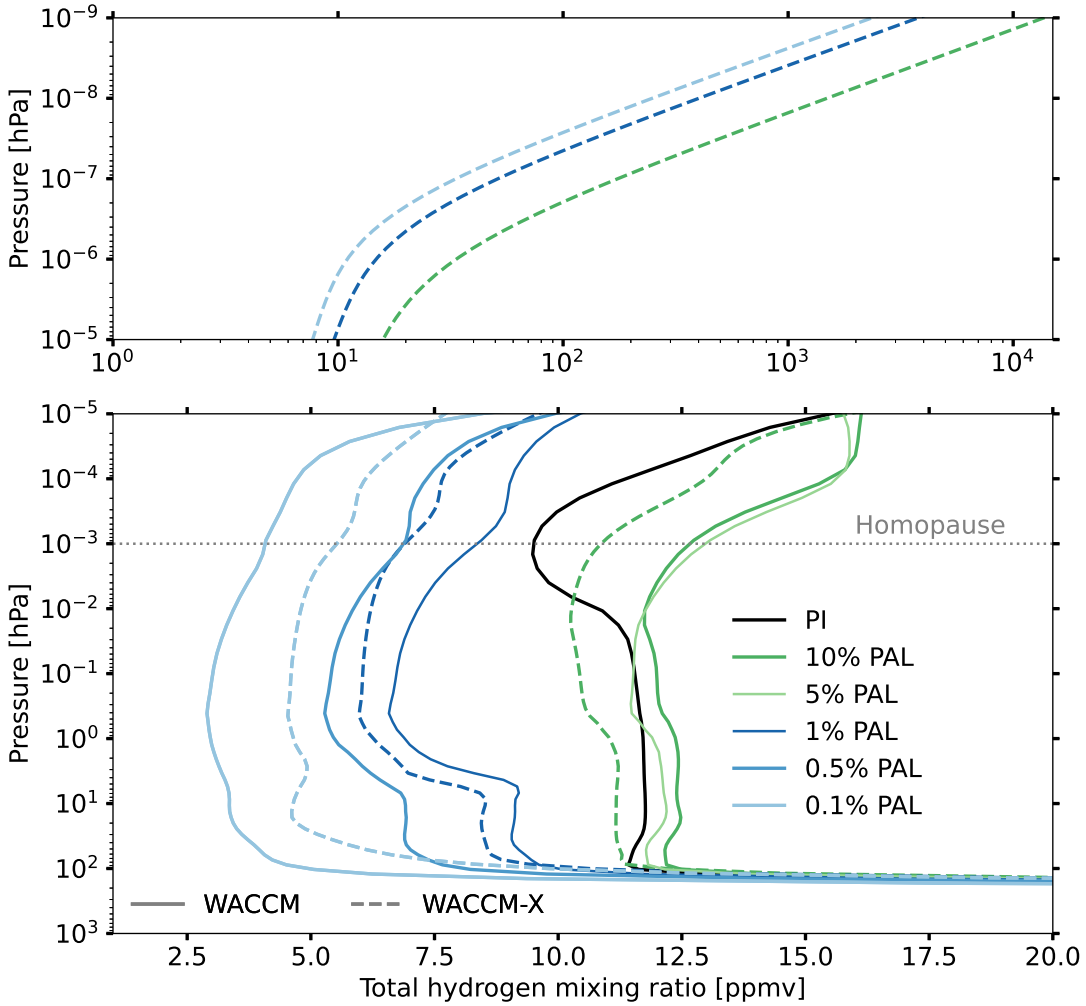

Fig. 4.8: The bottom panel shows the time-averaged global mean mixing ratio of total hydrogen, $f_T(H)$, plotted against pressure for the PI, 10% PAL, 5% PAL, 1% PAL, 0.5% PAL, and 0.1% PAL cases. $f_T(H) = f(\mathrm{H}) + 2 \cdot f(\mathrm{H_2}) + 2 \cdot f(\mathrm{H_2O}) + 4 \cdot f(\mathrm{CH_4})$. Three WACCM-X simulations at 10% PAL, 1% PAL, and 0.1% PAL, are included (dashed lines) and extend to the top panel because WACCM-X is able to simulate to lower atmospheric pressures (higher altitudes). Note the different scales on the horizontal axes. Assuming escape rate of hydrogen is diffusion limited, the total hydrogen mixing ratio at the homopause sets the maximum escape rate for hydrogen in the exosphere.

4.3.3 The Proterozoic Faint Young Sun Problem

The Faint Young Sun Paradox is the problem associated with the early Sun outputting less total energy, yet the surface temperatures of Earth remaining high enough for liquid water to exist (Feulner, 2012). Whilst the Faint Young Sun Paradox may have been solved for the Archean climate (Charnay *et al.*, 2020), the question of how the Earth maintained a mostly ice-free surface throughout most of the Proterozoic remains to be answered (Olson *et al.*, 2016; Fiorella & Sheldon, 2017). Some studies have suggested that an elevated CH_4 greenhouse can solve this problem (Pavlov *et al.*, 2003; Roberson *et al.*, 2011). In contrast with this, more recent work has suggested otherwise (Daines & Lenton, 2016; Olson *et al.*, 2016; Laakso & Schrag, 2019). Possible CH_4 concentrations during the Proterozoic are discussed in this section.

The chemical lifetime for a molecule in the atmosphere is the time for the concentration of that molecular species to decrease to $1/e$ of its initial concentration, where e is Euler's number. Reducing O_2 vastly reduces atmospheric chemical lifetimes for several important species, including the lifetime of CH_4 (τ_{CH_4}), as shown in Table 4.2. The lifetime of any molecule throughout the atmosphere varies depending on photochemical destruction rates and chemical reaction rates, as well as transport of the molecule.

Table 4.2 shows the τ_{CH_4} values for all the simulations. τ_{CH_4} is 9.18 years for the PI case and just 40 days for the 0.1% PAL case. Each of the varied O_2 simulations have a constant surface CH_4 mixing ratio. In reality, a flux to the atmosphere sustains a constant, or time-varying, surface mixing ratio. Despite using a constant mixing ratio, the approximate flux that would be needed to sustain CH_4 at 0.8 ppmv in each simulation can be predicted, as τ_{CH_4} does vary in each case. The ratio between the lifetimes is the inverse of the ratio of the surface fluxes. To illustrate, the ratio between the 1% PAL τ_{CH_4} and the PI

Table 4.2: The atmospheric lifetime of CH_4 (τ_{CH_4}) given in years for each simulation. The ratio of this lifetime and the lifetime of CH_4 in the PI atmosphere ($\tau_{CH_4,PI}$) is given as $\tau_{CH_4}/\tau_{CH_4,PI}$.

Simulation name	τ_{CH_4} [yr]	$\tau_{CH_4}/\tau_{CH_4,PI}$
PI	9.18	1.00
150% PAL	10.00	1.09
50% PAL	8.24	0.90
10% PAL	5.45	0.59
5% PAL	3.51	0.38
1% PAL	0.55	0.06
CH_4 em1	0.27	0.03
CH_4 em0.1	0.25	0.03
YS	1.25	0.14
YS 4×CO_2	1.17	0.13
0.5% PAL	0.28	0.03
0.1% PAL	0.11	0.01

τ_{CH_4} is 0.06, meaning that a flux increase of $1/0.06 \approx 17$ compared to the pre-industrial flux would be needed to sustain surface CH_4 at 0.8 ppmv in the 1% PAL simulation. All CH_4 lifetime ratios are given in Table 4.2.

In the CH_4 emissions simulations, CH_4 is reduced at the surface to ≈ 0.08 ppmv and ≈ 0.007 ppmv for the CH_4 em1 and CH_4 em0.1 simulations, respectively. Some recent studies have argued that CH_4 fluxes to the atmosphere during the Proterozoic were either reduced compared to the pre-industrial flux (Laakso & Schrag, 2019), or they were not much greater (Olson *et al.*, 2016; Daines & Lenton, 2016), and that the atmospheric chemical lifetime of CH_4 was reduced due to a diminished O_3 column. In such scenarios, CH_4 would not have been a significant greenhouse gas during the Mesoproterozoic.

4.4 Discussion

4.4.1 Habitability and increased UV radiation

Our results show that previous 1D and 3D modelling may have overestimated Earth's mean O_3 column for atmospheric O_2 mixing ratios between 0.1 – 50% PAL, with these mixing ratios having relevance for both the Phanerozoic and Proterozoic. In this section, the potential implications for habitability during

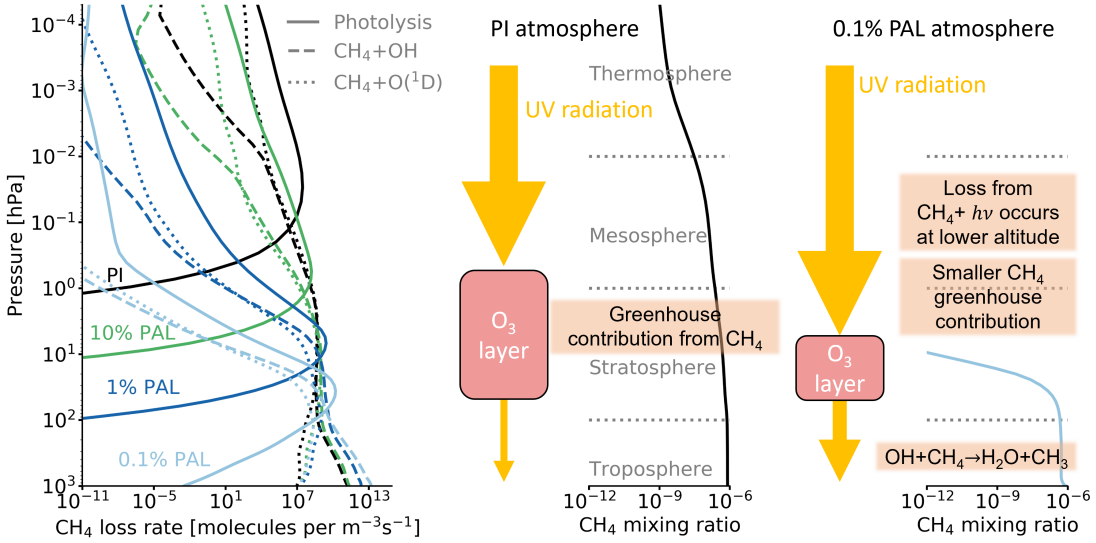

Fig. 4.9: When the O_2 concentration reduces in the WACCM6 simulations, the mixing ratio of CH_4 reduces too. On the left is how the CH_4 loss rate varies with atmospheric pressure for the three major loss mechanisms of CH_4: photolysis, reaction with OH, and reaction with $O(^1D)$. Shown alongside the CH_4 mixing ratio profiles for the the PI (middle) and 0.1% PAL (right) atmospheres are yellow arrows which indicate UV radiation travelling down through the atmosphere. UV radiation is attenuated by the O_3 layer. When O_2 decreases, the O_3 column abundance decreases, such that increased amounts of UV radiation penetrate into the troposphere. Through photolysis, this produces more OH (e.g. photolysis of H_2O and H_2O_2) molecules and $O(^1D)$ atoms (e.g. photolysis of H_2O, O_2, O_3, and N_2O) which then react with CH_4, decreasing its abundance. $CH_4 + h\nu$ represents photolysis of CH_4 by a photon with frequency ν, where h is Planck's constant. Note that the size of the arrows and the size of the O_3 layers are representative only.

these time periods is explored.

Assessing surface habitability is not simple. It depends on many factors, including the temperature and pressure at the surface, and also the type of life in the environment that is being evaluated. For instance, humans cannot survive in conditions where bacterial extremophiles flourish (Pikuta *et al.*, 2007). The discussion of habitability here will be limited to UV radiation, which has varying effects depending on the organism considered. Note that many organisms have developed strategies to avoid excessive UV damage, as well as repair mechanisms to mitigate its effects (Núñez-Pons *et al.*, 2018; Gill *et al.*, 2015; Singh *et al.*, 2010; Sinha & Häder, 2002). Although microbial life is known to survive enhanced UV irradiation environments (Rambler & Margulis, 1980; Pikuta *et al.*, 2007; Abrevaya *et al.*, 2020), many animals and plant species are impacted by high doses of UV radiation, resulting in infertility (Benca *et al.*, 2018), cell death (Nawkar *et al.*, 2013), and increased mortality rates (Davies & Forbes, 1986; Borgeraas & Hessen, 2000; Kouwenberg *et al.*, 1999), with UV radiation considered an environmental stressor (Häder *et al.*, 2015).

Higher surface UV fluxes during the early Paleozoic or throughout the Proterozoic could have exerted an ecological selection pressure on some organisms (Sagan, 1973; Rothschild, 1999; Cockell *et al.*, 2011). Indeed, some mass extinction events have been linked to reduced O_3 columns that have resulted in high UV-B fluxes (Melott *et al.*, 2004; Bond & Grasby, 2017; Benca *et al.*, 2018; Marshall *et al.*, 2020; LaViolette, 2011; Jardine *et al.*, 2023). Several decades ago, Berkner & Marshall (1965) suggested that UV radiation could have prevented the colonisation of dry land, but more recent literature suggests this was unlikely (Margulis *et al.*, 1976; Rambler & Margulis, 1980; Mills & Canfield, 2014; Cockell & Raven, 2007; Cockell & Horneck, 2001; Cockell *et al.*, 2011). However, UV radiation may have still played a role in the subsequent evolution of life on land once

it was colonised (Cockell, 1999; Zedek & Bureš, 2018; Zedek *et al.*, 2021; Benca *et al.*, 2018; Marshall *et al.*, 2020), just as stratospheric O_3 depletion in the last few decades, which has resulted in increased UV flux, has affected animals and plants in the southern hemisphere (Paul & Gwynn-Jones, 2003; Bornman *et al.*, 2019).

Life in the oceans experiences lower fluxes of UV radiation compared to life on land because water attenuates UV radiation (Tedetti & Sempéré, 2006). There is ample evidence of life existing in the Proterozoic oceans (Knoll *et al.*, 2006; Lyons *et al.*, 2021, and references therein), yet this does not mean that life in the photic zone (the topmost layer of the ocean which is illuminated by sunlight) would have been unaffected by UV radiation.

Photosynthesis may have been inhibited under the UV irradiance of the Proterozoic (Cockell & Horneck, 2001). In the modern ocean, it was estimated by Smith *et al.* (1992) that primary productivity[1] reduced by 6 – 12% under the Antarctic ozone hole. A decrease in growth rates and an increase in cell death was reported in phytoplankton by Llabrés & Agustí (2010) under ambient UV-B radiation compared to no UV-B radiation. Additionally, Bancroft *et al.* (2007) found through meta-analysis a widespread, overall negative effect on aquatic ecosystems from UV-B radiation, noting that the effects vary and are organism dependent. A larger meta-analysis on marine biota was performed by Llabrés *et al.* (2013), who determined that organisms such as protists, corals, and crustaceans were particularly susceptible to damage from increased levels of UV-B radiation. Mloszewska *et al.* (2018) argued that primary productivity from cyanobacteria would have remained low until a permanent ozone screen formed at 1% PAL, citing 1D modelling studies (Segura *et al.*, 2003; Kasting, 1987) in this assertion.

For O_2 concentrations between 0.1% PAL and 50% PAL, the total mean O_3

[1]Primary productivity is the rate at which organic compounds are produced from CO_2, usually through photosynthesis.

column quantities in the 3D simulations presented here are diminished by a factor of 1.2 – 2.9 times when compared to prior 1D and 3D simulations (Kasting & Catling, 2003; Segura *et al.*, 2003; Way *et al.*, 2017; Levine *et al.*, 1979; Kasting & Donahue, 1980). This reduction is maximised when considering the 1% PAL simulation minimum, with the minimum O_3 column reduced between 3 – 4.7 times when compared to previous mean O_3 column estimations. The lowest columns are usually associated with the equatorial regions (see Fig. 4.4), which cover a large proportion of the Earth's surface, receive the highest amounts of solar radiation, and are thus important for habitability predictions.

Whilst these reductions do not seem like large numbers, because O_3 reduces UV fluxes through a power law (Madronich *et al.*, 1998), an apparently small change in O_3 can lead to a large change in surface UV fluxes. For example, Black *et al.* (2014) studied O_3 depletion resulting from the Siberian Traps eruptions, calculating O_3 columns ranging between $\approx$ 55 and $\approx$ 145 DU, with estimated increases in biologically damaging UV-B radiation between 5 and 50 times that of present day fluxes. Rugheimer *et al.* (2015b) modelled the atmospheres of modern Earth and Earth in the past. They reported an 8.8 factor decrease in O_3 column (196.9 DU $\longrightarrow$ 22.4 DU) between their modern Earth case and their case of Earth 2 Gyr ago. Despite total top of atmosphere UV-B (280 – 315 nm) and UV-C (100 – 280 nm) radiation decreasing in their 2 Gyr ago simulations by 1.27 and 1.29 times, respectively, this O_3 reduction increased biologically damaging UV fluxes by 41.3 times, with surface UV-B and UV-C fluxes increasing by 2.74 and 2×10^{13}, respectively. Segura *et al.* (2003) report an O_3 column of 266 DU in a 10% PAL atmosphere, whilst a minimum of 130 DU at 10% PAL is reported here. Segura *et al.* (2003) had a mean O_3 column of $\approx$ 124 DU, but instead at 1% PAL rather than 10% PAL. For these two atmospheres (10% PAL $\rightarrow$ 1% PAL), they estimated that UV-B and UV-C surface fluxes increased by 2.08 times and

4437.5 times, respectively. The discrepancy between the WACCM6 simulations and prior simulations matters when estimating the habitability of a planet or exoplanet. Even the lower estimates in the literature, that suggest 0.5% PAL of O_2 is required to produce an effective O_3 screen (Cockell & Horneck, 2001), calculate UV attenuation based on O_3 column estimates from the 1D model used by Kasting & Donahue (1980). In the 0.5% PAL WACCM6 simulation, the mean and minimum O_3 columns (45 and 30 DU) are 2.2 and 3.3 times lower than the calculated value of 100 DU by Kasting & Donahue (1980).

Reasoning regarding the evolutionary impact of the O_3 layer and associated UV fluxes has generally been based on converged atmospheric simulations from 1D models (Levine *et al.*, 1979; Kasting & Donahue, 1980; Kasting & Catling, 2003), which estimate that roughly 1% of the present atmospheric level of O_2 gives rise to an O_3 layer that shields the biosphere (Catling & Claire, 2005). This was originally based on passing the threshold for full UV screen limits of $\approx$ 210 DU proposed by Berkner & Marshall (1965) and $\approx$ 260 DU proposed by Ratner & Walker (1972). More recently, atmospheric (Gregory *et al.*, 2021; Laakso & Schrag, 2019), biogeochemical (Och & Shields-Zhou, 2012; Gebauer *et al.*, 2017), biological (Mills & Canfield, 2014; Crockford *et al.*, 2018; Mloszewska *et al.*, 2018), and astrobiological/exoplanet work (Proedrou & Hocke, 2016; Gebauer *et al.*, 2017; Olson *et al.*, 2018b; Reinhard *et al.*, 2017; Schwieterman *et al.*, 2018a; Stüeken *et al.*, 2020; Reinhard *et al.*, 2019), have cited 1D results in Fig. 4.6, often with the statement that at least 1% PAL of O_2 is needed to establish a full UV shield. Therefore, prior studies in Fig. 4.6 show that at 1% the present atmospheric level of O_2, the fully UV shielding range is between 120 – 185 DU for the mean O_3 column, whereas the WACCM6 1% PAL simulation gives a mean O_3 column of just 66 DU, roughly half the lower end of the 120 – 185 DU range. The simulations presented here show that 5% PAL of oxygen is required

to reach a mean O_3 column of 136 DU, and 10% PAL is required to reach a mean of 169 DU and fully encompass the protective range when including the 10% PAL minimum of 130 DU. Thus, potentially 5 – 10 times more atmospheric oxygen is required than previously thought to fully UV shield the biosphere, showing that the common assumption that 1% PAL of O_2 provides a full UV shield is potentially incorrect. Additionally, the real atmosphere is 3D and varies temporally, and the O_3 layer can be influenced by biologically produced gases (e.g. O_2, CH_4), volcanic emissions (Black *et al.*, 2014), solar activity and flares (Pettit *et al.*, 2018), as well as asteroid or comet impacts (Pierazzo *et al.*, 2010).

A caveat for these simulations is that CO_2 mixing ratios above 1120 ppmv (4× the pre-industrial CO_2 mixing ratio) have not been simulated. It is noted that up to 2800 ppmv of CO_2 may be consistent with geological proxies during the Proterozoic (Olson *et al.*, 2018a; Fiorella & Sheldon, 2017). Additional CO_2 cooling would act to slightly increase the O_3 column through the temperature dependence on chemical reactions and also contribute to the absorption of UV radiation (including Lyman-α) in simulations with the very lowest O_2 concentrations. Higher CO_2 concentrations would reduce photolysis of H_2O and CH_4 in the upper atmosphere. However, since the absorption cross section for O_2 at Lyman-α is ≈ 3 times greater than that of CO_2 (Heays *et al.*, 2017; Lu *et al.*, 2010; Huestis & Berkowitz, 2010) and Lyman-α fluxes in the lower atmosphere would remain very small, it is expected that this does not significantly affect the new estimates of the ozone column or methane's contribution to the Proterozoic greenhouse.

These new results should not be treated as a real reconstruction of Earth's past O_3 states, just as this Chapter shows that taking 1D O_3 calculations as ground truth is problematic; instead, 1D O_3 calculations should be treated with caution. The lower O_3 columns predicted in this Chapter have important consequences for

life's history on Earth and future estimations regarding the habitability of exoplanets. At some point, Earth's atmosphere is likely to pass through varied lower oxygenated states, including analogous states to those simulated here (Ozaki & Reinhard, 2021). Following Ozaki & Reinhard (2021), these WACCM6 simulations can be used as a further step for predictions of Earth's future biosphere, its habitability, and observability from afar. Moreover, paleoclimate modelling of the Earth that investigates specific climate events and geological processes will benefit from whole atmosphere 3D chemistry-climate models that are coupled to dynamics. For instance, 1D atmospheric models that investigate oxygenated exoplanet and paleo atmospheres could be tuned to replicate the lower O_3 column values. This tuning will also likely be applicable to oxygenated exoplanets orbiting other stellar spectral types, especially tidally-locked M dwarf exoplanets, where simulating the dynamics is necessary to understand chemical transport between the day and night side of the planet.

Under reduced O_3 columns at O_2 mixing ratios between 0.1 – 50% PAL, the surface and the photic zone would have received more UV radiation than previously believed. Consequently, the efficiency of photosynthesis throughout the low-O_2 range of the Proterozoic atmosphere could have been restricted, and UV fluxes may have acted as a stronger evolutionary control for organisms that were susceptible to fluctuations in UV caused by O_3 column changes. The notion that there is a threshold above which a full-O_3 shield exists seems to simplify what is likely a complex interaction through Earth's oxygenated history between life's continuous evolution, and O_2, O_3, and UV radiation.

4.4.2 The dependence of hydrogen escape on oxygenation

Three WACCM-X simulations have been included in Fig. 4.8 in addition to the initial WACCM simulations from Cooke *et al.* (2022). The WACCM-X simula-

tions are for the 10% PAL, 1% PAL, and 0.1% PAL atmospheres. In order to perform simulations with WACCM-X, I copied temperature and chemical fields from the lowest 70 layers in altitude from the WACCM6 simulations, and scaled the rest of the layers above to smoothly connect to those profiles. I modified the lower boundary conditions so that the chemical fluxes and fixed mixing ratios in the WACCM-X simulations matched those from the WACCM6 simulations of oxygenated paleoclimates. These simulations confirm that the mixing ratio of hydrogen reaching the upper atmosphere decreases with decreasing O_2 concentrations. At 500 km in the WACCM-X simulations, the $f_T(H)$ ratio between 10% PAL and 1% PAL is 12.2, and the ratio between that of 10% PAL and 0.1% PAL is 52.2. At the model top (same pressure but different altitude), these ratios are 3.6 and 5.7, respectively. The estimates of $f_T(H)$ at various O_2 concentrations presented here compared with the pre-industrial atmosphere illustrate how evolving O_2 levels would have modulated generally low rates of hydrogen escape through the Proterozoic and Phanerozoic eons.

Whilst most of Earth's water loss through hydrogen escape is expected to have occurred in the preceding Archean and Hadean eons (Catling *et al.*, 2001; Zahnle *et al.*, 2013; Korenaga *et al.*, 2017), this mechanism through which O_2 may have affected the escape of hydrogen after the beginning of the Proterozoic by a factor of ~ 2.5 is still an important part of Earth's atmospheric history. This process may potentially be more important for particular planetary scenarios, such as: different stellar host types; planets in eccentric orbits; varied concentrations of greenhouse gases; lower initial water inventories; different total instellation. These parameters can affect both the vertical profile of temperature and H_2O. Furthermore, additional caveats include the assumed mixing ratios of H, H_2, CH_4, as well as the land-ocean coverage at the surface, which could all vary depending on the planet considered.

Whilst the WACCM-X simulations can simulate the concentrations of gases in the thermosphere, the model does not explicitly simulate atmospheric escape. To better estimate hydrogen escape at different O_2 concentrations, the WACCM-X simulations performed here could be coupled to a 3D hydrodynamic escape model (e.g. the model used in Dong *et al.*, 2018), or used as lower boundary initial conditions. This is left as future work.

4.4.3 Keeping the Mesoproterozoic ice-free

A reduced O_3 layer also affects the chemical composition of the troposphere, including the decreased abundance of CH_4 (Olson *et al.*, 2016; Kasting & Donahue, 1980) caused by an increase in OH and $O(^1D)$. Methane is an important greenhouse gas, so the Proterozoic greenhouse is considered here.

The lack of evidence for glaciation during Earth's Mesoproterozoic suggests a mostly ice-free surface during this era. Given that there is ice at Earth's poles today, and during the Proterozoic there was less solar heating, then an ice-free surface without at least some increased greenhouse warming under a fainter Sun creates a contradiction, because one would expect more ice with a lower solar energy flux. To investigate this issue, CH_4 concentrations at varied O_2 concentrations and atmospheric CH_4 fluxes have been simulated to explore whether it was likely that a Mesoproterozoic greenhouse had substantial contributions from CH_4.

3D simulations have shown that an ice-free surface can be sustained during the Mesoproterozoic if CO_2 is at 10 times its pre-industrial level and there is between 28 and 140 ppmv of CH_4 (Fiorella & Sheldon, 2017). The mixing ratio of CH_4 at the surface in the fixed lower boundary condition simulations is 0.8 ppmv. Consequently, given the surface τ_{CH_4} values for the low O_2 cases (10% - 0.1% PAL), the results show that an approximate CH_4 flux increase (compared

to present day) of a factor between 60 and 3500 is needed to reach levels of 28 ppmv during the Proterozoic (considering 10% PAL and 0.1% PAL, respectively), and 5 times these values to reach 140 ppmv.

Olson *et al.* (2016) estimated that at 1% PAL of O_2, net biogenic CH_4 would be $\approx$ 70 T mol yr^{-1}, and the CH_4 mixing ratio would be at 33 ppmv. At 10% PAL of O_2, methane production was estimated to be closer to 20 T mol yr^{-1}, with CH_4 concentrations of 22 ppmv (their CH_4 predictions vary non-linearly with O_2 because of further screening by the O_3 layer with rising O_2, and increased methanotrophic oxidation of CH_4). Laakso & Schrag (2019), using a marine carbon cycling model after analysing organic carbon to CH_4 conversion efficiency at Lake Matano (Kuntz *et al.*, 2015), calculated that for between 0.1% to 10% PAL of oxygen during the Proterozoic, atmospheric methane mixing ratios were between 0.04 ppmv and 1 ppmv. They also estimated methane generation rates that did not exceed 50 T mol yr^{-1} (similar to the pre-industrial flux) during the Precambrian, and that Proterozoic fluxes may have been 100 times lower than this. If atmospheric fluxes lower than 0.5 T mol yr^{-1} were simulated in WACCM6, then CH_4 surface mixing ratios would drop below 8 ppbv for 1% PAL of O_2. A Mesoproterozoic maximum of 10% PAL O_2 would allow for $\approx 10\times$ more atmospheric CH_4 for equivalent atmospheric fluxes, but with the Proterozoic fluxes considered here, the CH_4 concentration would likely not exceed 1 ppmv.

Methane fluxes remain uncertain and disputed as huge variations in literature predictions persist. For example, Cadeau *et al.* (2020) refuted the conclusions reached by Laakso & Schrag (2019) after analysis of biogeochemistry in Dziani Dzaha, a volcanic crater lake with similarities to expectations of the Proterozoic oceans (e.g. it has higher salinity compared to the modern oceans). Cadeau *et al.* (2020) concluded that methanogenesis (anaerobic methane production) resulted in efficient mineralisation of the lake's high primary productivity. In this argu-

ment, Cadeau *et al.* (2020) also cited Fakhraee *et al.* (2019), who evaluated that Proterozoic fluxes from the oceans to the atmosphere could have been as high as 60 to 140 T mol yr^{-1} ($9.6 - 22.4 \times 10^{14}$ g yr^{-1}), based on predicted low-sulphate Proterozoic oceans that were mostly anoxic. Liu *et al.* (2021) assumed the O_2 flux during the Proterozoic from microbial mats was balanced by CH_4, calculating a methane flux of up to 330 T mol yr^{-1}. Furthermore, Lambrecht *et al.* (2020) suggested that non-diffusive transport of CH_4, such as the example of rising bubbles in Lake La Cruz that carry gases to the atmosphere composed of 50% CH_4 (Camacho *et al.*, 2017), should be considered in atmospheric models that simulate the production of CH_4 and its transport to the atmosphere. Regardless, in the WACCM6 simulations at 1% PAL of O_2, 140 T mol yr^{-1} (22.4×10^{14} g yr^{-1}) would not be a large enough flux to achieve CH_4 mixing ratios of 1 ppmv. The Mesoproterozoic may not have been kept in an ice-free state by a CH_4 supported greenhouse if CH_4 concentrations did not reach 28 – 140 ppmv.

Could a photochemically produced haze layer prevent the reduction in CH_4 predicted here? Such a haze layer could reduce photolysis below, increasing the amount of atmospheric CH_4. WACCM6 does not currently support the formation of organic haze from CH_4 photolysis, although a haze layer is unlikely to exist in the simulated atmospheres because the C/O ratio (liberated from CH_4 and Ox photochemistry) is $\ll 1$ in the WACCM6 simulations and it needs to be closer to ~ 0.5 to create a haze layer (Trainer *et al.*, 2006; Pavlov *et al.*, 2001, and references therein). This is because photolysis produces O radicals that prevent haze particle formation (Trainer *et al.*, 2006). Although haze particles are still produced, it has been found experimentally that haze particle production decreases as O_2 levels increase above 10^{-4} PAL (Hörst *et al.*, 2018). At a pressure of $\approx$ 85000 Pa, 0.1% PAL of O_2, 260 ppmv of CO_2, and 158 ppmv of CH_4, Hörst *et al.* (2018) found a production of $\approx 1 \times 10^6$ haze particles cm^{-3}, such

that at a C/O ratio of 0.75 ($\sim$ 100 times greater than any C/O ratios simulated here), these haze particles had a mixing ratio of roughly 5×10^{-14}. Furthermore, Olson *et al.* (2016) found that hydrocarbon production from CH_4 photolysis during the Proterozoic would likely not result in a significant additional greenhouse contribution. When including atmospheric CH_4 fluxes considering some recent estimated CH_4 atmospheric fluxes (see Table 4.1; Olson *et al.*, 2016; Laakso & Schrag, 2019), CH_4 concentrations are even lower than 1 ppmv, thereby further reducing the likelihood of haze formation. Due to the fact that the simulations here consider atmospheres with a low C/O ratio and oxygen levels greater than 10^{-4} PAL, the effects of a haze layer are not considered important (in terms of the Proterozoic Faint Young Sun Paradox).

To summarise, the WACCM6 simulations support previous work (Daines & Lenton, 2016; Olson *et al.*, 2016; Laakso & Schrag, 2019) after demonstrating that a Proterozoic atmosphere with a negligible CH_4 greenhouse contribution may be more likely than one that supports a substantial CH_4 greenhouse. Even present day methane levels could be unlikely (see the schematic representation of this in Fig. 4.9) suggesting that a CH_4 supported greenhouse during the Mesoproterozoic is even more unlikely than previously estimated. Of course, there are uncertainties in the flux of CH_4 during the Proterozoic, but realistic increases in CH_4 atmospheric flux would not change the atmospheric lifetime of CH_4 enough to mitigate its tropospheric oxidation from OH and $O(^1D)$. Without a significant methane greenhouse, other mechanisms are required to explain a mostly ice-free Proterozoic, such as elevated levels of N_2O (also unlikely due to high rates of photolysis) or CO_2 (Fiorella & Sheldon, 2017), alterations in the continental coverage (Bradley, 2011; Korenaga *et al.*, 2017), cloud variability that acts to stabilise the climate system (Goldblatt *et al.*, 2021), or large-scale mantle thermal mixing variations (Jellinek *et al.*, 2020).

Whatever the solution, lower CH_4 mixing ratios have important consequences for predicted exoplanet observations that are based on Early Earth. Additionally, low CH_4 mixing ratios and a cool tropopause from reduced O_3 heating will limit the upward diffusion of hydrogen atoms to the thermosphere, with implications for atmospheric escape and exoplanetary ionospheric observations. These topics are left as future work.

4.5 Model intercomparison

Shortly after Cooke *et al.* (2022) was published, Aoshuang Ji and Professor James Kasting (Penn State University) requested a collaboration to conduct a model intercomparison. They proposed this in order to better understand the discrepancies in the O_3 column and CH_4 lifetime predictions between WACCM6 and previous modelling work in greater detail. Professor James Kasting was involved in both the Kasting & Donahue (1980) and Segura *et al.* (2003) papers, and since those two papers, the model used has been updated (it will be referred to as the Kasting 1D model hereafter). The intercomparison was performed between the Kasting 1D model, ROCKE-3D, and WACCM6.

During our investigation, it was revealed that the Kasting 1D model accounts for scattering of radiation in the Schumann-Runge bands (S-RB; 175 – 205 nm), as well as absorption by CO_2 and H_2O in this wavelength region. Neither WACCM6, nor ROCKE-3D, account for either of these physical processes. WACCM6 considers absorption only by O_2 and O_3 in the S-RB and does not include scattering at wavelengths shortward of 200 nm. At present day atmospheric levels of O_2, the transmission of solar actinic flux in the S-RB is primarily absorbed by O_2 high in the atmosphere (above $\approx$ 80 km). When O_2 concentrations decrease, absorption by H_2O and CO_2 becomes more important relative to O_2 and O_3 due to the relative columns and cross sections, with H_2O the most important asborber

by 1% PAL. Therefore, the WACCM6 source code was updated to account for absorption by CO_2 and H_2O in the S-RB.

In addition to the simulations described in Table 4.3, further investigations were made into the behaviour of O_3 abundance through the following parameters: horizontal transport; vertical transport; differences in incoming radiation; temperature structure; water vapour microphysics; chemical reaction rates; photolysis rates; parameterisation of O_2 in the Schumann-Runge bands; CO_2 and H_2O UV absorption in the Schumann-Runge bands; lightning NO production; varied solar zenith angle; seasonal cycle; and loss rates from the HOx, NOx, BrOx, and ClOx families. A summary of the findings will be provided here, but further details can be found in Ji *et al.* (2023).

Table 4.3: Simulations performed for the model intercomparison with the Kasting 1D photochemical model and ROCKE-3D. The O_2 mixing ratio is given in terms of present atmospheric level. LBC refers to the lower boundary conditions used. The fixed flux lower boundary conditions are from the Kasting 1D model present day simulation, or the fixed mixing ratios from the WACCM6 model pre-industrial run. In the '1% PAL 10^{-9} Cl and Br' simulation, all Br and Cl sources were reduced by a factor of 1 billion. S-RB indicates that absorption in the Schumann-Runge bands for H_2O and CO_2 were included. For comparison, the CH_4 lifetimes for the original 10% PAL, 1% PAL, and 0.1% PAL simulations were 5.45 yr, 0.55 yr, and 0.11 yr, respectively. These simulations had O_3 columns of 169 DU, 66 DU, and 18 DU, respectively.

Simulation	$f(O_2)$ [PAL]	LBC	$\tau_{CH_4[yr]}$	O_3 column [DU]
10% PAL S-RB LBC	0.100	Kasting 1D model	12.80	156.2
1% PAL 10^{-9} Cl and Br	0.010	WACCM6 with 10^{-9} multiplier for Cl and Br sources	0.62	84.0
1% PAL LBC	0.010	Kasting 1D model	0.25	72.3
1% PAL S-RB	0.010	WACCM6	3.15	60.1
1% PAL S-RB LBC	0.010	Kasting 1D model	5.22	55.2
0.1% PAL S-RB LBC	0.001	Kasting 1D model	3.23	13.3

4.5.1 The ozone discrepancy

The intercomparison determined that the O_3 column in both models is affected by the temperature structure, the lower boundary conditions, chemical destruction (the Kasting 1D model does not account O_3 destruction resulting from heterogeneous chemistry that activates chlorine on polar statospheric clouds), the solar data used, water vapour microphysics, dynamical transport, S-RB absorption and scattering, and O_2 photolysis. Including S-RB absorption by H_2O and CO_2 in WACCM6 reduced the total O_3 columns and further increased the O_3 column discrepancy between the models (see the results in Table 4.3). Including scattering in this wavelength region would likely have the same effect because less photons are reaching the lower atmosphere to photolyse O_2 and produce O_3.

Yassin Jaziri *et al.* (2022) used the 3D Generic Climate Model developed by the Laboratoire de Meteorologie Dynamique (LMD-g) to study the Great Oxidation Event. They used this 3D GCM alongside a 1D model which utilised the same chemical scheme. They did not include NOx, nor did they include CLOx, BROx, or SOx chemistry. They investigated O_2 concentrations between 5×10^{-5}% PAL and 0.5% PAL. At both solar zenith angles of 40° and 60°, their 1D model produces a higher mean O_3 column (especially at very low O_2 values) than their 3D model. At 0.5% PAL, the difference is a factor of ≈ 1.5. This work supports the conclusion that model geometry and transport are of critical importance for estimating the O_3 column.

Overall, the O_3 discrepancy between the models demonstrated in Fig. 4.6 has been mostly resolved, and is due to several of the investigated factors. One of the largest quantified discrepancies is Ox production (the production of O and O_3 from O_2 photolysis), which differs by up to a factor of 2. WACCM6 is much closer to line-by-line calculations than the Kasting 1D model, and future work is underway to update S-RB parameterisations in all participating models based on

new line-by-line calculations (Ji *et al.*, 2023).

4.5.2 The methane discrepancy

As the original WACCM6 model contained photolysis for H_2O and CO_2 at S-RB wavelengths, but not absorption or scattering, this means that WACCM6 was overestimating the photolysis reaction of H_2O ($H_2O + h\nu \longrightarrow OH + H$) in the troposphere at 1% PAL and lower O_2 levels, producing higher OH concentrations than the Kasting 1D model. With higher OH concentrations, CH_4 loss increased and the lifetime relative to the Kasting 1D model was reduced (as can be seen in Table 4.3 for the lowest O_2 scenarios). By including H_2O and CO_2 absorption at S-RB wavelengths, part of the CH_4 discrepancy between WACCM6 and the Kasting 1D model has been reconciled. However, the problem of the Proterozoic Faint Young Sun Paradox is far from solved. Future 3D chemistry-climate simulations will be required to narrow down the large range of CH_4 fluxes that can produce a sufficient CH_4 column under Mesoproterozoic O_2 that results in an ice-free surface. These simulations should also include: an array of different CO_2 mixing ratios, the younger Sun, a faster rotation rate for the Earth, and an alternative continental configuration that is representative of the Mesoproterozoic.

4.6 Conclusions

This Chapter used WACCM6, a 3D Earth System Model, to simulate changing O_2 concentrations since the beginning of the Proterozoic to a pre-industrial atmosphere. Between 0.1% and 50% the present atmospheric level of oxygen, the simulations presented here resulted in significantly lower mean O_3 columns when compared to previous 1D and 3D modelling (Fig. 4.6). Based on common literature assumptions, between 5 – 10 times more O_2 may be needed to produce an O_3 layer that fully shields the surface from biologically damaging radiation. New sim-

ulations with different lower boundary conditions and included absorption from H_2O and CO_2 in the Schumann-Runge bands showed that the O_3 discrepancy with previous results actually increased. As a consequence, UV surface fluxes may have been higher than previously estimated for much of Earth's history.

From the original WACCM6 simulations, it seemed likely that the mixing ratio of CH_4 was less than ≈ 0.1 ppmv for much of the Proterozoic. This conclusion was due to the possibility of a low CH_4 flux to the atmosphere, as well as the increased production of tropospheric OH and $O(^1D)$ from chemical photolysis. However, with the new simulations performed in the model intercomparison, the lifetime of CH_4 increased and was comparable to the pre-industrial CH_4 lifetime. Despite this, a larger flux of CH_4 during the Mesoproterozoic would still have been required to reach a tropospheric mixing ratio of 28 ppmv. Accordingly, it is still unclear whether a CH_4 supported greenhouse effect alone can solve the Proterozoic Faint Young Sun Paradox.

O_3 is a crucial constituent of Earth's modern atmosphere. The results presented in this Chapter demonstrate the importance of 3D whole atmosphere chemistry-climate modelling, as well as the requirement to update community models to better simulate paleoclimates. Tighter constraints on Proterozoic and Phanerozoic O_2 levels (see Fig. 4.1) will aid future work in reconstructing the history of Earth's atmosphere, the O_3 layer (based on the new estimates in this Chapter), and linking mass extinction and evolutionary events to the changing O_3 layer.

The O_3 layer varies substantially over a range of O_2 values, and due to its spatial variation, there were likely habitable niches across the globe as O_2 increased and the continents shifted. These fluctuating O_3 column levels through time regulated surface UV fluxes, with consequences for surface life and atmospheric chemistry. Therefore, it is recommended that the biological and geological impact

of the O_3 layer through time should be re-visited. Addressing the discordance in paleoclimate estimates will also have significant implications for simulated exoplanet atmospheres and predicted spectra.

Chapter 5

Observations of oxygenated Earth-analogue exoplanets

5.1 Introduction

During the current era of exoplanet discovery, the search for a temperate Earth-sized exoplanet orbiting around a G-type star continues. Data from telescopes and future observatories will add thousands more exoplanets to the list of over 5000 that have been discovered to date[1,2]. Upcoming transit and radial velocity surveys will make more precise measurements for the masses and radii of terrestrial exoplanets, thus enabling confident estimates of their bulk density and surface gravity. In the future, an Earth-sized exoplanet orbiting a G-type star at a semi-major axis of approximately 1 AU may be found. This poses the question: will it be habitable?

Atmospheric information can be gained from measurements of emission, reflection or transmission spectroscopy. Exoplanet atmospheres have been observed and characterised since the early 2000's (Charbonneau *et al.*, 2002), with larger, Jupiter-sized planets being the least challenging to observe (Seager & Deming, 2010). Detecting atmospheric properties and molecules for an Earth-sized exo-

[1] https://exoplanetarchive.ipac.caltech.edu/
[2] http://www.exoplanet.eu/

Table 5.1: A simplified chemical timeline of Earth's atmosphere is presented for O_2, CO_2, and CH_4, during the Archean, mid-Proterozoic and Phanerozoic. Molecular abundances are constraints from years of research, including geological evidence and modelling studies. The 'inclusive' data from Olson *et al.* (2018a) is listed. Data for O_2 and CH_4 during the mid-Proterozoic is also from Large *et al.* (2019), Steadman *et al.* (2020), and Lyons *et al.* (2021). The mixing ratio for O_2 is given relative to its present atmospheric level (PAL) of 0.21. The mixing ratios for CO_2 and CH_4 are given in terms of parts per million by volume (ppmv). 1 Ga represents 1 billion years in the past.

Molecular abundance	Archean 4 - 2.4 Ga	mid-Proterozoic 1.8 - 0.8 Ga	Phanerozoic 0.541 - 0 Ga
O_2 [PAL]	$10^{-12} - 10^{-5}$	$10^{-5} - 1$	$10^{-1} - 2$
CO_2 [ppmv]	$2500 - 40,000$	$1400 - 28,000$	$200 - 2,800$
CH_4 [ppmv]	$100 - 35,000$	$1 - 100$	$0.4 - 10$

planet around a G-type star is much more challenging due to the comparatively weaker spectroscopic signal.

Any measurement of an exoplanet's atmosphere will be taken during a specific period of its geological evolution (Kaltenegger *et al.*, 2007). As described in more detail in the previous Chapter, the Earth itself has had a complicated geological and biological history which is still not wholly understood (Catling & Zahnle, 2020; Steadman *et al.*, 2020; Cole *et al.*, 2020). At least three geological eons have harboured life on Earth: the Archean (4 – 2.4 Gyr ago), the Proterozoic (2.4 – 0.541 Gyr ago) and the Phanerozoic (0.541 Gyr ago - present; Lyons & Reinhard, 2009; Betts *et al.*, 2018; Dodd *et al.*, 2017). Table 5.1 presents a simplified overview of the composition of Earth's atmosphere for the past 4 billion years. These three geological eons represent important observational windows for Earth-analogue exoplanets (Rugheimer & Kaltenegger, 2018) and the search for habitable and inhabited exoplanets.

Gases such as O_2, N_2O, and CH_4, are primarily produced by life on Earth.

However, these gases can also be abiotically produced (Wordsworth & Pierrehumbert, 2014; Kleinböhl *et al.*, 2018) and the detection of such gases in an exoplanet atmosphere is not a conclusive detection of the presence of life (Selsis *et al.*, 2002; Grenfell, 2017). O_3 is the photochemical byproduct of O_2 and therefore indicates the presence of O_2 without a detection of O_2 itself. Several modelling studies have shown that the amount of O_3 in an Earth-analogue atmosphere increases as the concentration of O_2 rises (Kasting & Donahue, 1980; Segura *et al.*, 2003; Way *et al.*, 2017; Gregory *et al.*, 2021; Cooke *et al.*, 2022). Olson *et al.* (2018b) discussed how seasonal O_2 variations could give rise to seasonal changes in the reflectance spectra of O_3 in the UV region, noting that separate hemispheres which experience opposite seasons may mask the full seasonality signature.

Previous work has modelled modern Earth as an exoplanet (Kaltenegger & Traub, 2009), as well as Earth at different geological time periods (Rugheimer *et al.*, 2015b; Rugheimer & Kaltenegger, 2018; Arney *et al.*, 2016; Kaltenegger *et al.*, 2020a,b). Other studies investigated the photometric and spectroscopic variations of an Earth-analogue exoplanet (Ford *et al.*, 2001; Montañés-Rodríguez *et al.*, 2006; Tinetti *et al.*, 2006a,b). These investigations have used a variety of 1D and 3D models, and it is clear that numerous parameters, including geological eras with different atmospheric compositions, influence molecular detectability. The emission and transmission spectra of oxygenated exoplanets (varying through geological time) has been predicted with 1D models (e.g. Segura *et al.*, 2003; Rugheimer & Kaltenegger, 2018; Kaltenegger *et al.*, 2020a). Whilst most work in this area has focused on modelling, De Cock *et al.* (2022) performed a phase angle analysis of Earth using data from the EPOXI mission which observed Earth to test exoplanet observational predictions (Livengood *et al.*, 2011).

Emission and reflectance spectra can be observed through high-contrast imaging (HCI). This does not require the planet to transit the star, although the

observer's inclination to the plane of the orbit will affect the observations because the brightness amplitude is reduced as the orbital inclination decreases from 'edge-on' to 'face-on' (Maurin *et al.*, 2012). As the planet orbits, it reflects light, particularly in the ultraviolet and visible wavelength regions. The Earth's emission peaks in the infrared, where the emission (both in terms of its strength and wavelength variance) depends on temperature, clouds, and chemistry (Parmentier & Crossfield, 2018). The brightness of the host star (G-type) far outshines the brightness of an Earth-analogue exoplanet. Coronagraphs can be used to reduce the incoming light from the star, with a contrast of $\sim 10^{-10}$ required to reliably characterise an Earth-Sun analogue system (Lee, 2018; Currie *et al.*, 2022); hence, the use of a coronagraph is explored in this Chapter.

Recently, Checlair *et al.* (2021) evaluated the detectability of O_3 and O_2 on Earth-analogue (defined as possessing an oxygenated atmosphere due to life) exoplanets with four different telescope concepts: LUVOIR A (15 m diameter), LUVOIR B (8 m diameter), HabEx (4 m diameter) with and without a starshade. They simulated observations with these missions for O_2 concentrations of 10^{-5} PAL and upwards to 1 PAL, finding that larger diameter telescopes will better constrain the frequency of Earth-analogue worlds, commenting that this depends on the occurrence rate of exo-Earth candidates.

In this Chapter, thousands of synthetic high-contrast imaging spectra based on 3D simulations of Earth-analogue exoplanet atmospheres over various atmospheric O_2 concentrations are presented. This enables predictions for the variability in future observations, both within spectral features of interest, and in the broadband. These atmospheric simulations utilise a 3D Earth System Model with fully coupled chemistry and physics - the Whole Atmosphere Community Climate Model 6 (WACCM6). This Chapter uses the Planetary Spectrum Generator (PSG) to investigate the impact that changing oxygen concentrations has

on simulated observations, considering climate, chemistry, temporal, annual, and seasonal variations. The observability of such variations with next generation telescope concepts is determined.

5.2 Methods

5.2.1 WACCM6

This Chapter uses five different scenarios from the previous Chapter. These are presented in Table 5.2. The scenarios are: the pre-industrial atmosphere simulation (hereafter PI) and the simulations with atmospheres that have O_2 concentrations of 150% PAL, 10% PAL, 1% PAL, and 0.1% PAL. Each simulation had a 24 h rotation rate and the modern Earth's land and ocean configuration.

Model data was output as mean average values (the sum of the instantaneous output at each time step divided by the number of time steps considered) every 5 days, and mean average values every month. For the mean vertical profiles computed for Fig. 5.1, time and longitudinal means were taken, and latitudinal weights were averaged over (grid boxes near the poles have a smaller area than grid boxes near the equator), leaving just the vertical level dimension. Additionally, the instantaneous model state was output every 5 days (a 'snapshot' of the model). The snapshots were used for estimating reflection/emission spectra at a specific point in time. Time means presented in Fig. 5.1 and Table 5.2 were averaged over the last 4 years of each simulation.

Table 5.2: Time-averaged temperatures and O_3 columns under five different O_2 mixing ratio (f_{O_2}) scenarios. f_{O_2} is given in terms of present atmospheric level (PAL = 21% by volume of the atmosphere). Listed are the global mean surface temperature, $\overline{T}_S$, the global mean tropopause temperature ($\overline{T}_{Tp}$), and the minimum ($T_{Tp,min}$) and maximum values ($T_{Tp,max}$) of the tropopause temperature. Also listed is the global mean ozone column, $\overline{C}_{O_3}$, as well as the maximum $C_{O_3,max}$, and minimum, $C_{O_3,min}$, ozone columns in Dobson Units (DU), where 1 DU = 2.687×10^{20} molecules m^{-2}. All temperatures and O_3 columns are time-averaged over the final 4 years of each simulation.

Simulation	f_{O_2} [PAL]	$\overline{T}_S$ [K]	$\overline{T}_{Tp}$ [K]	$T_{Tp,\,min}$ [K]	$T_{Tp,\,max}$ [K]	$\overline{C}_{O_3}$ [DU]	$C_{O_3,min}$ [DU]	$C_{O_3,max}$
150% PAL	1.500	288.5	205.0	193.6	216.3	313	261	426
PI	1.000	288.5	204.4	193.3	216.0	279	236	375
10% PAL	0.100	288.9	204.9	194.0	215.7	169	130	235
1% PAL	0.010	288.5	202.4	191.6	213.5	66	41	83
0.1% PAL	0.001	286.0	196.6	184.4	210.0	18	13	23

5.2.2 Planetary Spectrum Generator

The Planetary Spectrum Generator (PSG; Villanueva *et al.*, 2018) was used to compute theoretical reflection/emission spectra for the WACCM6 atmospheric simulations. The GlobES 3D mapping tool was used to upload 3D data from the simulated atmospheres[1]. To reduce the memory footprint of the model input to be compatible with GlobES in PSG, the data were rebinned to a resolution of 10° in longitude only (with the latitudinal grid resolution unchanged at a value of 1.875°).

All of the synthetic spectra were calculated assuming an Earth-analogue exoplanet around a G2V star with a 1-year orbit at a 90° inclination angle (edge-on orbit). Edge-on systems are also likely to be best characterised in terms of mass and radius. All synthetic spectra were set to an exposure time of 60 seconds, with 1440 exposures, adding up to a total integration time of 24 hr. Although the noise estimates do not simply scale with distance because of reduced coronagraphic throughput at larger distances, to good approximation, the noise estimates do scale with total integration time, $T_{\rm int}$ ($\sigma_{\rm noise} \propto T_{\rm int}^{0.5}$). The spectra shown have an integration time of 48 h, where it was assumed that the noise was reduced by a factor of $\sqrt{2}$ from the 24 h PSG results. Synthetic spectra from HCI observations were computed with WACCM6 snapshots every 5 days at 00:00 UTC, from January 1$^{\rm st}$ until December 27$^{\rm th}$. Consequently, the illuminated side of the planet is centred at 180° longitude, where it is predominantly ocean (i.e. it is mostly the Pacific Ocean that is receiving sunlight at these times). Each snapshot was ingested into PSG by updating the orbital parameters for Earth (using the ephemeris data from the year 2020) every 5 days. This was then matched with the longitude and latitude of the Earth grid, to simulate the orbit in PSG to coincide with the orbit of the WACCM6 simulations.

[1] https://psg.gsfc.nasa.gov/apps/globes.php

The molecules used for the computation of reflection/emission spectra were N_2, O_2, CO_2, H_2O, O_3, CH_4, and N_2O. Each molecule used the default HITRAN opacity data (Gordon *et al.*, 2017). All available collision induced absorption coefficients were utilised. The effects of scattering were included, as well as that of ice clouds and water clouds (Villanueva *et al.*, 2018). The effective radius of the cloud particles was assumed to be 5 µm for water (stratocumulus) clouds and 100 µm for ice (cirrus) clouds, as is typical in the modern Earth's atmosphere.

Telescope templates are used for the Large Ultraviolet Optical Infrared Surveyor (LUVOIR; Bolcar *et al.*, 2017) concept and the Habitable Exoplanet Observatory (HabEx) concept. For LUVOIR, both the A (15 m primary mirror) and B (8 m primary mirror) templates were used. The B template was changed to a 6 m primary mirror based on the recent suggestions from the Decadal Survey (National Academies of Sciences & Medicine, 2021). The LUVOIR A and B concepts have spectral resolving powers of $R = 7$ (0.2 – 0.515 µm), $R = 140$ (0.515 – 1.0 µm) and $R = 70$ (1.01 – 2.0 µm) for the UV, VIS and NIR channels respectively (where $R = \lambda/\Delta\lambda$, λ is the wavelength, and $\Delta\lambda$ is the wavelength bin width). The HabEx concept had the same spectral resolving powers in the UV (0.2 – 0.45 µm and VIS channels (0.45 – 0.975 µm) but instead with $R = 40$ in the NIR channel (0.975 – 1.8 µm).

Idealised spectra were computed with PSG (Fig. 5.3). However, to deduce whether atmospheric constituents in any of the WACCM6 simulations are physically observable, the atmospheric signal-to-noise ratio (SNR) on the produced spectra is also estimated. PSG calculated the noise, σ_{noise}, on an observation set. σ_{noise} included contributions from the source (the star and planet), from the background sky, and from the telescope itself (read noise and dark noise).

The SNR of a molecular detection also depends on a 'baseline' atmosphere which does not contain that molecule. This provides a continuum with which

to estimate the absorption strength of the spectral features. A 1,000 hPa N_2 atmosphere was used as a baseline which was created from each simulation by removing all other atmospheric molecules, but keeping the presence of liquid and ice clouds in the atmosphere. SNRs were calculated at a specific wavelength with no rebinning performed on the simulated spectra. All simulations with PSG computed for this work are forward models. More details on the simulations completed are given in Appendix A.

5.3 Results

5.3.1 Summary of composition and temperature

Here the globally-averaged and time-averaged atmospheric chemistry of the simulations that were fed into PSG are summarised. See Chapter 4 for a more detailed discussion.

Fig. 5.1 shows the atmospheric mixing ratio vertical profiles from all five WACCM6 simulations for O_3, CO_2, H_2O, CH_4 and N_2O. Also shown are the vertical profiles for temperature. When the O_2 concentration decreases (from 150% PAL down to 0.1% PAL), the O_3 column also decreases. With less O_3 to absorb ultraviolet (UV) radiation, at $\leq 1\%$ PAL, there is reduced heating in the lower stratosphere and this cools the tropopause. Hence, more water is frozen out in the tropopause 'cold-trap' (Fueglistaler *et al.*, 2009), generally resulting in more liquid and ice clouds. Increased photolysis rates for CH_4, N_2O and CO_2 result in lower mixing ratios. The mixing ratios for N_2O and CO_2 are reduced by a factor of 100 or more by the mesopause, and that for CH_4 is reduced by several orders of magnitude above the tropopause. Furthermore, as O_2 reduces, H_2O is increasingly photolysed above the tropopause and has mixing ratios reduced below 0.1 ppmv (parts per million by volume) in the stratosphere for the 1% PAL and 0.1% PAL cases, or in the upper mesosphere for the 10% PAL case. This is

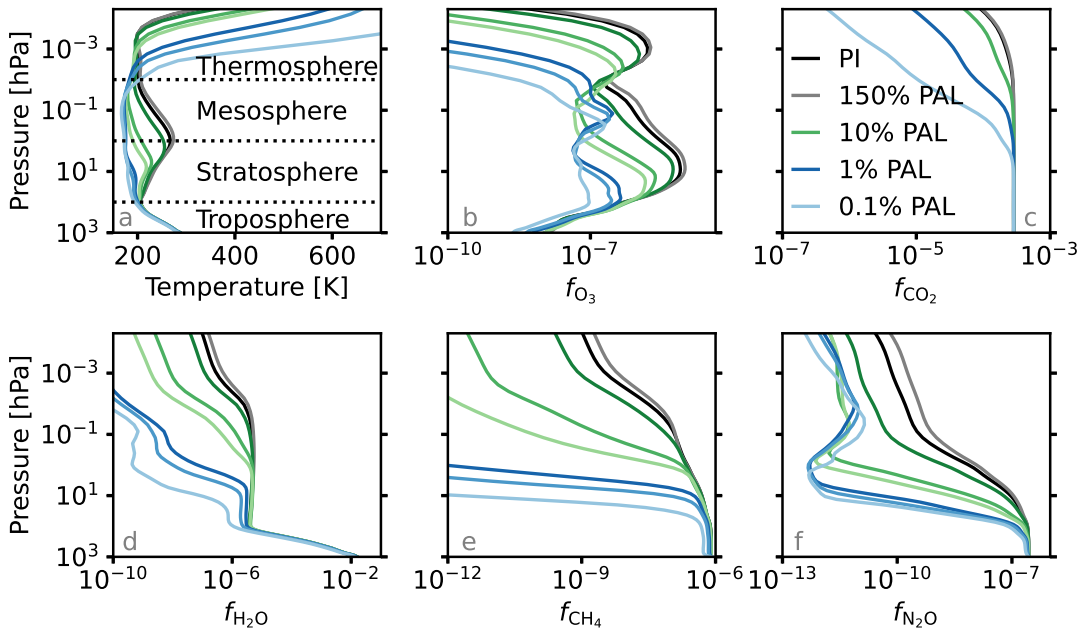

Fig. 5.1: (*a*) The global mean temperature is plotted for the following simulations: 150% PAL (grey), PI (black), 10% PAL (green), 1% PAL (dark blue), and 0.1% PAL (light blue) O_2 atmospheres. Black dashed lines indicate the transitions between the major temperature layers in the pre-industrial atmosphere. Mixing ratio vertical profiles, denoted as f_X, where X is the molecule shown, are plotted for O_3 (*b*), CO_2 (*c*), H_2O (*d*), CH_4 (*e*), and N_2O (*f*). These five molecules are Earth's major greenhouse gases, with important absorption features for exoplanet atmospheres located in the infrared.

in contrast to the PI atmosphere that retains at least 0.1 ppmv of H_2O in the lower thermosphere. Therefore, the five major greenhouse gases in Earth's atmosphere are all reduced above the tropopause when molecular oxygen is reduced. In addition to reduced heating from UV absorption by O_3, this results in cooling of the troposphere in the simulations with the lowest O_2 concentrations, resulting in a reduced water vapour column.

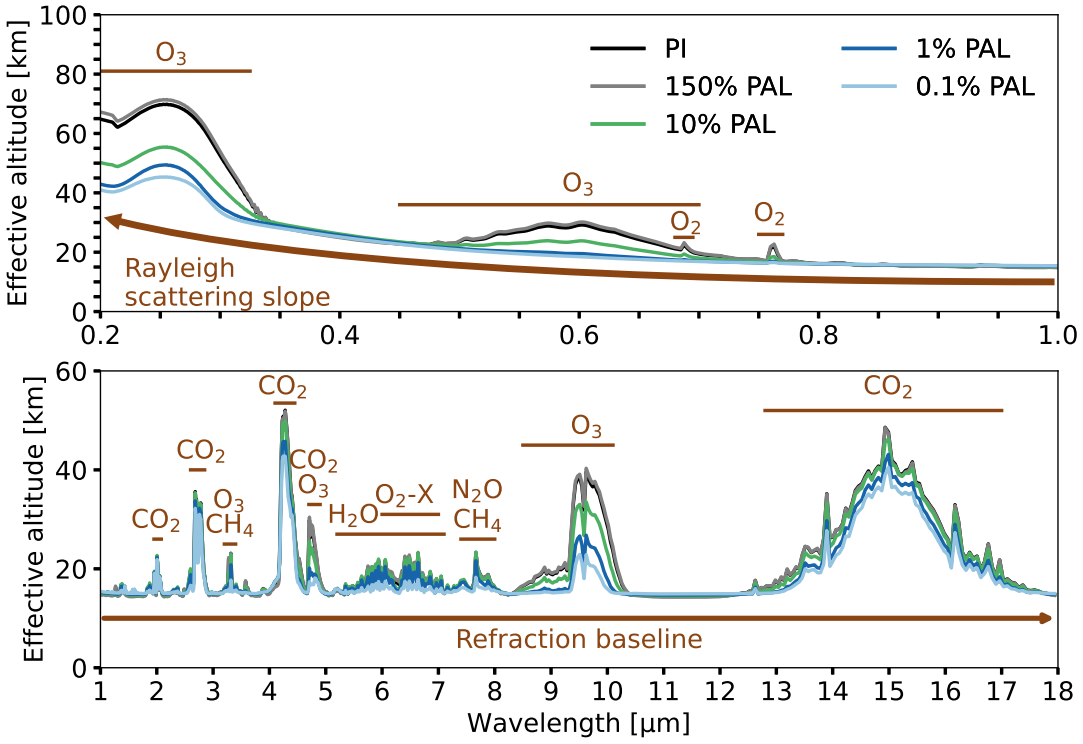

Fig. 5.2: Idealised transmission spectra, given in terms of atmospheric effective altitude, are shown for the PI (black), 150% PAL (grey), 10% PAL (green), 1% PAL (dark blue), 0.1% PAL (light blue) atmospheres between 0.2-1 µm (top) and 1 – 18 µm (bottom). Indicated in brown are chemical absorption features, such as O_3, O_2 and CO_2. The spectra are computed on model date January 1st and binned to a spectral resolving power of $R = 250$.

5.3.2 Transmission spectra of oxygenated Earth-analogues

Fig. 5.2 presents idealised transmission spectra for the PI, 150% PAL, 10% PAL, 1% PAL, and 0.1% PAL atmospheres, at a spectral resolving power of $R = 250$. With decreasing O_2, the detectability of several molecular signatures (e.g. H_2O, CO_2, and CH_4) indicated in Fig. 5.2 is reduced due to enhanced middle atmosphere photolysis. Spectral signatures for O_2, O_2–X, and O_3 all decrease with a reduction in O_2. Note that O_2–X represents the collision induced absorption between O_2 and other species such as N_2 and CO_2.

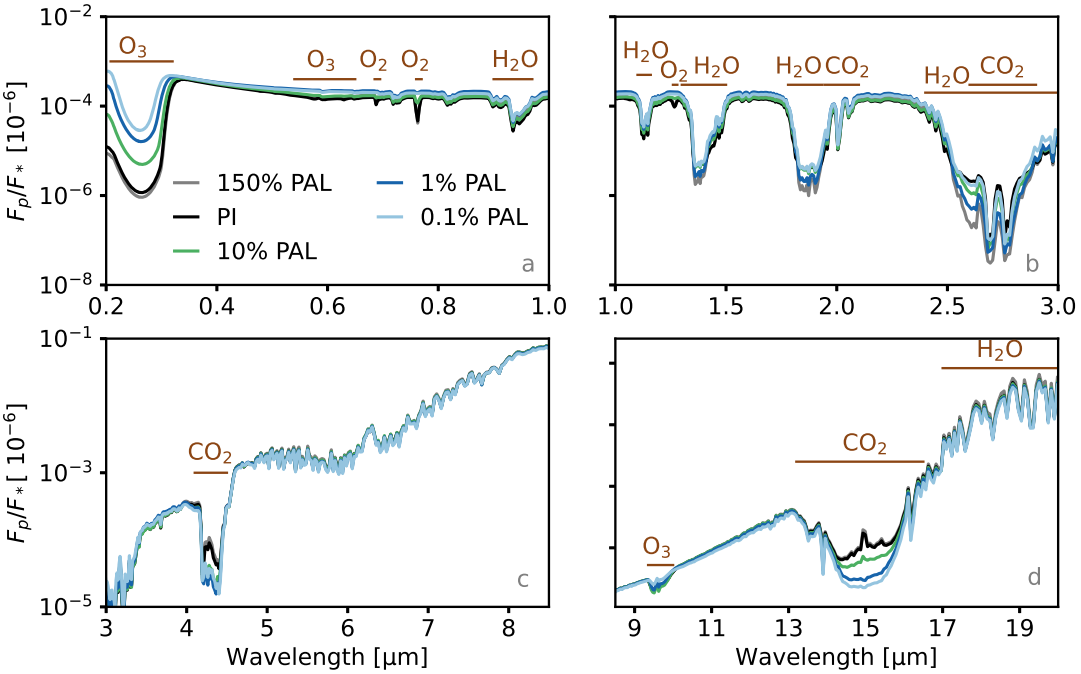

Fig. 5.3: Idealised reflection and emission spectra where a coronagraph is not utilised, given in terms of planet-star flux ratio in parts per million (F_p/F_* [10^{-6}]), are shown for the 150% PAL (grey), PI (black), 10% PAL (green), 1% PAL (dark blue), and 0.1% PAL (light blue) atmospheres between 0.2 µm – 1 µm (a), 1 µm – 3 µm (b), 3 µm – 8.5 µm (c), and 8.5 µm – 20 µm (d). Spectral features are indicated in brown. The spectra are computed at a phase of 395.5° for climate simulations at midnight, on March 22$^{\text{nd}}$. Note that each subplot has a different y axis. The spectra are binned to a spectral resolving power of $R = 250$, where $R = \lambda/\Delta\lambda$, λ is the wavelength of light and $\Delta\lambda$ is the wavelength width of the binning.

5.3.3 PSG reflection and emission spectra output

Fig. 5.3 shows reflection and emission spectra for the PI, 150% PAL, 10% PAL, 1% PAL, and 0.1% PAL atmospheres. These spectra are simulated on the 22$^{\text{nd}}$ of March, which is at 359.5° phase in the geometrical setup of the simulations, just before the exoplanet goes into secondary eclipse at 0° phase. In reality, this idealised spectrum will not be observable through HCI because of the small angular separation at this phase that results in low coronagraph throughput.

The emission from several spectral features are modified when oxygen is reduced. For example, the peak at 15 µm for CO_2, within an absorption trough, indicates the presence of a hot stratosphere, as has previously been reported (Selsis, 2000; Kaltenegger *et al.*, 2007; Rugheimer & Kaltenegger, 2018). Once O_2 has reduced to $\leq 1\%$ PAL in the climate simulations, the stratosphere no longer exists, so this feature is seen completely in absorption. O_2 features seen in absorption are at 0.69 µm, 0.76 µm, and 1.27 µm. An increase in oxygen increases the depth of these features relative to the continuum. There is a noticeable difference in depth between the PI and 150% PAL cases; the 150% PAL O_2 features are 13%, 9% and 28% deeper relative to the continuum at $R = 250$, respectively. When O_2 is reduced, there is less stratospheric O_3 resulting in a lower total O_3 column; hence, there is reduced atmospheric absorption by O_3. This is most noticeable at UV wavelengths, where the depth of the feature lies between $\approx 9 \times 10^{-7}$ ppm to $\approx 3 \times 10^{-5}$ ppm. The depth of H_2O features mostly result from the climate at the chosen time stamp and orbital phase, although the time-averaged water column is reduced by up to 20% at 0.1% PAL because of lower tropospheric temperatures.

The spectra in Fig. 5.3 are simulated at a single point in time. However, the spectra will change throughout the orbit, due to seasonal, climatic, and chemical changes in the atmosphere. The presence and distribution of clouds also affects reflection and emission spectra. Clouds can either mask molecular features, or boost them through reflectivity (Rugheimer & Kaltenegger, 2018). The spectra of these exoplanets as seen through HCI by sampling the climate system along the orbit is simulated. These simulations are then used to estimate the variations expected from future observations of oxygenated Earth-analogue exoplanets.

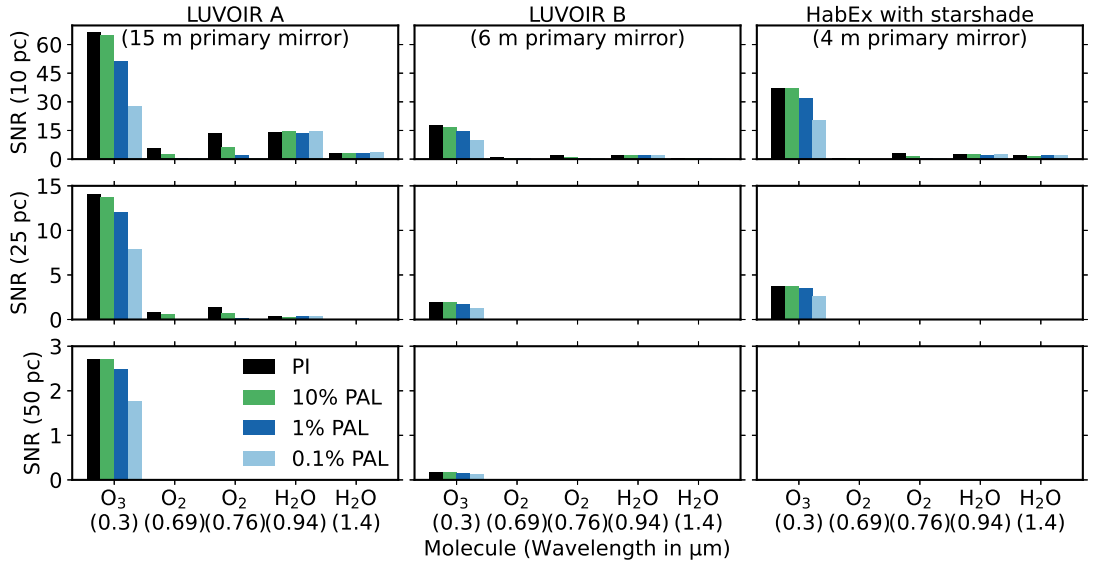

Fig. 5.4: The maximum signal-to-noise ratio for five molecular features are given for the PI (black), 10% PAL (green), 1% PAL (dark blue), and 0.1% PAL (light blue) atmospheres, at a distance of 10 pc (top row), 25 pc (middle row), and 50 pc (bottom row). The LUVOIR A (left column), LUVOIR B (middle column), and HabEx with a starshade (right column) telescope concepts are evaluated, each observing for a total integration time of 24 h. Only the first year of the final four years of each simulation is evaluated in this figure.

5.3.4 Spectra from high-contrast imaging

This section presents spectra generated using HCI for the PI and 0.1% PAL atmosphere with the LUVOIR A telescope concept for an exoplanet at 10 parsecs (pc, where 1 pc = 3.26 light years), with 24 h or 48 h of integration time (annual variability curves for the 10% PAL and 1% PAL simulations are included in Appendix B). It is recognised that this is an optimistic distance at which an Earth-analogue exoplanet could be found, so calculations at 25 pc and 50 pc are also included. Previous work has used 10 pc for a variety of rocky exoplanet predictions (e.g. Fujii *et al.*, 2011; Checlair *et al.*, 2021; Alei *et al.*, 2022) and so this distance also allows meaningful comparisons with those works.

The PSG radiation output is in terms of planetary flux (F_p), stellar flux (F_*),

and the total flux received by the detector ($F_T = F_p + F_*$). Note that F_p cannot be empirically detected in such coronagraphic observations where some stellar light still reaches the detector. The error bars on F_T depend on several sources of noise, as described in Section 5.2.2.

5.3.5 Maximum signal-to-noise ratio

The maximum SNR possible with the three telescope concepts is quantified in Fig. 5.4, at 10 pc, 25 pc, and 50 pc, after a total integration time of 24 h. According to the SIMBAD online database (Wenger *et al.*, 2000)[1], there are 13 G0V-G9V stars closer than 10 parsecs and 2,830 G0V-G9V stars closer than 75 pc. Assuming $\eta_\oplus$ (the occurrence rate estimates for Earth-analogue planets around G-type stars) is between 0.01 – 2, this implies that an Earth-analogue exoplanet with a random orbital inclination should be found somewhere between 10 pc and 75 pc. This is a large range and should be kept in mind when considering the results from Fig. 5.4.

Assuming the threshold for detection of a molecule is a SNR of ≥ 5, then O_3 in the UV can be detected for all atmospheres and telescopes for an exoplanet at 10 pc. O_2 can be detected in the PI atmosphere by LUVOIR A at both 0.69 µm and 0.76 µm, although for the 0.1% PAL atmosphere this would require an integration time of $\approx$ 50 days and $\approx$ 1.2 days for the 0.69 µm and 0.76 µm features, respectively. H_2O can be detected at 0.94 µm with LUVOIR A but not at 1.4 µm, and the LUVOIR B and HabEx with a starshade cannot detect it at 10 pc with a 24 h integration time. Rebinning of the two assessed H_2O features would improve their signal-to-noise ratios. At a distance of 25 pc, only LUVOIR A can detect any molecules (e.g. O_3). No molecules can be detected by any telescope in any atmosphere for an exoplanet at 50 pc, but O_3 in the PI and 10% PAL

[1] http://simbad.u-strasbg.fr/simbad/

atmospheres may be detectable for $T_{\text{int}} \approx 3.4$ days with LUVOIR A. LUVOIR A (15 m) is the best performing telescope overall, and HabEx with a starshade (4 m) performs better than LUVOIR B (6 m) despite the larger diameter telescope size of LUVOIR B. For example, the SNR for O_3 at 10 pc is up to a factor of 2.2 higher for HabEx with a starshade when compared to LUVOIR B.

Similar to Checlair *et al.* (2021), where a cloud-free atmosphere was assumed in their calculations, it is found here that the detection of O_2 and O_3 becomes increasingly difficult as the O_2 concentration reduces. Because a different O_2 concentration affects atmospheric chemistry and photolysis rates, the energy budget for the atmosphere changes. This results in different tropospheric temperatures which are positively correlated with the total water column and thus influences the reflection and emission spectra by modulating absorption and emission. Therefore, the SNR for detecting H_2O is also influenced by the O_2 concentration, although the change between atmospheres is small. The effect is more obvious for transmission spectra where the middle atmospheric concentration of H_2O reduces with reduced O_2 (as shown in Fig. 5.2).

Additionally, decreasing the diameter of cloud particle sizes from 5 µm and 100 µm to 1 µm and 1 µm (for water and ice clouds respectively) increases the maximum signal-to-noise ratio available during an orbit due to an increased amount of photons reaching the telescope detector. To give an example, the maximum SNR at 24 h integration time with LUVOIR A for O_3 at 0.3 µm in the PI atmosphere is 66 with the larger diameter particles, versus a SNR of 100 with the smaller diameter cloud particles.

5.3.6 Annual variations in high-contrast imaging

Fig. 5.5 shows how the same atmospheres exhibit inter-annual variability by modelling the spectra from HCI of four consecutive model years using the LUVOIR

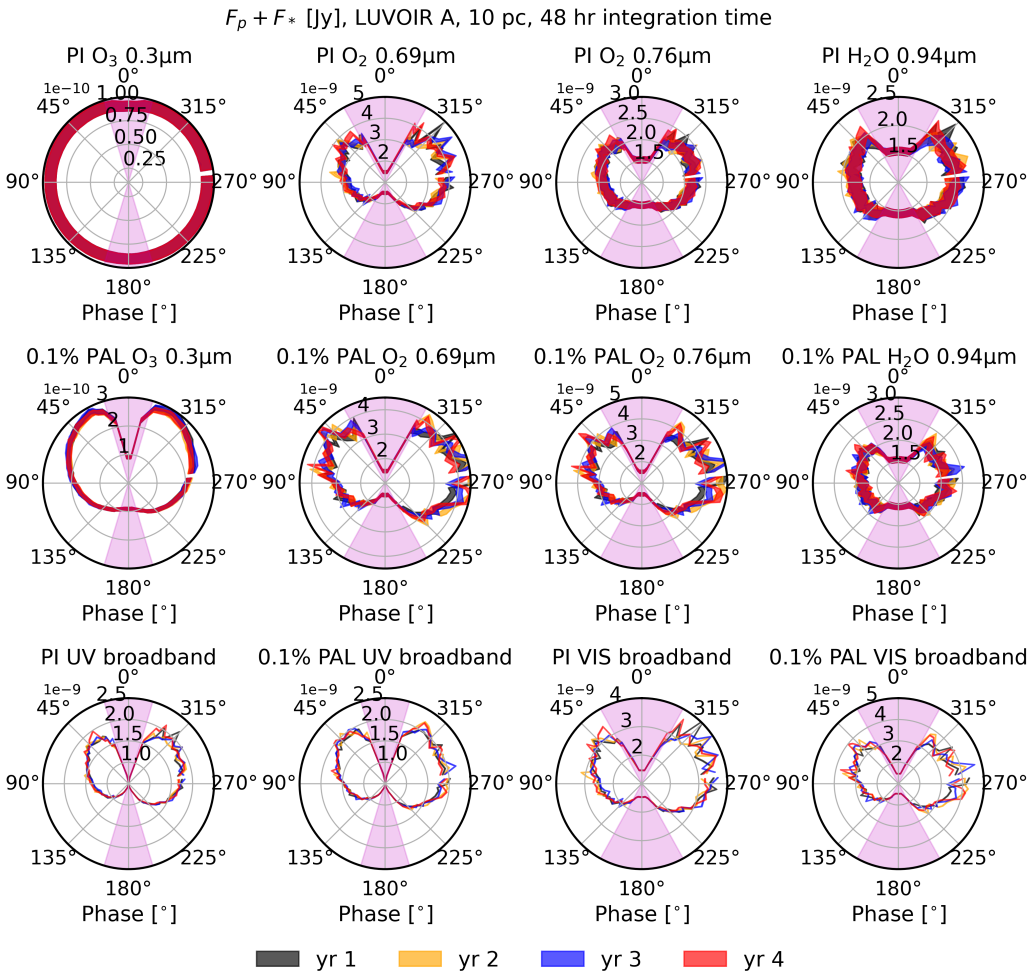

Fig. 5.5: Plotted in the radial direction in units of Jy is the total flux $F_T = F_p + F_*$ from the planet and star as seen by the telescope detector from the final 4 years (1st year = black, 2nd year = yellow, 3rd year = blue, 4th year = red) of the PI and 0.1% PAL simulated atmospheres, with orbital phase in the azimuthal direction. The total integration time is 48 h using LUVOIR A for an exoplanet at 10 pc. The width of the lines indicate the noise for that particular measurement. The magenta shaded regions represent phases where the exoplanet would be inside the inner working angle (IWA) of the LUVOIR A coronagraph. The discontinuity in the curves is between December 27$^{\text{th}}$ and January 1$^{\text{st}}$. (Top and Middle) The flux variation with phase at the 0.3 µm O_3 feature, at the 0.69 µm O_2 feature, at the 0.76 µm O_2 feature, and at the the 0.94 µm H_2O feature are shown. (Bottom) The bottom row shows the broadband variation in the PI and 0.1% PAL atmospheres for the LUVOIR A UV and VIS channels.

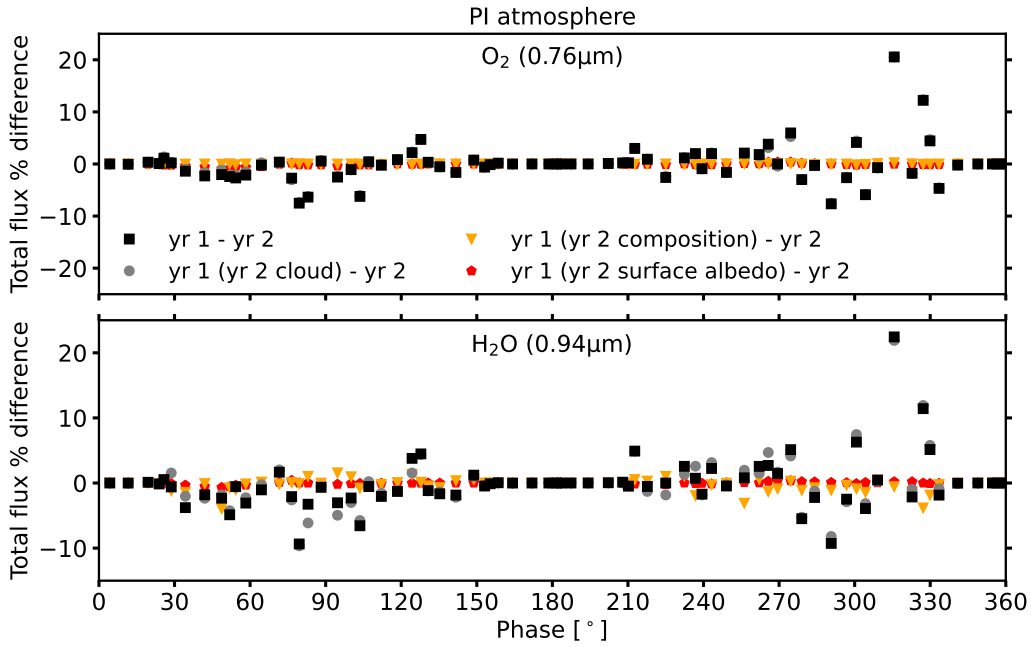

Fig. 5.6: The total flux difference (in terms of percentage difference) versus orbital phase is plotted for the first and second year of WACCM6 data from the PI atmosphere for the 0.76 µm O_2 feature (top) and for the 0.94 µm H_2O feature (bottom). Black squares indicate the difference between the standard output from the atmosphere with no changes. Grey circles, orange triangles, and red pentagons indicate the flux difference when clouds, composition, and surface albedo, respectively, from the second year, are swapped into the first year atmosphere before being processed by PSG. Although these swaps do not represent a physical atmospheric prediction, they enable quantification of what is affecting the atmospheric variability between years.

A telescope concept. This is the most optimistic future telescope concept assessed, as discussed in Section 5.3.5. The final four years for each simulation are shown because these data were used to assess the stability of the climate (see Section 6.2). Fig. 5.5 shows the measured total flux (F_T) as a function of orbital phase, where January 1st is at a phase of 279°.

For LUVOIR A observing an oxygenated Earth analogue exoplanet at 10 pc, the inter-annual variability for the broadband and individual spectral features year-on-year is larger than the noise in the VIS channel at multiple phases. Spe-

cific lines within the UV do not show observable year-to-year variations, although the broadband in this channel does. Because the inner working angle of the coronagraph is proportional to wavelength (see Appendix C), longer wavelengths are increasingly harder to observe due to reduced coronagraphic throughput. This means that longer wavelengths, especially in the NIR channel, cannot be differentiated year-on-year. Additionally, certain phases cannot be differentiated, and this is either because the magnitude of the year-on-year variations are within the noise, or the coronagraph throughput is too low to detect any meaningful planetary flux variation.

The H_2O and O_2 features have larger variations in flux when compared to O_3 features. Variations for H_2O and O_2 at some phases are distinguishable from the noise for some years, but not necessarily all of the years. Therefore, multiple years (≥ 3) of observations may be needed to witness variations at particular phases. Greater integration times will increase the amount of phases where inter-annual variation is observable. Almost all phases can be differentiated in broadband observations due to higher SNR.

In the UV channel, the same wavelength at the same phase between years can vary in brightness by up to 1.3 times and 2.4 times for F_T and F_p, respectively. In the VIS and NIR channels, these numbers can reach up to 1.5 and 2.5, and 1.7 and 5, respectively.

Fig. 5.6 shows the year 1 minus year 2 percentage differences in the total flux versus orbital phase for the 0.76 µm O_2 and 0.94 µm H_2O features. In addition, either clouds, composition, or surface albedo between the years were swapped to isolate the contribution of these planetary properties to the total year-to-year difference. The largest percentage difference for H_2O between these two years is +22.4%, occurring at an orbital phase of 316°, where the percentage difference from only swapping clouds is +21.9%. On the other hand, a swap in chemistry

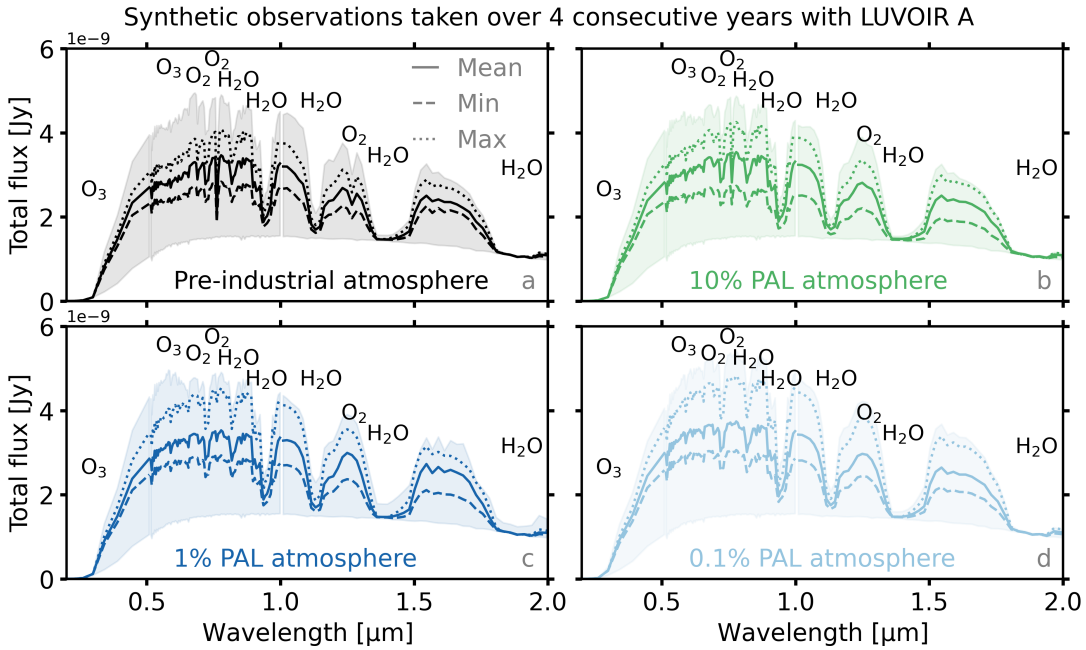

Fig. 5.7: The mean (unbroken line), minimum (dashed line), and maximum (dotted line) for observations taken at maximum star-exoplanet separation (orbital phases closest to 90° and 270°) are plotted for LUVOIR A at 10 pc. The minimum and maximum observations at quadrature are determined to be the date at which the 0.88 μm line (often the wavelength with the highest flux) exhibits minimum and maximum flux for that particular year, respectively. The shaded regions show the range between the maximum and minimum total flux at each wavelength, now accounting for all phases. The results from the PI (*a*), 10% PAL (*b*), 1% PAL (*c*), and 0.1% PAL (*d*) atmospheres are all plotted. Whilst maximum separation does not correspond to maximum planetary brightness, it does correspond to the most observable phase at different distances. Closer star-exoplanet separations may have reduced coronagraphic throughput.

never contributes a change of more than ±4%, and surface albedo never more than ±1%. To summarise, in these simulations, the inter-annual variation is primarily influenced by clouds, secondarily by chemistry (composition), and surface albedo plays only a minor role. This trend is similar across oxygenation states and wavelengths.

Total cloud coverage and cloud water path changes often for each atmosphere,

such that clouds change the overall albedo of the planet. The O_2 column does not significantly vary throughout an orbit, whereas the H_2O column does due to atmospheric temperature fluctuations and resultant changes in water phase. This is why a change in composition influences the spectra more for H_2O features than for O_2 features. For a specific date and corresponding phase, year-to-year, the surface albedo is almost constant. In the cases considered here, it has little effect on observed annual variations. The surface albedo does affect the seasonal variations however, as will be shown in the next section.

Fig. 5.7 displays how the received flux from each atmosphere varies over 4 consecutive years at quadrature (maximum planet-star separation, where the orbital phase is either 90° or 270°). The mean is plotted alongside the range. The largest positive percentage difference in flux from the mean flux at quadrature for each atmosphere is +18%, +21%, +29%, and +30%, for the PI, 10% PAL, 1% PAL, and 0.1% PAL atmosphere, respectively. Likewise, the largest negative percentage difference is -18%, -23%, -23%, and -19%, for the PI, 10% PAL, 1% PAL, and 0.1% PAL atmosphere, respectively.

The total range between all phases and wavelengths (shaded background in Fig. 5.7) is also shown. Although the signal-to-noise ratio for O_3 is high in the UV, O_3 column variations due to climate may not be detectable because of the very small range at 0.3 µm. The total flux range varies with wavelength, and the largest total flux range occurs in the 0.1% PAL case. The flux range of wavelengths which cover O_3 and O_2 features, including the continuum, generally increases with decreasing atmospheric O_2 concentration. This trend with O_2 concentration is not always linear for H_2O features. These results indicate that inter-annual variations in observations may be dependent on O_2 concentrations, but more than four orbits would be required to determine this as a statistically reliable result, rather than a consequence of chemistry-independent climate variability

within the WACCM6 model.

5.3.7 Seasonal variations in high-contrast imaging

Aside from inter-annual variations, observer geometry also affects the spectra as will be demonstrated in this section. The observer geometry has been varied by simply adding 90°, 180°, and 270° to the orbital phase to which each model date corresponds to. This is done for the synthetic spectra for two consecutive model years (year 2 and year 3 from the final 4 years of data) to demonstrate how seasonal variations affect exoplanet spectra in Fig. 5.8.

Seasonal variations are larger than inter-annual variations between the same phase, as would be expected for a planet like Earth where the seasons are set by Earth's obliquity. In other words, the climatic differences between July 1st and January 1st are more likely to exhibit a greater variation in magnitude than two consecutive years on January 1st. Because one would likely not know a priori which season is being observed, this can initially limit the observational information gained about a particular exoplanet's climate because of the potential for degenerate interpretations.

The reason why the phases between 180° – 360° in Fig. 5.5 are often (but not always) brighter than 0° – 180° by up to ≈ 15% is due to an increase in surface ice coverage. The H_2O column shows a seasonal cycle and this will affect the magnitude of the signal for H_2O features (e.g. more H_2O results in increased absorption). The influence from the cloud column is less obvious when comparing these two time periods because clouds do not vary with a seasonal cycle as clear as the ice seasonal cycle. 180° – 360° roughly corresponds to September – March, which covers winter in the Northern hemisphere, when Arctic ice is most prevalent. The period between 0° – 180° roughly corresponds to March – September, with increased surface ice around Antarctica during this time, although a

higher proportion of the Earth's surface in the Arctic is covered in ice during the northern hemisphere's winter. More ice raises the albedo of Earth, such that the phases between 180° – 360° are generally brighter.

By shifting the phases that the dates correspond to, the same wavelength at the same phase for shifted seasons can vary in brightness by up to 2.8 and 10.5 times for F_T and F_p, respectively, in the UV channel. In the VIS and NIR channels, these numbers can reach up to approximately 2.3 and 17, and 2 and 20, respectively. These results demonstrate significant advantages over 1D models that cannot capture such effects.

5.4 Discussion

This Chapter has demonstrated that chemistry and clouds impact the variability of high contrast imaging spectra for oxygenated terrestrial exoplanets. The variability depends upon the exoplanet's climate and chemistry, but the ability to detect this variation will be influenced by the distance, orbital geometry, and telescope design. Naturally, this will dictate what scientific results are retrievable from specific targets.

5.4.1 Transmission spectra

Due to lower ozone columns, enhanced photolysis reduces the detectability of several molecules in transmission spectra. The idealised transmission spectra in this Chapter show several differences with previous work.

As an example, Kaltenegger *et al.* (2020a) simulated high resolution transmission spectra for their atmospheres ($R > 100,000$) and displayed them at $R > 700$ and $R > 100,000$. There is mostly good agreement between the PI simulated transmission spectrum here and the modern Earth transmission spectrum from Kaltenegger *et al.* (2020a), with variations up to ± 5 km, especially for several

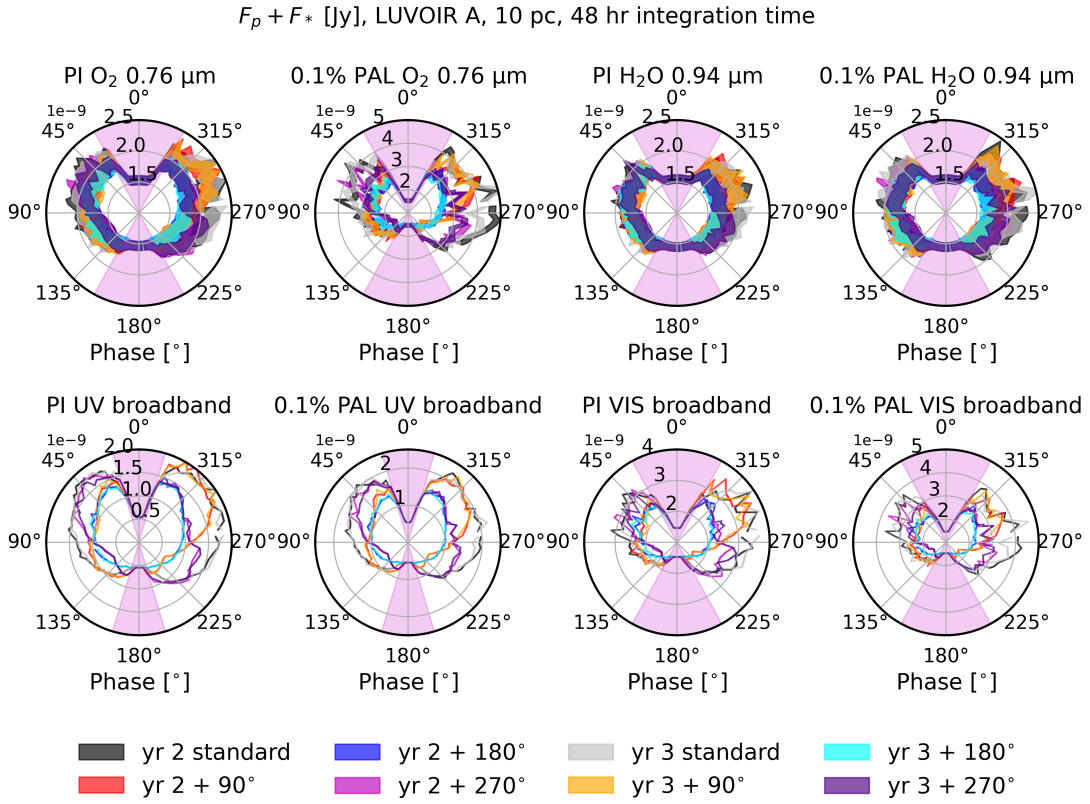

Fig. 5.8: This figure demonstrates how seasons can impact exoplanet spectra. In units of Jy the total flux received by the telescope ($F_T = F_p + F_*$) is plotted in the radial direction against phase in the azimuthal direction. This is for a 48 h integration time using LUVOIR A for an exoplanet at 10 pc. A standard year is plotted, and then observer geometry is rotated $+90°, +180°$ and $+270°$. 'yr 2' and 'yr 3' refer to the 2nd and 3rd years of the final 4-year dataset, respectively. Top: Variation for the pre-industrial and 0.1% PAL atmospheres are shown for O_2 at 0.76 µm and H_2O at 0.94 µm. The width of the lines represent the ± 1-σ_{noise} uncertainty on the observations. Bottom: The broadband variation is shown in the UV and VIS channels with phase. The discontinuity in the curves is between December 27th and January 1st. The magenta shaded regions represent phases where the exoplanet would be inside the inner working angle (IWA) of the LUVOIR A coronagraph. The width of the lines represent the ± 1-σ_{noise} broadband uncertainty.

CO_2 and CH_4 features because their modern Earth uses 1.3× the CO_2 and 2× the CH_4 surface mixing ratios used for the pre-industrial Earth simulated here. How-

ever, when the lower O_2 states are compared to the spectra displayed in Fig. 5.2 at the same resolution (calculated by smoothing their spectra to $R = 250$), molecular features for CH_4, CO_2 and O_3 have noticeable discrepancies. Decreasing detectability with decreasing O_2 were reported by Gebauer *et al.* (2021), albeit for an Earth-analogue exoplanet around an M dwarf star using a 1D cloud-free model. The simulations presented here generally predict higher levels of middle atmospheric photolysis compared to previous work due to lower simulated O_3 columns.

Differences in the atmospheric code used, as well as assumptions, can lead to different idealised observational predictions. Indeed, 'GCM uncertainty error bars' for transmission spectra were estimated to be $\approx$ 40% by Fauchez *et al.* (2022), where the exoplanet TRAPPIST-1 e was simulated with 4 different GCMs (ROCKE-3D, ExoCam, LMD-G, and UM). Therefore, the idealised transmission spectra shown in this Chapter are of interest for comparison with other models (both 1D and 3D), especially when considering how the predictions could relate to M dwarf exoplanets, which are expected to have their atmospheres characterised through transmission spectra.

In reality, it is difficult to detect the transmission spectral features for Earth-analogue exoplanets. Precise measurements for transmission spectra for Earth-like planets around Sun-like stars will be extremely challenging (Snellen *et al.*, 2013; Chiavassa *et al.*, 2017; Sarkar *et al.*, 2018) and will likely not be possible with the current proposed set of concept telescopes. For example, to detect a change in effective altitude (ΔR_p) requires a precision of $2R_\oplus \Delta R_p / R_\odot^2$, without accounting for chromatic stellar signal noise (Chiavassa *et al.*, 2017). There is a $\approx$ 20 km effective altitude difference for the 9.6 µm feature between the PI and 0.1% PAL scenarios, giving a 0.4 ppm difference in the signal. The best possible JWST noise floor is 5 ppm (Matsuo *et al.*, 2019; Schlawin *et al.*, 2020, 2021;

Rustamkulov *et al.*, 2022). Future technology may make transmission spectra of such exoplanets viable, but transmission spectra time variations for each scenario is not shown because the altitude variations are < 5 km.

5.4.2 Molecular detectability

It is acknowledged that the SNR estimates in Section 5.3.5 depend on various parameters that have been assumed, such as a 90° inclination angle, as well as the underpinning simulations from the Earth System Model WACCM6. Other chemistry-climate models when used in conjunction with PSG, as has been performed in this Chapter, would yield different results (Fauchez *et al.*, 2022). The estimates also depend on telescope concepts that have not been constructed. Therefore, the results are an indicative, not exhaustive, picture of possible future measurements based on the information available for each concept at the time of writing.

In the event that an Earth-like exoplanet is found even farther away (e.g. 75 pc) it would be much more challenging to detect any particular molecular feature. A longer integration time may not improve the performance because the coronagraph throughput significantly drops with distance for these concepts and the exoplanet would be observable only over a narrow range of phases and wavelengths, if any. The coronagraph throughput drops when the exoplanet passes inside the inner working angle of the coronagraph and is therefore partly or fully obscured by the coronagraph. The inner working angle for the LUVOIR concept is proportional to wavelength so longer wavelengths are cut off and cannot be detected (The LUVOIR Team, 2019) - see Appendix C.

The SNR of each feature is set in part by its depth relative to the continuum. It also depends on the telescope's diameter, the telescope's coronagraph, the total integration time, and distance to the planetary system. For example, even though

the H_2O feature at 1.4 µm is deeper than that at 0.94 µm, the SNR is lower because of reduced coronagraphic throughput, and higher noise, in the near infrared. The HabEx with a starshade concept, when compared to a LUVOIR concept with an identically sized primary mirror, enables characterisation at greater distance due to the enhanced coronagraphic throughput (Checlair *et al.*, 2021).

5.4.3 Temporal high-contrast imaging spectra variations

The O_2 concentrations in the lower and middle atmosphere are identical to those predicted by previous work (Kasting & Donahue, 1980; Segura *et al.*, 2003; Gregory *et al.*, 2021). However, the lower and middle atmospheric concentrations of H_2O, O_3, CH_4, OH, and other molecules, differ considerably compared to prior 1D and 3D modelling (Cooke *et al.*, 2022). The temporal variability of chemistry and climate was considered in this Chapter when making HCI predictions, and the consequences for computed emission and reflection spectra were presented.

Although the effect of chemistry on the spectra for different oxygenation states is evident in Fig. 5.3, chemistry has a smaller impact than when considering the time variability from the same simulation. The largest variation between years is caused by clouds, then chemistry, and then surface albedo. Nevertheless, surface albedo is important for seasonal cycles and is crucial for understanding the spectra presented in Section 5.3.7. 1D atmospheric models which run to steady state cannot access this temporal variability, nor can they assess the seasonal effect on exoplanet spectra. Because clouds in 3D global climate models show significant variability between models (Ceppi *et al.*, 2017; Lauer & Hamilton, 2013; Fauchez *et al.*, 2020a), future comparisons with 3D time-resolved simulations using a different global climate model will therefore be of interest to determine how the predicted magnitude of spectral variations from HCI differ between models and oxygenation states (or various other chemical regimes). A comparison has been

done for transmission spectra from 3D models in the TRAPPIST Habitable Atmosphere Intercomparison (Fauchez *et al.*, 2022). These comparisons could also be done with 1D models to evaluate the uncertainty across the entire range of models used in the exoplanet community, which would then be used to assign confidence to the interpretation of future observations.

Our simulated spectra were evaluated at 00:00 UTC, such that the Pacific Ocean is illuminated, with a small proportion of the Earth's land and ice illuminated. The albedos of land and ice are both greater than that of the ocean, so reflection spectra from HCI could be affected if the observations were calculated at different times. Additionally, the WACCM6 atmospheric time step is 30 minutes, but it was assumed that the instantaneous state at 00:00 UTC held for long enough to integrate observations for over 24 h or 48 h. This assumption was used because saving multiple 3D variables every time step for four model years and for multiple oxygenation states, then simulating each time step snapshot with PSG (and with three telescope concepts), would require vastly more data storage and computational expense. As this physical assumption likely does not hold true (see the diurnal variations predicted in low precision photometry measurements by Ford *et al.*, 2001), greater temporal variations may be introduced by further surface albedo and cloud variations. These variations during the timescale of the observations are likely to be important, especially when the observer does not know the rotation rate of the exoplanet. For instance, Guzewich *et al.* (2020) predicted how different planetary rotation rates affected the absorption depth of H_2O, O_2, and O_3 features. Fortunately, the rotation rate may be known provided that approximately 5 – 15 rotations are observed, and the integration time is less than 1/6 to 1/4 of the planetary rotation period (Li *et al.*, 2022).

The exoplanet is usually at its brightest just before secondary eclipse, but with the coronagraphs simulated here, such orbital phases are not observable as

the planet is also being blocked by the coronagraph. Therefore, there is a trade-off between detectability and brightness. Other orbital phases show different ranges between minimum and maximum flux (see Fig. 5.7), so the observer may not be able to constrain certain parameters, including the amount of year-to-year variation across multiple phases, depending on the telescope used and the distance to the exoplanetary system.

With the mission concepts evaluated in this Chapter, monitoring a nearby (< 25 pc) Earth-analogue exoplanet for a single orbit is long enough to inform the observer about short-term climate variability and is ample time to detect if molecules of interest (e.g. O_2, O_3, and H_2O) are present. The HCI simulations suggest that inter-annual climate variability is observable provided conditions are favourable. Fully characterising an exoplanet (determining temperature, chemistry, seasons, obliquity, cloud coverage, rotation rate, land and ocean coverage, etc.) will be aided by observations of multiple orbits. Nevertheless, there will remain significant challenges to interpreting those observations.

5.4.4 Future work

The atmospheric scenarios used in this Chapter are based on the current understanding of Earth's atmospheric history since the GOE, when Earth's atmospheric oxygen concentrations rose above 10^{-5} PAL. However, the abundance of gases throughout Earth's history is not well constrained. Even if better constraints are achieved in the future, there is no reason why the atmospheric evolution of exoplanets that are oxygenated must take a similar path to Earth (Krissansen-Totton *et al.*, 2021). Nonetheless, the Earth system provides the best known template for an oxygenated atmosphere of a terrestrial planet. Large changes in the magnitude of the mixing ratios of other chemical species (e.g. CO_2, CH_4), decreased or increased atmospheric pressure, and the proportion of land versus

ocean coverage (Macdonald *et al.*, 2022), will all affect the predictions from this Chapter.

Changes in assumed cloud properties will also modify the calculations presented in this work. Komacek *et al.* (2020) varied ice cloud particle radius between 20 µm and 200 µm and showed that this non-linearly affected the amount of transits required to detect water vapour in transmission spectra of a terrestrial exoplanet atmosphere using JWST. Although a large range of cloud parameters have not been covered here, the results show that assumed particle sizes are important in PSG, affecting both variability and signal-to-noise ratios. Thus, the effects of how clouds are modelled in global climate models and radiative transfer models, and their impacts on predictions, requires further investigation.

There are many unknowns for exoplanets that compound the difficulty of modelling and interpreting spectra from a directly-imaged exoplanet. This Chapter investigated a temporal and 3D problem that depends on: (1) albedo; (2) seasonal climatic variability; (3) clouds; (4) chemistry; (5) inter-annual climatic variability; (6) eccentricity (Cowan *et al.*, 2012); (7) obliquity (Gaidos & Williams, 2004; Cowan *et al.*, 2012); (8) observer inclination angle (Maurin *et al.*, 2012; Boutle *et al.*, 2017); and (9) other exoplanets in the system contaminating the signal (Parmentier & Crossfield, 2018). Some of these variables interact with each other. The high-contrast imaging spectra predictions account for some of these parameters (points 1 – 5) using a 3D fully coupled climate model for the first time, whilst others were not investigated in this Chapter (6 – 9). Further work should investigate how these other parameters affect the predicted spectra of oxygenated exoplanets. At greater distances, where less orbital phases are available to observe, assessments of the year-to-year variability demonstrated here in the PSG simulations will be less reliable. Additionally, the PSG simulations assume that whilst F_* varies with wavelength, the flux in each wavelength bin is assumed

to be constant over the duration of an orbit. If instead the simulations were modified to include realistic stellar flux variations, it is unclear how detectable the observed flux variations due to the exoplanet would be.

Several methods already exist to obtain information that is otherwise difficult to access. For example, exo-cartography has been studied as a process for retrieving the surface maps of exoplanets, despite the planetary surface being unresolved in observations. (Cowan & Fujii, 2018; Fan *et al.*, 2019; Berdyugina & Kuhn, 2019). Already it is clear that different surfaces produce similar light curves, and removing degeneracies to accurately map the surface of these exoplanets will be challenging. Teinturier *et al.* (2022) used Earth observation data and found that for exoplanets with a similar climate to Earth, removing clouds to obtain a surface albedo map may produce unreliable results. They remarked that longer, continuous observing periods will help with mapping. Indeed, clouds may have the largest impact on spectra variation (Paradise *et al.*, 2021), as found here in this Chapter. Additionally, Schwartz *et al.* (2016) found that, at least theoretically, it should be possible to determine the obliquity of an exoplanet by observing at 2 – 4 different orbital phases. With known obliquity, the impact of seasons can be estimated in 3D climate model simulations. Recently, Pham & Kaltenegger (2022) used a machine learning algorithm to analyse more than 50,000 synthetic spectra of cold, Earth-like planets. They showed that snow/clouds and water could be detected in 90% and 70% of cases, respectively. A similar evaluation using machine learning, and including both spectra produced from 1D and 3D atmospheric models, would be useful. Such a study would enable assessment of how reliably the community can use machine learning and 1D models to explore the parameter space that 3D models struggle to cover due to computational expense.

All of the simulations here presume a biotic source of O_2. Even if a biogenic molecule is detected with high SNR, this may not be enough to prove

that life exists on an exoplanet. Further information will likely be required for context to confirm that any potential biosignature that is detected has arisen from the presence of extraterrestrial life (Meadows, 2017; Catling *et al.*, 2018; Krissansen-Totton *et al.*, 2021). This includes but is not limited to the detection of chemical disequilibrium (e.g. O_2 and CH_4 Lovelock, 1965; Sagan *et al.*, 1993; Krissansen-Totton *et al.*, 2016), or temporal changes in biogenic gases that indicate atmospheric modulation by life (Olson *et al.*, 2018b) rather than by geological processes. However, detecting such temporal chemical variations will likely be complicated by temporal changes in planetary albedo. It is noted that detecting seasonal O_3 variations in the UV as suggested by Olson *et al.* (2018b) may be complicated by clouds, as well as the seasons available to the observer. Because not all observing geometries have been explored, the effect of different inclination angles will matter too (Olson *et al.*, 2018b).

It is apt to remind the reader here that abiotic build-up of O_2 is physically feasible on exoplanets (Meadows, 2017, and references therein). Moreover, there is the possibility of detecting an exoplanet-exomoon system which has O_2 and CH_4 in the spectra, but not on the same celestial body (Rein *et al.*, 2014). In the coming decades, observational data, computational procedures which identify the sources of biologically-relevant gases (Catling *et al.*, 2018; Lisse *et al.*, 2020), and simulations that utilise state-of-the art climate models, will all be needed to determine the most habitable exoplanets (Shields, 2019), and indeed to determine if any are inhabited.

Finally, this Chapter has only evaluated telescope concepts which will have spectroscopic capabilities between the ultraviolet and near infrared wavelength regions. To detect molecules such as O_3, H_2O, and CO_2 in the infrared, this will require a mission design different to LUVOIR or HabEx. Proposed candidates include the Large Interferometer For Exoplanets (LIFE; Quanz *et al.*, 2018;

Defrère *et al.*, 2018) and the Origins Space telescope (OST; Wiedner *et al.*, 2021) missions. These telescope concepts may be able to constrain planetary emission in the mid-infrared and detect molecules such as H_2O, O_3, and CH_4 (Alei *et al.*, 2022), potentially enabling the confirmation of chemical disequilibrium. Certainly, multi-wavelength observations which cover ultraviolet wavelengths to mid infrared wavelengths will enable a greater degree of atmospheric characterisation. Evaluating the OST and LIFE missions with the simulated WACCM6 climates and calculating any variability that may be detected is left as future work.

5.5 Conclusions

This Chapter made use of a state-of-the-art Earth System Model, WACCM6, to simulate Earth-analogue exoplanets around a G2V star with varying concentrations of O_2 (0.1% PAL $\rightarrow$ 150% PAL). Based on the Earth System Model output for these hypothetical exoplanets, the Planetary Spectrum Generator was used to simulate thousands of high-contrast imaging observations with three future telescope concepts: LUVOIR A, LUVOIR B, and HabEx with a starshade.

All telescopes are capable of detecting O_3 at 10 pc after one day of integration time. H_2O and O_2 detection may require longer integration times, or high O_2 concentrations for improved SNR for O_2 (e.g. $\geq$ 10% PAL). At 25 pc, O_3 in the UV can still be detected with LUVOIR A, but integration times longer 30 days may be required for H_2O and O_2 detection.

Long term inter-annual climate variations and short-term variations can theoretically be observed in the simulated atmospheres with a telescope concept such as LUVOIR or HabEx. Both annual and seasonal variability can affect the brightness of key chemical features such as O_2 and H_2O. The annual variability is primarily caused by clouds, and the variability appears to depend non-linearly on atmospheric O_2 concentration (although more that four orbits would enable this

to be a statistically robust result), as well as depending on wavelength, distance, and telescope design. The seasons that can be accessed through observations will affect the maximum magnitude of the incoming flux, with more ice coverage increasing this limit.

Future potential missions, such as the 6-metre diameter UV/VIS/IR telescope that was recommended by the Decadal Survey, and the LIFE mission, will present exciting opportunities to characterise the atmospheres of possible Earth-analogues. Confident interpretation of future observations that next-generation telescopes return will require sophisticated planetary modelling and observational analysis. It is important that future work continues to account for the complexity of chemistry and clouds, as well as long- and short-term climate variations.

Chapter 6

Tidally locked Earth-like exoplanets

6.1 Introduction

Because M dwarf stars are large in abundance, the most frequent occurrence of habitable exoplanets may be terrestrial exoplanets orbiting these relatively cool main sequence stars. As a consequence of gravitational tidal interactions with their host star, these close-in (generally $\lesssim 0.4$ AU; Barnes, 2017) exoplanets could be tidally locked in 1:1 spin-orbit synchronous rotation. Such a scenario would enable a climate state with a fixed terminator (i.e. a permanent day side and a permanent night side), with implications for the climates and habitability of these unfamiliar exoplanets.

I use WACCM6 for the first time to simulate two known habitable zone exoplanets: Proxima Centauri b and TRAPPIST-1e. Illustrated in Fig. 6.1, Proxima Centauri b orbits the star Proxima Centauri, which is the closest star to the Sun (1.3 pc distant; Gaia Collaboration *et al.*, 2016). TRAPPIST-1e is part of a 7-planet system, illustrated in Fig. 6.2, that orbits the star TRAPPIST-1 (12.1 pc distant; Costa *et al.*, 2006). This Chapter investigates how the incoming irradiance and atmospheric dynamics affect the atmospheric composition in each

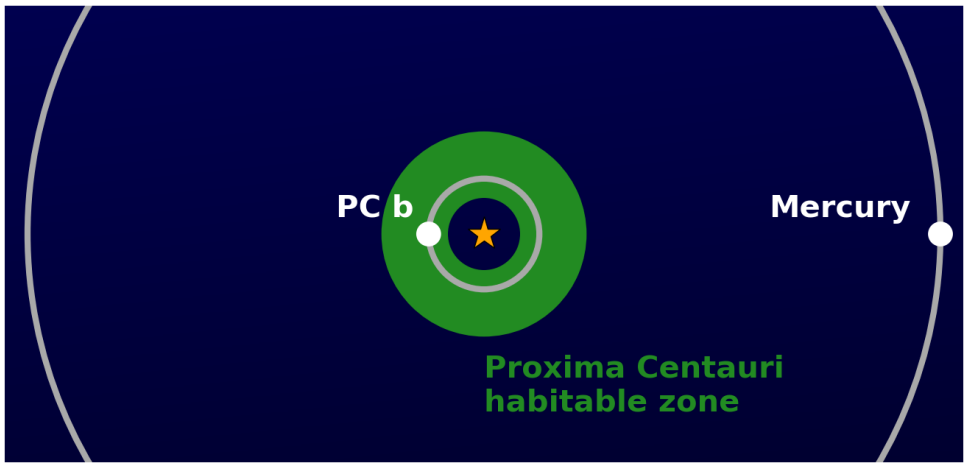

Fig. 6.1: The schematic shows the semi-major axis (assuming a circular orbit) of Mercury and Proxima Centauri b around their host stars, which is indicated by the central orange star. The semi-major axes are to scale, but the size of the star and planets are not to scale. The HZ width (shown in green) is calculated from Ribas *et al.* (2016), and references therein. Two other potential exoplanets, Proxima Centauri c and d, are not shown because they are currently candidate exoplanets according to the NASA Exoplanet Archive.

scenario, and how these exoplanet atmosphere simulations compare with previous work.

6.1.1 Habitability

In recent years, many habitable zone (HZ) terrestrial exoplanets have been located around M dwarf stars[1]. Despite several studies showing how these M dwarf terrestrial exoplanets could be habitable (Tarter *et al.*, 2007; Abrevaya *et al.*, 2020; Segura *et al.*, 2005; France *et al.*, 2020; Lobo *et al.*, 2023), the likelihood of such habitability has been debated (Lissauer, 2007; Luger & Barnes, 2015; Owen & Mohanty, 2016; Tilley *et al.*, 2019; Godolt *et al.*, 2019; Airapetian *et al.*, 2017). For example, M dwarfs are relatively active, emitting flares and coronal mass ejections more frequently and at higher energies than G dwarfs, for instance.

[1] https://exoplanetarchive.ipac.caltech.edu/

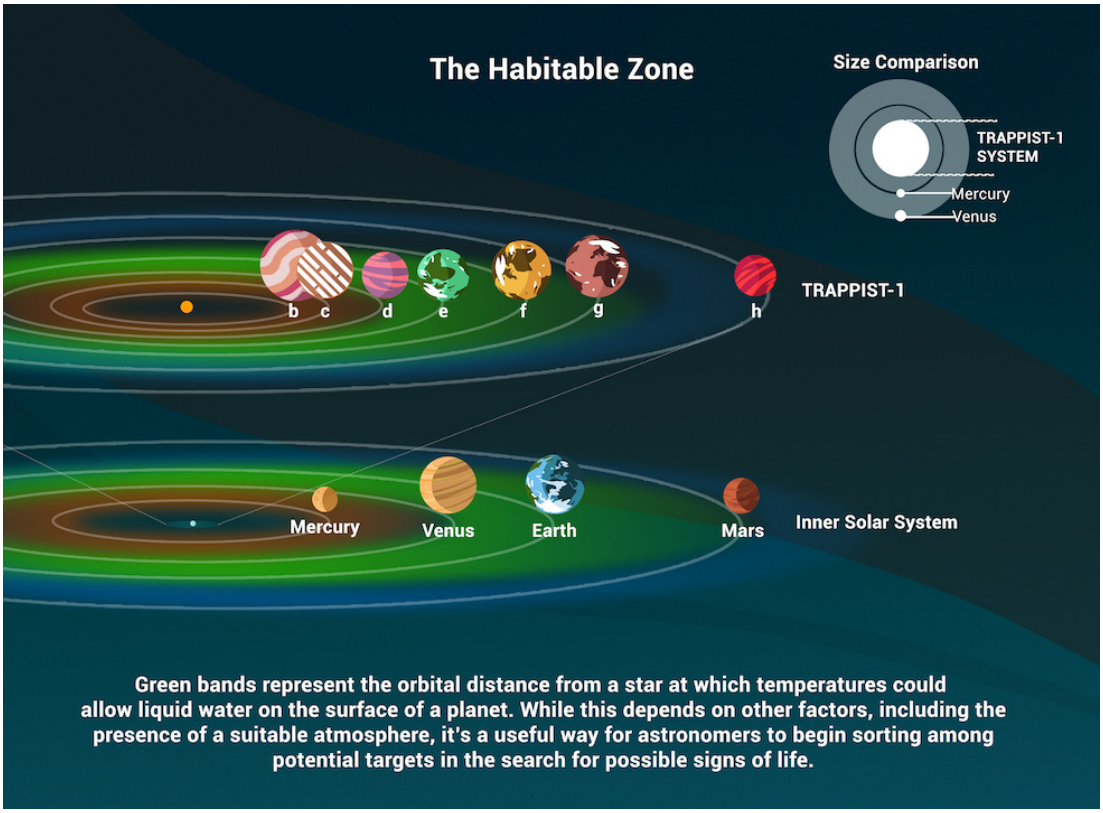

Fig. 6.2: The TRAPPIST-1 system of seven terrestrial exoplanets (Gillon *et al.*, 2017) is illustrated in the figure and compared to the inner solar system planets (Mercury, Venus, Earth, and Mars). All seven TRAPPIST-1e exoplanets orbit TRAPPIST-1 closer than Mercury orbits the Sun. TRAPPIST-1 is ≈ 1800 times less luminous than the Sun, so its habitable zone (indicated in green shading) is much closer in and has a smaller width when compared to the solar system's habitable zone. Note that the star and planet sizes are not to scale. Image credit: NASA/JPL-Caltech/Lizbeth B. De La Torre.

Flares can reach up to $10^{34} - 10^{37}$ erg (Segura *et al.*, 2005), which is greater than the estimated energy released by the Carrington flare at 4×10^{32} erg (Hudson, 2021). Increased flux of ionising radiation could damage the prospects for surface-dwelling life, but in contrast, some studies indicate the requirement for environments with high UV fluxes from M dwarfs to support habitability (Ranjan & Sasselov, 2016; Rimmer *et al.*, 2018). Research by Segura *et al.* (2005) and Chen *et al.* (2021) argued that frequent flares striking an exoplanet's at-

mosphere may not be a problem for life because the atmosphere recovers quickly after such events. This assumes that an atmosphere can form and persist at all; M dwarf stars may strip their orbiting planets through atmospheric erosion (Zendejas *et al.*, 2010; Rodríguez-Mozos & Moya, 2019), with global planetary magnetic fields potentially reducing the rate of atmospheric loss if they are present (Vidotto *et al.*, 2013; López-Morales *et al.*, 2011; Cohen *et al.*, 2015).

The exoplanet's ocean and land distribution affects heat advection around the exoplanet. Whilst research has often used slab ocean models, where a depth and heat capacity are specified with no ocean heat transport, the use of an interactive deep ocean has shown that oceans play an important role in simulations of tidally locked exoplanets (Yang *et al.*, 2013; Hu & Yang, 2014; Yang *et al.*, 2019). Whether the substellar point is over ocean or land makes a difference to ocean and atmospheric dynamics (Lewis *et al.*, 2018; Salazar *et al.*, 2020; Zhao *et al.*, 2021), in addition to the size of any substellar continent (Salazar *et al.*, 2020), where the continent is, and whether the continent moves (Zhao *et al.*, 2021), which will occur over long geological timescales.

Through absorption, scattering and emission of electromagnetic radiation, clouds play a crucial role in modelling when determining the surface temperature of an exoplanet. Due to constant stellar heating, 3D numerical models indicate that clouds will accumulate at the substellar point for tidally locked exoplanets (Yang *et al.*, 2013; Wolf, 2017; Sergeev *et al.*, 2020). This aggregation of clouds reflect incident radiation and can potentially keep synchronously rotating early-type M dwarf exoplanets habitable up to total instellations as high as 1.9 times that of the Earth (Chen *et al.*, 2019). However, note that the resolution of the simulations governs whether convection can be resolved and determines the efficiency of heat transport in model results (Sergeev *et al.*, 2020).

In summary, the habitability of M dwarf terrestrial exoplanets remains de-

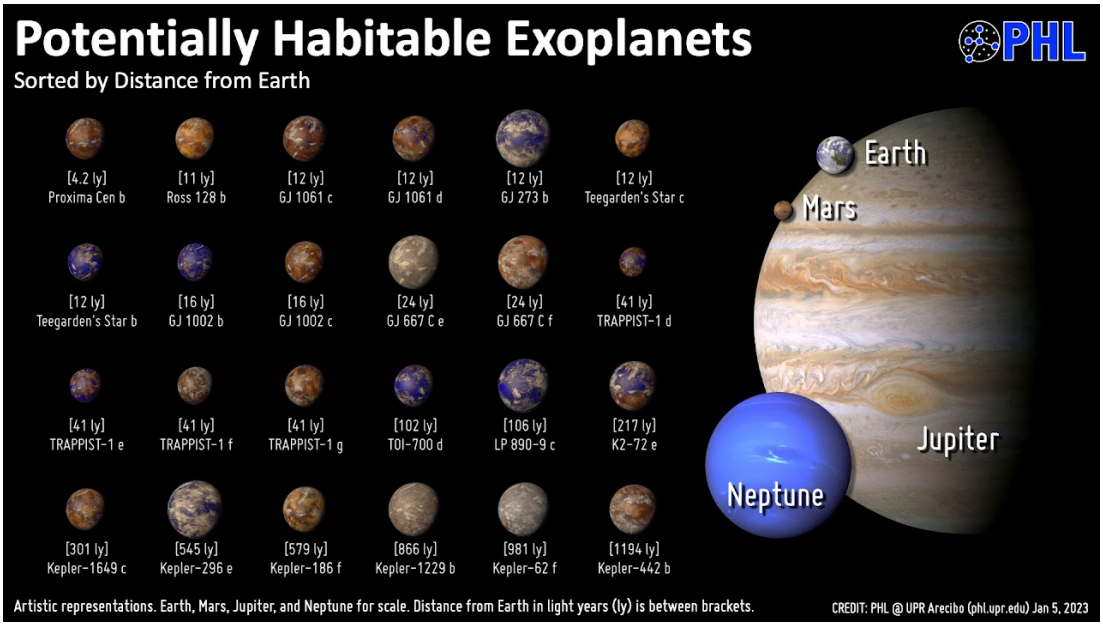

Fig. 6.3: Figure from The Habitable Exoplanets Catalog, courtesy of the The Planetary Habitability Laboratory at the University of Puerto Rico at Arecibo. The figure shows the 24 exoplanets from the 'Conservative Sample of Potentially Habitable Exoplanets', sorted by distance from Earth. All exoplanets shown are artists impressions. The Catalog was last updated on the 5th January 2023.

bated, with several of the aforementioned parameters requiring further investigation.

6.1.2 Exoplanets of interest

Ranked via the Earth Similarity Index (Schulze-Makuch *et al.*, 2011), there is now a list of over 60 potentially habitable exoplanets (see Fig. 6.3) based on data from the NASA exoplanet archive (Akeson *et al.*, 2013), and the majority of these orbit M dwarf stars[1].

Currently, two exoplanets of particular interest are Proxima Centauri b (Anglada-Escudé *et al.*, 2016) and TRAPPIST-1e (Gillon *et al.*, 2017). Proxima Centauri b and TRAPPIST-1e are 1.3 pc and 12.1 pc distant from Earth, respectively, mak-

[1] https://phl.upr.edu/projects/habitable-exoplanets-catalog

ing then both good candidates for telescope observations. 3D modelling studies suggest that they are both potentially habitable exoplanets because they may be able to retain liquid water on their surface (Quarles *et al.*, 2017; Ribas *et al.*, 2016; Turbet *et al.*, 2016; Meadows *et al.*, 2018a; Del Genio *et al.*, 2019b). To maintain this state, both exoplanets are estimated to require an atmosphere with a larger inventory of greenhouse gases when compared to Earth's atmosphere (Turbet *et al.*, 2016; Wolf, 2017).

If these potentially tidally locked exoplanets do have atmospheres, then they are expected to have dynamical properties that differ from any solar system planet, which in turn will affect the distribution and abundance of chemical species within the atmosphere.

6.1.3 Dynamics

Atmospheric super rotation is where the angular momentum of the zonal winds are greater than the angular momentum of the planet's solid surface (Read & Lebonnois, 2018). The axial component of specific angular momentum, m (Read, 1986), is given as

$$m = R_p \cos\phi(\Omega R_p \cos\phi + u), \tag{6.1}$$

where R_p is the planetary radius, ϕ is the latitude, u is the zonal wind velocity, and Ω is the planetary angular velocity. The local super rotation index (s) is defined in Read (1986) as

$$s = \left(\frac{m}{\Omega R_p^2}\right) - 1. \tag{6.2}$$

For $s > 0$, the winds are considered to be super rotating. The phenomenon of atmospheric super rotation on terrestrial exoplanets has been studied in the

troposphere by many authors. Carone *et al.* (2015) showed how the flow regime (from super rotation through to radial flow which is depicted in Fig. 6.4) depends on the orbital period and the radius of the exoplanet. Haqq-Misra *et al.* (2018) discussed the theoretical existence of three rotation regimes: the 'Rhines rotator', 'fast rotator', and 'slow rotator' regimes, characterised by the Rossby deformation radius, the Rhines length, orbital period, and the planetary radius. The Rossby deformation radius quantifies the length scale at which either rotational forces or buoyancy forces dominate (Haqq-Misra *et al.*, 2018). The Rhines length demarcates the latitudinal length at which turbulent flows become more important than wave-driven motion and produce zonal jets (Rhines, 1975; Haqq-Misra *et al.*, 2018). Simulated atmospheric heat advection depends on which circulation regime is dominant in an exoplanet atmosphere.

Fewer authors have demonstrated super rotation above the troposphere (Carone *et al.*, 2018; Chen *et al.*, 2019). One of these examples is Carone *et al.* (2018), who used a 3D model which had a maximum vertical extent up to 1 hPa (compared to 5×10^{-6} hPa for WACCM). They found that the planetary waves forming in the troposphere induce super rotation in the stratosphere, where the winds reach up to speeds of 100 m s^{-1}. They also determined that tropical Rossby waves can act to impede equator-to-pole transport.

The meridional mass streamfunction (Ψ) can be used to analyse the meridional overturning circulation of an atmosphere, with faster rotating planets exhibiting more zonal jet streams and meridional overturning cells (Wang *et al.*, 2018). It is given by

$$\Psi = \frac{2\pi R_p \cos\phi}{g} \int_0^p \overline{v} dp', \tag{6.3}$$

where R_p is the radius of the planet, g is the gravitational acceleration, p is the atmospheric pressure, and $\overline{v}$ is the zonally averaged meridional velocity.

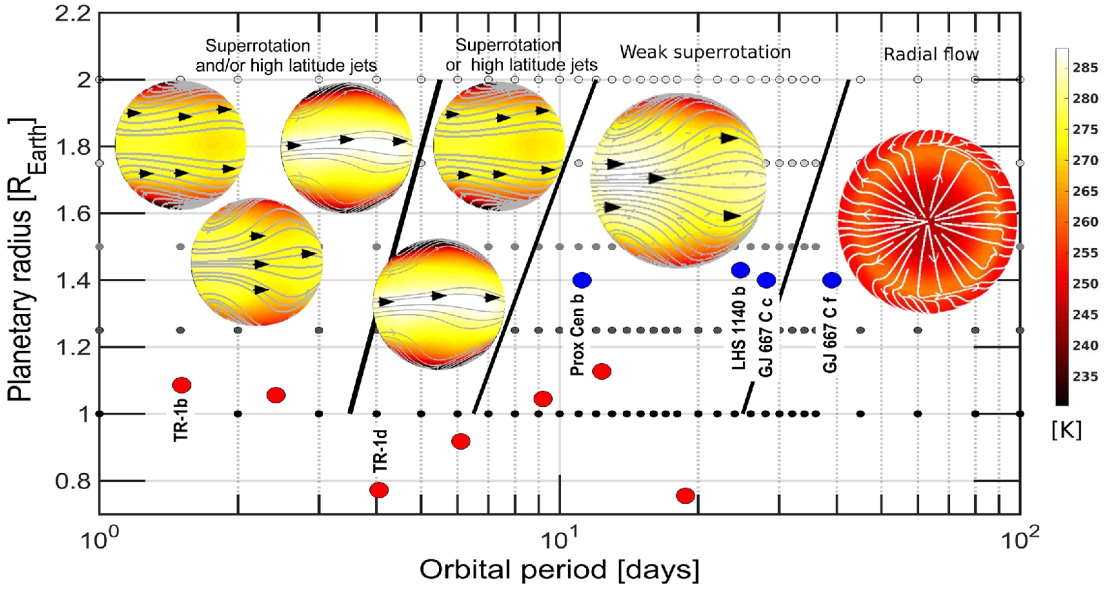

Fig. 6.4: The planetary radius (in $R_\oplus$) is plotted against orbital period (in days) for tidally locked simulations, showing the various tropospheric circulation regimes as identified by Carone *et al.* (2015). The regime depends on planetary size and orbital period. This assumes a 1 bar atmosphere and an irradiation equal to the instellation Earth receives (1 S_0), assuming an Earth-like atmosphere and thermal forcing. Lines and arrows indicate the direction of flow at a pressure of 225 hPa and facing the substellar point. Examples of known exoplanets are indicated by blue circles (Proxima Centauri b, LHS 1440 b, GJ 667 C-c and -f) and red circles (TRAPPIST-1 b, c, d, e, f, g, h). Figure from Carone *et al.* (2018). For other papers which discuss circulation regimes, see Haqq-Misra *et al.* (2018) and Noda *et al.* (2017).

Generally for exoplanet simulations, the zonal circulation and meridional circulation are discussed as time averages. However, Cohen *et al.* (2022) used the Unified Model (UM) to simulate the exoplanet Proxima Centauri b, with the dynamics producing a longitudinally asymmetric stratospheric wind oscillation (dubbed 'LASO'), which is similar, although not identical to, the present day Earth's quasi-biennial oscillation (QBO). In contrast to the QBO which has a period of $\sim$ 28 months, the predicted LASO has a period of 5 – 6.5 months, with longitudinal asymmetries where the western terminator exhibits faster zonal wind

speeds than the eastern terminator. Cohen *et al.* (2022) suggested chemistry-climate models should investigate the impact of such time variability on theoretical observations.

6.1.4 Chemistry, biosignatures and observational prospects

One-dimensional (1D) modelling has investigated the climates of Earth-like exoplanets around M dwarfs (Segura *et al.*, 2005; Grenfell *et al.*, 2014; Kozakis *et al.*, 2022; Meadows *et al.*, 2018b), in addition to Venus-like exoplanets (Jordan *et al.*, 2021). Generally, these works have found that photochemically active species, such as CH_4, H_2O, SO_2, and OCS, have longer lifetimes and persist in greater concentrations when compared to exoplanets orbiting G dwarf stars, for instance. This is attributed to the weaker quiescent UV emission from M dwarf stars.

Chen *et al.* (2018) used the Community Atmosphere Model with Chemistry (CAM-chem) from CESM 1.2 to investigate the 3D composition for tidally locked exoplanets over various rotation rates and stellar energy distributions (SEDs). They found that the mixing ratio contrast between the day side and night side was generally $< 20\%$ for several biosignatures, but molecules such as C_2H_6S exhibited larger ($\sim 67\%$) variations, which could be important for observations. Boutle *et al.* (2017) used the UM to simulate climate states for Proxima Centauri b, finding the simulated exoplanet is potentially habitable under diverse conditions due to its insensitivity to instellation variations. Building on the UM Proxima Centauri b aquaplanet (slab ocean) simulations from Boutle *et al.* (2017), which considered an Earth-like and an N_2 dominated atmosphere, Yates *et al.* (2020), Braam *et al.* (2022) and Ridgway *et al.* (2023), focused on O_3, lighting, and flares, respectively. In Yates *et al.* (2020), the night side had the largest O_3 mixing ratios and the stratospheric O_3 distribution was heavily influenced by the presence of an equatorial jet.

Although there has been observations of M dwarf terrestrial exoplanets, including a phase curve of LHS 3844b (Kreidberg *et al.*, 2019), to date, the primary source of understanding atmospheres of terrestrial M dwarf exoplanets comes from numerical simulations because the observations reveal limited information about the exoplanet's climate. Hot spots shifts have been predicted in models (Selsis *et al.*, 2011; Penn & Vallis, 2017). The hot spot shift can be observed in the thermal phase curve, just as Demory *et al.* (2016) observed 55 Cancri e using the 4.5 µm channel of the *Spitzer*/IRAC, finding that it had a hot spot that was eastward of the substellar point by $41° \pm 12°$.

Given their relatively close proximity to Earth, both Proxima Centauri b and TRAPPIST-1e are compelling observational candidates. TRAPPIST-1e transits its host star, whilst Proxima Centauri b is unlikely to transit (Kipping *et al.*, 2017; Kreidberg & Loeb, 2016). Multiple studies (using both 1D and 3D model atmospheres) have been undertaken to predict possible transmission and direct imaging spectra for these exoplanets (Lin & Kaltenegger, 2020; Lin *et al.*, 2021; May *et al.*, 2021; Fauchez *et al.*, 2022; Braam *et al.*, 2022; Ridgway *et al.*, 2023), serving as useful templates for the possible atmospheres we may expect to observe in the future.

6.2 Simulations

Here I use WACCM6 to simulate both Proxima Centauri b and TRAPPIST-1e. Proxima Centauri is a M5.5V dwarf star at a distance of 1.3 pc, and TRAPPIST-1 is an ultra cool M8.5V dwarf at a distance of 12.1 pc. Their stellar properties are summarised in Table 6.1. In this work, it is assumed that Proxima Centauri b receives 884 W m^{-2} of irradiation whilst TRAPPIST-1e receives 900 W m^{-2} (0.65 S_0 and 0.66 S_0 respectively, where S_0 is the total insolation that the Earth receives). This is consistent with previous work on Proxima Centauri b (Boutle

Table 6.1: Orbital and planetary parameters used in this study, for the exoplanet Proxima Centauri b and its star (Proxima Centauri), and for the exoplanet TRAPPIST-1e and its star (TRAPPIST-1). The parameters are from Schlaufman & Laughlin (2010), Delfosse *et al.* (2000), Boyajian *et al.* (2012), and Anglada-Escudé *et al.* (2016) for Proxima Centauri b, and Delrez *et al.* (2018) and Agol *et al.* (2021) for TRAPPIST-1e.

Parameter	Proxima Centauri b	TRAPPIST-1e
Stellar luminosity [$L_\odot$]	0.001548	0.000553
Stellar effective temperature [K]	3050	2566
Stellar radius [$R_\odot$]	0.141	0.119
Stellar mass [$M_\odot$]	0.12	0.08
Stellar metallicity	0.21	0.04
Planetary radius [$R_\oplus$]	1.05	0.92
Planetary mass [$M_\oplus$]	1.07	0.69
Planetary gravitational acceleration [m s^{-2}]	12.2	9.15

et al., 2017; Yates *et al.*, 2020; Braam *et al.*, 2022; Ridgway *et al.*, 2023) and with the TRAPPIST-1 Habitable Atmosphere Intercomparison project (THAI; Fauchez *et al.*, 2020a; Turbet *et al.*, 2022). Note that the latest data available for TRAPPIST-1e in the NASA Exoplanet Archive (Akeson *et al.*, 2013) lists a value of 0.646 ± 0.025 $S_\oplus$ (Agol *et al.*, 2021).

The ocean and atmosphere are fully interactive (meaning they respond to physical perturbations such as temperature, and in the case of the atmosphere, chemical perturbations). Because Proxima Centauri b and TRAPPIST-1e are suspected to be tidally locked (Gillon *et al.*, 2017) even if any atmospheric tides are present (Leconte *et al.*, 2015; Luger *et al.*, 2017; Salazar *et al.*, 2020), the substellar point is static in the model. This is achieved by fixing the solar zenith angle in each grid cell, and setting the exoplanet's obliquity and orbital eccentricity to zero (although note that the eccentricity may be non-zero, albeit < 0.01; Luger *et al.*, 2017).

The substellar point was placed at 0° latitude and at 180° longitude (over the

Pacific Ocean). In one simulation, the substellar point was placed at 0° latitude and at 30° longitude (over Africa), to test the differences between a substellar point over land or over ocean. Each atmosphere had a surface pressure of 1,000 hPa. In simulations in which O_2 has been reduced, N_2 has been increased to maintain 1,000 hPa of surface pressure in the model. In the standard BWma1850 case, the QBO is forced, meaning that the model perturbs the middle atmospheric winds in order to produce a QBO with a period of $\sim$ 28 months. The QBO forcing was removed as this is set to reproduce the QBO on modern Earth, which is unlikely to occur in the same manner on exoplanets with orbital configurations dissimilar to Earth's (Cohen *et al.*, 2022).

The chemical mechanism used in the simulations had 98 chemical species, and 298 chemical reactions (including photochemical reactions). The full details of the model set-up are available via the simulation scripts that can be accessed via GitHub[1].

The UV flux from TRAPPIST-1 remains uncertain because of the intrinsic faintness of the star (V = 18.798 mag; Costa *et al.*, 2006). Similar uncertainties apply for Proxima Centauri b, but for proof of concept, it is only necessary to demonstrate the differences UV uncertainties can induce for a single exoplanet. Peacock *et al.* (2019), henceforth known as P19, modelled the spectrum of TRAPPIST-1 using the stellar atmospheric code PHOENIX (Baron & Hauschildt, 2007; Hauschildt, 1993; Hauschildt & Baron, 2006). P19 added a treatment of the chromosphere to PHOENIX to produce synthetic stellar spectra of cool dwarf stars (including TRAPPIST-1) whose ultraviolet light have negligible flux contribution from the photosphere. The PHOENIX synthetic spectrum was benchmarked to Hubble Space Telescope (HST) observations of the Lyman-α line from TRAPPIST-1 and distance-corrected GALEX photometry of stars

[1] https://github.com/exo-cesm/CESM2.1.3/tree/main/Tidally_locked_exoplanets

with similar spectral type to TRAPPIST-1. More recently, Wilson *et al.* (2021), hereafter known as W21, used new HST (1100 – 5500 Å) and XMM-Newton (10 – 50 Å) observations of TRAPPIST-1 from the Mega-MUSCLES (Measurements of the Ultraviolet Spectral Characteristics of Low-Mass Exoplanetary Systems) Treasury Survey (Froning *et al.*, 2019; Wilson *et al.*, 2021) to construct a 5 Å – 100 µm SED of the star. Four models were used to fill in gaps in wavelength coverage, including a PHOENIX model for wavelengths > 5500 Å. Because of TRAPPIST-1's relatively low luminosity, W21 substituted the noisy 1100 – 4200 Å HST spectrum with a semi-empirical, noiseless spectrum that reproduced the measured flux of detected UV emission lines and agreed with the upper limits on the stellar continuum established by the HST spectra. Whilst neither spectrum wholly represents the true stellar irradiation environment of the TRAPPIST-1 planets, the W21 spectrum is in significantly better agreement with available observations of TRAPPIST-1.

The P19 and W21 spectra are scaled to the total instellation received by TRAPPIST-1e (900 W m^{-2}), rebinning them to match the wavelength grid required for WACCM6 simulations. The same process is performed for the MUSCLES Proxima Centauri spectrum, scaling it to 884 W m^{-2}. The resulting spectra used are shown in Fig. 6.5. For the wavelength regions over which O_2 and O_3 photolyse, the integrated flux is listed in Table 6.2 for each spectrum, and compared to the flux received by Earth.

For TRAPPIST-1e, four simulations were conducted with the P19 spectrum and three with the W21 spectrum. The four simulations with the P19 spectra consisted of one with the standard initial composition (TP-1 e P19 PI), another similar simulation but with the substellar point over land (TP-1 e P19 PI SSPL), one with a composition that had 1000 times less O_2 (TP-1 e P19 0.1% PAL), and one where the P19 spectrum was used, but the planet was not tidally locked

(TP-1 e P19 noTL). The simulations with W21 are similar (TP-1 e W21 PI, TP-1 e W21 0.1% PAL, TP-1 e W21 noTL), apart from there is no substellar point over land simulation with W21. These simulations allow the assessment of the influence of different incoming UV spectra, the influence of tidal locking, and the effects of reducing O_2 in order to explore the degeneracies between O_2, O_3, and incident UV light. A single Proxima Centauri b simulation is performed, starting with a pre-industrial initial condition (PC b PI). Table 6.3 summarises the simulations. Whilst all M dwarf terrestrial exoplanet simulations are introduced in this Chapter, some of them will be discussed in this Chapter, and the remainder in the following Chapter.

Proxima Centauri b has a minimum mass measured of $M_P \sin i = 1.07\ M_\oplus$ (Faria *et al.*, 2022) only, where M_P is the mass of the exoplanet and i is the inclination angle. Therefore, a recently estimated mass-radius relationship from (Otegi *et al.*, 2020), given as $R_p = 1.03\ M_p^{0.29}$, is used. Assuming $M_P = 1.07\ M_\oplus$, this places the radius of Proxima Centauri as 1.05 $R_\oplus$, and the surface gravity of Proxima Centauri b at 12.2 m s^{-2}. The surface gravity of TRAPPIST-1e, calculated from its mass and radius, is 9.1454 m s^{-2}.

Using equation 2.22, the tidal locking timescales for Proxima Centauri b and TRAPPIST-1e are 2.8 Myr and 150 kyr, respectively. Whilst in reality other processes (Leconte *et al.*, 2015) may stop a synchronous 1:1 resonance from occurring, it is reasonable (and currently standard practise) to assume that both exoplanets are tidally locked, given that TRAPPIST-1 is estimated to be 7.6 $\pm$ 2.2 Gyr years old (Burgasser & Mamajek, 2017), and the age of Proxima Centauri is estimated to be between 4.85 and $\sim$ 6 Gyr (Morel, 2018; Vida *et al.*, 2019; Garraffo *et al.*, 2022).

Table 6.2: For the three different spectra used in the WACCM6 simulations (two for TRAPPIST-1 and one for Proxima Centauri b), the integrated flux [W m^{-2}] received by the simulated exoplanets is given for the total flux and six different wavelength bands: Schumman-Runge continuum (S-RC), Schumman-Runge bands (S-RB), Herzberg continuum (HC), Hartley band (HaB), Huggins band (HuB), and the Chappuis band (CB). For reference, the Earth receives 1361 W m^{-2} of irradiation. Photons in the Schumman-Runge continuum, Schumann-Runge bands, and Herzberg continuum are able to photolyse O_2. Photons in the Hartley band, Huggins band, and Chappuis band, are able to photolyse O_3.

Spectrum	Total 10.5 – 99975.0 nm	S-RC 130 – 175 nm	S-RB 176 – 192 nm	HC 200 – 240 nm	HaB 200-310 nm	HuB 310 – 340 nm	CB 400 – 650 nm
Sun	1361	0.0092	0.0373	1.2997	19.8916	23.4556	453.7313
PC	884	0.0130	0.0013	0.0086	0.3853	0.0107	2.1355
TP-1 P19	900	0.0382	0.0239	0.0841	0.3953	0.0829	2.1355
TP-1 W21	900	0.0025	0.0001	0.0002	0.0050	0.0133	2.3045
Flux ratio $\frac{\text{P19}}{\text{W21}}$	1.00000	15.54313	451.81237	528.84516	79.58648	6.21028	0.92668

Table 6.3: Seven simulations have been performed for TRAPPIST-1e, each with an obliquity of 0° and a circular orbit (eccentricity = 0). The "P19 PI" and "W21 PI" simulations were set up in a tidally locked configuration with a 6.1 day rotation rate, using two different spectra for TRAPPIST-1 from P19 and W21 (see text for details). They assume an initial PI atmosphere with lower boundary conditions for the PI atmosphere. The substellar point is placed at 180° longitude and 0° latitude, such that it is over the Pacific Ocean. The "P19 PI SSPL" simulation has the substellar point over Africa at 30° longitude and 0° latitude. The "P19 noTL" and "W21 noTL" simulations are not tidally locked, rotate with a period of 1 day, and have a diurnal cycle. For the "P19 0.1% PAL" and "W21 0.1% PAL" simulations, the mixing ratio of atmospheric O_2 was reduced by a factor of 1000. PAL means present atmospheric level, where the present atmospheric level of oxygen is a mixing ratio of 0.21 by volume. A single Proxima Centauri b simulation was performed ("PC b PI") using the GJ 551 MUSCLES spectrum.

Simulation	Spectrum	O_2 mixing ratio	Orbital parameters
TP-1 e P19 PI	P19	1	Tidally locked, 6.1 day rotational period
TP-1 e P19 PI SSPL	P19	1	Tidally locked, 6.1 day rotational period
TP-1 e P19 noTL	P19	1	Not tidally locked, 1 day rotational period
TP-1 e P19 0.1% PAL	P19	0.001	Tidally locked, 6.1 day rotational period
TP-1 e W21 PI	W21	1	Tidally locked, 6.1 day rotational period
TP-1 e W21 noTL	W21	1	Not tidally locked, 1 day rotational period
TP-1 e W21 0.1% PAL	W21	0.001	Tidally locked, 6.1 day rotational period
PC b PI	GJ 551 MUSCLES	1	Tidally locked, 6.1 day rotational period

Each simulation was run for 200 Earth model years or more, and then the data presented were averaged over the last ten years for each simulation (e.g. years 250 – 259 for a simulation that lasted 259 years). To compute transmission and emission spectra, instantaneous snapshots were saved for each simulation, either every 5 days or every time step.

6.3 Results

6.3.1 Surface and atmospheric temperatures

Surface temperatures for selected simulations are shown in Fig. 6.6. The global mean surface temperatures for the TRAPPIST-1e simulations range from 219 – 232 K, which is well below the freezing temperature of water which is subjected to 1,000 hPa of surface pressure. All grid boxes have atmospheric temperatures

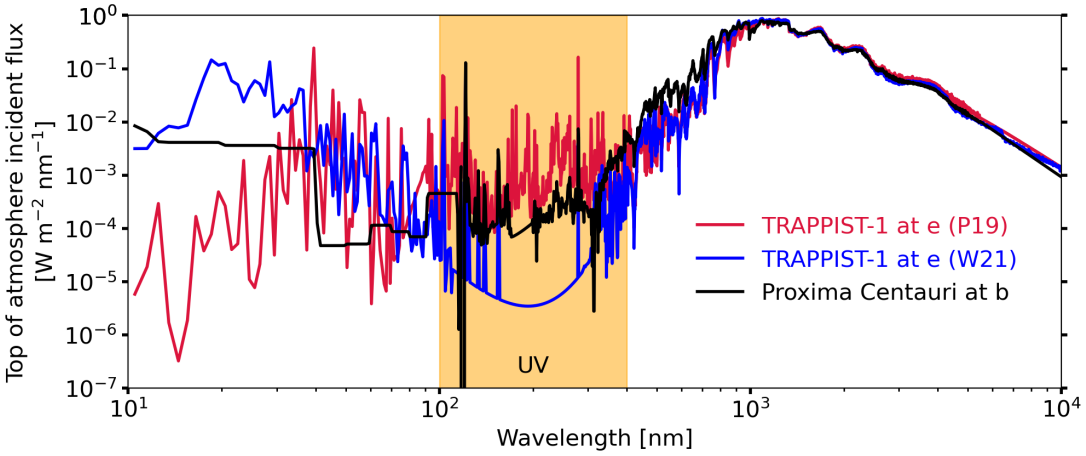

Fig. 6.5: The flux incident at the top of the exoplanetary atmosphere is plotted against wavelength for three separate stellar spectra. The shaded region indicates UV wavelengths (between 100 – 400 nm). Two of the spectra are scaled to the total instellation that TRAPPIST-1e receives (900 W m^{-2} which is 0.66 S_0). One of these is the P19 spectrum and is shown in red, and the other is the W21 spectrum which is shown in blue. In black, the Proxima Centauri spectrum is shown scaled to the total instellation that Proxima Centauri b receives (884 W m^{-2} which is 0.65 S_0).

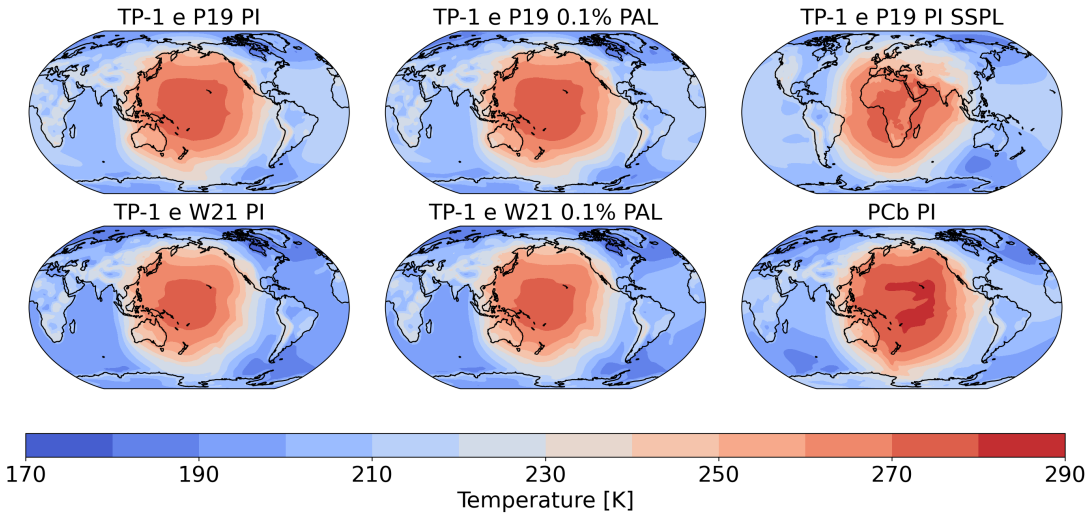

Fig. 6.6: The surface temperatures (in kelvin) for the TP-1 e P19 PI, TP-1 e P19 0.1% PAL, TP-1 e P19 PI SSPL, TP-1 e W21 PI, TP-1 e W21 0.1% PAL, and PC b PI simulations, are shown. A relatively warm region exists around the substellar point, which receives constant irradiation. The coldest surface temperatures can be found on the night side.

$>$ 159 K on time average, which is warmer than the coldest temperatures found in Earth's mesosphere (Lübken *et al.*, 1999). For Proxima Centauri b, the global mean surface temperature was 227.6 K.

When the substellar point is placed over land, the entire surface of the ocean has frozen over (as shown in Fig. 6.7). In the TP-1 e P19 spectrum tidally locked cases, when the substellar point is placed over ocean, there remains grid cells near the substellar point where the grid box sea ice fraction is less than 1 and open ocean is present. However, in the TP-1 e W21 cases, the ocean has fully frozen over. The PC b PI simulation has the largest area of open ocean.

Figure 6.8 shows the atmospheric temperature in the tidally locked simulations. When averaging globally, all tidally locked simulations have higher middle tropospheric temperatures than the global mean surface temperature. This is consistent with previous work (e.g. Boutle *et al.*, 2017) and is due to the lapse rate on the day side (decreasing temperature with altitude from the surface);

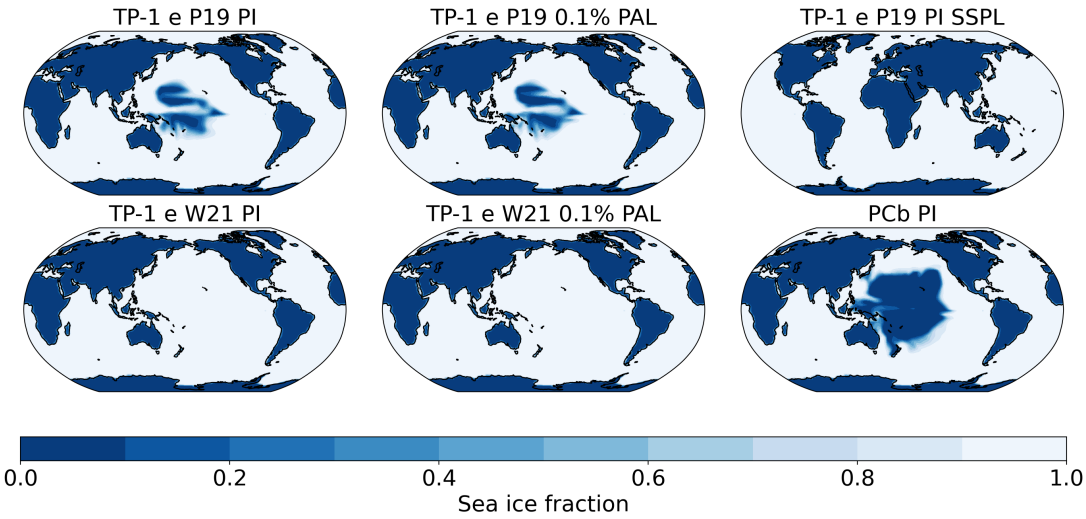

Fig. 6.7: The sea ice fraction for the TP-1 e P19 PI, TP-1 e P19 0.1% PAL, TP-1 e P19 PI SSPL, TP-1 e W21 PI, TP-1 e W21 0.1% PAL, and PC b PI simulations, is shown. In some simulations, open ocean remains, whilst in others, the entire surface is frozen over. The grid boxes which contain only land have snow and ice on them, but this is not indicated here because only sea ice is displayed.

meanwhile, the tropospheric jets carry heat to the night side and heat the middle troposphere but the night side surface remains much cooler. The surface exhibits an eastward hot spot shift of 7.5° in the TP-1 e P19 PI and TP-1 e P19 0.1% PAL simulations, −10.0° in the TP-1 e P19 PI SSPL simulation, and 10.0° in the PC b PI simulation, with no obvious eastward hot spot shift in all the other simulations.

6.3.2 Atmospheric dynamics

All tidally locked atmospheres from the WACCM6 simulations exhibit super rotation. This phenomenon was previously reported by many previous studies (Showman & Polvani, 2011; Showman *et al.*, 2013; Carone *et al.*, 2015, 2018; Chen *et al.*, 2019; Hammond *et al.*, 2020). The time-averaged zonal mean of the zonal winds and super rotation index are shown in Fig. 6.9. In each synchronously rotating atmosphere simulated here, there are super rotating equatorial winds all the way

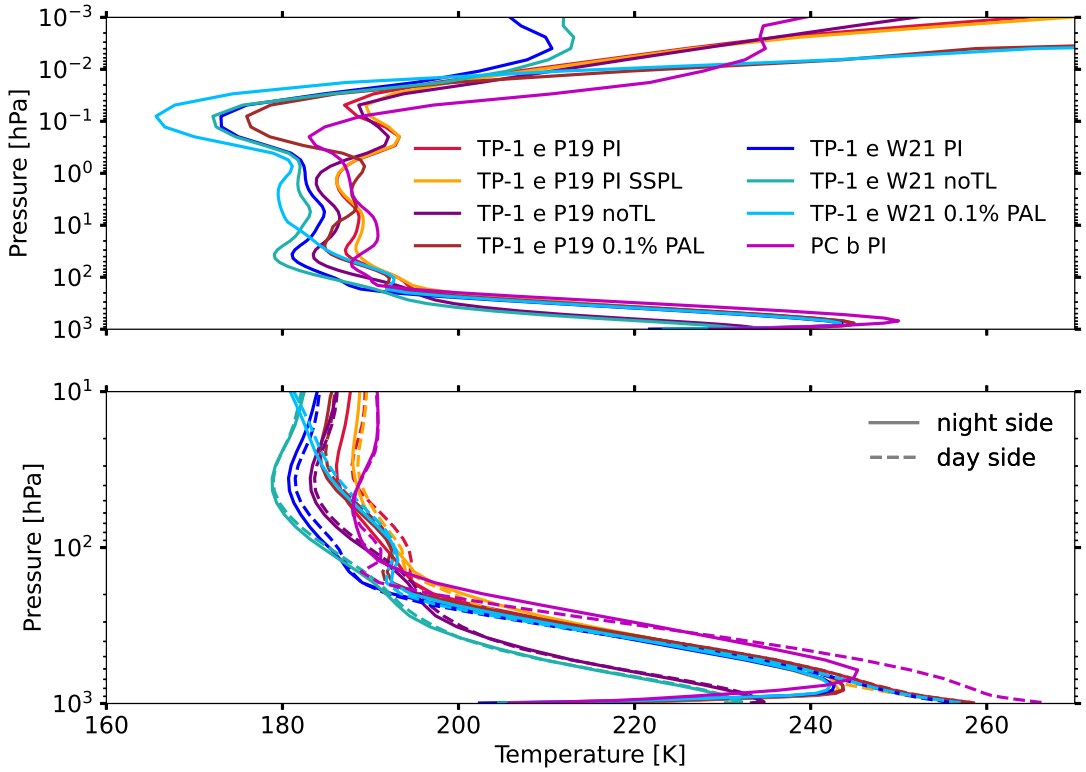

Fig. 6.8: This figure shows the global mean temperature profile (top) and the day side and night side (bottom) temperature profiles for the TP-1 e P19 PI (red), TP-1 e P19 PI SSPL (orange), TP-1 e P19 0.1% PAL (brown), TP-1 e P19 noTL (purple), TP-1 e W21 PI (blue), TP-1 e W21 noTL (turquoise), TP-1 e W21 0.1% PAL (cyan), and PC b PI (magenta) simulations. Note the different scale limits for pressure on the vertical axes. For the cases which have the substellar point over ocean, the day side profile (dashed line) is averaged over 180° longitude, and the night side profile (thick line) is averaged over 0° longitude. When the substellar point is over land, this is instead 30° longitude and 210° longitude, respectively.

from the troposphere to the thermosphere. The maximum zonal mean speed of the middle atmospheric jets for the Proxima Centauri b and TRAPPIST-1e simulations are 87 m s^{-1} and 71 m s^{-1}, respectively, compared with the typical maximum of approximately 60 m s^{-1} in Earth's stratosphere (Brasseur & Solomon, 2005; Waugh *et al.*, 2017). The maximum jet speeds occur between 30° and 70° in each hemisphere (with the Proxima Centauri b jets closer to the poles

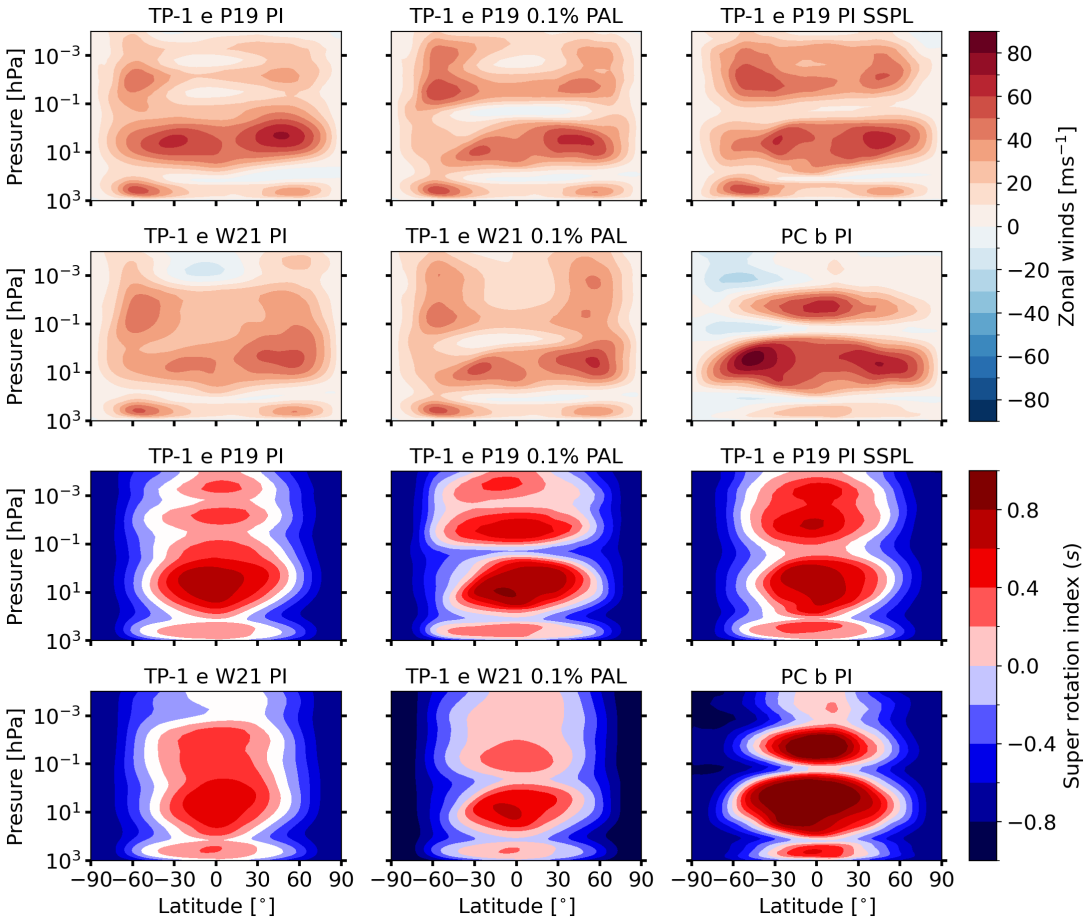

Fig. 6.9: This figure shows the time-averaged zonal mean of the zonal wind velocity in the top two rows, as well as the super rotation index s (see Eq. 6.2), in the bottom two rows. The TP-1 e P19 PI, TP-1 e P19 0.1% PAL, TP-1 e P19 PI SSPL, TP-1 e W21 PI, TP-1 e W21 0.1% PAL, and PC b PI simulations are shown. All simulations shown exhibit atmospheric super rotation (indicated by the red regions in the bottom two rows).

when compared to the TRAPPIST-1e simulations) and do not necessarily occur where the atmosphere is super rotating. This is because at higher latitudes, the specific angular momentum of the wind is reduced (see Eq. 6.1) when compared to the equator (where $\cos\phi = 1$).

Fig. 6.10 shows the meridional transport in the tidally locked cases compared to pre-industrial Earth case. The tidally locked cases exhibit two hemispheric cells

which transport air parcels from the substellar point to the poles. Transformation to tidally locked coordinates would actually show that the meridional transport is in fact from the substellar point to the antistellar point (Hammond & Lewis, 2021). The extent of the strong tropospheric meridional circulation ($\Psi > 10^{10}$ kg s^{-1}) is greater in the PC b PI simulation compared to the TRAPPIST-1e cases because of the weaker Coriolis force which is due to the slower rotation of Proxima Centauri b.

Sergeev *et al.* (2022b) used the UM to simulate simulate TRAPPIST-1e as an aquaplanet (slab ocean) with a N_2-dominated 1 bar moist atmosphere. They

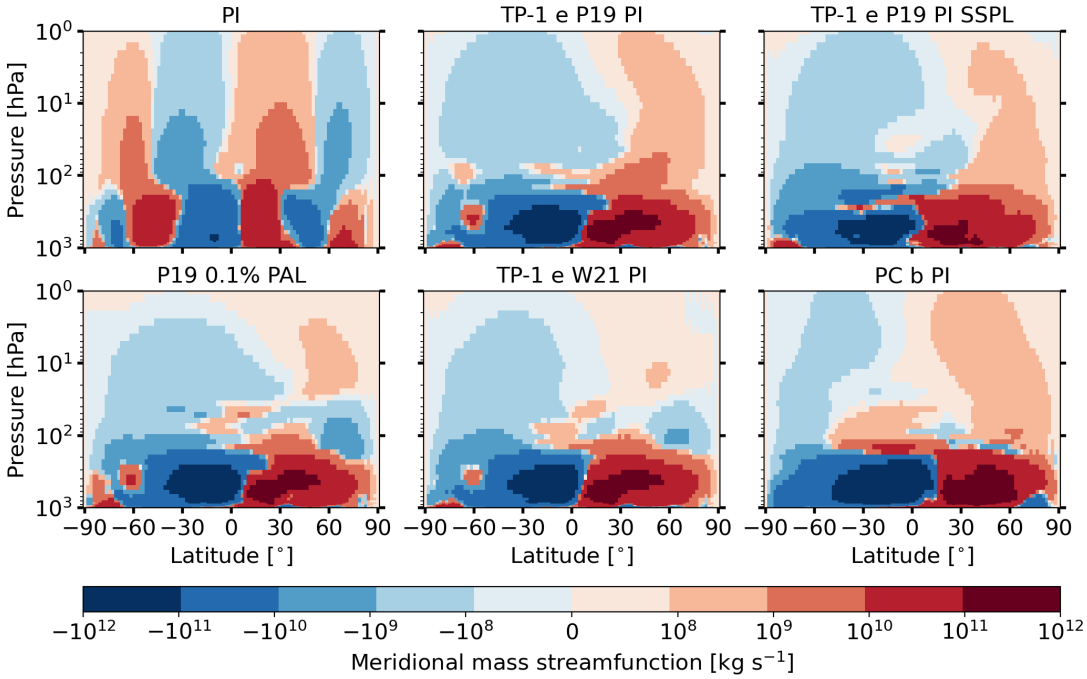

Fig. 6.10: The meridional mass streamfunction (Ψ; see Eq. 6.3) for selected tidally locked cases is compared to pre-industrial simulation for context. The tidally locked cases are the TP-1 e P19 PI, TP-1 e P19 PI SSPL, TP-1 e P19 0.1% PAL, TP-1 e W21, and PC b PI simulations. Red indicates large-scale clockwise rotation of air masses, and blue indicates anti-clockwise rotation. The three hemispheric cells (Hadley, Ferrel, and polar) seen in the PI case has changed to one hemispheric cell in each tidally locked case.

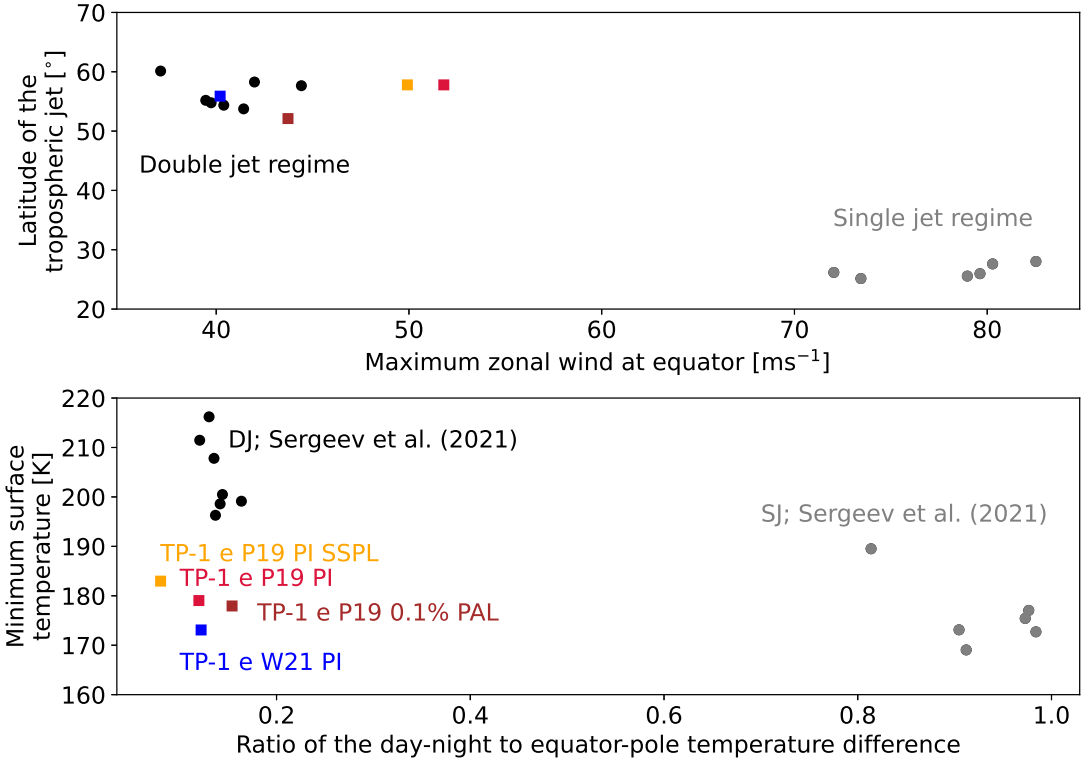

Fig. 6.11: The top panel shows the latitude of the tropospheric jet in ° (taken to be the latitude at which the maximum wind velocity in each hemisphere occurs at 400 hPa) plotted against the maximum zonal wind at the equator in m s^{-1}. The bottom panels shows the minimum surface temperature plotted against the ratio of the day-night to equator-to-pole temperature gradient. The day-night temperature difference is calculated by finding the mean tropospheric air temperature across the day side and subtracting the mean tropospheric air temperature across the night side. The equator-to-pole temperature difference is found by subtracting the zonally averaged tropospheric air temperature from $\pm(65° \mp 90°)$ from the zonally averaged tropospheric air temperature from $0° \pm 25°$. These calculations are performed as described in Sergeev *et al.* (2022b). WACCM6 results shown are for the TP-1 e P19 PI (red), TP-1 e P19 PI SSPL (orange), P19 0.1% PAL (brown), and TP-1 e W21 PI (blue) simulations. These simulations are shown alongside the results of Sergeev *et al.* (2022b), where the double jet regime is indicated by black circles, and the single jet regime is indicated in grey circles.

explored the atmospheric circulation response to several experimental choices, including the convection schemes implemented, and the initial temperatures.

Two distinct tropospheric circulation regimes existed in the simulations, with initial conditions responsible for their final dynamical state. The tropospheric circulation regime was demarcated by two parameters: (1) the latitude of the tropospheric zonal jet against the maximum zonal wind speed at 300 hPa at the equator, and (2) the minimum surface temperature against the ratio of the day-to-night equator-to-pole temperature difference. The 'double jet' and 'single jet' regimes in Sergeev *et al.* (2022b) show a distinct separation in this parameter space. The WACCM6 results do not overlap directly with the results from Sergeev *et al.* (2022b); in particular, the minimum surface temperature is up to 43 K colder in the WACCM6 simulations when compared to the UM simulations. Future work could test whether this is on account of the use of a slab ocean model or fully interactive ocean model. It can be seen that all simulated TRAPPIST-1e cases in this chapter are clearly in the 'double jet' regime (see Fig. 6.11), which makes sense when comparing with Fig. 6.9. All TP-1 e simulations were initialised as a pre-industrial control simulation. Therefore, it is possible that the WACCM6 simulations may have evolved to the single jet regime if different experimental conditions were applied.

Some simulations exhibit significant time variability in the atmospheric winds above the troposphere, resulting in periodic and transient winds that propagate downwards periodically, similar to Earth's QBO. This is shown in Fig. 6.12 for the last 40 years of data from the TP-1 e P19 PI SSPL, TP-1 e W21 PI, and PC b PI scenarios. These results are dissimilar to the LASO results from Cohen *et al.* (2022), who simulated the climate of Proxima Centauri b. For example, the oscillatory wind periods predicted here are 9 – 12 yr and 10 – 14 yr for the TP-1 e P19 PI SSPL and TP-1 e W21 PI simulations, respectively, which are both much longer than the $\sim$ 6 months in the Proxima Centauri b UM simulations by Cohen *et al.* (2022). For the PC b PI simulation, there is no downward propagation of

the wind field and there is no clear oscillatory period. Fig. 6.12 also displays time variability in the mixing ratios of O_3 and H_2O, confirming the variability in composition that Cohen *et al.* (2022) predicted may occur when using a 3D chemistry-climate model. Finding the cause of these temporally varying winds, including why differences exist between these results and those from Cohen *et al.* (2022), is left as future work. The periodic winds imply there may also be time variability in observations (which will be explored in the next Chapter).

6.3.3 Clouds and precipitation

As a consequence of constant stellar heating, upwelling is strong at the substellar point, with downwelling at the antistellar point. The upwelling and convection causes clouds to form on the day side. Fig. 6.13 shows the substellar point is covered by high clouds (clouds at pressures < 400 hPa). The shape of the high cloud distribution is significantly affected by the tropospheric jets. In the tidally locked simulations, clouds provide a positive climate forcing (between 9 – 13 W m^{-2} depending on the simulation) for the combination of both shortwave and longwave radiation, which results in a net warming of the exoplanet. This is in contrast to Earth, where clouds reduce the surface temperature by reflecting shortwave radiation, and warm the surface through trapping longwave radiation. Overall they contribute a net cooling effect of -24 W m^{-2} in the PI simulation (pre-industrial Earth case from Chapter 4).

Precipitation (snow and liquid) in the tidally locked cases occurs mainly over the substellar point, and overall is lower compared to the PI Earth simulation. For example, the globally-averaged convective precipitation rate of liquid and ice is between 21 and 188 times greater in the PI simulation compared to the tidally locked cases. This is to be expected because, despite high amounts of cloud cover around the substellar point in the tidally locked cases, the total cloud ice and

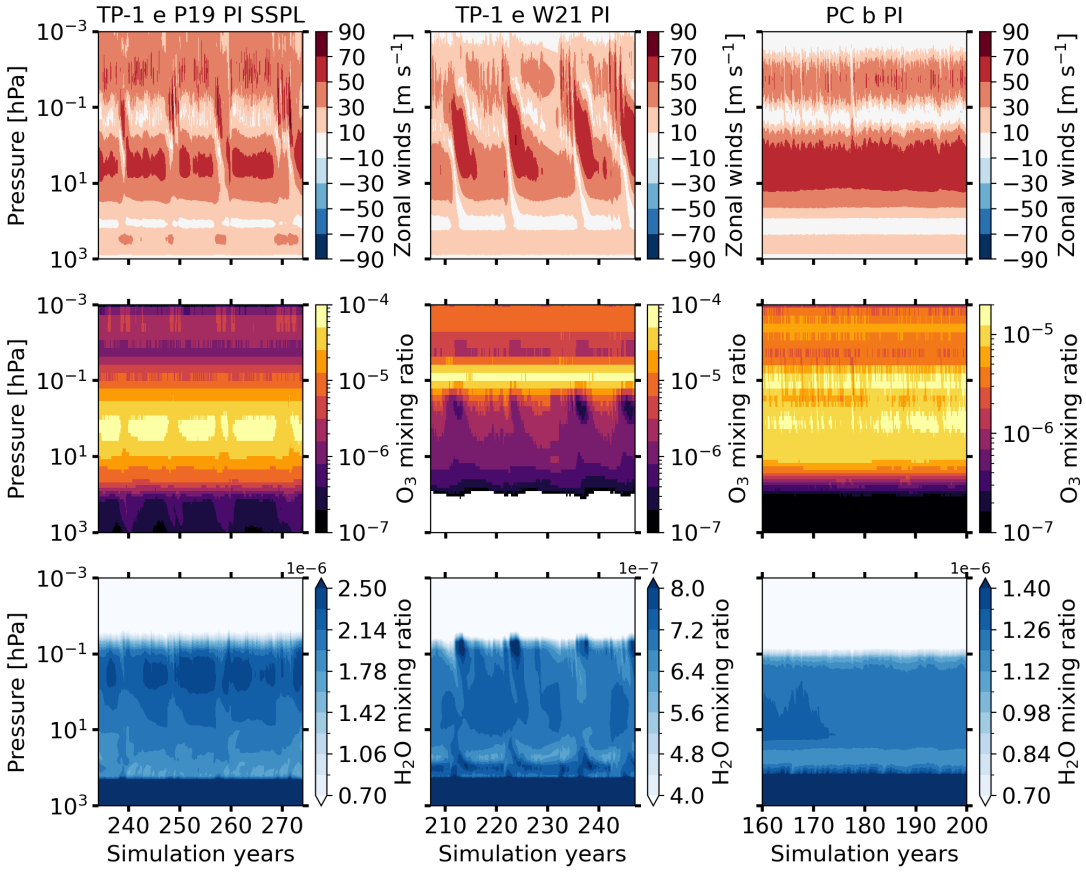

Fig. 6.12: In the top row, this figure shows how the zonal mean of the zonal wind velocity varies with pressure and time over the last 40 years of each scenario, for the TP-1 e P19 PI SSPL, TP-1 e W21 PI, and PC b PI simulations. The downward propagation of wind speed with time is analogous to the QBO that occurs on Earth. The middle row shows the time variability of the zonal mean O_3 mixing ratio, whilst the bottom panels show the time variability of the zonal mean H_2O mixing ratio (for these two rows, note the differing colour bar scales).

liquid water path is greater (due to warmer temperatures and hence increased evaporation rates) in the PI simulation and exists over a larger proportion of the surface.

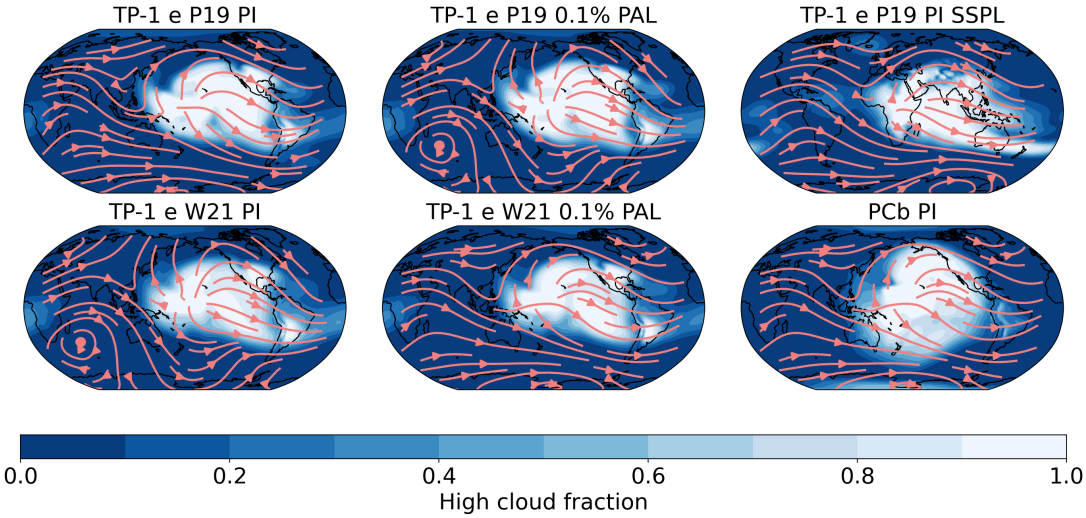

Fig. 6.13: The high cloud fraction for the TP-1 e P19 PI, TP-1 e P19 0.1% PAL, TP-1 e P19 PI SSPL, TP-1 e W21 PI, TP-1 e W21 0.1% PAL, and PC b PI simulations, is shown. High clouds are defined in the model as clouds at pressures < 400 hPa. Superimposed on top of the high clouds are atmospheric wind streamlines averaged between 275 hPa and 445 hPa. The winds significantly affect the distribution of the high clouds.

6.3.4 Composition

Fig. 6.14 shows the global mean vertical profiles for the mixing ratios of the following chemical species: $O, O_2, O_3, H_2O, CH_4, N_2O, OH, H$, and H_2. This figure includes all of the tidally locked simulations and the PI simulation for context. The O_3 mixing ratio profile shows large deviations between the TP-1 e P19 PI (red) and TP-1 e W21 PI (blue) simulations,. In terms of O_3 number density (not shown), the TP-1 e P19 PI and TP-1 e W21 PI simulations have a difference of a factor of 81 at the surface. The O_3 number density peaks at 1.26×10^{19} molecules m^{-3} in the TP-1 e P19 PI case and at 7.00×10^{17} molecules m^{-3} in the TP-1 e W21 PI case, both peaking at a pressure of 62 hPa. The TP-1 e noTL simulations (purple and turquoise) show that tidal locking increases the amount of O_3 in the middle atmosphere, whilst reducing the O_3 concentration

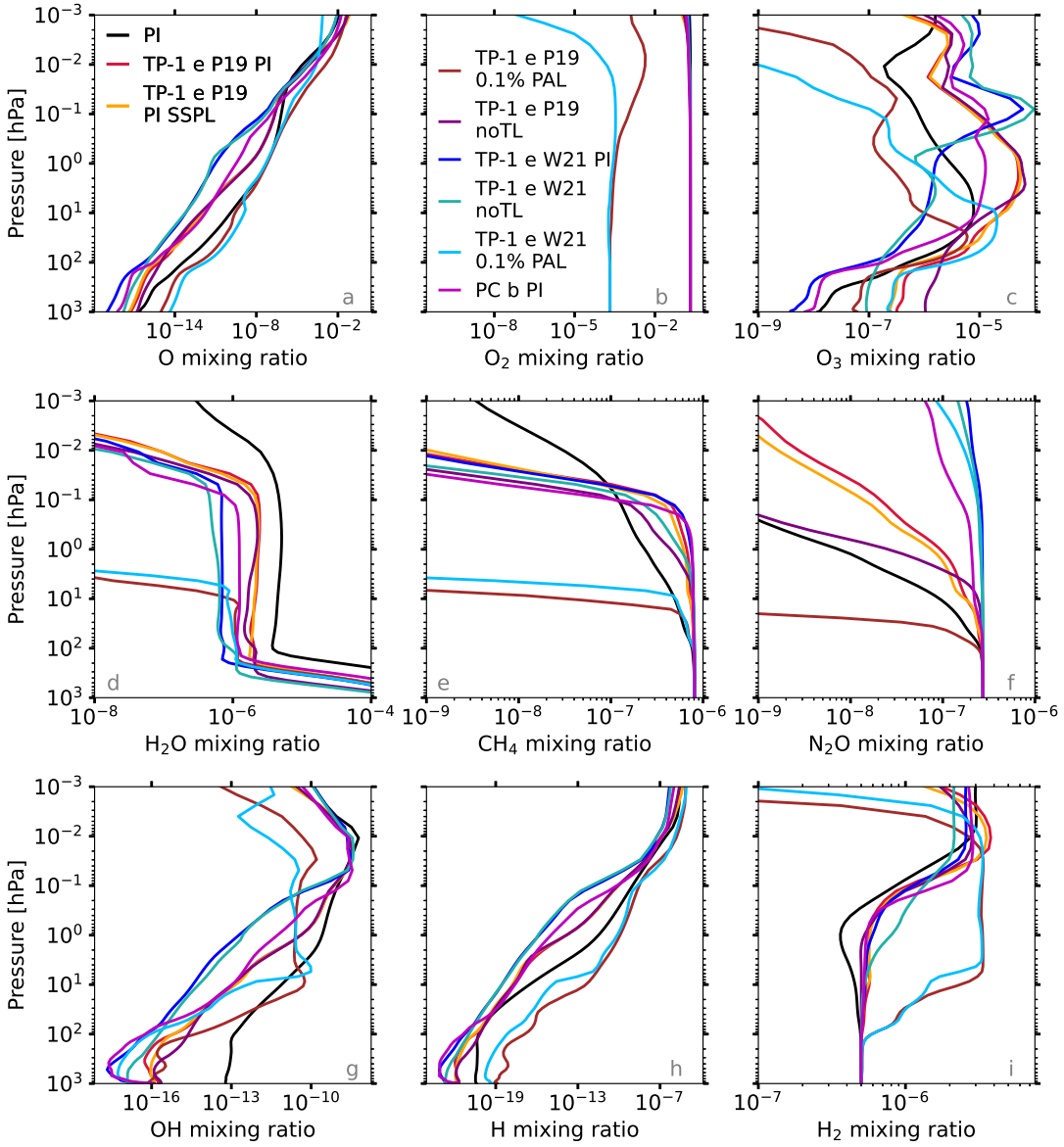

Fig. 6.14: The time-averaged globally-averaged volume mixing ratios for all of the simulations in Table 6.3 are plotted against pressure. The chemical species shown are O (*a*), O_2 (*b*), O_3 (*c*), H_2O (*d*), CH_4 (*e*), N_2O (*f*), OH (*g*), H (*h*) and H_2 (*i*). The colour scheme is the same as Fig. 6.8.

in the troposphere. Peak Ox ($O + O_3$) production from O_2 photolysis occurs at ≈ 0.01 hPa in the tidally locked cases that have an O_2 mixing ratio of 0.21, which is significantly higher in the atmosphere than where the peak O_3 concentration

occurs. Reducing O_2 by a factor of 1000 in the TP-1 e P19 0.1% PAL simulation (brown) decreases the O_3 number density because O_2 photolysis is the source of O_3 production and UV light that photolyses O_2 is able to penetrate to the surface. Remarkably, a 1000 times reduction in O_2 between the TP-1 e W21 PI and TP-1 e W21 0.1% PAL simulations increases the O_3 column by a factor of ≈ 24. This strange result occurs because of the interplay between O_3 production and optical depth for UV radiation. Whilst approximately the same amount of O is produced from O_2 photolysis in both the TP-1 e W21 PI and TP-1 e W21 0.1% PAL scenarios, more O_3 is produced when O_2 is lowered because the O is produced in denser atmospheric layers. This provides a greater availability of third bodies (M) such that reaction 2.16 proceeds quicker. A peak of the O_3 column at lower O_2 levels (e.g. 10% – 50% PAL) has been found by previous studies (e.g. Ratner & Walker, 1972; Kasting *et al.*, 1985; Kozakis *et al.*, 2022), but this is the first time such a large increase in O_3 has been predicted at the much lower O_2 concentration of 0.1% PAL.

Fig. 6.15 displays the longitudinal and latitudinal variation of the O_3 column for selected simulations. O_3 is inhomogeneously distributed, highlighting the important difference in results between 1D and 3D models. The P19 PI simulation has a global mean O_3 column of 1130 DU (almost 4 times Earth's global mean value of ≈ 300 DU, where 1 DU $= 2.687 \times 10^{20}$ molecules m^{-2}), whilst the W21 PI simulation predicts a global mean O_3 column of 52 DU. The O_3 column maxima, at 5378 DU and 126 DU for the P19 PI and W21 PI simulations, respectively, occur on the night side of the exoplanet, where O_3 is shielded from stellar UV light. The mean O_3 columns for the TP-1 e P19 PI SSPL, TP-1 e P19 0.1% PAL, TP-1 e W21 0.1% PAL, and PC b PI simulations are 1038 DU, 346 DU, 1238 DU, and 146 DU, respectively.

In the tidally locked scenarios when O_2 is at 1 PAL, CH_4 and N_2O have larger

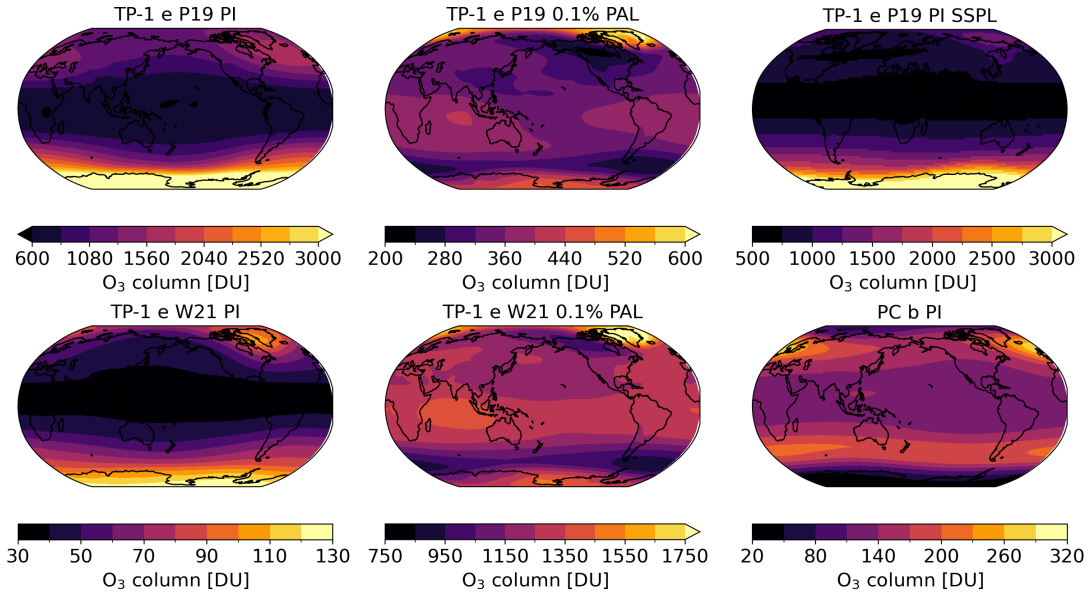

Fig. 6.15: The spatial distribution of the O_3 column (given in terms of Dobson Units) for the TP-1 e P19 PI, TP-1 e P19 0.1% PAL, TP-1 e P19 PI SSPL, TP-1 e W21 PI, TP-1 e W21 0.1% PAL, and PC b PI simulations, is shown. Note that each colour bar has a different scale. Yellow and orange contours indicate higher amounts of O_3 coverage, whilst purple and black indicate relatively lower O_3 coverage.

mixing ratios when compared to the PI simulation (Fig. 6.14). This is expected from previous modelling results due to the lower incident UV fluxes from M dwarf stars when compared to the Sun, which increases the photochemical lifetime of CH_4 and N_2O. For the same reason, O and H mixing ratios are generally reduced in the lower and middle atmosphere because there is less photochemical production from photolysis. Placing the substellar point over land or ocean has very little effect on globally-averaged chemical mixing ratios.

Generally, between 200 and 10 hPa, the relative H_2O mixing ratio in each simulation correlates with the relative temperature profile in each simulation (i.e. a lower temperature results in less H_2O). H_2O columns for some of the tidally locked cases are shown in Fig. 6.16. The globally-averaged total H_2O columns

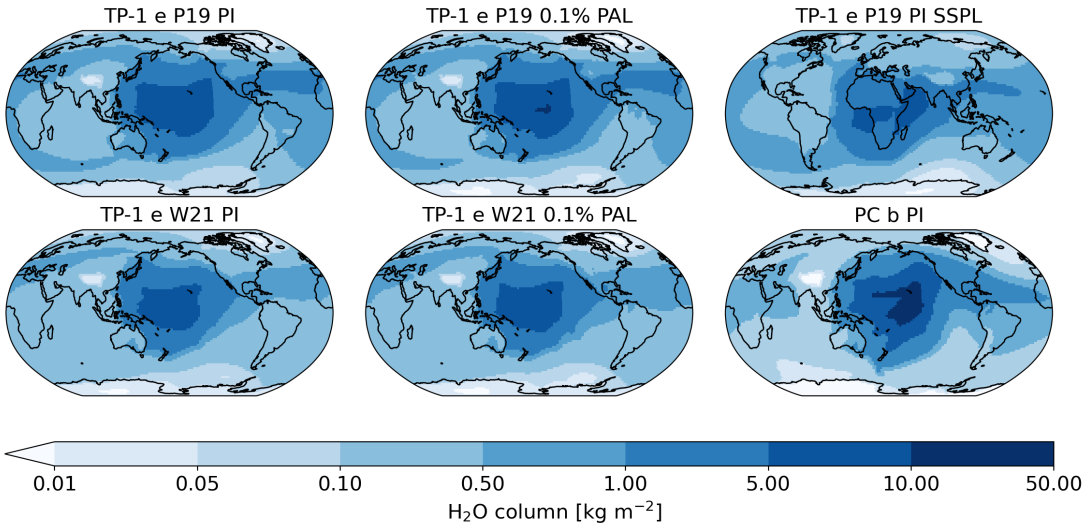

Fig. 6.16: The spatial distribution of the H_2O column (given in kg m^{-2}) is shown for the TP-1 e P19 PI, TP-1 e P19 0.1% PAL, TP-1 e P19 PI SSPL, TP-1 e W21 PI, TP-1 e W21 0.1% PAL, and PC b PI simulations. Larger columns are found near the substellar point which receives the most amount of irradiation. This causes convection and upwelling of air parcels, carrying the H_2O upwards.

are each lower by between 14.0 – 24.8 times when compared to the total H_2O column for the PI Earth, and the majority of the H_2O is located in the vertical columns close to the substellar point, rather than spread out across the rest of the planet. Away from the substellar point, the H_2O columns can be seen to trace the high latitude tropospheric jets which exist between $100 - 700$ hPa. There is a reduced atmospheric column of water vapour over the substellar point when the substellar point is placed over Africa, rather than the Pacific Ocean, indicating less evaporation.

6.4 Discussion

6.4.1 Habitability

The THAI series (Fauchez *et al.*, 2020a; Sergeev *et al.*, 2022a; Turbet *et al.*, 2022) investigated the climate of TRAPPIST-1e using four different 3D GCMs, assum-

ing either an N_2 or CO_2 dominated atmosphere and not including interactive chemistry, where the composition evolves depending on chemical and photochemical reactions. The surface temperatures obtained in the WACCM6 simulations are similar although slightly lower (219 – 232 K global mean compared to 230 – 240 K in the THAI simulations), which may be due to differences in assumptions regarding the surface (including the distribution of the continents and the fact that an interactive ocean is used here) or the composition of the atmosphere. The same is true for the 240 K mean surface temperature found for the Earth-like TRAPPIST-1e scenario from (Wolf *et al.*, 2017). The PC b PI surface temperatures are broadly consistent with the aquaplanet cases from Boutle *et al.* (2017) and Braam *et al.* (2022), although the range of temperatures is lower in the WACCM6 cases.

In all of the cases simulated here, there is still liquid water underneath the surface ice, which means each of the simulated exoplanets are still potentially habitable, just as Enceladus (a cold solar system moon orbiting Saturn) is potentially habitable because it has permanent liquid water under its icy surface. This result is for an initial PI atmospheric composition and is broadly consistent with the findings of Wolf (2017), who showed that larger amounts of atmospheric CO_2 may be able to increase the surface temperature and thaw parts of the ocean, at least near the substellar point. A similar conclusion can be reached for the PC b PI simulation, although there is a larger area of open ocean near the substellar point. This is due to increased meridional heat transport via a reduction in the Coriolis force (Proxima Centauri b rotates 1.8 times slower than TRAPPIST-1e).

Whilst it has been assumed that 1000 hPa surface pressure atmospheres are present on these exoplanets, it is noted that there have been atmospheric loss scenarios predicted for Proxima Centauri b and the exoplanets in the TRAPPIST-1 system (Dong *et al.*, 2017; Garcia-Sage *et al.*, 2017; Dong *et al.*, 2018). These have

shown how the stellar wind environment may swiftly erode atmospheres in time frames less than 1 Gyr, raising significant doubts over whether these exoplanets can retain atmospheres. Recently, TRAPPIST-1 b, the innermost exoplanet in the TRAPPIST-1 system, has been observed with JWST by Greene *et al.* (2023). The authors concluded that the secondary eclipse measurements were consistent with no atmosphere present on the exoplanet. Observations will ultimately be required to determine if HZ exoplanets are able to retain any atmospheres in these M dwarf systems. Interestingly, an atmosphere may not be needed at all for life to exist on a planet's surface: Abrevaya *et al.* (2020) demonstrated that some microbes (an archaeon species and a bacterium species) can survive flare-like fluxes in a vacuum. Nonetheless, this does not reveal whether life could emerge on such an exoplanet.

One potential problem for life is elevated surface O_3 concentrations. O_3 can cause oxidative stress and harm to plants and animals (Silva *et al.*, 2013; Avnery *et al.*, 2011; Squire *et al.*, 2014), with 40 ppbv for vegetation given as a critical limit above which crop yield and species biomass may be reduced (World Health Organization *et al.*, 2000). The World Health Organisation stated that significant health effects were exhibited by humans at 80 ppbv (World Health Organization *et al.*, 2000), with O_3 damaging lung function at 100 ppbv for 1 – 8 hours of exposure. The only simulations to exceed a 80 ppbv surface mixing ratio on global-average and time-average are the TP-1 e P19 PI and TP-1 e P19 PI SSPL simulations (316 ppbv and 243 ppbv, respectively). Areas near Canada and Greenland reach above 80 ppbv in the W21 0.1% PAL and P19 0.1% PAL simulations. Thus, depending on the O_2 concentration and incoming UV irradiation, some exoplanets may have harmful levels (at least for life as it has arisen on Earth) of O_3. Future work should use 1D models in order to narrow down the parameter space (in UV irradiation, composition, and atmospheric pressure) for

which detrimental levels of surface level O_3 may occur, before utilising 3D models to predict where surface O_3 concentrations maximise. For example, it is hypothesized that atmospheres with lower pressures and high O_2 mixing ratios will have an O_3 layer closer to the surface, resulting in potentially dangerous levels of O_3 for several known species.

6.4.2 Clouds

As cloud physics is one of the largest unknowns in planetary and exoplanetary science, and numerical models differ in their treatment of clouds (e.g. see the recent GCM intercomparison by Fauchez *et al.*, 2021), understanding the differences between models is paramount to predicting observational states and habitability conditions. As reported in many other studies, strong upwelling caused by continuous heating of the substellar point causes air to rise and cool adiabatically, forming clouds high in the atmosphere (Wolf, 2017; Chen *et al.*, 2019). These high clouds (between 400 and 50 hPa) also modulate the albedo of the exoplanet. The atmosphere component of CESM2 has undergone modifications to physical parameterizations since CESM1, and the only component left untouched was the radiative transfer module (Gettelman *et al.*, 2019a; Bacmeister *et al.*, 2020). WACCM6 from CESM2 utilises a state of the art cloud scheme which is different from WACCM6 in the previous iteration of CESM1, with CESM2 more closely producing the climate of the Earth than CESM1. Thus, it is unsurprising to see differences in the simulations here compared to ExoCam (Wolf, 2017), and previous work that has used CESM1 (Proedrou & Hocke, 2016; Proedrou *et al.*, 2016; Chen *et al.*, 2018, 2019). Differences with other models are naturally expected, and detailed intercomparisons are required to fully understand the discrepancies in calculated parameters.

For instance, when comparing to the moist cases from the THAI papers

(Sergeev *et al.*, 2022a), whilst a large amount of the exoplanet is covered in clouds, the distribution seen in the WACCM6 simulations here, as well as the total cloud water path, is markedly different from the UM, ExoCam, ROCKE-3D, and LMD-G results. This is likely due to three reasons: the moist physics parameterisations between the models are different; the resulting tropospheric dynamics are all different; and the THAI cases use an aquaplanet, whilst the simulations here use Earth's land and ocean configuration.

The closest simulations to the work presented here with WACCM4 where cloud coverage is shown are the 10F26T and 11F30T simulations in Chen *et al.* (2019), which have rotational periods of 4.41 d and 7.91 d, respectively, with total instellation of 1 S_0 and 1.1 S_0, respectively. There are some important differences in high clouds; notably, the Chen *et al.* (2019) simulations have high cloud coverage on the night side. This difference may be in part due to their use of a slab ocean with no heat flux and higher instellations. However, the approximate distribution of the high clouds east of the substellar point is similar, and they also demonstrate a greater latitudinal width of the high cloud coverage as rotational period increases, which is seen here when comparing between the TRAPPIST-1e and Proxima Centauri b scenarios. This shows that major cloud features are similarly produced despite different moist physics schemes.

6.4.3 Composition

The O_3 distribution in tidally locked exoplanet simulations is highly influenced by the incoming stellar radiation and atmospheric transport. The 10F26T and 11F30T simulations from Chen *et al.* (2019) were for Earth-sized exoplanets around late M dwarf stars with stellar effective temperatures of 2600 K and 3000 K, respectively. Chen *et al.* (2019) found that O_3 mixing ratios were confined to the equator, demonstrating that in simulations of terrestrial exoplanets with a

period of < 25 days, an anti-Brewer-Dobson circulation would restrict air masses to the equator and photochemically produced species would not be transported to the poles, just as Carone *et al.* (2018) had predicted. Interestingly, the WACCM6 simulations here for TRAPPIST-1e show that although high O_3 mixing ratios are near the tropics, the highest O_3 number densities, and thus total columns, are found near the high latitudes and poles. This can be explained by the single equatorial jet in the stratosphere from the work of Chen *et al.* (2019), whereas the TRAPPIST-1e simulations in WACCM6 have two high latitude stratospheric jets, as does the troposphere. The simulations here use a lower instellation than Chen *et al.* (2019), different stellar input spectra, were run out for much longer, and used an interactive ocean with heat transport, all of which likely give rise to the differences in chemical transport. Additionally, taking a time average for O_3 can be misleading because the location of the O_3 column maxima move depending on which time step frame is examined (e.g. see Fig. 6.12).

The UM Proxima Centauri b simulations from Yates *et al.* (2020) produced larger quantities of O_3 than the WACCM6 simulations here, seemingly because they only included Chapman and HOx chemistry for O_3 destruction, as well as a different stellar spectrum. Braam *et al.* (2022) used the UM and included NOx chemistry, and updated the Proxima Centauri spectrum to the MUSCLES spectrum. The O_3 layer peaked at 40 km in their simulations, as opposed to at 20 km in the WACCM6 simulations. This is presumably in part due to the differences in gravitational constants (g) used, with 10.9 m s^{-2} used in Braam *et al.* (2022) and 12.2 m s^{-2} used here. Assuming a larger g, the scale height (H) decreases, meaning that the number density at an altitude of 30 km for instance, will be lower. Therefore, this explains why the peak O_3 number density in the WACCM6 simulations occurs closer to the surface.

Lightning flashes produce nitrogen oxides (NOx = NO + NO_2; Murray, 2016)

and the resulting high temperatures are able to thermally decompose O_2 (Chameides, 1986) to produce NO via the overall reaction $N_2 + O_2 \longleftrightarrow 2\,NO$. Braam *et al.* (2022) found greater amounts of atmospheric NO and NO_2 on the day side in their Proxima Centauri b simulations because of NO production following lightning flashes, whilst NO_3 was found in greater quantities on the night side. Quantitatively, the results are not exactly the same, but the WACCM6 PC b PI simulation follows a similar trend, exhibiting lightning flashes (not shown) that occur predominantly near the substellar point, and less frequently than on Earth. The TP-1 e P19 PI SSPL scenario, where the substellar point was placed over land, had simulated flashes occurring in greater frequency than when the substellar point was placed over ocean.

Both TRAPPIST-1 and Proxima Centauri are expected to flare frequently (Vida *et al.*, 2017; Davenport *et al.*, 2016). Chen *et al.* (2021) tested the impact of flares on the atmospheres of terrestrial exoplanets around G, K and M dwarf stars, using WACCM4 with time dependent changes to UV irradiation and energetic particle flux associated with both flares and coronal mass ejections. They determined that stellar flares disrupt the equilibrium chemistry on K and M dwarf terrestrial exoplanets, whereas G dwarf terrestrial exoplanets will swiftly revert (e.g. nitric oxide on a timescale < 50 days) to pre-flare chemical profiles. Future work could use WACCM6 and the climate configurations discussed here to perform similar experiments to Chen *et al.* (2021).

6.5 Conclusions

In the tidally locked simulations presented in this Chapter, Proxima Centauri b and TRAPPIST-1e receive total instellations which are within 2% of each other (884 W m^{-2} versus 900 W m^{-2}). Thus, the major differences in the simulation results for these two exoplanets arises from the UV irradiation spectral shape (which

affects O_3 and atmospheric heating), gravitational acceleration (which affects dynamics and the atmospheric scale height), and rotation rate which modifies the Coriolis force (affecting dynamics).

The simulations presented here show key differences with previous work that has simulated Proxima Centauri b and TRAPPIST-1e for several parameters including surface temperatures, the atmospheric temperature structure, dynamics, and clouds. This work shows that these exoplanets could provide liquid water in subsurface oceans, making them potentially habitable. Yet, too little is known about these exoplanets and their potential atmospheres to make robust conclusions about the climates of these exoplanets (or their habitability) at the present time.

There are several more specific differences in cloud coverage (spatial and vertical extent) and chemical composition (e.g. O_3 and H_2O columns) which will affect the direct imaging spectra and transmission spectra of these exoplanets. The work presented in this Chapter demonstrates that chemistry-climate simulations produce climate states which are expected to lead to observational predictions with time variability. This has implications for future observations that will be made with the extremely large class of telescopes, and with JWST.

Chapter 7

Synthetic TRAPPIST-1e spectra

7.1 Introduction

To begin the processes of characterising the TRAPPIST-1 system exoplanets and determining the composition of any atmospheres present, several observational programs with JWST are scheduled at the time of writing, including the observation of four transits of TRAPPIST-1e in 2023 (see program 1331[1]).

In general, the detection of O_2 on an exoplanet is of profound interest because of its importance for life on Earth (Segura *et al.*, 2003; Meadows *et al.*, 2018b). It has been calculated that in some situations the detection of O_3 is easier to achieve than a detection of O_2; for example, for low O_2 concentrations like those potentially present during Earth's Proterozoic eon, but where O_3 concentrations are still detectable (Kozakis *et al.*, 2022). Thus, in such cases, it has been proposed that the detection of O_3 may be used as a proxy to confirm the presence of O_2 (Leger *et al.*, 1993; Segura *et al.*, 2003; Meadows *et al.*, 2018b; Quanz *et al.*, 2021; Kozakis *et al.*, 2022).

One-dimensional (1D) photochemical modelling has demonstrated that planetary atmospheric composition (including O_3 and H_2O) is influenced by the

[1] https://www.stsci.edu/jwst/science-execution/program-information.html?id=1331, accessed Wed April 12 2023

strength and shape of the incoming ultraviolet (UV) radiation from the host star (e.g. Grenfell *et al.*, 2014; Rugheimer *et al.*, 2013; Kozakis *et al.*, 2022; Meadows *et al.*, 2018b, and references therein). Because the atmospheric composition with respect to altitude affects molecular detectability in remote sensing, the link between O_3 abundance and O_2 abundance will be difficult to ascertain because it depends on several parameters, including the catalytic cycles that remove O_3, and atmospheric pressure. A well-characterised spectrum of the host star is required for confident modelling of planetary climate (Eager-Nash *et al.*, 2020), atmospheric chemistry (Kozakis *et al.*, 2022), and atmospheric escape (Dong *et al.*, 2018). However, the host star's SED may not be known to high precision when analysing exoplanet observations.

In addition to the incoming spectrum, the 3D transport and chemistry of the exoplanet is important for understanding the distribution and abundance of chemical species. Proedrou & Hocke (2016), Chen *et al.* (2018) and Yates *et al.* (2020) found that O_3, which is photochemically generated on the dayside, can be transported to the night side, where its lifetime increases due to the lack of UV irradiation and a reduction in catalytic cycle destruction. This previous work motivates the need to use 3D models when investigating the climate and chemistry of specific exoplanets, in particular, with respect to their molecular observability linked to the oxygenation state of the atmosphere.

In this Chapter, possible future observations (transmission and emission spectra) of TRAPPIST-1e are simulated using the outputs from the WACCM6 simulations presented in the previous Chapter. This Chapter discusses how uncertainties in the stellar UV spectrum has implications for the interpretation of future observations of terrestrial exoplanets. Also considered are the potential methods for removing ambiguities in derived atmospheric composition for the cases where the host star's spectrum is not well characterised.

The Planetary Spectrum Generator (PSG; Villanueva *et al.*, 2018) GlobES[1] 3D mapping tool is used to compute transmission and emission spectra from the WACCM6 atmospheric simulations presented in the previous Chapter. The methods used to do so are the same as in Chapter 5.

7.2 Results

7.2.1 Transmission spectra

Fig. 7.1 shows idealised transmission spectra between 0.1 – 18 µm generated using the WACCM6 simulations with PSG. The model date chosen for the transit is arbitrary; whilst time variability in transmission spectra is investigated in Section 7.2.2, Fauchez *et al.* (2022) showed that such variability is within the measurement uncertainties of JWST. The spectra are binned to approximate a resolving power of $R = 250$ to show detail in spectral features, where $R = \lambda/\Delta\lambda$, λ is the wavelength, and $\Delta\lambda$ is width of the wavelength bin. Error bars corresponding to the lowest achievable noise with JWST are indicated. The lowest achievable noise is the noise floor of each instrument, which may be between 5 – 20 ppm as calculated by Matsuo *et al.* (2019), Schlawin *et al.* (2020), Schlawin *et al.* (2021), and Rustamkulov *et al.* (2022).

The differences in the effective altitude of O_3 spectral features between the P19 PI (red) and W21 PI (blue) transmission spectra are −3 km, +20 km, +16 km, and +20 km for the 0.3 µm, 0.6 µm, 4.7 µm, and 9.63 µm O_3 features, respectively. Despite the W21 PI simulation having an O_3 column ≈ 22 times lower than the P19 PI simulation, the W21 PI UV feature (centred at 0.25 µm) due to the Hartley band (0.2 – 0.31 µm) actually has the largest effective altitude of all the simulations between 0.2 – 0.3 µm. This is because the Hartley band saturates quickly and the W21 PI atmosphere has more O_3 molecules than the

[1] https://psg.gsfc.nasa.gov/apps/globes.php

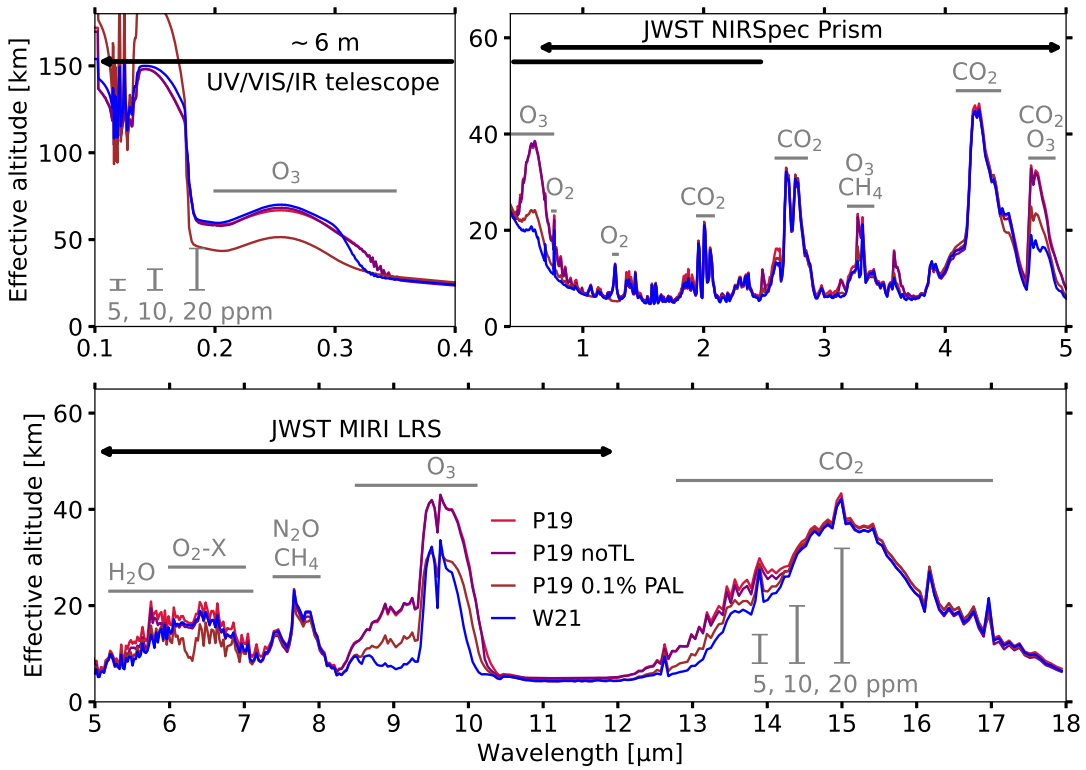

Fig. 7.1: The transmission spectrum atmospheric effective altitude is plotted against wavelength between 0.1 µm and 18.0 µm for the TP-1 e P19 PI (red), TP-1 e P19 noTL (purple), and TP-1 e P19 0.1% PAL (brown) simulations, and for the W21 PI simulation (blue). The spectra are split up into three wavelength regions, 0.1 – 0.4 µm (*a*), 0.4 – 1.0 µm (*b*), and 1.0 – 18.0 µm (*c*) The spectra are binned to a spectral resolving power of $R = 250$. Spectral features are indicated in grey. The wavelength range of the proposed ∼ 6 m UV/VIS/IR telescope, and that of the JWST NIRSpec and JWST MIRI instruments, are shown. Grey error bars represent the uncertainty that would be present on a measurement that has reached the noise floor of the instrument, where the noise floor is indicated as either 5 ppm, 10 ppm, or 20 ppm. Note these error bars are estimates of the performance of the telescope and do not indicate estimated measurements.

P19 PI atmosphere above ≈ 0.5 hPa. Between 0.3 – 0.35 µm, the temperature dependence of the Hartley and Huggins bands reduces the effective altitude of the W21 PI transmission spectra due to the colder middle atmosphere in the W21 PI simulation. At 0.6 µm, a significant detection of O_3 with JWST in the

W21 PI simulation scenario would be improbable given that the noise floor is larger than the height of the feature. Therefore, assuming that the W21 spectrum is closest to the true spectrum of TRAPPIST-1, or the case that the true stellar UV emission is weaker, a null detection of the 0.6 µm O_3 feature should not rule out the presence of O_2 abundances at levels as high as the present-day Earth. For H_2O, the spectral features are stronger in the TP-1 e P19 PI transmission spectra compared to TP-1 e W21 PI by up to 5 km which is a result of a larger number density of H_2O in the middle atmosphere. Despite the difference in temperature and O_3 number density profiles between the TP-1 e P19 noTL simulation (purple) and the TP-1 e P19 PI (red) simulation, the transmission spectra are remarkably similar (within ±2.5 km longward of 0.2 µm). The TP-1 e P19 0.1% PAL transmission spectrum (brown) produces a quantitatively similar transmission spectrum feature at 9.63 µm to the TP-1 e W21 PI simulation (blue), even though there is a 1000 times difference in O_2 mixing ratio between the two cases. There is a noticeable difference between the spectra at 4.8 µm and 9 µm, but this would require reaching the most optimistic 5 ppm noise floor in order to show the two O_2 scenarios are not consistent with each other when there exist alternative stellar UV flux estimates. Also note that the effective altitude of the O_2–X collision induced absorption feature at 6.4 µm (see Fauchez *et al.*, 2020b, for more details) is 7 km shallower when O_2 is at 0.1% PAL.

7.2.2 Time variability in transmission spectra

Climates and composition vary in atmospheres as time changes, such that one may expect to observe temporal changes in atmospheric observations when revisiting targets. Time variability in transmission spectra was assessed by producing theoretical transmission spectra every 6 model months for 20 years (40 transmission spectra simulations total), in the TP-1 e P19 PI, TP-1 e P19 PI SSPL,

TP-1 e P19 W21 PI, and TP-1 e P19 0.1% PAL simulations. The maximum differences in effective altitude between any two spectra for selected spectral features (O_2, O_3, and H_2O) from the same simulation is shown in Table 7.1. The maximum variability is exhibited in the TP-1 e W21 PI scenario, and is 0.3 km and 2.3 km in effective altitude for O_3 features at 3.3 µm and 9.0 µm respectively, and 0.1 km for H_2O at 6.50 µm. Thus it seems that the dynamical fluctuations shown in Fig. 6.12 could influence the observed transmission spectra due to its impact on O_3 and H_2O concentrations, albeit through relatively small changes to the feature depths which will be undetectable with JWST. A full analysis would require transmission spectra simulations every 6.1 days from $\sim$ 20 Earth years of model data (in order to cover more than one oscillatory wind period), which is a significant undertaking ($\sim 1,200$ radiative transfer simulations per scenario) and beyond the scope here.

Table 7.1: Transmission spectra were produced in PSG every 6 months for the last 20 years of data in each simulation (40 transmission spectra simulations in total). This was for the TP-1 e P19 PI, TP-1 e P19 PI SSPL, TP-1 e P19 0.1% PAL, and TP-1 e W21 PI simulations. The maximum effective altitude differences (in km) are given for the O_2 0.76 µm, O_2 0.76 µm, O_3 3.3 µm, H_2O 5.8 µm, and O_3 9.63 µm, features.

Spectral feature	Maximum effective altitude variability [km]			
	TP-1 e P19 PI	TP-1 e P19 PI SSPL	TP-1 e P19 PI 0.1% PAL	TP-1 e W21 PI
O_2 (0.76 µm)	0.4	0.4	0.4	0.2
O_3 (3.30 µm)	0.3	0.3	0.2	0.3
H_2O (6.50 µm)	0.3	0.3	0.1	0.1
O_3 (9.0 µm)	1.3	1.2	0.9	1.6
O_3 (9.63 µm)	0.6	0.5	0.3	2.3

7.2.3 Emission spectra

Fig. 7.2 shows the emission spectra from each simulation for the atmospheric absorption O_3 features at 4.71 µm and 9.63 µm at 90° orbital phase (the maximum planet-star separation as viewed in an edge-on system with a circular orbit). The 4.71 µm feature overlaps with a CO_2 feature, but O_3 is the dominant absorber at 4.71 µm. The P19 PI simulation (red) predicts higher O_3 columns than the W21 PI case (blue); hence, the depth of the features relative to the continuum in the W21 PI case are weaker than the P19 PI scenario by a factor of 23.4 and 6.2 at 4.71 µm and 9.6 µm, respectively. With respect to the P19 PI emission spectrum (red), the P19 0.1% PAL emission spectrum (brown) has a greater depth by a factor of 2.1 at 9.6 µm and a similar depth at 4.71 µm, even though it has a mean O_3 column which is 3.3 times lower (1130 DU vs 346 DU).

The P19 noTL simulation (purple) has the deepest O_3 emission spectral features due to two major differences: the temperature difference between the surface and absorbing region (middle atmosphere) is larger; and, the tidally locked simulations exhibit strong convection and high clouds around the substellar point, whereas the P19 noTL simulation has mainly low clouds with comparatively little high cloud coverage.

7.2.4 Time variability in direct imaging spectra

As shown by previous work, flux variations during the phase curve are expected (Selsis *et al.*, 2011; Koll & Abbot, 2015; Kreidberg *et al.*, 2019) because various fractions of the illuminated face of the exoplanet are revealed to the observer as the exoplanet orbits its star, in addition to the presence of any hot spot shift. Fig. 7.3 shows the time variability present for the reflection and emission spectra (separate panels) from the TP-1 e P19 PI and TP-1 e W21 PI simulations, when all the spectra were predicted assuming a phase of 90° (at quadrature). What this

figure demonstrates is that there is observational variability in terms of the planet-to-star flux ratio which is independent of the phase curve, and independent of the angle that the observer views from. Between 0.1 µm and 2.5 µm, the TP-1 e P19 PI simulation has a maximum temporal variability of 48% (occurring at 0.6 µm) in planet-to-star flux ratio, whilst the TP-1 e W21 PI shows up to 43% variation (the maximum occurring at 2.0 µm). Between 5 µm and 18 µm, the TP-1 e W21 PI simulation exhibits a maximum of 10% variation in planet-to-star flux ratio (occurring at 7.5 µm), whilst the TP-1 e P19 PI scenario has a maximum of 8% variation. The variation occurring for the CO_2 15 µm feature is $< 1\%$. Therefore, the expected temporal variation in the mid-infrared (5 – 30 µm) is lower than for the visible (0.4 – 0.75 µm) and near-infrared (0.75 – 5 µm) wavelengths.

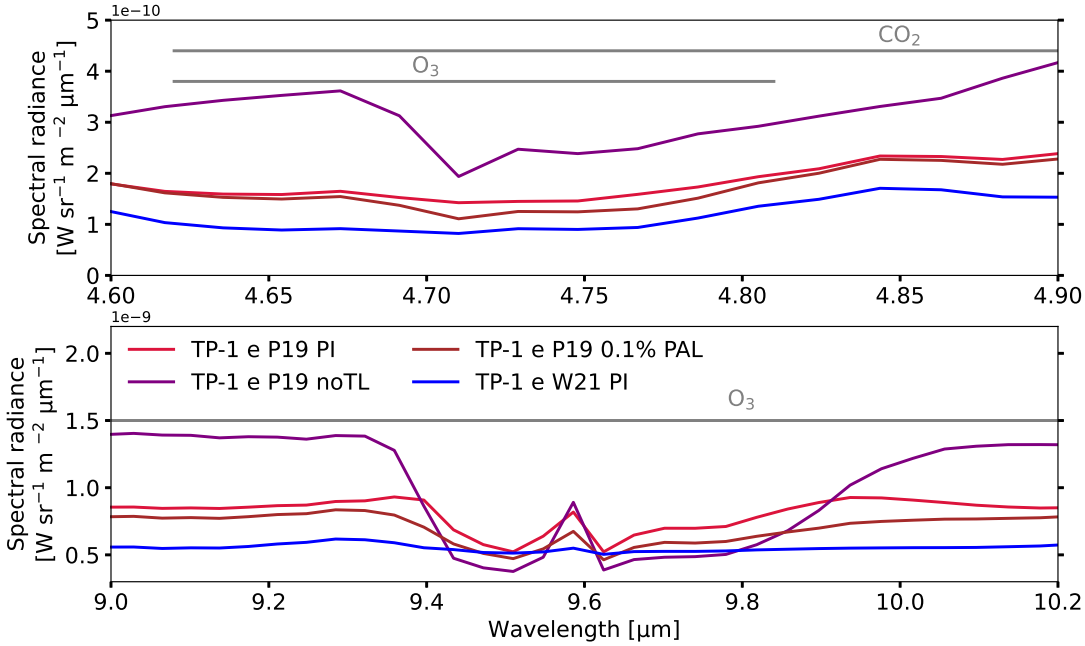

Fig. 7.2: The top panel shows the PSG simulations of planetary spectral radiance from emission spectra focused on the 4.71 µm O_3 feature (which overlaps with a CO_2 feature) for the P19 PI (red), P19 noTL (purple), P19 0.1% PAL (brown), and the W21 PI simulations (blue). The bottom panel shows the same for the 9.6 µm O_3 feature.

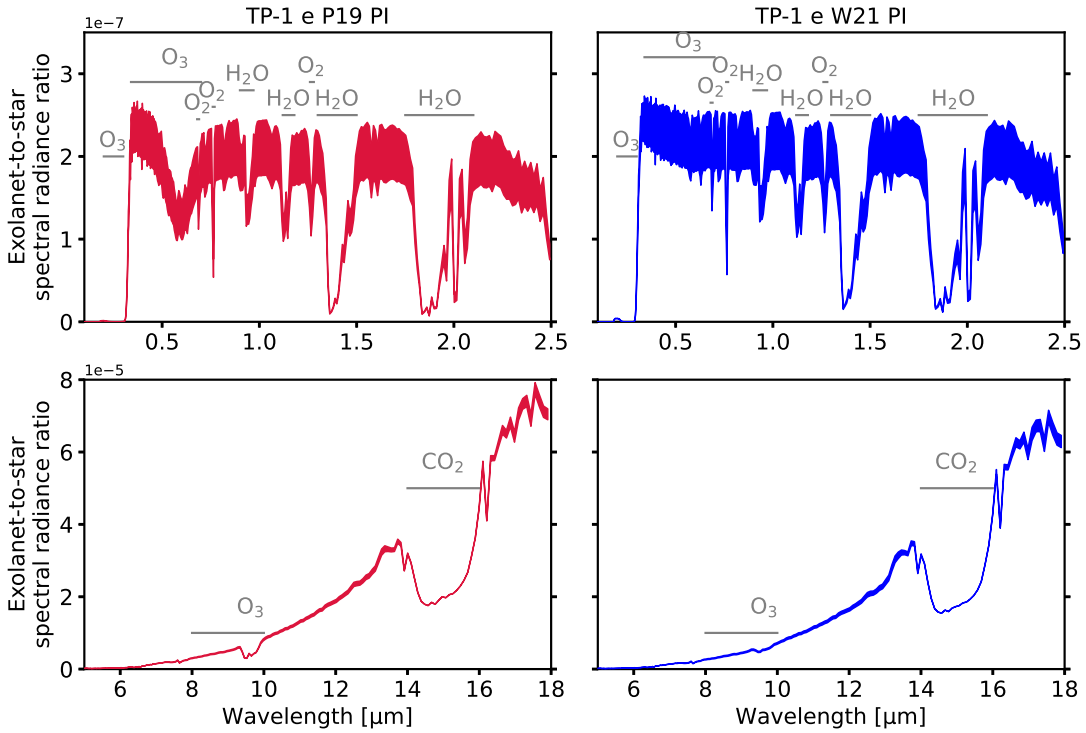

Fig. 7.3: Both reflection spectra and emission spectra were computed at every time step during 6.1 model days (a single orbit for TRAPPIST-1e) and shown at an orbital phase of 90°, meaning that this figure does not represent the observational variability during a full phase curve. The variation in reflection spectra taken between 0.1 – 2.5 µm ($R = 150$) are displayed in the top panels, and the variation in emission spectra taken between 5 – 18 µm ($R = 250$) are shown in the bottom panels for the TP-1 e P19 PI (red, left) and TP-1 e W21 PI (blue, right) simulations. The maximum flux and minimum flux from each simulation is plotted, and the range is filled in between these two lines.

It is important to note that other orbital phases may show quantitatively different results because variability in spectral features may occur due to the fraction of clouds, land and ice that can be seen from various observer angles (e.g. Chapter 5). Additionally, longer term variations may be expected due to the possible presence of a LASO or other oscillatory dynamics.

7.3 Discussion

7.3.1 Temporal variability in observations

Temporal variability was assessed for TRAPPIST-1e by May *et al.* (2021), who used ExoCam and varied partial pressures of CO_2 between 10^{-4} bar and 1 bar, finding that atmospheres with more CO_2 were hotter and resulted in more observational variability. Despite this, none of the atmospheres displayed variability that would be detectable by JWST. The THAI series also investigated temporal variability (Fauchez *et al.*, 2022), this time for 4 GCM models and two different scenarios (either a N_2-dominated or a CO_2-dominated atmosphere). They found that the median variability was $\sim 2-3$ ppm, depending on the simulated case, concluding that such variability would not be expected to be observed with JWST. Here, WACCM6 produces slightly more variability corresponding to approximately 3.9 ppm maximum variability for O_3 at 9.63 µm. This may be slightly larger than previous results because WACCM6 includes both climate variations and interactive chemistry, rather than climate variations alone.

The lowest estimated noise floor of JWST (5 ppm) corresponds to a change in transmission spectra features of an effective altitude equal to 3 km. Even if the maximum noise floor was reached for each transmission spectrum taken, temporal variability in transmission spectral features would not be observed. Future technology could conceivably reduce the noise floor of telescope instruments and allow for smaller differences to be detectable. However, in practise, it would be unlikely that this variability would be observed because many transmission spectra will have to be 'stacked' (where multiple spectra are merged to produce a single averaged spectrum) in order to reach such a noise floor, and this stacking will average over the variability between each transmission spectrum. Nevertheless, observational variability in transmission spectra may be more detectable in

atmospheres with different surface pressures, temperatures (e.g. higher temperatures may produce more H_2O and cloud variation), and composition (e.g. hazy atmospheres).

Kane *et al.* (2021) predicted photometric observations integrated over wide passbands (0.2 – 20 µm and 3.33 – 10.000 µm) for the TRAPPIST-1 system. They showed that any measurements of the TRAPPIST-1e exoplanets in reflected and emitted light will actually observe all 7 exoplanets, noting that a multiplanet fit to the phase curve data will involve several degeneracies between atmospheres and surface features. Whilst the peak fluxes from these phase curves are offset from the secondary eclipse phase (by up to 17° in orbital phase) due to asymmetries in the outgoing longwave variation from the simulated exoplanet's surface, they exhibited no obvious temporal variations. Although the signal for TRAPPIST-1e and the other exoplanets can theoretically be extracted from their orbital periods, future work should investigate how temporal variability from each exoplanet will affect attempts to isolate the actual signal from each exoplanet, especially for spectroscopic measurements.

7.3.2 Uncertainties due to UV input spectra

The results in this Chapter demonstrate that large differences in assumed stellar UV spectra can lead to different predictions for the strength of O_3 spectral features when using a 3D model to simulate TRAPPIST-1e with an initial Earth-like composition. In this Section, the results are compared to previous work, known uncertainties are considered, and work that should be done in preparation for future exoplanet observations is discussed.

1D photochemical modelling of M dwarf terrestrial exoplanet atmospheres has demonstrated that CH_4 and N_2O could have greater abundances in the middle atmosphere compared to the modern Earth's atmosphere (e.g. Segura *et al.*,

2005; Wunderlich *et al.*, 2019), which is found in the WACCM6 simulations of TRAPPIST-1e presented here (see Fig. 6.14). Teal *et al.* (2022) used MUSCLES Treasury survey M-dwarf spectra combined with UV spectra reconstructions as stellar spectra input to Atmos (a coupled 1D photochemistry and climate model; Arney *et al.*, 2016), and showed changes of over two orders of magnitude in the middle atmosphere O_3 mixing ratios when modelling a modern Earth-like exoplanet that received 1 $S_\oplus$ of irradiation around GJ 176 (an M2.5V star), but with various UV irradiation scenarios. They derived transmission spectra predictions from their atmospheric simulations and found the maximum transit depth differences to be < 2 ppm, which is insignificant for JWST observations (possible noise floor of 5 ppm or greater). This is in contrast to the TP-1 e W21 PI and TP-1 e P19 PI transmission spectra results shown here, where estimated O_3 features here are distinct at the 5 ppm level. Whilst separate modelling methods are used in Teal *et al.* (2022), the difference in observational significance is primarily due to the size of the stars modelled: the radius of GJ 176 is 0.45 $R_\odot$, and the radius of TRAPPIST-1 is 0.12 $R_\odot$. This size contrast creates a factor ~ 14 difference in the relative amount of host starlight absorbed (see Eq. 2.24). Teal *et al.* (2022) also demonstrated that hazy Archean Earth atmospheres were more sensitive to changes in the incoming UV spectra compared to the modern Earth's atmosphere, which warrants future investigations for how uncertainties in the UV spectrum of the host star affect hazy atmospheres in 3D models.

In terms of 3D modelling, Chen *et al.* (2019) used a previous version of WACCM (CESM1) to investigate an exoplanet with a 43.87 day orbital period around a star with an effective temperature of 4000 K and an insolation of 1.9 $S_\oplus$ (as opposed to the 0.66 $S_\oplus$ used here). They also assessed the impact of uncertain host-star UV flux on the atmosphere. Chen *et al.* (2019) showed that two different spectra (representing a quiescent and an active M dwarf star) impacted

the middle atmospheric concentrations of O_3, OH, N_2O, CH_4, and H_2O. They calculated transmission spectra for the two simulated atmospheres, finding that the only observable difference was for the O_3 feature at 9.6 µm (although the UV O_3 feature is not shown in their figure 11). On the other hand, the transmission spectra simulations shown here in Fig. 7.1 display noticeable spectral differences for O_3 at 0.3, 0.6, 4.7, and 9 µm, as well as at 13 – 14 µm, and for H_2O between 5 – 6 µm. The differences in predicted observations between the results in this Chapter and that of Chen *et al.* (2019) likely arise due to the differences in exoplanetary system setup, the different stellar spectra, and the calculated lower O_3 columns from Chen *et al.* (2019), compared to the simulated atmospheres here. 43.87 days is in the 'slow rotator' regime (for the definition of tidally locked rotation regimes see Haqq-Misra *et al.*, 2018), and 6.1 days for TRAPPIST-1e can correspond to either the 'Rhines rotator' or 'fast rotator' regime (Sergeev *et al.*, 2022b). Thus, the WACCM6 results, alongside those from Chen *et al.* (2019), demonstrate that 3D modelling results are sensitive to the choice of the assumed stellar UV spectra for potentially habitable tidally locked exoplanets across early and late M dwarf stars and different rotation periods. Future work should also investigate the influence of orbital perturbations from a synchronous 1:1 spin-orbit resonance (e.g. Chen *et al.*, 2023) on composition.

Note that detecting O_3 will be difficult with JWST within the nominal 5 year mission lifetime (although JWST is expected to continue science operations for at least 10 years), even for a modern Earth scenario (Lin *et al.*, 2021). Indeed, Fauchez *et al.* (2019) found that gases other than CO_2 may require hundreds or thousands of transits to be detectable. Simulations of high-resolution observations with the extremely large class of telescopes indicate that O_2 at 0.76 µm may be detectable in the case of TRAPPIST-1e within $\sim$ 100 transits (Snellen *et al.*, 2013; Rodler & López-Morales, 2014; Serindag & Snellen, 2019). In addition to

previous work, the WACCM6 and PSG simulations presented here, which focus on the specific target of TRAPPIST-1e, further motivates the need for a dedicated next generation observatory with UV capabilities to characterise exoplanet host stars.

The derived Mega-MUSCLES spectrum of TRAPPIST-1 (W21; Wilson *et al.*, 2021) is constrained by more observations than the P19 spectrum, but both spectra have significant flux uncertainties. Whilst neither spectrum used in this Chapter is likely to wholly represent the true stellar irradiation environment of TRAPPIST-1e, there are at least observational constraints on the 'ground truth' of its parent star's spectrum. For many planetary systems, there will only be estimates from stellar models, and this will cause significant problems for predicting the photochemical environment of potentially habitable exoplanets. Furthermore, in each wavelength bin, it has been assumed that the flux does not vary with time. Due to M dwarf stellar activity, such an assumption is unlikely to be accurate (Loyd *et al.*, 2018). The O_3 abundance will be perturbed by the inclusion of incident stellar flares (Segura *et al.*, 2010; Tilley *et al.*, 2019; Chen *et al.*, 2021; Ridgway *et al.*, 2023) which has not been investigated here. Based on previous results, it seems that stellar flares will exacerbate the interpretation of observed spectra, so future work on incoming UV uncertainties could evaluate the additional impact of stellar flares. The present modelling uncertainties in the O_2-O_3 non-linear relationship arising from differences in predictions between 1D and 3D models (see Chapter 4) will compound these issues in analysis.

UV flux measurements from a telescope such as the $\sim$ 6 m UV/VIS/NIR telescope that was recommended by the Decadal Survey (National Academies of Sciences & Medicine, 2021) will aid the interpretation of observed exoplanet spectra and help to infer the concentration of O_2 and trace gases in the atmosphere without direct measurements (Kozakis *et al.*, 2022). However, this telescope is

not expected to be operational until the late 2030s at the earliest. Determining the EUV fluxes from a host star (which will require a dedicated observatory; Youngblood *et al.*, 2019) will also provide important information about atmospheric escape, habitability, and help to examine the atmospheric history of the exoplanets in the system.

Before next generation telescopes are online, there are other clues available to characterise oxygenated terrestrial atmospheres if the interpretation of the spectral features (e.g. O_3) leaves degeneracies in the parameter space between O_2 concentration, O_3 concentration, UV irradiation, and O_3 depleting catalytic cycles. For example, the major differences between the TP-1 e P19 PI and the TP-1 e P19 0.1% PAL transmission spectra are between the H_2O, O_2, and O_3 features. Moreover, the estimated inter-simulation trends with wavelength in transmission spectra are not mirrored in emission spectra predictions. Namely, the depth relative to the continuum in emission spectra for O_3 at 4.7 µm and 9.6 µm contrasts with the relative strength of associated transmission spectra features between the simulations. This means that if both transmission spectra and emission spectra are acquired with adequate precision, multi-wavelength observations combined with atmospheric retrieval methods (Quanz *et al.*, 2021) will be useful when delineating between possible atmospheric composition scenarios. Even so, Batalha *et al.* (2018) showed that confident estimates on atmospheric composition from emission spectra observed with JWST MIRI LRS will prove difficult to achieve, using TRAPPIST-1 f as an example. Finally, it is currently unknown how sensitive observational results are to the efficiency of catalytic cycles that destroy O_3, and future work should carefully consider boundary conditions for chemical species as a result.

7.4 Conclusions

This Chapter used a 3D chemistry-climate model (WACCM6) to simulate the exoplanet TRAPPIST-1e (assuming an initial Earth-like composition), whilst including two different incoming UV spectra the first time. The results demonstrated that utilising a single observed O_3 feature outside of UV wavelengths to extrapolate to undetected molecules, such as O_2, may lead to degeneracies over multiple orders of magnitude in the parameter space for atmospheric composition. The incident flux between the two stellar spectra used varies by up to a factor of ≈ 500 for important photolysis bands, and up to ≈ 5000 for individual wavelength bins. Whilst the atmospheric columns of many species (including O_2 and CO_2) are virtually unaffected by the difference between the two spectra, for an O_2 mixing ratio of 0.21, the O_3 columns differ by a factor of 22 due to different O_3 production rates that are sensitive to the shape and strength of the incoming spectrum.

Consequently, the associated O_3 transmission spectral features differ in effective altitude by up to 20 km, whilst the O_3 features in emission spectra differ by a factor of up to 23.4 in relative depth. One implication of this work is that a non-detection of O_3 at visible wavelengths may not indicate the absence of an oxygenated atmosphere. Furthermore, tidal locking of the model results in substantially different emission spectra features which are shallower relative to the emission continuum.

Without the direct detection of O_2, additional context for determining the oxygenation state of the atmosphere can be gained from either 1) future missions that are able to better characterise the UV spectra of faint stars, 2) sensitive direct imaging observations combined with transmission spectra observations targeting individual features, or 3) sensitive multi-wavelength observations that span the visible and infrared regions.

Chapter 8

Conclusions

8.1 Summary

In this thesis, I used WACCM6, a 3D Earth System Model with fully coupled chemistry and physics, to simulate Earth's oxygenated paleoclimates, as well as Earth-like exoplanets orbiting M dwarf stars. I used the Planetary Spectrum Generator (PSG) to produce transmission, reflection, and emission spectra from these simulations and assessed the potential observability of atmospheric molecules (e.g. O_3, O_2, H_2O) and flux variations.

8.1.1 Oxygenated Earth

In Chapter 4, the simulations of Earth at various atmospheric O_2 concentrations ($10^{-3} - 1.5$ PAL) accounted for a range of estimates from the beginning of the Proterozoic 2.4 billion years ago to the pre-industrial atmosphere. These simulations demonstrated, for the first time using a 3D chemistry-climate model, how the O_3 layer may have varied throughout Earth's history, both in terms of total column depth, and spatially. The simulations predicted global mean O_3 columns to be 1.2 – 2.9 times lower between the O_2 concentrations of 0.1 – 50% PAL when compared to previous 1D and 3D atmospheric modelling. If the WACCM6 scenarios calculated are closer to Earth's true atmospheric history, then higher

amounts of UV radiation would have penetrated to the surface than previously believed, which may have resulted in a greater selection pressure between organisms which had various degrees of protection against UV damage. Greater fluxes of UV radiation increases photolysis rates, with significant destruction of several important atmospheric molecules, such as H_2O, N_2O, and CH_4. Given the CO_2 constraints during the Proterozoic, higher amounts of CH_4 would be required to warm the Proterozoic into a glaciation-free state. The WACCM6 simulations initially indicated that this would be unlikely given the low CH_4 lifetimes calculated. Additionally, reduced O_3 concentrations led to colder temperatures around the tropical tropopause, with the potential to reduce diffusion limited hydrogen escape by a factor ~ 2. The work from Cooke *et al.* (2022) has sparked renewed interest in the rise of O_2 on Earth, and more results using 3D models have since followed (Deitrick & Goldblatt, 2022; Józefiak *et al.*, 2022; Yassin Jaziri *et al.*, 2022).

However, several uncertainties remain regarding the O_2-O_3 relationship, some of which were explored in a model intercomparison between the Kasting 1D model and two 3D models (WACCM6 and ROCKE-3D). The confidence in the lower O_3 columns predicted by WACCM6 have been strengthened by the findings of the intercomparison, in conjunction with results from Yassin Jaziri *et al.* (2022). When including Schumann-Runge (S-R) band absorption in WACCM6 for CO_2 and H_2O, the O_3 columns were reduced and the discrepancy with previous 1D and 3D model results increased. Furthermore, including S-R band scattering would likely reduce the O_3 column even more, but this should be tested once implemented in WACCM6.

This intercomparison demonstrates that: the O_2-O_3 relationship is more complicated than previously believed, 3D models should be used to inform the assumed representation of transport in 1D models, and significant updates for all

models capable of simulating O_3 perturbations will be required to improve community confidence in understanding the O_2-O_3 relationship.

The original results for lower CH_4 lifetimes from WACCM6 have now been updated to yield longer lifetimes which are closer to the Kasting 1D model, yet further work is required to solve the Proterozoic Faint Young Sun Paradox because large fluxes of CH_4 may still not produce a sufficient greenhouse effect because the O_2 concentrations are uncertain, and atmospheric photolysis of CH_4 could have been high.

The O_2-O_3 relationship is paramount for the comprehension of how life and the atmosphere co-evolved. Exploring how changing O_2 influenced the O_3 layer and the effects on atmospheric structure, climate, and the UV surface environment, will enable a more informed reconstruction of Earth's past climates. Finally, this modelling work is a key part in the search for extraterrestrial life in the universe, with the confirmed detection of O_2 or O_3 in an exoplanet atmosphere as one of the starting points for assessing whether an exoplanet is hosting life.

8.1.2 Predicted exoplanetary spectra

Earth and its climate through the geological ages represents the best template for a continuously habitable and inhabited planet. Multiple studies have used variations of the Kasting 1D model to calculate how Earth's composition would have evolved through time, and then predicted exoplanetary spectra around various types of stars, including Sun-like stars (e.g. Segura *et al.*, 2003; Kaltenegger *et al.*, 2007; Rugheimer *et al.*, 2015a; Rugheimer & Kaltenegger, 2018). In a similar manner, I used the WACCM6 simulations of the oxygenated Earth scenarios from Chapter 4 to calculate transmission and reflection spectra for Earth-analogue exoplanets over multiple orbits using PSG in Chapter 5. Transmission spectra features show currently undetectable time variations (maximum $\sim$ 0.1

ppmv), but theoretical reflection spectra exhibit annual variations which depend on albedo, observer angle, chemistry, and clouds. These results denote the value gained from using a 3D chemistry-climate model as such effects are not accessible from steady-state 1D simulations. Given favourable conditions, such as a close-by (within $\sim$ 10 pc) Earth-analogue exoplanet in an edge-on orbit, and a large enough telescope with high coronagraphic throughput (e.g. the $\sim$ 6 m UV/VIS/IR telescope), it may be possible to observe inter-annual climate variations, as well short-term variations due to clouds. Intriguingly, as a consequence of reducing O_2 and thus O_3, the chemical variations impact the albedo of the exoplanet. This results from the generally increasing liquid and ice cloud content for atmospheres with O_2 concentrations of $< 1\%$ PAL, for the first time showing that the variability of some spectral features depends non-linearly on atmospheric O_2 concentration. This result should be validated by other models, and investigated for various atmospheric compositions (e.g. a Titan-like CH_4 dominated atmosphere) which may also give rise to significant observational variability.

If any future sensitive observations are made of Earth-analogue exoplanets, their spectra can inform astronomers about the likely composition and potential habitability of the exoplanet, and also the weather and climate variations that might be occurring. This thesis shows that 3D chemistry-climate model results in combination with spectroscopic radiative transfer calculations are a powerful predictive tool for future observations of exoplanet atmospheres.

8.1.3 Tidally locked exoplanets

No solar system planet is tidally locked in a synchronous 1:1 spin-orbit resonance, and limited observations have been made of terrestrial tidally locked exoplanets. Therefore, knowledge regarding habitable zone terrestrial tidally locked exoplanets primarily comes from numerical modelling studies using either 1D

photochemical-climate models or 3D global climate models.

In this thesis, I used WACCM6 to simulate the habitable zone (HZ) terrestrial exoplanet TRAPPIST-1e, as well as Proxima Centauri b, a potentially terrestrial exoplanet in the HZ. Similar to previous studies, both exoplanets were assumed to be synchronously rotating around their M dwarf host stars.

Results with WACCM6 shows similarities to previous work such as the UM Proxima Centauri b simulations and the THAI series (which used 4 GCMs to simulate several TRAPPIST-1e scenarios). Each tidally locked simulation performed resulted in liquid water under the sea ice, but relatively small portions of the surface, if any, had liquid water. Thus, it is predicted that a larger greenhouse effect would be necessary for permanent surface liquid water, consistent with previous results.

The WACCM6 TRAPPIST-1e simulations fall into the 'double jet' regime. They exhibit atmospheric winds changing with time analogous to the LASO, although with crucial differences in period. The TRAPPIST-1e simulations had oscillatory periods of 9 – 14 yr in the downward propagation of zonal winds, but the PC b PI simulation did not exhibit wind perturbations that cut through the middle atmospheric jet.

Some M dwarf stars have constraints on their UV spectrum, but for many, only estimates can be made because there exist no measurements or the stars are too faint. This thesis explored the effect of different incoming UV spectra on the simulated climate of TRAPPIST-1e, how it impacted the chemistry, and thus potential observations of TRAPPIST-1e. Stronger UV, by up to a factor of 5,000, led to greater simulated abundances of atmospheric O_3 (e.g. 1130 DU compared to 52 DU), as well as larger heating rates in the middle atmosphere. Both the predicted transmission spectra and direct imaging spectra are subsequently affected. For instance, depending on the true UV environment of the exoplanet, it may be

possible that visible wavelength transmission spectra observations do not detect O_3, but this should not rule out the presence of high amounts of atmospheric O_2 (e.g. 0.21 bar). This work provides strong motivation for future UV observatories to provide more precise constraints on faint planet-hosting stars, with sensitive multi-wavelength observations required to obtain confidence in the interpretation of exoplanetary spectra.

8.2 Future work

8.2.1 Earth's oxygenation history

Many parameters involved in reconstructing Earth's atmospheric and climate history are poorly constrained, offering numerous future research opportunities. These parameters include: rotation rate and a changing Earth-moon distance (Zahnle & Walker, 1987; Bartlett & Stevenson, 2016); changing atmospheric composition; a dynamic ocean-land coverage; varied obliquity (Williams, 1993); and cloud feedback. Thus, there is a multitude of unknowns from Earth's past left to explore in biogeochemical models, 1D photochemical models, and 3D GCMs.

During a large proportion of the Proterozoic, the rotation rate of Earth may have been ≈ 21 h (Bartlett & Stevenson, 2016). Through sampling of cyanobacterial mats from the Middle Island Sinkhole in Michigan (USA), and through cyanobacterial mat modelling, Klatt *et al.* (2021) inferred that there may have been a connection between the Earth's rotation rate and the oxygenation of the atmosphere. This change in rotation rate in climate models for Earth is underexplored, and will likely have implications for atmospheric chemistry, dynamics, and habitability. A limited set of faster rotating simulations based on the low O_2 scenarios explored in this thesis are underway with WACCM6.

Future work should use the hierarchy of climate models to inform specific models in terms of inputs and parameterisations. For example, if a 1D model

and 3D model share the same chemical and photochemical schemes and assume the same initial conditions and lower boundary conditions (such as in Yassin Jaziri *et al.*, 2022), then the transport in the 3D model could be used to inform the transport missing in 1D models. This work is possible analytically, but may be expedited by machine learning techniques (Kashinath *et al.*, 2021) that can successfully interpolate between models, similar to techniques developed in the Earth science communities for single column models and 3D GCMs (Couvreux *et al.*, 2021; Villefranque *et al.*, 2021; Hourdin *et al.*, 2021). Despite some limitations, such as the quality of data the machine learning algorithms are trained on, deep neural networks have been successfully implemented to represent cloud processes and reduce computational cost (e.g. Rasp *et al.*, 2018).

The accuracy of both 1D and 3D models with photochemistry at lower than present day O_2 concentrations needs to be validated to have confidence in predicting the chemistry, climate and surface conditions for Earth's past, which is crucial for deciphering the circumstances that influenced the evolution of life on Earth. This will involve ongoing model development and model intercomparison. Once improved O_2 photolysis parameterisations have been validated with line-by-line calculations and incorporated into models, different atmospheric pressures should be investigated, based on the possible ranges of surface pressure during Earth's history (Catling & Zahnle, 2020; Marty *et al.*, 2013; Avice *et al.*, 2018; Som *et al.*, 2012, 2016), but also for a variety of theoretical exoplanets.

Geological constraints and biogeochemical modelling should be used to narrow down the possible past surface-to-atmosphere fluxes. Paleogeographic reconstructions of Earth's Archean, Proterozoic and Phanerozoic eons, which have yet to be agreed upon (Mitchell *et al.*, 2021), will be useful for understanding the climate during those times. 3D models should include these reconstructions because this will affect heating, convection, cloud distribution, planetary waves, and the mid-

dle atmospheric circulation (e.g. the Brewer-Dobson circulation, resulting in O_3 column changes).

Eventually, as the Sun's luminosity increases, Earth will lose all of its water through the moist greenhouse effect (Kasting *et al.*, 1984). Ozaki & Reinhard (2021) calculated that in 1.08 ± 0.14 billion years ($1\ \sigma$) in the future, Earth's atmospheric O_2 will drop to 1% PAL, which is before the Earth is predicted to lose its water approximately 2 Gyr in the future (Wolf & Toon, 2014; Ozaki & Reinhard, 2021), although estimates vary (Kasting, 1988). As O_2 levels drop, the upper troposphere will cool, diminishing the amount of hydrogen available in the upper atmosphere which can escape to space and cause irreversible water loss. Hence, the ocean loss timescale could be extended via this effect, such that investigations aiming to assess the lifetime of Earth's future biosphere should include detailed atmospheric oxygen chemistry.

The abundance of atmospheric oxygen before the GOE is inferred from sulphur mass-independent fractionation (MIF; Farquhar *et al.*, 2000; Uveges *et al.*, 2023), which could have only taken place without a sufficient ozone screen (Farquhar *et al.*, 2001; Pavlov & Kasting, 2002). Whilst the simulations in Chapter 4 did not simulate down to low enough levels of O_2 ($\sim 10^{-6}$ PAL), Yassin Jaziri *et al.* (2022) did, and similar to this thesis, their results imply lower levels of O_3 when compared to 1D models. Further work should use updated 3D models to investigate sulphur MIF to more comprehensively understand the chemistry and O_2 concentrations prior to the Proterozoic, and the eventual transition to an oxygenated atmosphere.

Based on the preliminary results of the intercomparison for low O_2 atmospheres, and accounting for any future changes to photochemical models which improve their accuracy with respect to line-by-line calculations, the results from Chapters 4 and 5 could be updated. Including CO_2 and H_2O absorption in the Schumann-Runge bands would likely lead to an increase in the detectability of

CH_4 features (for a fixed surface flux or surface mixing ratio), but it is currently less clear what the impact would be for O_3 features; the feedbacks which set the total O_3 column are more complex, depend on the assumed lower boundary conditions for various gases, and are model dependent. Additionally, as the albedo variations depend on composition, clouds, ocean, ice, and land, different continental coverage will alter the predictions made in Chapter 5. Using climate simulations to ascertain possible observational techniques that can leverage the rotation rate and obliquity from photometric and spectroscopic variations will be of interest when establishing the climate states of potentially habitable exoplanets.

3D chemistry-climate models are also essential for the interpretation of exoplanetary spectra and biosignatures: for an exoplanet and its exomoon, it has been suggested that two atmospheres present in an exoplanet-exomoon system could give the appearance of disequilibrium chemistry (e.g. high quantities of O_2 and CH_4) from observations which lack the spatial resolving power to physically separate the two bodies (Rein *et al.*, 2014). Crucially, 3D time-dependent modelling could be used to unravel how to robustly interpret observations which track the system through time. If a wider parameter space of O_2 is explored for this problem, the work should account for the new O_3 predictions presented in this thesis. If exomoons are found to be frequent, astronomers will target these bodies in the search for life beyond Earth. Certainly, the climates of exomoons themselves remain inadequately evaluated, and it is anticipated that the spectroscopic appearance of exoplanet-exomoon systems will become a unique research avenue.

8.2.2 Tidally locked exoplanets and future observations

One of the major uncertainties in climate science arises from the inter-model variability between cloud predictions. Now, diverging calculations between coarse resolution and high resolution simulations has been demonstrated for tidally locked exoplanets (Sergeev *et al.*, 2020). Higher resolution simulations are more computationally expensive, yet are likely to be valuable pertaining to the characterisation of unfamiliar tidally locked worlds.

Several 3D exoplanet models are based on Earth System Models (e.g. WACCM, ExoCAM, ROCKE-3D). Whilst modern Earth-like exoplanets are a natural starting point for habitable exoplanet simulations, more 3D chemistry-climate M dwarf terrestrial exoplanet simulations with compositions that diverge from modern Earth-like (e.g. CO_2 or H_2O dominated, or the inclusion of hazes for a Titan-like or Archean Earth-like exoplanet; Arney *et al.*, 2016), will be of interest because it is known that the Archean was inhabited. More laboratory work is needed to accurately model haze formation (e.g. Hörst & Tolbert, 2014; Hörst *et al.*, 2018) and radiative transfer for several different types of atmospheres (e.g. Tennyson & Yurchenko, 2012; Tennyson *et al.*, 2020). To illustrate, the role of CO_2 clouds are even less understood than that of H_2O clouds (Forget & Pierrehumbert, 1997; Kitzmann, 2016), and a full comprehension of the CH_4 cycle on Titan, including cloud formation and precipitation, is yet to be appreciated (Tokano *et al.*, 2006; Lunine & Atreya, 2008; Mitchell & Lora, 2016). It is suggested that the following significant modifications could be made to upgrade the flexibility of the WACCM6 model:

- The implementation of condensation for gases such as methane (CH_4), ethane (C_2H_6), and carbon dioxide (CO_2), resulting in clouds and precipitation for these species.

- The integration of versatile land and ocean configurations to enable explorations of surface features on climate and observational predictions.
  - An adaptable land model implemented to interchange different surface properties, including regions of sand, basalt, granite, and limestone.
  - An adjustment to allow for oceans with different depths and liquids (e.g. NH_3, CH_4, H_2SO_4).
- The incorporation of various atmospheric hazes, including hydrocarbon haze.
- A flexible radiative transfer model to permit the use of various atmospheres dominated by gases other than O_2 or N_2, and with a large range of surface pressures.
- A single column model that shares the same chemical scheme, to explore a larger parameter space in 1D and run comparisons with 3D results.

Subsequent investigations using an updated WACCM6 model could include simulating CO_2 clouds on Mars and the CH_4 cycle on Titan to closely resemble available observations before confidence can be placed in exoplanet modelling with such processes. Venus, with its dense, super rotating atmosphere, provides similar opportunities. It seems likely that many different atmospheric compositions are possible, such that reliable simulations of exoplanets with no solar system analogue will require model improvements.

Several authors have now discussed the possibility that planets that are very close to their host star, and potentially tidally locked, may not actually exist in a perfect 1:1 synchronous rotation. Some studies have investigated a 3:2 spin–orbit resonance (Běhounková *et al.*, 2011; Yang *et al.*, 2020), and Chen *et al.* (2023) showed that orbital disruptions induced by gravitational interactions in tightly

packed planetary systems will disturb exoplanets away from synchronous 1:1 spin-orbit rotation. More investigations which use models with interactive chemistry need to be done in the future to delineate observational signature differences between synchronously rotating exoplanets and those that are not. This will aid in identifying the climate states of known exoplanets.

Super rotating winds have been detected for hot Jupiters (Snellen *et al.*, 2010; Miller-Ricci Kempton & Rauscher, 2012). Super rotating jets in terrestrial exoplanets with speeds up to 100 m s^{-1} have been reported from models (Hammond *et al.*, 2020), with winds on Titan reaching up to 200 m s^{-1} (Read & Lebonnois, 2018). Whilst speculative, these speeds could potentially be detected using remote sensing by observing the Doppler shift from specific molecular features.

There is a common phrase among the exoplanet community: 'Know thy star, know thy planet'[1] (Carrillo *et al.*, 2020; Fu *et al.*, 2022). With an ageing Hubble Space Telescope, and no dedicated UV observatory on the immediate horizon, there is a growing demand to better measure the photochemical environment of exoplanet atmospheres. Currently, modelling is best placed to provide examples where the UV flux can lead to degenerate observational states, such as for oxygenated atmospheres, and anoxic, hazy Archean Earth-like atmospheres (Teal *et al.*, 2022). Including time-dependent stellar activity in a variety of models is a desirable goal, however, the reliability of stellar flare UV flux predictions from models which rely on only white-light observations has been called into question (Jackman *et al.*, 2023). Indeed, whilst flares from TRAPPIST-1 have been observed (Vida *et al.*, 2017), they may be less intense than previously suspected (Maas *et al.*, 2022). Furthermore, the frequency at which stellar flares hit their orbiting exoplanets could be scarcer than some studies have assumed owing to the directionality of ejections (Ilin *et al.*, 2021), improving the long-term habitability

[1] https://www.nasa.gov/feature/ames/kepler/know-thy-star-know-thy-planet

prospects of these exoplanets. Thus, the space weather of terrestrial exoplanets provides plenty of opportunities for further study.

It is likely that the most precise observations yet for habitable zone terrestrial exoplanets will first be made by JWST and the ELTs for M dwarf systems. This is because of their relative ease of characterisation in transmission spectra when compared to G dwarf exoplanets, in addition to the difficulty in obtaining high-contrast imaging observations of G dwarf terrestrial exoplanets (likely requiring a dedicated observatory like the $\sim$ 6 m UV/VIS/IR telescope which won't be constructed until the late 2030s). Despite being rather speculative, there is a proposed telescope that will fly into the outer solar system and use the Sun as a gravitational lens, with the prodigious ability to resolve the surface of exoplanets (Turyshev & Toth, 2022). The next decade will offer up further observations of TRAPPIST-1e and likely Proxima Centauri b, in addition to other potentially habitable exoplanets of interest. The knowledge gained from studying these systems will guide the search towards characterising some of the most intriguing exoplanets in the universe.

8.3 Final remarks

Currently, the oxygenated Earth we inhabit is the gem of the cosmos, giving life to organisms all across the surface and within the oceans. For several decades the rise of the O_3 layer from the rise in O_2 was treated in the literature as well-constrained. As a result of work done in this thesis, and subsequent papers, this picture has evolved. It now seems that the size of the established O_3 layer may have been lower than previously calculated for many O_2 concentrations, whilst specific events (e.g. the GOE, incident solar flares) will have caused O_3 concentrations to fluctuate dramatically over the past 2.4 billion years. Attempts to ascertain past climate states must account for a faster rotation rate, a younger

Sun, alternative continental coverage, larger quantities of greenhouse gases, and updated O_3 calculations. Lessons from Earth's atmospheric history can provide insights into the potential evolution of rocky exoplanets. In parallel, exoplanets yield an unprecedented parameter space over which to study terrestrial climates.

Oxygenated terrestrial exoplanets might be frequent, but it is also undeniable that they might be scarce. At the time of writing, this frequency is unknown. Many compelling discoveries could be revealed by upcoming telescope campaigns which observe exoplanets, yet caution is required: it is possible that a proposed biosignature (such as O_2) on a terrestrial habitable zone exoplanet may be detected within the next couple of decades. In such an event, the possibility of extraterrestrial life becomes apparent, whilst far from certain. The exoplanet community will need to use a combination of observations, atmospheric retrievals, 3D global climate modelling, and biogeochemical modelling to infer the environmental context that could produce the observed spectrum. The confidence we have in this integrated approach will define whether any detected biosignatures are unequivocally attributed to the existence of a biosphere, or whether the captivating search for life beyond Earth goes on.

Appendix A

Further details of completed PSG simulations

The parameter space for possible telescope simulations in Chapter 5 is vast and to cover every future telescope concept, planet distance, oxygenation state, etc. is beyond the scope of that Chapter. Table A.1 shows the simulations that have been performed. The PSG packages required for these calculations were `BASE`, `PROGRAMS`, and `CORRKLOW`. The versions used were last updated on 20/05/2022, 04/02/2022, and 01/03/2022, respectively.

Each simulation used NMAX = 3 and LMAX = 41. NMAX is defined as the number of stream pairs, and the Legendre terms is given as LMAX - see the Fundamentals of the Planetary Spectrum Generator for more details (Villanueva *et al.*, 2022). Calculation speed is proportional to LMAX but is approximately proportional to NMAX^3 (Villanueva *et al.*, 2022). Multiple tests with different values of NMAX and LMAX were performed to ensure spectra contributions from scattering were accurate whilst not compromising the speed in such a way that collating the simulations would be unachievable within a reasonable time frame. In a small proportion of cases ($< 2\%$) where unusually large brightness occurred, likely due to an asymmetry calculation in PSG, the substellar point was slightly shifted horizontally ($< 3°$) to produce consistent results.

Table A.1: For each of the PI, 10% PAL, 1% PAL, and 0.1% PAL atmospheres, the PSG simulations that have been run are listed below. A single checkmark means that LUVOIR A has been evaluated in all three channels (UV, VIS, NIR) for 73 phase points around the orbit (one snapshot every 5 days), for a 24 hour integration time. Three checkmarks mean that simulated HCI observations for a full orbit for LUVOIR A, LUVOIR B, and HabEx with a starshade, have been evaluated. If they have also been evaluated at 25 pc and 50 pc, this is indicated in brackets. A dash means no telescope observations have been evaluated. A standard orbit is the where PSG has been used to calculate the total flux in Jy for each particular date and phase, using the ephemeris data from the year 2020. Signal-to-noise ratios (SNRs) have been calculated where a full orbit has been simulated in PSG for a particular atmosphere which has had all molecules removed apart from N_2 and clouds. A phase shift orbit has a checkmark if spectra have been produced for the $+90°$, $+180°$, and $+270°$ configurations. The water cloud particle size (WCPS) and the ice cloud particle size (ICPS) is indicated.

	year 1	year 2	year 3	year 4
Standard orbit (5 µm WCPS, 100 µm ICPS)	✓✓✓(10, 25, and 50 pc)	✓(10 pc)	✓(10 pc)	✓(10 pc)
Standard orbit SNR (5 µm WCPS, 100 µm ICPS)	✓✓✓(10, 25, and 50 pc)	-	-	-
Phase shift orbit (5 µm WCPS, 100 µm ICPS)	-	✓(10 pc)	✓(10 pc)	-
Standard orbit (1 µm WCPS, 1 µm ICPS)	✓✓✓(10, 25, and 50 pc)	✓(10 pc)	✓(10 pc)	✓(10 pc)
Standard orbit SNR (1 µm WCPS, 1 µm ICPS)	✓✓✓(10, 25, and 50 pc)	-	-	-
Phase shift orbit (1 µm WCPS, 1 µm ICPS)	-	✓(10 pc)	✓(10 pc)	-

Appendix B

Annual variability in reflected light for the 10% PAL and 1% PAL scenarios

Fig. B.1 shows the analogue of Fig. 5.5 from the main text, but instead for the 10% present atmospheric level (PAL) of O_2 and 1% PAL of O_2 simulations. It shows the annual variability of spectral features for the 10% PAL and 1% PAL atmospheres. The ± 1-σ_{noise} is shown by the width of the lines, where σ_{noise} represents the uncertainty on the observations as calculated by the Planetary Spectrum Generator (PSG).

B. ANNUAL VARIABILITY IN REFLECTED LIGHT FOR THE 10% PAL AND 1% PAL SCENARIOS

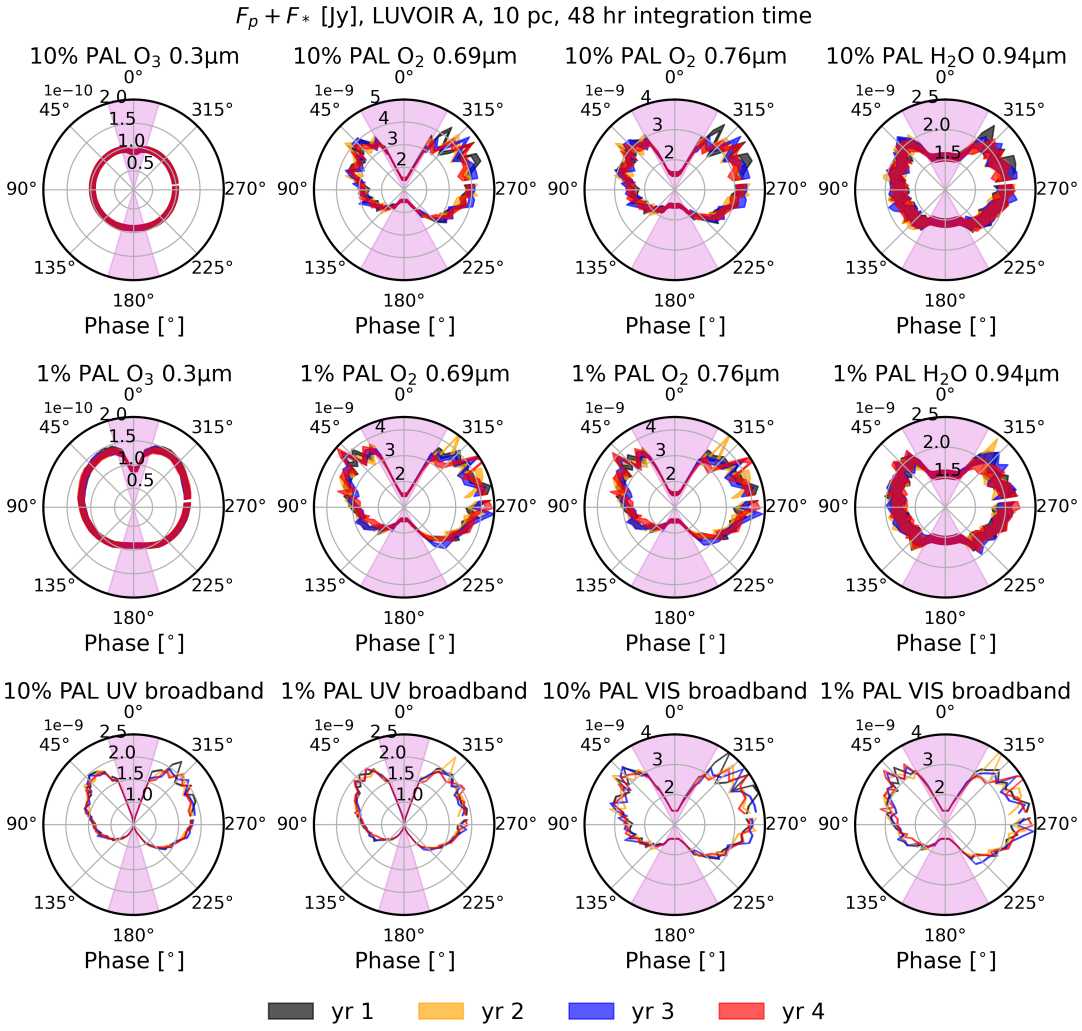

Fig. B.1: Plotted in the radial direction in units of Jy is the total flux $F_T = F_p + F_*$ from the planet and star as seen by the telescope detector from the final 4 years (1st year = black, 2nd year = yellow, 3rd year = blue, 4th year = red) of the simulations. This is the same as Fig. 5.5, apart from for the 10% PAL and 1% PAL simulated scenarios instead of the PI and 0.1% PAL scenarios.

Appendix C

Observability of exoplanets in high-contrast imaging

As an exoplanet orbits a star, with an orbital phase denoted by ψ, the coronagraph throughput varies because the projected exoplanet-star angular separation changes for the observer. When using a coronagraph, the Inner Working Angle (IWA) is typically defined as

$$\text{IWA} \approx \frac{\lambda}{D}, \tag{C.1}$$

where λ is the wavelength of light and D is the diameter of the telescope. The telescope coronagraphs evaluated here are the LUVOIR ECLIPS instrument and HabEx with a starshade. For LUVOIR, the IWA is given in the LUVOIR Final Report (The LUVOIR Team, 2019) as $4\lambda/D$ for the UV channel, and $3.5\lambda/D$ for the VIS and NIR channels. For HabEx with a starshade, an IWA of 58 mas between 0.3 – 1.0 µm is given in the HabEx Final Report (Gaudi *et al.*, 2020). For the planet to be visible (and not blocked by the coronagraph), the IWA must be smaller than the angular separation of the star and planet (θ), which is given by

$$\theta \approx \frac{s}{d}, \tag{C.2}$$

where s is the projected separation and d is the distance to the planet-star system. The maximum projected separation for a circular orbit is the semi-major axis (a; 1 AU for Earth). For circular orbits of inclination, i, the separation, s, takes the general form

$$s = a\sqrt{\sin^2(\psi) + \cos^2(i)\cos^2(\psi)}. \tag{C.3}$$

In the simplified case of a system inclined at 90° from the perspective of an observer,

$$s = \pm a\sin(\psi). \tag{C.4}$$

When the IWA $< \theta$, the exoplanet is fully observable and when the IWA $> \theta$, the coronagraph throughput is reduced. The equations can be rearranged to find the orbital phase at which the exoplanet is about to enter inside the IWA, such that

$$\psi = \sin^{-1}\left(\frac{\lambda d}{aD}\right) \text{for} \frac{\lambda d}{aD} \leq 1. \tag{C.5}$$

Thus, one can see that as the wavelength λ increases or the distance d increases, then a smaller proportion of the orbit will be observable with the coronagraph. On the other hand, if the semi-major axis or the telescope diameter increases, then a larger proportion of the total orbit will be accessible for higher SNR observations.

References

Abrevaya, X.C., Leitzinger, M., Oppezzo, O.J., Odert, P., Patel, M.R., Luna, G.J.M., Forte Giacobone, A.F. & Hanslmeier, A. (2020). The UV surface habitability of Proxima b: first experiments revealing probable life survival to stellar flares. *MNRAS*, **494**, L69–L74.

Agol, E., Dorn, C., Grimm, S.L., Turbet, M., Ducrot, E., Delrez, L., Gillon, M., Demory, B.O., Burdanov, A., Barkaoui, K., Benkhaldoun, Z., Bolmont, E., Burgasser, A., Carey, S., de Wit, J., Fabrycky, D., Foreman-Mackey, D., Haldemann, J., Hernandez, D.M., Ingalls, J., Jehin, E., Langford, Z., Leconte, J., Lederer, S.M., Luger, R., Malhotra, R., Meadows, V.S., Morris, B.M., Pozuelos, F.J., Queloz, D., Raymond, S.N., Selsis, F., Sestovic, M., Triaud, A.H.M.J. & Van Grootel, V. (2021). Refining the Transit-timing and Photometric Analysis of TRAPPIST-1: Masses, Radii, Densities, Dynamics, and Ephemerides. , **2**, 1.

Airapetian, V.S., Glocer, A., Khazanov, G.V., Loyd, R.O.P., France, K., Sojka, J., Danchi, W.C. & Liemohn, M.W. (2017). How Hospitable Are Space Weather Affected Habitable Zones? The Role of Ion Escape. *ApJ*, **836**, L3.

Akeson, R.L., Chen, X., Ciardi, D., Crane, M., Good, J., Harbut, M., Jackson, E., Kane, S.R., Laity, A.C., Leifer, S., Lynn, M.,

McElroy, D.L., Papin, M., Plavchan, P., Ramírez, S.V., Rey, R., von Braun, K., Wittman, M., Abajian, M., Ali, B., Beichman, C., Beekley, A., Berriman, G.B., Berukoff, S., Bryden, G., Chan, B., Groom, S., Lau, C., Payne, A.N., Regelson, M., Saucedo, M., Schmitz, M., Stauffer, J., Wyatt, P. & Zhang, A. (2013). The NASA Exoplanet Archive: Data and Tools for Exoplanet Research. *PASP*, **125**, 989.

Alei, E., Konrad, B.S., Angerhausen, D., Grenfell, J.L., Mollière, P., Quanz, S.P., Rugheimer, S., Wunderlich, F. & LIFE Collaboration (2022). Large Interferometer For Exoplanets (LIFE). V. Diagnostic potential of a mid-infrared space interferometer for studying Earth analogs. *A&A*, **665**, A106.

Alexander, M., Geller, M., McLandress, C., Polavarapu, S., Preusse, P., Sassi, F., Sato, K., Eckermann, S., Ern, M., Hertzog, A. *et al.* (2010). Recent developments in gravity-wave effects in climate models and the global distribution of gravity-wave momentum flux from observations and models. *Quarterly Journal of the Royal Meteorological Society*, **136**, 1103–1124.

Anbar, A.D., Duan, Y., Lyons, T.W., Arnold, G.L., Kendall, B., Creaser, R.A., Kaufman, A.J., Gordon, G.W., Scott, C., Garvin, J. & Buick, R. (2007). A Whiff of Oxygen Before the Great Oxidation Event? *Science*, **317**, 1903.

Anders, E. & Owen, T. (1977). Mars and Earth: Origin and Abundance of Volatiles. *Science*, **198**, 453–465.

Anglada-Escudé, G., Amado, P.J., Barnes, J., Berdiñas, Z.M., Butler, R.P., Coleman, G.A.L., de La Cueva, I., Dreizler, S., Endl,

M., Giesers, B., Jeffers, S.V., Jenkins, J.S., Jones, H.R.A., Kiraga, M., Kürster, M., López-González, M.J., Marvin, C.J., Morales, N., Morin, J., Nelson, R.P., Ortiz, J.L., Ofir, A., Paardekooper, S.J., Reiners, A., Rodríguez, E., Rodríguez-López, C., Sarmiento, L.F., Strachan, J.P., Tsapras, Y., Tuomi, M. & Zechmeister, M. (2016). A terrestrial planet candidate in a temperate orbit around Proxima Centauri. *Nature*, **536**, 437–440.

Arney, G., Domagal-Goldman, S.D., Meadows, V.S., Wolf, E.T., Schwieterman, E., Charnay, B., Claire, M., Hébrard, E. & Trainer, M.G. (2016). The Pale Orange Dot: The Spectrum and Habitability of Hazy Archean Earth. *Astrobiology*, **16**, 873–899.

Aubert, E.J. (1957). O the Release of Latent Heat as a Factor in Large Scale Atmospheric Motions. *Journal of Atmospheric Sciences*, **14**, 527–542.

Avice, G., Marty, B., Burgess, R., Hofmann, A., Philippot, P., Zahnle, K. & Zakharov, D. (2018). Evolution of atmospheric xenon and other noble gases inferred from Archean to Paleoproterozoic rocks. *Geochimica Cosmochimica Acta*, **232**, 82–100.

Avnery, S., Mauzerall, D.L., Liu, J. & Horowitz, L.W. (2011). Global crop yield reductions due to surface ozone exposure: 1. Year 2000 crop production losses and economic damage. *Atmospheric Environment*, **45**, 2284–2296.

Bachan, A. & Kump, L.R. (2015). The rise of oxygen and siderite oxidation during the Lomagundi Event. *Proceedings of the National Academy of Science*, **112**, 6562–6567.

Bacmeister, J.T., Hannay, C., Medeiros, B., Gettelman, A., Neale, R., Fredriksen, H.B., Lipscomb, W.H., Simpson, I., Bailey, D.A.,

Holland, M., Lindsay, K. & Otto-Bliesner, B. (2020). CO_2 Increase Experiments Using the CESM: Relationship to Climate Sensitivity and Comparison of CESM1 to CESM2. *Journal of Advances in Modeling Earth Systems*, **12**, e2020MS002120.

Baeyens, R., Decin, L., Carone, L., Venot, O., Agúndez, M. & Mollière, P. (2021). Grid of pseudo-2D chemistry models for tidally locked exoplanets - I. The role of vertical and horizontal mixing. *MNRAS*, **505**, 5603–5653.

Bahcall, J.N., Pinsonneault, M.H. & Basu, S. (2001). Solar Models: Current Epoch and Time Dependences, Neutrinos, and Helioseismological Properties. *The Astrophysical Journal*, **555**, 990–1012.

Baldwin, M., Gray, L., Dunkerton, T., Hamilton, K., Haynes, P., Randel, W.J., Holton, J.R., Alexander, M., Hirota, I., Horinouchi, T. *et al.* (2001). The quasi-biennial oscillation. *Reviews of Geophysics*, **39**, 179–229.

Bancroft, B.A., Baker, N.J. & Blaustein, A.R. (2007). Effects of uvb radiation on marine and freshwater organisms: a synthesis through meta-analysis. *Ecology letters*, **10**, 332–345.

Banks, P.M. & Kockarts, G. (1973). *Aeronomy.*.

Barclay, T., Pepper, J. & Quintana, E.V. (2018). A revised exoplanet yield from the transiting exoplanet survey satellite (tess). *The Astrophysical Journal Supplement Series*, **239**, 2.

Barnes, R. (2017). Tidal locking of habitable exoplanets. *Celestial Mechanics and Dynamical Astronomy*, **129**, 509–536.

Barnes, R., Meadows, V.S. & Evans, N. (2015). Comparative Habitability of Transiting Exoplanets. *ApJ*, **814**, 91.

Baron, E. & Hauschildt, P.H. (2007). A 3D radiative transfer framework. II. Line transfer problems. *A&A*, **468**, 255–261.

Bartlett, B.C. & Stevenson, D.J. (2016). Analysis of a Precambrian resonance-stabilized day length. *Geophysics Research Letters*, **43**, 5716–5724.

Batalha, N.E., Lewis, N.K., Line, M.R., Valenti, J. & Stevenson, K. (2018). Strategies for Constraining the Atmospheres of Temperate Terrestrial Planets with JWST. *ApJ*, **856**, L34.

Beer (1852). Bestimmung der Absorption des rothen Lichts in farbigen Flüssigkeiten. *Annalen der Physik*, **162**, 78–88.

Beig, G., Scheer, J., Mlynczak, M.G. & Keckhut, P. (2008). Overview of the temperature response in the mesosphere and lower thermosphere to solar activity. *Reviews of Geophysics*, **46**, RG3002.

Bekker, A. & Holland, H.D. (2012). Oxygen overshoot and recovery during the early Paleoproterozoic. *Earth and Planetary Science Letters*, **317**, 295–304.

Bekker, A., Holland, H.D., Wang, P.L., Rumble, D., Stein, H.J., Hannah, J.L., Coetzee, L.L. & Beukes, N.J. (2004). Dating the rise of atmospheric oxygen. *Nature*, **427**, 117–120.

Beljaars Anton, C.M., Brown, R.A. & Wood, N. (2004). A new parametrization of turbulent orographic form drag. *Quarterly Journal of the Royal Meteorological Society*, **130**, 1327–1347.

Benca, J.P., Duijnstee, I.A.P. & Looy, C.V. (2018). UV-B-induced forest sterility: Implications of ozone shield failure in Earth's largest extinction. *Science Advances*, **4**, e1700618.

Benneke, B., Wong, I., Piaulet, C., Knutson, H.A., Lothringer, J., Morley, C.V., Crossfield, I.J.M., Gao, P., Greene, T.P., Dressing, C., Dragomir, D., Howard, A.W., McCullough, P.R., Kempton, E.M.R., Fortney, J.J. & Fraine, J. (2019). Water Vapor and Clouds on the Habitable-zone Sub-Neptune Exoplanet K2-18b. *ApJ*, **887**, L14.

Berdyugina, S.V. & Kuhn, J.R. (2019). Surface Imaging of Proxima b and Other Exoplanets: Albedo Maps, Biosignatures, and Technosignatures. *AJ*, **158**, 246.

Berkner, L.V. & Marshall, L.C. (1965). On the Origin and Rise of Oxygen Concentration in the Earth's Atmosphere. *Journal of Atmospheric Sciences*, **22**, 225–261.

Bétrémieux, Y. & Kaltenegger, L. (2014). Impact of Atmospheric Refraction: How Deeply can We Probe Exo-Earth's Atmospheres during Primary Eclipse Observations? *The Astrophysical Journal*, **791**, 7.

Betts, H.C., Puttick, M.N., Clark, J.W., Williams, T.A., Donoghue, P.C. & Pisani, D. (2018). Integrated genomic and fossil evidence illuminates life's early evolution and eukaryote origin. *Nature ecology & evolution*, **2**, 1556–1562.

Birner, T. & Bönisch, H. (2011). Residual circulation trajectories and transit times into the extratropical lowermost stratosphere. *Atmospheric Chemistry & Physics*, **11**, 817–827.

Black, B.A., Lamarque, J.F., Shields, C.A., Elkins-Tanton, L.T. & Kiehl, J.T. (2014). Acid rain and ozone depletion from pulsed Siberian Traps magmatism. *Geology*, **42**, 67–70.

Bobrovskiy, I., Hope, J.M., Ivantsov, A., Nettersheim, B.J., Hallmann, C. & Brocks, J.J. (2018). Ancient steroids establish the Ediacaran fossil Dickinsonia as one of the earliest animals. *Science*, **361**, 1246–1249.

Bobrovskiy, I., Hope, J.M., Nettersheim, B.J., Volkman, J.K., Hallmann, C. & Brocks, J.J. (2021). Algal origin of sponge sterane biomarkers negates the oldest evidence for animals in the rock record. *Nature Ecology & Evolution*, **5**, 165–168.

Bogenschutz, P.A., Gettelman, A., Morrison, H., Larson, V.E., Craig, C. & Schanen, D.P. (2013). Higher-order turbulence closure and its impact on climate simulations in the community atmosphere model. *Journal of Climate*, **26**, 9655–9676.

Bolcar, M.R., Aloezos, S., Bly, V.T., Collins, C., Crooke, J., Dressing, C.D., Fantano, L., Feinberg, L.D., France, K., Gochar, G., Gong, Q., Hylan, J.E., Jones, A., Linares, I., Postman, M., Pueyo, L., Roberge, A., Sacks, L., Tompkins, S. & West, G. (2017). The Large UV/Optical/Infrared Surveyor (LUVOIR): Decadal Mission concept design update. In *Society of Photo-Optical Instrumentation Engineers (SPIE) Conference Series*, vol. 10398 of *Society of Photo-Optical Instrumentation Engineers (SPIE) Conference Series*, 1039809.

Bond, D.P.G. & Grasby, S.E. (2017). On the causes of mass extinctions. *Palaeogeography Palaeoclimatology Palaeoecology*, **478**, 3–29.

Borgeraas, J. & Hessen, D.O. (2000). Uv-b induced mortality and antioxidant enzyme activities in daphnia magna at different oxygen concentrations and temperatures. *Journal of Plankton Research*, **22**, 1167–1183.

Bornman, J.F., Barnes, P.W., Robson, T.M., Robinson, S.A., Jansen, M.A., Ballaré, C.L. & Flint, S.D. (2019). Linkages between stratospheric ozone, uv radiation and climate change and their implications for terrestrial ecosystems. *Photochemical & Photobiological Sciences*, **18**, 681–716.

Boutle, I.A., Mayne, N.J., Drummond, B., Manners, J., Goyal, J., Hugo Lambert, F., Acreman, D.M. & Earnshaw, P.D. (2017). Exploring the climate of Proxima B with the Met Office Unified Model. *A&A*, **601**, A120.

Boyajian, T.S., von Braun, K., van Belle, G., McAlister, H.A., ten Brummelaar, T.A., Kane, S.R., Muirhead, P.S., Jones, J., White, R., Schaefer, G., Ciardi, D., Henry, T., López-Morales, M., Ridgway, S., Gies, D., Jao, W.C., Rojas-Ayala, B., Parks, J.R., Sturmann, L., Sturmann, J., Turner, N.H., Farrington, C., Goldfinger, P.J. & Berger, D.H. (2012). Stellar Diameters and Temperatures. II. Main-sequence K- and M-stars. *ApJ*, **757**, 112.

Braam, M., Palmer, P.I., Decin, L., Ridgway, R.J., Zamyatina, M., Mayne, N.J., Sergeev, D.E. & Abraham, N.L. (2022). Lightning-induced chemistry on tidally-locked Earth-like exoplanets. *MNRAS*, **517**, 2383–2402.

Bradley, D.C. (2011). Secular trends in the geologic record and the supercontinent cycle. *Earth Science Reviews*, **108**, 16–33.

Brand, U., Davis, A.M., Shaver, K.K., Blamey, N.J.F., Heizler, M. & Lécuyer, C. (2021). Atmospheric oxygen of the Paleozoic. *Earth Science Reviews*, **216**, 103560.

Brasseur, G.P. & Solomon, S. (2005). *Aeronomy of the Middle Atmosphere: Chemistry and Physics of the Stratosphere and Mesosphere*.

Brown, A., Vallenari, A., Prusti, T., De Bruijne, J., Babusiaux, C., Bailer-Jones, C., Biermann, M., Evans, D.W., Eyer, L., Jansen, F. *et al.* (2018). Gaia data release 2-summary of the contents and survey properties. *Astronomy & astrophysics*, **616**, A1.

Bryson, S., Kunimoto, M., Kopparapu, R.K., Coughlin, J.L., Borucki, W.J., Koch, D., Aguirre, V.S., Allen, C., Barentsen, G., Batalha, N.M., Berger, T., Boss, A., Buchhave, L.A., Burke, C.J., Caldwell, D.A., Campbell, J.R., Catanzarite, J., Chandrasekaran, H., Chaplin, W.J., Christiansen, J.L., Christensen-Dalsgaard, J., Ciardi, D.R., Clarke, B.D., Cochran, W.D., Dotson, J.L., Doyle, L.R., Duarte, E.S., Dunham, E.W., Dupree, A.K., Endl, M., Fanson, J.L., Ford, E.B., Fujieh, M., Gautier, I., Thomas N., Geary, J.C., Gilliland, R.L., Girouard, F.R., Gould, A., Haas, M.R., Henze, C.E., Holman, M.J., Howard, A.W., Howell, S.B., Huber, D., Hunter, R.C., Jenkins, J.M., Kjeldsen, H., Kolodziejczak, J., Larson, K., Latham, D.W., Li, J., Mathur, S., Meibom, S., Middour, C., Morris, R.L., Morton, T.D., Mullally, F., Mullally, S.E., Pletcher, D., Prsa, A., Quinn, S.N., Quintana, E.V., Ragozzine, D., Ramirez, S.V., Sanderfer, D.T., Sasselov, D., Seader, S.E., Shabram, M., Shporer, A., Smith, J.C., Steffen, J.H., Still, M., Torres, G., Troeltzsch, J., Twicken, J.D., Uddin, A.K.,

Van Cleve, J.E., Voss, J., Weiss, L.M., Welsh, W.F., Wohler, B. & Zamudio, K.A. (2021). The Occurrence of Rocky Habitable-zone Planets around Solar-like Stars from Kepler Data. *AJ*, **161**, 36.

Burgasser, A.J. & Mamajek, E.E. (2017). On the Age of the TRAPPIST-1 System. *ApJ*, **845**, 110.

Burke, C.J., Christiansen, J.L., Mullally, F., Seader, S., Huber, D., Rowe, J.F., Coughlin, J.L., Thompson, S.E., Catanzarite, J., Clarke, B.D., Morton, T.D., Caldwell, D.A., Bryson, S.T., Haas, M.R., Batalha, N.M., Jenkins, J.M., Tenenbaum, P., Twicken, J.D., Li, J., Quintana, E., Barclay, T., Henze, C.E., Borucki, W.J., Howell, S.B. & Still, M. (2015). Terrestrial Planet Occurrence Rates for the Kepler GK Dwarf Sample. *ApJ*, **809**, 8.

Butchart, N. (2014). The Brewer-Dobson circulation. *Reviews of Geophysics*, **52**, 157–184.

Běhounková, M., Tobie, G., Choblet, G. & Čadek, O. (2011). Tidally Induced Thermal Runaways on Extrasolar Earths: Impact on Habitability. *ApJ*, **728**, 89.

Caballero, R. (2014). *Physics of the Atmosphere*, vol. 150. IOP Publishing Bristol.

Cadeau, P., Jézéquel, D., Leboulanger, C., Fouilland, É., Le Floc'h, E., Chaduteau, C., Milesi, V., Guélard, J., Sarazin, G., Katz, A. *et al.* (2020). Carbon isotope evidence for large methane emissions to the proterozoic atmosphere. *Scientific reports*, **10**, 1–13.

Camacho, A., Miracle, M.R., Romero-Viana, L., Picazo, A. & Vicente, E. (2017). Lake la cruz, an iron-rich karstic meromictic lake in central

spain. In R.D. Gulati, E.S. Zadereev & A.G. Degermendzhi, eds., *Ecology of meromictic lakes*, 187–233, Springer, Cham.

Campbell, I.H. & Squire, R.J. (2010). The mountains that triggered the Late Neoproterozoic increase in oxygen: The Second Great Oxidation Event. *Geochimica Cosmochimica Acta*, **74**, 4187–4206.

Canfield, D.E., Ngombi-Pemba, L., Hammarlund, E.U., Bengtson, S., Chaussidon, M., Gauthier-Lafaye, F., Meunier, A., Riboulleau, A., Rollion-Bard, C., Rouxel, O., Asael, D., Pierson-Wickmann, A.C. & El Albani, A. (2013). Oxygen dynamics in the aftermath of the Great Oxidation of Earth's atmosphere. *Proceedings of the National Academy of Science*, **110**, 16736–16741.

Carnall, A.C. (2017). SpectRes: A Fast Spectral Resampling Tool in Python. *arXiv e-prints*, arXiv:1705.05165.

Carone, L., Keppens, R. & Decin, L. (2015). Connecting the dots - II. Phase changes in the climate dynamics of tidally locked terrestrial exoplanets. *MNRAS*, **453**, 2412–2437.

Carone, L., Keppens, R., Decin, L. & Henning, T. (2018). Stratosphere circulation on tidally locked ExoEarths. *MNRAS*, **473**, 4672–4685.

Carrillo, A., Hawkins, K., Bowler, B.P., Cochran, W. & Vanderburg, A. (2020). Know thy star, know thy planet: chemo-kinematically characterizing TESS targets. *MNRAS*, **491**, 4365–4381.

Catanzarite, J. & Shao, M. (2011). The Occurrence Rate of Earth Analog Planets Orbiting Sun-like Stars. *ApJ*, **738**, 151.

Catling, D.C. & Claire, M.W. (2005). How Earth's atmosphere evolved to an oxic state: A status report. *Earth and Planetary Science Letters*, **237**, 1–20.

Catling, D.C. & Zahnle, K.J. (2020). The Archean atmosphere. *Science Advances*, **6**, eaax1420.

Catling, D.C., Zahnle, K.J. & McKay, C.P. (2001). Biogenic Methane, Hydrogen Escape, and the Irreversible Oxidation of Early Earth. *Science*, **293**, 839–843.

Catling, D.C., Krissansen-Totton, J., Kiang, N.Y., Crisp, D., Robinson, T.D., DasSarma, S., Rushby, A.J., Del Genio, A., Bains, W. & Domagal-Goldman, S. (2018). Exoplanet Biosignatures: A Framework for Their Assessment. *Astrobiology*, **18**, 709–738.

Ceppi, P., Brient, F., Zelinka, M.D. & Hartmann, D.L. (2017). Cloud feedback mechanisms and their representation in global climate models. *Wiley Interdisciplinary Reviews: Climate Change*, **8**, e465.

Chameides, W.L. (1986). The role of lightning in the chemistry of the atmosphere. *The Earth's Electrical Environment*, **70**, 80.

Chapman, S. (1930). Xxxv. on ozone and atomic oxygen in the upper atmosphere. *The London, Edinburgh, and Dublin Philosophical Magazine and Journal of Science*, **10**, 369–383.

Charbonneau, D., Brown, T.M., Noyes, R.W. & Gilliland, R.L. (2002). Detection of an extrasolar planet atmosphere. *The Astrophysical Journal*, **568**, 377–384.

Charnay, B., Wolf, E.T., Marty, B. & Forget, F. (2020). Is the Faint Young Sun Problem for Earth Solved? *Space Science Reviews*, **216**, 90.

Checlair, J., Menou, K. & Abbot, D.S. (2017). No Snowball on Habitable Tidally Locked Planets. *ApJ*, **845**, 132.

Checlair, J.H., Villanueva, G.L., Hayworth, B.P.C., Olson, S.L., Komacek, T.D., Robinson, T.D., Popović, P., Yang, H. & Abbot, D.S. (2021). Probing the Capability of Future Direct-imaging Missions to Spectrally Constrain the Frequency of Earth-like Planets. *AJ*, **161**, 150.

Chen, H., Wolf, E.T., Kopparapu, R., Domagal-Goldman, S. & Horton, D.E. (2018). Biosignature Anisotropy Modeled on Temperate Tidally Locked M-dwarf Planets. *ApJ*, **868**, L6.

Chen, H., Wolf, E.T., Zhan, Z. & Horton, D.E. (2019). Habitability and Spectroscopic Observability of Warm M-dwarf Exoplanets Evaluated with a 3D Chemistry-Climate Model. *ApJ*, **886**, 16.

Chen, H., Zhan, Z., Youngblood, A., Wolf, E.T., Feinstein, A.D. & Horton, D.E. (2021). Persistence of flare-driven atmospheric chemistry on rocky habitable zone worlds. *Nature Astronomy*, **5**, 298–310.

Chen, H., Li, G., Paradise, A. & Kopparapu, R. (2023). Sporadic Spin-Orbit Variations in Compact Multi-planet Systems and their Influence on Exoplanet Climate. *arXiv e-prints*, arXiv:2302.11561.

Chen, J. & Kipping, D. (2017). Probabilistic Forecasting of the Masses and Radii of Other Worlds. *ApJ*, **834**, 17.

Chen, T., Rossow, W.B. & Zhang, Y. (2000). Radiative Effects of Cloud-Type Variations. *Journal of Climate*, **13**, 264–286.

Chen, X., Ling, H.F., Vance, D., Shields-Zhou, G.A., Zhu, M., Poulton, S.W., Och, L.M., Jiang, S.Y., Li, D., Cremonese, L. & Archer,

C. (2015). Rise to modern levels of ocean oxygenation coincided with the Cambrian radiation of animals. *Nature Communications*, **6**, 7142.

Chiavassa, A., Caldas, A., Selsis, F., Leconte, J., Von Paris, P., Bordé, P., Magic, Z., Collet, R. & Asplund, M. (2017). Measuring stellar granulation during planet transits. *A&A*, **597**, A94.

Chipperfield, M. & Arnold, S. (2015). Numerical models — chemistry models. In G.R. North, J. Pyle & F. Zhang, eds., *Encyclopedia of Atmospheric Sciences (Second Edition)*, 135–143, Academic Press, Oxford, second edition edn.

Claire, M.W., Sheets, J., Cohen, M., Ribas, I., Meadows, V.S. & Catling, D.C. (2012). The Evolution of Solar Flux from 0.1 nm to 160 μm: Quantitative Estimates for Planetary Studies. *The Astrophysical Journal*, **757**, 95.

Clough, S.A., Iacono, M.J. & Moncet, J.L. (1992). Line-by-Line Calculations of Atmospheric Fluxes and Cooling Rates: Application to Water Vapor. *J. Geophys. Res.*, **97**, 15,761–15,785.

Clough, S.A., Shephard, M.W., Mlawer, E.J., Delamere, J.S., Iacono, M.J., Cady-Pereira, K., Boukabara, S. & Brown, P.D. (2005). Atmospheric radiative transfer modeling: a summary of the AER codes. *J. Quant. Spec. Radiat. Transf.*, **91**, 233–244.

Cockell, C.S. (1999). Crises and extinction in the fossil record—a role for ultraviolet radiation? *Paleobiology*, **25**, 212–225.

Cockell, C.S. & Horneck, G. (2001). The history of the uv radiation climate of the earth—theoretical and space-based observations. *Photochemistry and Photobiology*, **73**, 447–451.

Cockell, C.S. & Raven, J.A. (2007). Ozone and life on the Archaean Earth. *Philosophical Transactions of the Royal Society of London Series A*, **365**, 1889–1901.

Cockell, C.S., Rettberg, P., Rabbow, E. & Olsson-Francis, K. (2011). Exposure of phototrophs to 548 days in low earth orbit: microbial selection pressures in outer space and on early earth. *The ISME Journal*, **5**, 1671–1682.

Cockell, C.S., Bush, T., Bryce, C., Direito, S., Fox-Powell, M., Harrison, J.P., Lammer, H., Landenmark, H., Martin-Torres, J., Nicholson, N., Noack, L., O'Malley-James, J., Payler, S.J., Rushby, A., Samuels, T., Schwendner, P., Wadsworth, J. & Zorzano, M.P. (2016). Habitability: A Review. *Astrobiology*, **16**, 89–117.

Cohen, M., Bollasina, M.A., Palmer, P.I., Sergeev, D.E., Boutle, I.A., Mayne, N.J. & Manners, J. (2022). Longitudinally Asymmetric Stratospheric Oscillation on a Tidally Locked Exoplanet. *ApJ*, **930**, 152.

Cohen, N.Y., Gerber, E.P. & Bühler, O. (2014). What Drives the Brewer-Dobson Circulation? *Journal of Atmospheric Sciences*, **71**, 3837–3855.

Cohen, O., Ma, Y., Drake, J.J., Glocer, A., Garraffo, C., Bell, J.M. & Gombosi, T.I. (2015). The Interaction of Venus-like, M-dwarf Planets with the Stellar Wind of Their Host Star. *ApJ*, **806**, 41.

Cole, D.B., Mills, D.B., Erwin, D.H., Sperling, E.A., Porter, S.M., Reinhard, C.T. & Planavsky, N.J. (2020). On the co-evolution of surface oxygen levels and animals. *Geobiology*, **18**, 260–281.

Cooke, G.J., Marsh, D.R., Walsh, C., Black, B. & Lamarque, J.F. (2022). A revised lower estimate of ozone columns during Earth's oxygenated history. *Royal Society Open Science*, **9**, 211165.

Cooke, G.J., Marsh, D.R., Walsh, C., Rugheimer, S. & Villanueva, G.L. (2023). Variability due to climate and chemistry in observations of oxygenated Earth-analogue exoplanets. *MNRAS*, **518**, 206–219.

Costa, E., Méndez, R.A., Jao, W.C., Henry, T.J., Subasavage, J.P. & Ianna, P.A. (2006). The Solar Neighborhood. XVI. Parallaxes from CTIOPI: Final Results from the 1.5 m Telescope Program. *AJ*, **132**, 1234–1247.

Couvreux, F., Hourdin, F., Williamson, D., Roehrig, R., Volodina, V., Villefranque, N., Rio, C., Audouin, O., Salter, J., Bazile, E., Brient, F., Favot, F., Honnert, R., Lefebvre, M.P., Madeleine, J.B., Rodier, Q. & Xu, W. (2021). Process Based Climate Model Development Harnessing Machine Learning: I. A Calibration Tool for Parameterization Improvement. *Journal of Advances in Modeling Earth Systems*, **13**, e2020MS002217.

Cowan, N.B. & Fujii, Y. (2018). *Mapping Exoplanets*, 147.

Cowan, N.B., Voigt, A. & Abbot, D.S. (2012). Thermal Phases of Earth-like Planets: Estimating Thermal Inertia from Eccentricity, Obliquity, and Diurnal Forcing. *ApJ*, **757**, 80.

Crockford, P.W., Hayles, J.A., Bao, H., Planavsky, N.J., Bekker, A., Fralick, P.W., Halverson, G.P., Bui, T.H., Peng, Y. & Wing, B.A. (2018). Triple oxygen isotope evidence for limited mid-Proterozoic primary productivity. *Nature*, **559**, 613–616.

Currie, T., Biller, B., Lagrange, A.M., Marois, C., Guyon, O., Nielsen, E., Bonnefoy, M. & De Rosa, R. (2022). Direct Imaging and Spectroscopy of Extrasolar Planets. *arXiv e-prints*, arXiv:2205.05696.

Daines, S.J. & Lenton, T.M. (2016). The effect of widespread early aerobic marine ecosystems on methane cycling and the Great Oxidation. *Earth and Planetary Science Letters*, **434**, 42–51.

Danabasoglu, G., Lamarque, J.F., Bacmeister, J., Bailey, D.A., DuVivier, A.K.Â., Edwards, J., Emmons, L.K., Fasullo, J., Garcia, R., Gettelman, A., Hannay, C., Holland, M.M., Large, W.G., Lauritzen, P.H., Lawrence, D.M., Lenaerts, J.T.M., Lindsay, K., Lipscomb, W.H., Mills, M.J., Neale, R., Oleson, K.W., Otto-Bliesner, B., Phillips, A.S., Sacks, W., Tilmes, S., van Kampenhout, L., Vertenstein, M., Bertini, A., Dennis, J., Deser, C., Fischer, C., Fox-Kemper, B., Kay, J.E., Kinnison, D., Kushner, P.J., Larson, V.E., Long, M.C., Mickelson, S., Moore, J.K., Nienhouse, E., Polvani, L., Rasch, P.J. & Strand, W.G. (2020). The Community Earth System Model Version 2 (CESM2). *Journal of Advances in Modeling Earth Systems*, **12**, e01916.

Davenport, J.R.A., Kipping, D.M., Sasselov, D., Matthews, J.M. & Cameron, C. (2016). MOST Observations of Our Nearest Neighbor: Flares on Proxima Centauri. *ApJ*, **829**, L31.

Davies, R.E. & Forbes, P.D. (1986). Effect of uv radiation on survival of non-haired mice. *Photochemistry and photobiology*, **43**, 267–274.

De Cock, R., Livengood, T.A., Stam, D.M., Lisse, C.M., Hewagama, T. & Deming, L.D. (2022). Terrestrial Planet Optical Phase Curves. I. Direct Measurements of the Earth. *AJ*, **163**, 5.

de Wit, J., Wakeford, H.R., Lewis, N.K., Delrez, L., Gillon, M., Selsis, F., Leconte, J., Demory, B.O., Bolmont, E., Bourrier, V., Burgasser, A.J., Grimm, S., Jehin, E., Lederer, S.M., Owen, J.E., Stamenković, V. & Triaud, A.H.M.J. (2018). Atmospheric reconnaissance of the habitable-zone Earth-sized planets orbiting TRAPPIST-1. *Nature Astronomy*, **2**, 214–219.

Defrère, D., Léger, A., Absil, O., Beichman, C., Biller, B., Danchi, W.C., Ergenzinger, K., Eiroa, C., Ertel, S., Fridlund, M., Muñoz, A.G., Gillon, M., Glasse, A., Godolt, M., Grenfell, J.L., Kraus, S., Labadie, L., Lacour, S., Liseau, R., Martin, G., Mennesson, B., Micela, G., Minardi, S., Quanz, S.P., Rauer, H., Rinehart, S., Santos, N.C., Selsis, F., Surdej, J., Tian, F., Villaver, E., Wheatley, P.J. & Wyatt, M. (2018). Space-based infrared interferometry to study exoplanetary atmospheres. *Experimental Astronomy*, **46**, 543–560.

Deitrick, R. & Goldblatt, C. (2022). Effects of ozone levels on climate through earth history. *EGUsphere*, 1–27.

Del Genio, A.D., Kiang, N.Y., Way, M.J., Amundsen, D.S., Sohl, L.E., Fujii, Y., Chandler, M., Aleinov, I., Colose, C.M., Guzewich, S.D. & Kelley, M. (2019a). Albedos, Equilibrium Temperatures, and Surface Temperatures of Habitable Planets. *ApJ*, **884**, 75.

Del Genio, A.D., Way, M.J., Amundsen, D.S., Aleinov, I., Kelley, M., Kiang, N.Y. & Clune, T.L. (2019b). Habitable Climate Scenarios for Proxima Centauri b with a Dynamic Ocean. *Astrobiology*, **19**, 99–125.

Delfosse, X., Forveille, T., Ségransan, D., Beuzit, J.L., Udry, S., Perrier, C. & Mayor, M. (2000). Accurate masses of very low mass stars. IV. Improved mass-luminosity relations. *A&A*, **364**, 217–224.

Delrez, L., Gillon, M., Triaud, A.H.M.J., Demory, B.O., de Wit, J., Ingalls, J.G., Agol, E., Bolmont, E., Burdanov, A., Burgasser, A.J., Carey, S.J., Jehin, E., Leconte, J., Lederer, S., Queloz, D., Selsis, F. & Van Grootel, V. (2018). Early 2017 observations of TRAPPIST-1 with Spitzer. *MNRAS*, **475**, 3577–3597.

Demory, B.O., Gillon, M., de Wit, J., Madhusudhan, N., Bolmont, E., Heng, K., Kataria, T., Lewis, N., Hu, R., Krick, J., Stamenković, V., Benneke, B., Kane, S. & Queloz, D. (2016). A map of the large day-night temperature gradient of a super-Earth exoplanet. *Nature*, **532**, 207–209.

Dittmann, J.A., Irwin, J.M., Charbonneau, D., Bonfils, X., Astudillo-Defru, N., Haywood, R.D., Berta-Thompson, Z.K., Newton, E.R., Rodriguez, J.E., Winters, J.G., Tan, T.G., Almenara, J.M., Bouchy, F., Delfosse, X., Forveille, T., Lovis, C., Murgas, F., Pepe, F., Santos, N.C., Udry, S., Wünsche, A., Esquerdo, G.A., Latham, D.W. & Dressing, C.D. (2017). A temperate rocky super-Earth transiting a nearby cool star. *Nature*, **544**, 333–336.

Dobos, V., Heller, R. & Turner, E.L. (2017). The effect of multiple heat sources on exomoon habitable zones. *A&A*, **601**, A91.

Dodd, M.S., Papineau, D., Grenne, T., Slack, J.F., Rittner, M., Pirajno, F., O'Neil, J. & Little, C.T.S. (2017). Evidence for early life in Earth's oldest hydrothermal vent precipitates. *Nature*, **543**, 60–64.

Domagal-Goldman, S.D., Segura, A., Claire, M.W., Robinson, T.D. & Meadows, V.S. (2014). Abiotic Ozone and Oxygen in Atmospheres Similar to Prebiotic Earth. *ApJ*, **792**, 90.

Dong, C., Lingam, M., Ma, Y. & Cohen, O. (2017). Is Proxima Centauri b Habitable? A Study of Atmospheric Loss. *ApJ*, **837**, L26.

Dong, C., Jin, M., Lingam, M., Airapetian, V.S., Ma, Y. & van der Holst, B. (2018). Atmospheric escape from the TRAPPIST-1 planets and implications for habitability. *Proceedings of the National Academy of Science*, **115**, 260–265.

Dunkerton, T.J. (1997). The role of gravity waves in the quasi-biennial oscillation. *J. Geophys. Res.*, **102**, 26053–26076.

Eager-Nash, J.K., Reichelt, D.J., Mayne, N.J., Hugo Lambert, F., Sergeev, D.E., Ridgway, R.J., Manners, J., Boutle, I.A., Lenton, T.M. & Kohary, K. (2020). Implications of different stellar spectra for the climate of tidally locked Earth-like exoplanets. *A&A*, **639**, A99.

Edwards, P.N. (2011). History of climate modeling. *Wiley Interdisciplinary Reviews: Climate Change*, **2**, 128–139.

Ehrenreich, D., Tinetti, G., Lecavelier Des Etangs, A., Vidal-Madjar, A. & Selsis, F. (2006). The transmission spectrum of Earth-size transiting planets. *A&A*, **448**, 379–393.

Emmons, L.K., Walters, S., Hess, P.G., Lamarque, J.F., Pfister, G.G., Fillmore, D., Granier, C., Guenther, A., Kinnison, D., Laepple, T., Orlando, J., Tie, X., Tyndall, G., Wiedinmyer, C., Baughcum, S.L. & Kloster, S. (2010). Description and evaluation of the Model for Ozone and Related chemical Tracers, version 4 (MOZART-4). *Geoscientific Model Development*, **3**, 43–67.

Emmons, L.K., Schwantes, R.H., Orlando, J.J., Tyndall, G., Kinnison, D., Lamarque, J.F., Marsh, D., Mills, M.J., Tilmes, S., Bardeen, C., Buchholz, R.R., Conley, A., Gettelman, A., Garcia, R., Simpson, I., Blake, D.R., Meinardi, S. & Pétron, G. (2020). The Chemistry Mechanism in the Community Earth System Model Version 2 (CESM2). *Journal of Advances in Modeling Earth Systems*, **12**, e01882.

Encrenaz, T. (2014). Infrared spectroscopy of exoplanets: observational constraints. *Philosophical Transactions of the Royal Society of London Series A*, **372**, 20130083–20130083.

Erwin, D.H. (2020). The origin of animal body plans: a view from fossil evidence and the regulatory genome. *Development*, **147**, dev182899.

Espinoza, N. & Jordán, A. (2015). Limb darkening and exoplanets: testing stellar model atmospheres and identifying biases in transit parameters. *MNRAS*, **450**, 1879–1899.

Fakhraee, M., Hancisse, O., Canfield, D.E., Crowe, S.A. & Katsev, S. (2019). Proterozoic seawater sulfate scarcity and the evolution of ocean-atmosphere chemistry. *Nature Geoscience*, **12**, 375–380.

Fan, S., Li, C., Li, J.Z., Bartlett, S., Jiang, J.H., Natraj, V., Crisp, D. & Yung, Y.L. (2019). Earth as an Exoplanet: A Two-dimensional Alien Map. *The Astrophysical Journal Letters*, **882**, L1.

Fanson, J., Bernstein, R., Angeli, G., Ashby, D., Bigelow, B., Brossus, G., Bouchez, A., Burgett, W., Contos, A., Demers, R., Figueroa, F., Fischer, B., Groark, F., Laskin, R., Millan-Gabet, R., Pi, M. & Wheeler, N. (2020). Overview and status of the Giant Magellan Telescope project. In *Society of Photo-Optical Instrumentation Engineers (SPIE) Conference Series*, vol. 11445 of *Society of Photo-Optical Instrumentation Engineers (SPIE) Conference Series*, 114451F.

Faria, J.P., Suárez Mascareño, A., Figueira, P., Silva, A.M., Damasso, M., Demangeon, O., Pepe, F., Santos, N.C., Rebolo, R., Cristiani, S., Adibekyan, V., Alibert, Y., Allart, R., Barros, S.C.C., Cabral, A., D'Odorico, V., Di Marcantonio, P., Dumusque, X., Ehrenreich, D., González Hernández, J.I., Hara, N., Lillo-Box, J., Lo Curto, G., Lovis, C., Martins, C.J.A.P., Mégevand, D., Mehner, A., Micela, G., Molaro, P., Nunes, N.J., Pallé, E., Poretti, E., Sousa, S.G., Sozzetti, A., Tabernero, H., Udry, S. & Zapatero Osorio, M.R. (2022). A candidate short-period sub-Earth orbiting Proxima Centauri. *A&A*, **658**, A115.

Farmer, D.K., Cappa, C.D. & Kreidenweis, S.M. (2015). Atmospheric processes and their controlling influence on cloud condensation nuclei activity. *Chemical Reviews*, **115**, 4199–4217.

Farquhar, J., Bao, H. & Thiemens, M. (2000). Atmospheric Influence of Earth's Earliest Sulfur Cycle. *Science*, **289**, 756–759.

Farquhar, J., Savarino, J., Airieau, S. & Thiemens, M.H. (2001). Observation of wavelength-sensitive mass-independent sulfur isotope effects during SO_2 photolysis: Implications for the early atmosphere. *J. Geophys. Res.*, **106**, 32829–32840.

Fauchez, T.J., Turbet, M., Villanueva, G.L., Wolf, E.T., Arney, G., Kopparapu, R.K., Lincowski, A., Mandell, A., de Wit, J., Pidhorodetska, D., Domagal-Goldman, S.D. & Stevenson, K.B. (2019). Impact of Clouds and Hazes on the Simulated JWST Transmission Spectra of Habitable Zone Planets in the TRAPPIST-1 System. *ApJ*, **887**, 194.

Fauchez, T.J., Turbet, M., Wolf, E.T., Boutle, I., Way, M.J., Del Genio, A.D., Mayne, N.J., Tsigaridis, K., Kopparapu, R.K., Yang, J., Forget, F., Mandell, A. & Domagal Goldman, S.D. (2020a). TRAPPIST-1 Habitable Atmosphere Intercomparison (THAI): motivations and protocol version 1.0. *Geoscientific Model Development*, **13**, 707–716.

Fauchez, T.J., Villanueva, G.L., Schwieterman, E.W., Turbet, M., Arney, G., Pidhorodetska, D., Kopparapu, R.K., Mandell, A. & Domagal-Goldman, S.D. (2020b). Sensitive probing of exoplanetary oxygen via mid-infrared collisional absorption. *Nature Astronomy*, **4**, 372–376.

Fauchez, T.J., Turbet, M., Sergeev, D.E., Mayne, N.J., Spiga, A., Sohl, L., Saxena, P., Deitrick, R., Gilli, G., Domagal-Goldman, S.D., Forget, F., Consentino, R., Barnes, R., Haqq-Misra, J., Way, M.J., Wolf, E.T., Olson, S., Crouse, J.S., Janin, E., Bolmont, E., Leconte, J., Chaverot, G., Jaziri, Y., Tsigaridis, K., Yang, J., Pidhorodetska, D., Kopparapu, R.K., Chen, H., Boutle, I.A., Lefevre, M., Charnay, B., Burnett, A., Cabra, J. & Bouldin, N.

(2021). TRAPPIST Habitable Atmosphere Intercomparison (THAI) Workshop Report. , **2**, 106.

Fauchez, T.J., Villanueva, G.L., Sergeev, D.E., Turbet, M., Boutle, I.A., Tsigaridis, K., Way, M.J., Wolf, E.T., Domagal-Goldman, S.D., Forget, F., Haqq-Misra, J., Kopparapu, R.K., Manners, J. & Mayne, N.J. (2022). The TRAPPIST-1 Habitable Atmosphere Intercomparison (THAI). III. Simulated Observables-the Return of the Spectrum. , **3**, 213.

Feulner, G. (2012). The faint young Sun problem. *Reviews of Geophysics*, **50**, RG2006.

Fiorella, R.P. & Sheldon, N.D. (2017). Equable end Mesoproterozoic climate in the absence of high CO2. *Geology*, **45**, 231–234.

Foias, C., Manley, O., Rosa, R. & Temam, R. (2001). *Navier-Stokes equations and turbulence*, vol. 83. Cambridge University Press.

Ford, E.B., Seager, S. & Turner, E.L. (2001). Characterization of extrasolar terrestrial planets from diurnal photometric variability. *Nature*, **412**, 885–887.

Forget, F. & Pierrehumbert, R.T. (1997). Warming Early Mars with Carbon Dioxide Clouds That Scatter Infrared Radiation. *Science*, **278**, 1273.

France, K., Duvvuri, G., Egan, H., Koskinen, T., Wilson, D.J., Youngblood, A., Froning, C.S., Brown, A., Alvarado-Gómez, J.D., Berta-Thompson, Z.K., Drake, J.J., Garraffo, C., Kaltenegger, L., Kowalski, A.F., Linsky, J.L., Loyd, R.O.P., Mauas, P.J.D., Miguel, Y., Pineda, J.S., Rugheimer, S., Schneider, P.C., Tian,

F. & Vieytes, M. (2020). The High-energy Radiation Environment around a 10 Gyr M Dwarf: Habitable at Last? *AJ*, **160**, 237.

Fressin, F., Torres, G., Charbonneau, D., Bryson, S.T., Christiansen, J., Dressing, C.D., Jenkins, J.M., Walkowicz, L.M. & Batalha, N.M. (2013). The False Positive Rate of Kepler and the Occurrence of Planets. *ApJ*, **766**, 81.

Froning, C.S., Kowalski, A., France, K., Loyd, R.O.P., Schneider, P.C., Youngblood, A., Wilson, D., Brown, A., Berta-Thompson, Z., Pineda, J.S., Linsky, J., Rugheimer, S. & Miguel, Y. (2019). A Hot Ultraviolet Flare on the M Dwarf Star GJ 674. *ApJ*, **871**, L26.

Fu, G., Sing, D.K., Lothringer, J.D., Deming, D., Ih, J., Kempton, E.M.R., Malik, M., Komacek, T.D., Mansfield, M. & Bean, J.L. (2022). Strong H_2O and CO Emission Features in the Spectrum of KELT-20b Driven by Stellar UV Irradiation. *ApJ*, **925**, L3.

Fueglistaler, S., Dessler, A.E., Dunkerton, T.J., Folkins, I., Fu, Q. & Mote, P.W. (2009). Tropical tropopause layer. *Reviews of Geophysics*, **47**, RG1004.

Fujii, Y., Kawahara, H., Suto, Y., Fukuda, S., Nakajima, T., Livengood, T.A. & Turner, E.L. (2011). Colors of a Second Earth. II. Effects of Clouds on Photometric Characterization of Earth-like Exoplanets. *ApJ*, **738**, 184.

Fulton, B.J., Petigura, E.A., Howard, A.W., Isaacson, H., Marcy, G.W., Cargile, P.A., Hebb, L., Weiss, L.M., Johnson, J.A., Morton, T.D., Sinukoff, E., Crossfield, I.J.M. & Hirsch, L.A. (2017).

The California-Kepler Survey. III. A Gap in the Radius Distribution of Small Planets. *AJ*, **154**, 109.

Gaia Collaboration, Brown, A.G.A., Vallenari, A., Prusti, T., de Bruijne, J.H.J., Mignard, F., Drimmel, R., Babusiaux, C., Bailer-Jones, C.A.L., Bastian, U., Biermann, M., Evans, D.W., Eyer, L., Jansen, F., Jordi, C., Katz, D., Klioner, S.A., Lammers, U., Lindegren, L., Luri, X., O'Mullane, W., Panem, C., Pourbaix, D., Randich, S., Sartoretti, P., Siddiqui, H.I., Soubiran, C., Valette, V., van Leeuwen, F., Walton, N.A., Aerts, C., Arenou, F., Cropper, M., Høg, E., Lattanzi, M.G., Grebel, E.K., Holland, A.D., Huc, C., Passot, X., Perryman, M., Bramante, L., Cacciari, C., Castañeda, J., Chaoul, L., Cheek, N., De Angeli, F., Fabricius, C., Guerra, R., Hernández, J., Jean-Antoine-Piccolo, A., Masana, E., Messineo, R., Mowlavi, N., Nienartowicz, K., Ordóñez-Blanco, D., Panuzzo, P., Portell, J., Richards, P.J., Riello, M., Seabroke, G.M., Tanga, P., Thévenin, F., Torra, J., Els, S.G., Gracia-Abril, G., Comoretto, G., Garcia-Reinaldos, M., Lock, T., Mercier, E., Altmann, M., Andrae, R., Astraatmadja, T.L., Bellas-Velidis, I., Benson, K., Berthier, J., Blomme, R., Busso, G., Carry, B., Cellino, A., Clementini, G., Cowell, S., Creevey, O., Cuypers, J., Davidson, M., De Ridder, J., de Torres, A., Delchambre, L., Dell'Oro, A., Ducourant, C., Frémat, Y., García-Torres, M., Gosset, E., Halbwachs, J.L., Hambly, N.C., Harrison, D.L., Hauser, M., Hestroffer, D., Hodgkin, S.T., Huckle, H.E., Hutton, A., Jasniewicz, G., Jordan, S., Kontizas, M., Korn, A.J., Lanzafame, A.C., Manteiga, M., Moitinho, A., Muinonen, K., Osinde, J., Pancino, E., Pauwels, T., Petit, J.M., Recio-Blanco,

A., Robin, A.C., Sarro, L.M., Siopis, C., Smith, M., Smith, K.W., Sozzetti, A., Thuillot, W., van Reeven, W., Viala, Y., Abbas, U., Abreu Aramburu, A., Accart, S., Aguado, J.J., Allan, P.M., Allasia, W., Altavilla, G., Álvarez, M.A., Alves, J., Anderson, R.I., Andrei, A.H., Anglada Varela, E., Antiche, E., Antoja, T., Antón, S., Arcay, B., Bach, N., Baker, S.G., Balaguer-Núñez, L., Barache, C., Barata, C., Barbier, A., Barblan, F., Barrado y Navascués, D., Barros, M., Barstow, M.A., Becciani, U., Bellazzini, M., Bello García, A., Belokurov, V., Bendjoya, P., Berihuete, A., Bianchi, L., Bienaymé, O., Billebaud, F., Blagorodnova, N., Blanco-Cuaresma, S., Boch, T., Bombrun, A., Borrachero, R., Bouquillon, S., Bourda, G., Bouy, H., Bragaglia, A., Breddels, M.A., Brouillet, N., Brüsemeister, T., Bucciarelli, B., Burgess, P., Burgon, R., Burlacu, A., Busonero, D., Buzzi, R., Caffau, E., Cambras, J., Campbell, H., Cancelliere, R., Cantat-Gaudin, T., Carlucci, T., Carrasco, J.M., Castellani, M., Charlot, P., Charnas, J., Chiavassa, A., Clotet, M., Cocozza, G., Collins, R.S., Costigan, G., Crifo, F., Cross, N.J.G., Crosta, M., Crowley, C., Dafonte, C., Damerdji, Y., Dapergolas, A., David, P., David, M., De Cat, P., de Felice, F., de Laverny, P., De Luise, F., De March, R., de Martino, D., de Souza, R., Debosscher, J., del Pozo, E., Delbo, M., Delgado, A., Delgado, H.E., Di Matteo, P., Diakite, S., Distefano, E., Dolding, C., Dos Anjos, S., Drazinos, P., Duran, J., Dzigan, Y., Edvardsson, B., Enke, H., Evans, N.W., Eynard Bontemps, G., Fabre, C., Fabrizio, M., Faigler, S., Falcão, A.J., Farràs Casas, M., Federici, L., Fedorets, G., Fernández-Hernández, J., Fernique, P., Fienga, A., Figueras, F.,

Filippi, F., Findeisen, K., Fonti, A., Fouesneau, M., Fraile, E., Fraser, M., Fuchs, J., Gai, M., Galleti, S., Galluccio, L., Garabato, D., García-Sedano, F., Garofalo, A., Garralda, N., Gavras, P., Gerssen, J., Geyer, R., Gilmore, G., Girona, S., Giuffrida, G., Gomes, M., González-Marcos, A., González-Núñez, J., González-Vidal, J.J., Granvik, M., Guerrier, A., Guillout, P., Guiraud, J., Gúrpide, A., Gutiérrez-Sánchez, R., Guy, L.P., Haigron, R., Hatzidimitriou, D., Haywood, M., Heiter, U., Helmi, A., Hobbs, D., Hofmann, W., Holl, B., Holland, G., Hunt, J.A.S., Hypki, A., Icardi, V., Irwin, M., Jevardat de Fombelle, G., Jofré, P., Jonker, P.G., Jorissen, A., Julbe, F., Karampelas, A., Kochoska, A., Kohley, R., Kolenberg, K., Kontizas, E., Koposov, S.E., Kordopatis, G., Koubsky, P., Krone-Martins, A., Kudryashova, M., Kull, I., Bachchan, R.K., Lacoste-Seris, F., Lanza, A.F., Lavigne, J.B., Le Poncin-Lafitte, C., Lebreton, Y., Lebzelter, T., Leccia, S., Leclerc, N., Lecoeur-Taibi, I., Lemaitre, V., Lenhardt, H., Leroux, F., Liao, S., Licata, E., Lindstrøm, H.E.P., Lister, T.A., Livanou, E., Lobel, A., Löffler, W., López, M., Lorenz, D., MacDonald, I., Magalhães Fernandes, T., Managau, S., Mann, R.G., Mantelet, G., Marchal, O., Marchant, J.M., Marconi, M., Marinoni, S., Marrese, P.M., Marschalkó, G., Marshall, D.J., Martín-Fleitas, J.M., Martino, M., Mary, N., Matijevič, G., Mazeh, T., McMillan, P.J., Messina, S., Michalik, D., Millar, N.R., Miranda, B.M.H., Molina, D., Molinaro, R., Molinaro, M., Molnár, L., Moniez, M., Montegriffo, P., Mor, R., Mora, A., Morbidelli, R., Morel, T., Morgenthaler, S., Morris, D., Mulone, A.F., Muraveva, T., Musella, I., Narbonne, J., Nelemans, G., Nicastro, L.,

Noval, L., Ordénovic, C., Ordieres-Meré, J., Osborne, P., Pagani, C., Pagano, I., Pailler, F., Palacin, H., Palaversa, L., Parsons, P., Pecoraro, M., Pedrosa, R., Pentikäinen, H., Pichon, B., Piersimoni, A.M., Pineau, F.X., Plachy, E., Plum, G., Poujoulet, E., Prša, A., Pulone, L., Ragaini, S., Rago, S., Rambaux, N., Ramos-Lerate, M., Ranalli, P., Rauw, G., Read, A., Regibo, S., Reylé, C., Ribeiro, R.A., Rimoldini, L., Ripepi, V., Riva, A., Rixon, G., Roelens, M., Romero-Gómez, M., Rowell, N., Royer, F., Ruiz-Dern, L., Sadowski, G., Sagristà Sellés, T., Sahlmann, J., Salgado, J., Salguero, E., Sarasso, M., Savietto, H., Schultheis, M., Sciacca, E., Segol, M., Segovia, J.C., Segransan, D., Shih, I.C., Smareglia, R., Smart, R.L., Solano, E., Solitro, F., Sordo, R., Soria Nieto, S., Souchay, J., Spagna, A., Spoto, F., Stampa, U., Steele, I.A., Steidelmüller, H., Stephenson, C.A., Stoev, H., Suess, F.F., Süveges, M., Surdej, J., Szabados, L., Szegedi-Elek, E., Tapiador, D., Taris, F., Tauran, G., Taylor, M.B., Teixeira, R., Terrett, D., Tingley, B., Trager, S.C., Turon, C., Ulla, A., Utrilla, E., Valentini, G., van Elteren, A., Van Hemelryck, E., van Leeuwen, M., Varadi, M., Vecchiato, A., Veljanoski, J., Via, T., Vicente, D., Vogt, S., Voss, H., Votruba, V., Voutsinas, S., Walmsley, G., Weiler, M., Weingrill, K., Wevers, T., Wyrzykowski, Ł., Yoldas, A., Žerjal, M., Zucker, S., Zurbach, C., Zwitter, T., Alecu, A., Allen, M., Allende Prieto, C., Amorim, A., Anglada-Escudé, G., Arsenijevic, V., Azaz, S., Balm, P., Beck, M., Bernstein, H.H., Bigot, L., Bijaoui, A., Blasco, C., Bonfigli, M., Bono, G., Boudreault, S., Bressan, A., Brown, S., Brunet, P.M., Bunclark, P., Buonanno, R., Butkevich, A.G., Carret, C.,

Carrion, C., Chemin, L., Chéreau, F., Corcione, L., Darmigny, E., de Boer, K.S., de Teodoro, P., de Zeeuw, P.T., Delle Luche, C., Domingues, C.D., Dubath, P., Fodor, F., Frézouls, B., Fries, A., Fustes, D., Fyfe, D., Gallardo, E., Gallegos, J., Gardiol, D., Gebran, M., Gomboc, A., Gómez, A., Grux, E., Gueguen, A., Heyrovsky, A., Hoar, J., Iannicola, G., Isasi Parache, Y., Janotto, A.M., Joliet, E., Jonckheere, A., Keil, R., Kim, D.W., Klagyivik, P., Klar, J., Knude, J., Kochukhov, O., Kolka, I., Kos, J., Kutka, A., Lainey, V., LeBouquin, D., Liu, C., Loreggia, D., Makarov, V.V., Marseille, M.G., Martayan, C., Martinez-Rubi, O., Massart, B., Meynadier, F., Mignot, S., Munari, U., Nguyen, A.T., Nordlander, T., Ocvirk, P., O'Flaherty, K.S., Olias Sanz, A., Ortiz, P., Osorio, J., Oszkiewicz, D., Ouzounis, A., Palmer, M., Park, P., Pasquato, E., Peltzer, C., Peralta, J., Péturaud, F., Pieniluoma, T., Pigozzi, E., Poels, J., Prat, G., Prod'homme, T., Raison, F., Rebordao, J.M., Risquez, D., Rocca-Volmerange, B., Rosen, S., Ruiz-Fuertes, M.I., Russo, F., Sembay, S., Serraller Vizcaino, I., Short, A., Siebert, A., Silva, H., Sinachopoulos, D., Slezak, E., Soffel, M., Sosnowska, D., Straižys, V., ter Linden, M., Terrell, D., Theil, S., Tiede, C., Troisi, L., Tsalmantza, P., Tur, D., Vaccari, M., Vachier, F., Valles, P., Van Hamme, W., Veltz, L., Virtanen, J., Wallut, J.M., Wichmann, R., Wilkinson, M.I., Ziaeepour, H. & Zschocke, S. (2016). Gaia Data Release 1. Summary of the astrometric, photometric, and survey properties. *A&A*, **595**, A2.

Gaidos, E. & Williams, D.M. (2004). Seasonality on terrestrial extrasolar planets: inferring obliquity and surface conditions from infrared light curves. *New A*, **10**, 67–77.

Garcia, R.R., Marsh, D.R., Kinnison, D.E., Boville, B.A. & Sassi, F. (2007). Simulation of secular trends in the middle atmosphere, 1950-2003. *Journal of Geophysical Research (Atmospheres)*, **112**, D09301.

Garcia-Sage, K., Glocer, A., Drake, J.J., Gronoff, G. & Cohen, O. (2017). On the Magnetic Protection of the Atmosphere of Proxima Centauri b. *ApJ*, **844**, L13.

Garfinkel, D., Marbach, C.B. & Shapiro, N.Z. (1977). Stiff differential equations. *Annual review of biophysics and bioengineering*, **6**, 525–542.

Garraffo, C., Alvarado-Gómez, J.D., Cohen, O. & Drake, J.J. (2022). Revisiting the Space Weather Environment of Proxima Centauri b. *ApJ*, **941**, L8.

Gaudi, B.S., Seager, S., Mennesson, B., Kiessling, A., Warfield, K., Cahoy, K., Clarke, J.T., Domagal-Goldman, S., Feinberg, L., Guyon, O., Kasdin, J., Mawet, D., Plavchan, P., Robinson, T., Rogers, L., Scowen, P., Somerville, R., Stapelfeldt, K., Stark, C., Stern, D., Turnbull, M., Amini, R., Kuan, G., Martin, S., Morgan, R., Redding, D., Stahl, H.P., Webb, R., Alvarez-Salazar, O., Arnold, W.L., Arya, M., Balasubramanian, B., Baysinger, M., Bell, R., Below, C., Benson, J., Blais, L., Booth, J., Bourgeois, R., Bradford, C., Brewer, A., Brooks, T., Cady, E., Caldwell, M., Calvet, R., Carr, S., Chan, D., Cormarkovic, V., Coste, K., Cox, C., Danner, R., Davis, J., Dewell, L., Dorsett, L., Dunn, D., East, M., Effinger, M., Eng, R., Freebury, G., Garcia, J., Gaskin, J., Greene, S., Hennessy, J., Hilgemann, E., Hood, B., Holota, W., Howe, S., Huang, P., Hull, T., Hunt, R., Hurd, K., Johnson, S., Kissil, A., Knight, B., Kolenz, D., Kraus, O., Krist, J., Li, M.,

Lisman, D., Mandic, M., Mann, J., Marchen, L., Marrese-Reading, C., McCready, J., McGown, J., Missun, J., Miyaguchi, A., Moore, B., Nemati, B., Nikzad, S., Nissen, J., Novicki, M., Perrine, T., Pineda, C., Polanco, O., Putnam, D., Qureshi, A., Richards, M., Eldorado Riggs, A.J., Rodgers, M., Rud, M., Saini, N., Scalisi, D., Scharf, D., Schulz, K., Serabyn, G., Sigrist, N., Sikkia, G., Singleton, A., Shaklan, S., Smith, S., Southerd, B., Stahl, M., Steeves, J., Sturges, B., Sullivan, C., Tang, H., Taras, N., Tesch, J., Therrell, M., Tseng, H., Valente, M., Van Buren, D., Villalvazo, J., Warwick, S., Webb, D., Westerhoff, T., Wofford, R., Wu, G., Woo, J., Wood, M., Ziemer, J., Arney, G., Anderson, J., Maíz-Apellániz, J., Bartlett, J., Belikov, R., Bendek, E., Cenko, B., Douglas, E., Dulz, S., Evans, C., Faramaz, V., Feng, Y.K., Ferguson, H., Follette, K., Ford, S., García, M., Geha, M., Gelino, D., Götberg, Y., Hildebrandt, S., Hu, R., Jahnke, K., Kennedy, G., Kreidberg, L., Isella, A., Lopez, E., Marchis, F., Macri, L., Marley, M., Matzko, W., Mazoyer, J., McCandliss, S., Meshkat, T., Mordasini, C., Morris, P., Nielsen, E., Newman, P., Petigura, E., Postman, M., Reines, A., Roberge, A., Roederer, I., Ruane, G., Schwieterman, E., Sirbu, D., Spalding, C., Teplitz, H., Tumlinson, J., Turner, N., Werk, J., Wofford, A., Wyatt, M., Young, A. & Zellem, R. (2020). The Habitable Exoplanet Observatory (HabEx) Mission Concept Study Final Report. *arXiv e-prints*, arXiv:2001.06683.

Gebauer, S., Grenfell, J.L., Stock, J.W., Lehmann, R., Godolt, M., von Paris, P. & Rauer, H. (2017). Evolution of Earth-like Extrasolar Planetary Atmospheres: Assessing the Atmospheres and Biospheres of Early Earth Analog Planets with a Coupled Atmosphere Biogeochemical Model. *Astrobiol-*

ogy, **17**, 27–54.

Gebauer, S., Vilović, I., Lee Grenfell, J., Wunderlich, F., Schreier, F. & Rauer, H. (2021). Influence of Biomass Emissions on Habitability, Biosignatures, and Detectability in Earth-like Atmospheres. *ApJ*, **909**, 128.

Gettelman, A. & Morrison, H. (2015). Advanced two-moment bulk microphysics for global models. part i: Off-line tests and comparison with other schemes. *Journal of Climate*, **28**, 1268–1287.

Gettelman, A., Hannay, C., Bacmeister, J.T., Neale, R.B., Pendergrass, A.G., Danabasoglu, G., Lamarque, J.F., Fasullo, J.T., Bailey, D.A., Lawrence, D.M. & Mills, M.J. (2019a). High Climate Sensitivity in the Community Earth System Model Version 2 (CESM2). *Geophys. Res. Lett.*, **46**, 8329–8337.

Gettelman, A., Mills, M.J., Kinnison, D.E., Garcia, R.R., Smith, A.K., Marsh, D.R., Tilmes, S., Vitt, F., Bardeen, C.G., McInerny, J., Liu, H.L., Solomon, S.C., Polvani, L.M., Emmons, L.K., Lamarque, J.F., Richter, J.H., Glanville, A.S., Bacmeister, J.T., Phillips, A.S., Neale, R.B., Simpson, I.R., DuVivier, A.K., Hodzic, A. & Randel, W.J. (2019b). The Whole Atmosphere Community Climate Model Version 6 (WACCM6). *Journal of Geophysical Research (Atmospheres)*, **124**, 12,380–12,403.

Gill, S.S., Anjum, N.A., Gill, R., Jha, M. & Tuteja, N. (2015). Dna damage and repair in plants under ultraviolet and ionizing radiations. *The Scientific World Journal*, **2015**.

Gillon, M., Triaud, A.H.M.J., Demory, B.O., Jehin, E., Agol, E., Deck, K.M., Lederer, S.M., de Wit, J., Burdanov, A., Ingalls,

J.G., Bolmont, E., Leconte, J., Raymond, S.N., Selsis, F., Turbet, M., Barkaoui, K., Burgasser, A., Burleigh, M.R., Carey, S.J., Chaushev, A., Copperwheat, C.M., Delrez, L., Fernandes, C.S., Holdsworth, D.L., Kotze, E.J., Van Grootel, V., Almleaky, Y., Benkhaldoun, Z., Magain, P. & Queloz, D. (2017). Seven temperate terrestrial planets around the nearby ultracool dwarf star TRAPPIST-1. *Nature*, **542**, 456–460.

Gilmozzi, R. & Spyromilio, J. (2007). The european extremely large telescope (e-elt). *The Messenger*, **127**, 3.

Godfrey, L.V. & Falkowski, P.G. (2009). The cycling and redox state of nitrogen in the archaean ocean. *Nature Geoscience*, **2**, 725–729.

Godolt, M., Tosi, N., Stracke, B., Grenfell, J.L., Ruedas, T., Spohn, T. & Rauer, H. (2019). The habitability of stagnant-lid Earths around dwarf stars. *A&A*, **625**, A12.

Golaz, J.C., Larson, V.E. & Cotton, W.R. (2002). A PDF-Based Model for Boundary Layer Clouds. Part I: Method and Model Description. *Journal of Atmospheric Sciences*, **59**, 3540–3551.

Goldblatt, C., Lenton, T.M. & Watson, A.J. (2006). Bistability of atmospheric oxygen and the Great Oxidation. *Nature*, **443**, 683–686.

Goldblatt, C., McDonald, V.L. & McCusker, K.E. (2021). Earth's long-term climate stabilized by clouds. *Nature Geoscience*, **14**, 143–150.

Gordon, I.E., Rothman, L.S., Hill, C., Kochanov, R.V., Tan, Y., Bernath, P.F., Birk, M., Boudon, V., Campargue, A., Chance, K.V., Drouin, B.J., Flaud, J.M., Gamache, R.R., Hodges, J.T.,

Jacquemart, D., Perevalov, V.I., Perrin, A., Shine, K.P., Smith, M.A.H., Tennyson, J., Toon, G.C., Tran, H., Tyuterev, V.G., Barbe, A., Császár, A.G., Devi, V.M., Furtenbacher, T., Harrison, J.J., Hartmann, J.M., Jolly, A., Johnson, T.J., Karman, T., Kleiner, I., Kyuberis, A.A., Loos, J., Lyulin, O.M., Massie, S.T., Mikhailenko, S.N., Moazzen-Ahmadi, N., Müller, H.S.P., Naumenko, O.V., Nikitin, A.V., Polyansky, O.L., Rey, M., Rotger, M., Sharpe, S.W., Sung, K., Starikova, E., Tashkun, S.A., Auwera, J.V., Wagner, G., Wilzewski, J., Wcisło, P., Yu, S. & Zak, E.J. (2017). The HITRAN2016 molecular spectroscopic database. *J. Quant. Spec. Radiat. Transf.*, **203**, 3–69.

Greene, T.P., Bell, T.J., Ducrot, E., Dyrek, A., Lagage, P.O. & Fortney, J.J. (2023). Thermal emission from the Earth-sized exoplanet TRAPPIST-1 b using JWST. *arXiv e-prints*, arXiv:2303.14849.

Gregory, B.S., Claire, M.W. & Rugheimer, S. (2021). Photochemical modelling of atmospheric oxygen levels confirms two stable states. *Earth and Planetary Science Letters*, **561**, 116818.

Grenfell, J.L. (2017). A review of exoplanetary biosignatures. *Phys. Rep.*, **713**, 1–17.

Grenfell, J.L., Lehmann, R., Mieth, P., Langematz, U. & Steil, B. (2006). Chemical reaction pathways affecting stratospheric and mesospheric ozone. *Journal of Geophysical Research (Atmospheres)*, **111**, D17311.

Grenfell, J.L., Gebauer, S., v. Paris, P., Godolt, M. & Rauer, H. (2014). Sensitivity of biosignatures on Earth-like planets orbiting in the hab-

itable zone of cool M-dwarf Stars to varying stellar UV radiation and surface biomass emissions. *Planet. Space Sci.*, **98**, 66–76.

Grimm, S.L., Demory, B.O., Gillon, M., Dorn, C., Agol, E., Burdanov, A., Delrez, L., Sestovic, M., Triaud, A.H.M.J., Turbet, M., Bolmont, É., Caldas, A., de Wit, J., Jehin, E., Leconte, J., Raymond, S.N., Van Grootel, V., Burgasser, A.J., Carey, S., Fabrycky, D., Heng, K., Hernandez, D.M., Ingalls, J.G., Lederer, S., Selsis, F. & Queloz, D. (2018). The nature of the TRAPPIST-1 exoplanets. *A&A*, **613**, A68.

Gronoff, G., Arras, P., Baraka, S., Bell, J.M., Cessateur, G., Cohen, O., Curry, S.M., Drake, J.J., Elrod, M., Erwin, J., Garcia-Sage, K., Garraffo, C., Glocer, A., Heavens, N.G., Lovato, K., Maggiolo, R., Parkinson, C.D., Simon Wedlund, C., Weimer, D.R. & Moore, W.B. (2020). Atmospheric Escape Processes and Planetary Atmospheric Evolution. *Journal of Geophysical Research (Space Physics)*, **125**, e27639.

Gumsley, A.P., Chamberlain, K.R., Bleeker, W., Söderlund, U., de Kock, M.O., Larsson, E.R. & Bekker, A. (2017). Timing and tempo of the Great Oxidation Event. *Proceedings of the National Academy of Science*, **114**, 1811–1816.

Guzewich, S.D., Lustig-Yaeger, J., Davis, C.E., Kopparapu, R.K., Way, M.J. & Meadows, V.S. (2020). The Impact of Planetary Rotation Rate on the Reflectance and Thermal Emission Spectrum of Terrestrial Exoplanets around Sunlike Stars. *ApJ*, **893**, 140.

Habets, G.M.H.J. & Heintze, J.R.W. (1981). Empirical bolometric corrections for the main-sequence. *A&AS*, **46**, 193–237.

Häder, D.P., Williamson, C.E., Wängberg, S.Å., Rautio, M., Rose, K.C., Gao, K., Helbling, E.W., Sinha, R.P. & Worrest, R. (2015). Effects of uv radiation on aquatic ecosystems and interactions with other environmental factors. *Photochemical & Photobiological Sciences*, **14**, 108–126.

Hallmann, C., Nettersheim, B.J., Brocks, J.J., Schwelm, A., Hope, J.M., Not, F., Lomas, M., Schmidt, C., Schiebel, R., Nowack, E.C. *et al.* (2020). Reply to: Sources of c 30 steroid biomarkers in neoproterozoic–cambrian rocks and oils. *Nature ecology & evolution*, **4**, 37–39.

Hammond, M. & Lewis, N.T. (2021). The rotational and divergent components of atmospheric circulation on tidally locked planets. *Proceedings of the National Academy of Science*, **118**, e2022705118.

Hammond, M., Tsai, S.M. & Pierrehumbert, R.T. (2020). The Equatorial Jet Speed on Tidally Locked Planets. I. Terrestrial Planets. *ApJ*, **901**, 78.

Han, T.M. & Runnegar, B. (1992). Megascopic Eukaryotic Algae from the 2.1-Billion-Year-Old Negaunee Iron-Formation, Michigan. *Science*, **257**, 232–235.

Haqq-Misra, J., Wolf, E.T., Joshi, M., Zhang, X. & Kopparapu, R.K. (2018). Demarcating Circulation Regimes of Synchronously Rotating Terrestrial Planets within the Habitable Zone. *ApJ*, **852**, 67.

Harman, C.E. & Domagal-Goldman, S. (2018). Biosignature False Positives. In H.J. Deeg & J.A. Belmonte, eds., *Handbook of Exoplanets*, 71.

Hart, M.H. (1979). Habitable Zones about Main Sequence Stars. *Icarus*, **37**, 351–357.

Hartmann, D.L. & Doelling, D. (1991). On the net radiative effectiveness of clouds. *J. Geophys. Res.*, **96**, 869–891.

Hauschildt, P.H. (1993). Multi-level non-LTE radiative transfer in expanding shells. *J. Quant. Spec. Radiat. Transf.*, **50**, 301–318.

Hauschildt, P.H. & Baron, E. (2006). A 3D radiative transfer framework. I. Non-local operator splitting and continuum scattering problems. *A&A*, **451**, 273–284.

Heays, A.N., Bosman, A.D. & van Dishoeck, E.F. (2017). Photodissociation and photoionisation of atoms and molecules of astrophysical interest. *Astronomy and Astrophysics*, **602**, A105.

Heller, R. & Barnes, R. (2013). Exomoon Habitability Constrained by Illumination and Tidal Heating. *Astrobiology*, **13**, 18–46.

Hogan, R.J. & Matricardi, M. (2020). Evaluating and improving the treatment of gases in radiation schemes: the Correlated K-Distribution Model Intercomparison Project (CKDMIP). *Geoscientific Model Development*, **13**, 6501–6521.

Holland, H.D. (2006). The oxygenation of the atmosphere and oceans. *Philosophical Transactions of the Royal Society B: Biological Sciences*, **361**, 903–915.

Horowitz, L.W., Walters, S., Mauzerall, D.L., Emmons, L.K., Rasch, P.J., Granier, C., Tie, X., Lamarque, J.F., Schultz, M.G.,

Tyndall, G.S., Orlando, J.J. & Brasseur, G.P. (2003). A global simulation of tropospheric ozone and related tracers: Description and evaluation of MOZART, version 2. *Journal of Geophysical Research (Atmospheres)*, **108**, 4784.

Hörst, S.M. & Tolbert, M.A. (2014). The Effect of Carbon Monoxide on Planetary Haze Formation. *ApJ*, **781**, 53.

Hörst, S.M., He, C., Ugelow, M.S., Jellinek, A.M., Pierrehumbert, R.T. & Tolbert, M.A. (2018). Exploring the Atmosphere of Neoproterozoic Earth: The Effect of O_2 on Haze Formation and Composition. *The Astrophysical Journal*, **858**, 119.

Hourdin, F., Williamson, D., Rio, C., Couvreux, F., Roehrig, R., Villefranque, N., Musat, I., Fairhead, L., Diallo, F.B. & Volodina, V. (2021). Process-Based Climate Model Development Harnessing Machine Learning: II. Model Calibration From Single Column to Global. *Journal of Advances in Modeling Earth Systems*, **13**, e2020MS002225.

Hu, Y. & Yang, J. (2014). Role of ocean heat transport in climates of tidally locked exoplanets around M dwarf stars. *Proceedings of the National Academy of Science*, **111**, 629–634.

Hudson, H.S. (2021). Carrington Events. *ARA&A*, **59**, 445–477.

Huebner, W.F. & Carpenter, C.W. (1979). Solar photo rate coefficients.

Huebner, W.F. & Mukherjee, J. (2015). Photoionization and photodissociation rates in solar and blackbody radiation fields. *Planet. Space Sci.*, **106**, 11–45.

Huebner, W.F., Keady, J.J. & Lyon, S.P. (1992). Solar Photo Rates for Planetary Atmospheres and Atmospheric Pollutants. *Ap&SS*, **195**, 1–294.

Huestis, D.L. & Berkowitz, J. (2010). Critical Evaluation of the Photoabsorption Cross Section of CO_2 from 0.125 to 201.6 nm at Room Temperature. In *AAS/Division for Planetary Sciences Meeting Abstracts #42*, vol. 42 of *AAS/Division for Planetary Sciences Meeting Abstracts*, 48.13.

Hunke, E., Lipscomb, W., Turner, A., Jeffrey, N. & Elliott, S. (2015). Cice: The los alamos sea ice model documentation and software user's manual, version 5.1. doc. Tech. rep., LA-CC-06-012, 116 pp., http://www.ccpo. odu. edu.

Hunten, D.M. (1973). The Escape of Light Gases from Planetary Atmospheres. *Journal of Atmospheric Sciences*, **30**, 1481–1494.

Iacono, M.J., Delamere, J.S., Mlawer, E.J., Shephard, M.W., Clough, S.A. & Collins, W.D. (2008). Radiative forcing by long-lived greenhouse gases: Calculations with the AER radiative transfer models. *Journal of Geophysical Research (Atmospheres)*, **113**, D13103.

Ilin, E., Poppenhaeger, K., Schmidt, S.J., Järvinen, S.P., Newton, E.R., Alvarado-Gómez, J.D., Pineda, J.S., Davenport, J.R.A., Oshagh, M. & Ilyin, I. (2021). Giant white-light flares on fully convective stars occur at high latitudes. *MNRAS*, **507**, 1723–1745.

Jackman, J.A.G., Shkolnik, E.L., Million, C., Fleming, S., Richey-Yowell, T. & Loyd, R.O.P. (2023). Extending optical flare models to the UV: results from comparing of TESS and GALEX flare observations for M Dwarfs. *MNRAS*, **519**, 3564–3583.

Jardine, P., Peng, H., Marshall, J., Lomax, B., Bomfleur, B., Kent, M., Fraser, W. & Lui, F. (2023). Direct evidence for elevated uv-b radiation and ozone layer disruption during the end-permian mass extinction. Tech. rep., Copernicus Meetings.

Jellinek, A.M., Lenardic, A. & Pierrehumbert, R.T. (2020). Ice, Fire, or Fizzle: The Climate Footprint of Earth's Supercontinental Cycles. *Geochemistry, Geophysics, Geosystems*, **21**, e08464.

Ji, A., Kasting, J.F., Cooke, G.J., Marsh, D.R. & Tsigaridis, K. (2023). Comparison between ozone column depths and methane lifetimes computed by one- and three-dimensional models at different atmospheric O2 levels. *Royal Society Open Science*, **10**, 230056.

Johnson, R.E., Combi, M.R., Fox, J.L., Ip, W.H., Leblanc, F., McGrath, M.A., Shematovich, V.I., Strobel, D.F. & Waite, J.H. (2008). Exospheres and Atmospheric Escape. *Space Sci. Rev.*, **139**, 355–397.

Jordan, S., Rimmer, P.B., Shorttle, O. & Constantinou, T. (2021). Photochemistry of Venus-like Planets Orbiting K- and M-dwarf Stars. *ApJ*, **922**, 44.

Joshi, M.M., Haberle, R.M. & Reynolds, R.T. (1997). Simulations of the Atmospheres of Synchronously Rotating Terrestrial Planets Orbiting M Dwarfs: Conditions for Atmospheric Collapse and the Implications for Habitability. *Icarus*, **129**, 450–465.

Józefiak, I., Sukhodolov, T., Egorova, T., Chiodo, G., Stenke, A., Rieder, H., Peter, T. & Rozanov, E. (2022). Contemporary atmospheric oxygen levels maximize global protection by ozone.

Kaltenegger, L. & Sasselov, D. (2010). Detecting Planetary Geochemical Cycles on Exoplanets: Atmospheric Signatures and the Case of SO_2. *ApJ*, **708**, 1162–1167.

Kaltenegger, L. & Traub, W.A. (2009). Transits of Earth-like Planets. *The Astrophysical Journal*, **698**, 519–527.

Kaltenegger, L., Traub, W.A. & Jucks, K.W. (2007). Spectral Evolution of an Earth-like Planet. *The Astrophysical Journal*, **658**, 598–616.

Kaltenegger, L., Selsis, F., Fridlund, M., Lammer, H., Beichman, C., Danchi, W., Eiroa, C., Henning, T., Herbst, T., Léger, A., Liseau, R., Lunine, J., Paresce, F., Penny, A., Quirrenbach, A., Röttgering, H., Schneider, J., Stam, D., Tinetti, G. & White, G.J. (2010). Deciphering Spectral Fingerprints of Habitable Exoplanets. *Astrobiology*, **10**, 89–102.

Kaltenegger, L., Lin, Z. & Madden, J. (2020a). High-resolution Transmission Spectra of Earth Through Geological Time. *ApJ*, **892**, L17.

Kaltenegger, L., Lin, Z. & Rugheimer, S. (2020b). Finding Signs of Life on Transiting Earthlike Planets: High-resolution Transmission Spectra of Earth through Time around FGKM Host Stars. *ApJ*, **904**, 10.

Kane, S.R., Jansen, T., Fauchez, T., Selsis, F. & Ceja, A.Y. (2021). Phase Modeling of the TRAPPIST-1 Planetary Atmospheres. *AJ*, **161**, 53.

Kashinath, K., Mustafa, M., Albert, A., Wu, J.L., Jiang, C., Esmaeilzadeh, S., Azizzadenesheli, K., Wang, R., Chattopadhyay, A., Singh, A., Manepalli, A., Chirila, D., Yu, R., Walters, R., White, B., Xiao, H., Tchelepi, H.A., Marcus, P., Anandkumar, A., Hassanzadeh, P. & Prabhat (2021). Physics-informed machine learning: case

studies for weather and climate modelling. *Philosophical Transactions of the Royal Society of London Series A*, **379**, 20200093.

Kasting, J.F. (1987). Theoretical constraints on oxygen and carbon dioxide concentrations in the Precambrian atmosphere. *Precambrian Research*, **34**, 205–229.

Kasting, J.F. (1988). Runaway and moist greenhouse atmospheres and the evolution of Earth and Venus. *Icarus*, **74**, 472–494.

Kasting, J.F. (2010). Early Earth: Faint young Sun redux. *Nature*, **464**, 687–689.

Kasting, J.F. & Catling, D. (2003). Evolution of a Habitable Planet. *Annual Review of Astronomy and Astrophysics*, **41**, 429–463.

Kasting, J.F. & Donahue, T.M. (1980). The evolution of atmospheric ozone. *J. Geophys. Res.*, **85**, 3255–3263.

Kasting, J.F., Pollack, J.B. & Ackerman, T.P. (1984). Response of Earth's atmosphere to increases in solar flux and implications for loss of water from Venus. *Icarus*, **57**, 335–355.

Kasting, J.F., Holland, H.D. & Pinto, J.P. (1985). Oxidant abundances in rainwater and the evolution of atmospheric oxygen. *J. Geophys. Res.*, **90**, 10,497–10,510.

Kasting, J.F., Whitmire, D.P. & Reynolds, R.T. (1993). Habitable Zones around Main Sequence Stars. *Icarus*, **101**, 108–128.

Kasting, J.F., Kopparapu, R., Ramirez, R.M. & Harman, C.E. (2014). Remote life-detection criteria, habitable zone boundaries, and the frequency

of Earth-like planets around M and late K stars. *Proceedings of the National Academy of Science*, **111**, 12641–12646.

Kaufman, A.J., Johnston, D.T., Farquhar, J., Masterson, A.L., Lyons, T.W., Bates, S., Anbar, A.D., Arnold, G.L., Garvin, J. & Buick, R. (2007). Late Archean Biospheric Oxygenation and Atmospheric Evolution. *Science*, **317**, 1900.

Kendall, B., Creaser, R.A., Reinhard, C.T., Lyons, T.W. & Anbar, A.D. (2015). Transient episodes of mild environmental oxygenation and oxidative continental weathering during the late Archean. *Science Advances*, **1**, e1500777–e1500777.

Kinnison, D.E., Brasseur, G.P., Walters, S., Garcia, R.R., Marsh, D.R., Sassi, F., Harvey, V.L., Randall, C.E., Emmons, L., Lamarque, J.F., Hess, P., Orlando, J.J., Tie, X.X., Randel, W., Pan, L.L., Gettelman, A., Granier, C., Diehl, T., Niemeier, U. & Simmons, A.J. (2007). Sensitivity of chemical tracers to meteorological parameters in the MOZART-3 chemical transport model. *Journal of Geophysical Research (Atmospheres)*, **112**, D20302.

Kipping, D.M., Cameron, C., Hartman, J.D., Davenport, J.R.A., Matthews, J.M., Sasselov, D., Rowe, J., Siverd, R.J., Chen, J., Sandford, E., Bakos, G.Á., Jordán, A., Bayliss, D., Henning, T., Mancini, L., Penev, K., Csubry, Z., Bhatti, W., Da Silva Bento, J., Guenther, D.B., Kuschnig, R., Moffat, A.F.J., Rucinski, S.M. & Weiss, W.W. (2017). No Conclusive Evidence for Transits of Proxima b in MOST Photometry. *AJ*, **153**, 93.

Kitzmann, D. (2016). Revisiting the Scattering Greenhouse Effect of CO_2 Ice Clouds. *ApJ*, **817**, L18.

Klatt, J.M., Chennu, A., Arbic, B.K., Biddanda, B.A. & Dick, G.J. (2021). Possible link between Earth's rotation rate and oxygenation. *Nature Geoscience*, **14**, 564–570.

Kleinböhl, A., Willacy, K., Friedson, A.J., Chen, P. & Swain, M.R. (2018). Buildup of Abiotic Oxygen and Ozone in Moist Atmospheres of Temperate Terrestrial Exoplanets and Its Impact on the Spectral Fingerprint in Transit Observations. *ApJ*, **862**, 92.

Knoll, A.H., Javaux, E.J., Hewitt, D. & Cohen, P. (2006). Eukaryotic organisms in proterozoic oceans. *Philosophical Transactions of the Royal Society B: Biological Sciences*, **361**, 1023–1038.

Koll, D.D.B. & Abbot, D.S. (2015). Deciphering Thermal Phase Curves of Dry, Tidally Locked Terrestrial Planets. *ApJ*, **802**, 21.

Komacek, T.D., Fauchez, T.J., Wolf, E.T. & Abbot, D.S. (2020). Clouds will Likely Prevent the Detection of Water Vapor in JWST Transmission Spectra of Terrestrial Exoplanets. *ApJ*, **888**, L20.

Konrad, B.S., Alei, E., Quanz, S.P., Angerhausen, D., Carrión-González, Ó., Fortney, J.J., Grenfell, J.L., Kitzmann, D., Mollière, P., Rugheimer, S., Wunderlich, F. & LIFE Collaboration (2022). Large Interferometer For Exoplanets (LIFE). III. Spectral resolution, wavelength range, and sensitivity requirements based on atmospheric retrieval analyses of an exo-Earth. *A&A*, **664**, A23.

Kopparapu, R.K., Ramirez, R., Kasting, J.F., Eymet, V., Robinson, T.D., Mahadevan, S., Terrien, R.C., Domagal-Goldman, S., Mead-

ows, V. & Deshpande, R. (2013). Habitable zones around main-sequence stars: new estimates. *The Astrophysical Journal*, **765**, 131.

Kopparapu, R.k., Wolf, E.T., Haqq-Misra, J., Yang, J., Kasting, J.F., Meadows, V., Terrien, R. & Mahadevan, S. (2016). The Inner Edge of the Habitable Zone for Synchronously Rotating Planets around Low-mass Stars Using General Circulation Models. *ApJ*, **819**, 84.

Korenaga, J., Planavsky, N.J. & Evans, D.A.D. (2017). Global water cycle and the coevolution of the Earth's interior and surface environment. *Philosophical Transactions of the Royal Society of London Series A*, **375**, 20150393.

Kouwenberg, J., Browman, H., Cullen, J., Davis, R., St-Pierre, J.F. & Runge, J. (1999). Biological weighting of ultraviolet (280–400 nm) induced mortality in marine zooplankton and fish. i. atlantic cod (gadus morhua) eggs. *Marine Biology*, **134**, 269–284.

Kozakis, T., Mendonça, J.M. & Buchhave, L.A. (2022). Is ozone a reliable proxy for molecular oxygen?. I. The O_2-O_3 relationship for Earth-like atmospheres. *A&A*, **665**, A156.

Krasnopolsky, V.A. & Lefèvre, F. (2013). Chemistry of the Atmospheres of Mars, Venus, and Titan. In S.J. Mackwell, A.A. Simon-Miller, J.W. Harder & M.A. Bullock, eds., *Comparative Climatology of Terrestrial Planets*, 231–276.

Kreidberg, L. & Loeb, A. (2016). Prospects for Characterizing the Atmosphere of Proxima Centauri b. *ApJ*, **832**, L12.

Kreidberg, L., Koll, D.D.B., Morley, C., Hu, R., Schaefer, L., Deming, D., Stevenson, K.B., Dittmann, J., Vanderburg, A., Berardo, D., Guo, X., Stassun, K., Crossfield, I., Charbonneau, D., Latham,

D.W., Loeb, A., Ricker, G., Seager, S. & Vanderspek, R. (2019). Absence of a thick atmosphere on the terrestrial exoplanet LHS 3844b. *Nature*, **573**, 87–90.

Krissansen-Totton, J., Bergsman, D.S. & Catling, D.C. (2016). On Detecting Biospheres from Chemical Thermodynamic Disequilibrium in Planetary Atmospheres. *Astrobiology*, **16**, 39–67.

Krissansen-Totton, J., Fortney, J.J., Nimmo, F. & Wogan, N. (2021). Oxygen False Positives on Habitable Zone Planets Around Sun-Like Stars. *AGU Advances*, **2**, e00294.

Kump, L.R. (2008). The rise of atmospheric oxygen. *Nature*, **451**, 277–278.

Kuntz, L., Laakso, T., Schrag, D. & Crowe, S. (2015). Modeling the carbon cycle in lake matano. *Geobiology*, **13**, 454–461.

Kurokawa, H., Foriel, J., Laneuville, M., Houser, C. & Usui, T. (2018). Subduction and atmospheric escape of Earth's seawater constrained by hydrogen isotopes. *Earth and Planetary Science Letters*, **497**, 149–160.

Laakso, T.A. & Schrag, D.P. (2019). Methane in the Precambrian atmosphere. *Earth and Planetary Science Letters*, **522**, 48–54.

Lambrecht, N., Katsev, S., Wittkop, C., Hall, S.J., Sheik, C.S., Picard, A., Fakhraee, M. & Swanner, E.D. (2020). Biogeochemical and physical controls on methane fluxes from two ferruginous meromictic lakes. *Geobiology*, **18**, 54–69.

Lammer, H., Bredehöft, J.H., Coustenis, A., Khodachenko, M.L., Kaltenegger, L., Grasset, O., Prieur, D., Raulin, F., Ehrenfreund, P., Yamauchi, M., Wahlund, J.E., Griessmeier, J.M., Stangl,

G., Cockell, C.S., Kulikov, Y.N., Grenfell, J.L. & Rauer, H. (2009). What makes a planet habitable? *Astron Astrophys Rev*, **17**, 181–249.

Lammer, H., Zerkle, A.L., Gebauer, S., Tosi, N., Noack, L., Scherf, M., Manuel, E.P.L., Lee, J., Mareike, G. & Athanasia, G. (2018). Origin and evolution of the atmospheres of early Venus , Earth and Mars. *The Astronomy and Astrophysics Review*, **26**, 1–72.

Large, R.R., Mukherjee, I., Gregory, D., Steadman, J., Corkrey, R. & Danyushevsky, L.V. (2019). Atmosphere oxygen cycling through the Proterozoic and Phanerozoic. *Mineralium Deposita*, **54**, 485–506.

Larson, V.E. (2017). CLUBB-SILHS: A parameterization of subgrid variability in the atmosphere. *arXiv e-prints*, arXiv:1711.03675.

Lary, D.J. (1997). Catalytic destruction of stratospheric ozone. *Journal of Geophysics*, **102**, 21,515–21,526.

Lauer, A. & Hamilton, K. (2013). Simulating Clouds with Global Climate Models: A Comparison of CMIP5 Results with CMIP3 and Satellite Data. *Journal of Climate*, **26**, 3823–3845.

LaViolette, P.A. (2011). Evidence for a solar flare cause of the pleistocene mass extinction. *Radiocarbon*, **53**, 303–323.

Lawrence, D.M., Fisher, R.A., Koven, C.D., Oleson, K.W., Swenson, S.C., Bonan, G., Collier, N., Ghimire, B., van Kampenhout, L., Kennedy, D., Kluzek, E., Lawrence, P.J., Li, F., Li, H., Lombardozzi, D., Riley, W.J., Sacks, W.J., Shi, M., Vertenstein, M., Wieder, W.R., Xu, C., Ali, A.A., Badger, A.M., Bisht, G., van den Broeke, M., Brunke, M.A., Burns, S.P., Buzan, J., Clark, M.,

Craig, A., Dahlin, K., Drewniak, B., Fisher, J.B., Flanner, M., Fox, A.M., Gentine, P., Hoffman, F., Keppel-Aleks, G., Knox, R., Kumar, S., Lenaerts, J., Leung, L.R., Lipscomb, W.H., Lu, Y., Pandey, A., Pelletier, J.D., Perket, J., Randerson, J.T., Ricciuto, D.M., Sanderson, B.M., Slater, A., Subin, Z.M., Tang, J., Thomas, R.Q., Val Martin, M. & Zeng, X. (2019). The Community Land Model Version 5: Description of New Features, Benchmarking, and Impact of Forcing Uncertainty. *Journal of Advances in Modeling Earth Systems*, **11**, 4245–4287.

Leconte, J. (2021). Spectral binning of precomputed correlated-k coefficients. *A&A*, **645**, A20.

Leconte, J., Wu, H., Menou, K. & Murray, N. (2015). Asynchronous rotation of Earth-mass planets in the habitable zone of lower-mass stars. *Science*, **347**, 632–635.

Lee, C.H. (2018). Exoplanets: Past, Present, and Future. *Galaxies*, **6**, 51.

Leger, A., Pirre, M. & Marceau, F.J. (1993). Search for primitive life on a distant planet: relevance of 02 and 03 detections. *A&A*, **277**, 309.

Lehmer, O.R., Catling, D.C., Buick, R., Brownlee, D.E. & Newport, S. (2020). Atmospheric CO2 levels from 2.7 billion years ago inferred from micrometeorite oxidation. *Science Advances*, **6**, eaay4644.

Lenton, T.M., Boyle, R.A., Poulton, S.W., Shields-Zhou, G.A. & Butterfield, N.J. (2014). Co-evolution of eukaryotes and ocean oxygenation in the Neoproterozoic era. *Nature Geoscience*, **7**, 257–265.

Levine, J.S., Hays, P.B. & Walker, J.C.G. (1979). The evolution and variability of atmospheric ozone over geological time. *Icarus*, **39**, 295–309.

Lewis, N.T., Lambert, F.H., Boutle, I.A., Mayne, N.J., Manners, J. & Acreman, D.M. (2018). The Influence of a Substellar Continent on the Climate of a Tidally Locked Exoplanet. *ApJ*, **854**, 171.

Li, H., Wigmosta, M.S., Wu, H., Huang, M., Ke, Y., Coleman, A.M. & Leung, L.R. (2013). A Physically Based Runoff Routing Model for Land Surface and Earth System Models. *Journal of Hydrometeorology*, **14**, 808–828.

Li, J., Jiang, J.H., Yang, H., Abbot, D.S., Hu, R., Komacek, T.D., Bartlett, S.J. & Yung, Y.L. (2022). Rotation Period Detection for Earth-like Exoplanets. *AJ*, **163**, 27.

Lin, S. & Rood, R.B. (1997). An explicit flux-form semi-Lagrangian shallow-water model on the sphere. *Quarterly Journal of the Royal Meteorological Society*, **123**, 2477–2498.

Lin, Z. & Kaltenegger, L. (2020). High-resolution reflection spectra for Proxima b and Trappist-1e models for ELT observations. *MNRAS*, **491**, 2845–2854.

Lin, Z., MacDonald, R.J., Kaltenegger, L. & Wilson, D.J. (2021). Differentiating modern and prebiotic Earth scenarios for TRAPPIST-1e: high-resolution transmission spectra and predictions for JWST. *MNRAS*, **505**, 3562–3578.

Lipscomb, W.H., Price, S.F., Hoffman, M.J., Leguy, G.R., Bennett, A.R., Bradley, S.L., Evans, K.J., Fyke, J.G., Kennedy, J.H., Perego, M., Ranken, D.M., Sacks, W.J., Salinger, A.G., Vargo, L.J. & Worley, P.H. (2019). Description and evaluation of the Community Ice Sheet Model (CISM) v2.1. *Geoscientific Model Development*, **12**, 387–424.

Lissauer, J.J. (2007). Planets Formed in Habitable Zones of M Dwarf Stars Probably Are Deficient in Volatiles. *ApJ*, **660**, L149–L152.

Lisse, C.M., Desch, S.J., Unterborn, C.T., Kane, S.R., Young, P.R., Hartnett, H.E., Hinkel, N.R., Shim, S.H., Mamajek, E.E. & Izenberg, N.R. (2020). A Geologically Robust Procedure for Observing Rocky Exoplanets to Ensure that Detection of Atmospheric Oxygen Is a Modern Earth-like Biosignature. *ApJ*, **898**, L17.

Liu, H.L., Bardeen, C.G., Foster, B.T., Lauritzen, P., Liu, J., Lu, G., Marsh, D.R., Maute, A., McInerney, J.M., Pedatella, N.M., Qian, L., Richmond, A.D., Roble, R.G., Solomon, S.C., Vitt, F.M. & Wang, W. (2018). Development and Validation of the Whole Atmosphere Community Climate Model With Thermosphere and Ionosphere Extension (WACCM-X 2.0). *Journal of Advances in Modeling Earth Systems*, **10**, 381–402.

Liu, P., Liu, J., Ji, A., Reinhard, C.T., Planavsky, N.J., Babikov, D., Najjar, R.G. & Kasting, J.F. (2021). Triple oxygen isotope constraints on atmospheric O_2 and biological productivity during the mid-Proterozoic. *Proceedings of the National Academy of Science*, **118**, e2105074118.

Liu, X., Ma, P.L., Wang, H., Tilmes, S., Singh, B., Easter, R.C., Ghan, S.J. & Rasch, P.J. (2016). Description and evaluation of a new four-mode version of the Modal Aerosol Module (MAM4) within version 5.3 of the Community Atmosphere Model. *Geoscientific Model Development*, **9**, 505–522.

Livengood, T.A., Deming, L.D., A'Hearn, M.F., Charbonneau, D., Hewagama, T., Lisse, C.M., McFadden, L.A., Meadows, V.S., Robinson, T.D., Seager, S. & Wellnitz, D.D. (2011). Properties of an Earth-Like Planet Orbiting a Sun-Like Star: Earth Observed by the EPOXI Mission. *Astrobiology*, **11**, 907–930.

Llabrés, M. & Agustí, S. (2010). Effects of ultraviolet radiation on growth, cell death and the standing stock of antarctic phytoplankton. *Aquatic Microbial Ecology*, **59**, 151–160.

Llabrés, M., Agustí, S., Fernández, M., Canepa, A., Maurin, F., Vidal, F. & Duarte, C.M. (2013). Impact of elevated uvb radiation on marine biota: a meta-analysis.

Lobo, A.H., Shields, A.L., Palubski, I.Z. & Wolf, E. (2023). Terminator Habitability: The Case for Limited Water Availability on M-dwarf Planets. *ApJ*, **945**, 161.

Long, M.C., Moore, J.K., Lindsay, K., Levy, M., Doney, S.C., Luo, J.Y., Krumhardt, K.M., Letscher, R.T., Grover, M. & Sylvester, Z.T. (2021). Simulations With the Marine Biogeochemistry Library (MARBL). *Journal of Advances in Modeling Earth Systems*, **13**, e02647.

López-Morales, M., Gómez-Pérez, N. & Ruedas, T. (2011). Magnetic Fields in Earth-like Exoplanets and Implications for Habitability around M-dwarfs. *Origins of Life and Evolution of the Biosphere*, **41**, 533–537.

Love, G.D., Zumberge, J.A., Cárdenas, P., Sperling, E.A., Rohrssen, M., Grosjean, E., Grotzinger, J.P. & Summons, R.E. (2020). Sources of c 30 steroid biomarkers in neoproterozoic–cambrian rocks and oils. *Nature ecology & evolution*, **4**, 34–36.

Lovelock, J.E. (1965). A Physical Basis for Life Detection Experiments. *Nature*, **207**, 568–570.

Loyd, R.O.P., France, K., Youngblood, A., Schneider, C., Brown, A., Hu, R., Segura, A., Linsky, J., Redfield, S., Tian, F.,

Rugheimer, S., Miguel, Y. & Froning, C.S. (2018). The MUSCLES Treasury Survey. V. FUV Flares on Active and Inactive M Dwarfs. *ApJ*, **867**, 71.

Lu, H.C., Chen, H.K., Chen, H.F., Cheng, B.M. & Ogilvie, J.F. (2010). Absorption cross section of molecular oxygen in the transition E $^3\Sigma_u^-$ v = 0 - X $^3\Sigma_g^-$ v = 0 at 38 K. *Astronomy and Astrophysics*, **520**, A19.

Lübken, F.J., Jarvis, M.J. & Jones, G.O.L. (1999). First in situ temperature measurements at the Antarctic summer mesopause. *Geophys. Res. Lett.*, **26**, 3581–3584.

Luger, R. & Barnes, R. (2015). Extreme Water Loss and Abiotic O2Buildup on Planets Throughout the Habitable Zones of M Dwarfs. *Astrobiology*, **15**, 119–143.

Luger, R., Sestovic, M., Kruse, E., Grimm, S.L., Demory, B.O., Agol, E., Bolmont, E., Fabrycky, D., Fernandes, C.S., Van Grootel, V., Burgasser, A., Gillon, M., Ingalls, J.G., Jehin, E., Raymond, S.N., Selsis, F., Triaud, A.H.M.J., Barclay, T., Barentsen, G., Howell, S.B., Delrez, L., de Wit, J., Foreman-Mackey, D., Holdsworth, D.L., Leconte, J., Lederer, S., Turbet, M., Almleaky, Y., Benkhaldoun, Z., Magain, P., Morris, B.M., Heng, K. & Queloz, D. (2017). A seven-planet resonant chain in TRAPPIST-1. *Nature Astronomy*, **1**, 0129.

Lunine, J.I. & Atreya, S.K. (2008). The methane cycle on Titan. *Nature Geoscience*, **1**, 159–164.

Luo, G., Ono, S., Beukes, N.J., Wang, D.T., Xie, S. & Summons, R.E. (2016). Rapid oxygenation of Earths atmosphere 2.33 billion years ago. *Science Advances*, **2**, e1600134–e1600134.

Lustig-Yaeger, J., Meadows, V.S. & Lincowski, A.P. (2019). A Mirage of the Cosmic Shoreline: Venus-like Clouds as a Statistical False Positive for Exoplanet Atmospheric Erosion. *ApJ*, **887**, L11.

Lustig-Yaeger, J., Meadows, V.S. & Lincowski, A.P. (2019). The detectability and characterization of the trappist-1 exoplanet atmospheres with jwst. *The Astronomical Journal*, **158**, 27.

Lyons, T.W. & Reinhard, C.T. (2009). Early Earth: Oxygen for heavy-metal fans. *Nature*, **461**, 179–181.

Lyons, T.W., Reinhard, C.T. & Planavsky, N.J. (2014). The rise of oxygen in Earth's early ocean and atmosphere. *Nature*, **506**, 307–315.

Lyons, T.W., Diamond, C.W., Planavsky, N.J., Reinhard, C.T. & Li, C. (2021). Oxygenation, Life, and the Planetary System during Earth's Middle History: An Overview. *Astrobiology*, **21**, 906–923.

Maas, A.J., Ilin, E., Oshagh, M., Pallé, E., Parviainen, H., Molaverdikhani, K., Quirrenbach, A., Esparza-Borges, E., Murgas, F., Béjar, V.J.S., Narita, N., Fukui, A., Lin, C.L., Mori, M. & Klagyivik, P. (2022). Lower-than-expected flare temperatures for TRAPPIST-1. *A&A*, **668**, A111.

Macdonald, E., Paradise, A., Menou, K. & Lee, C. (2022). Climate uncertainties caused by unknown land distribution on habitable M-Earths. *MNRAS*, **513**, 2761–2769.

MacDonald, G.J.F. (1964). Tidal Friction. *Reviews of Geophysics and Space Physics*, **2**, 467–541.

Madhusudhan, N. (2018). *Atmospheric Retrieval of Exoplanets*, 104.

Madhusudhan, N. & Seager, S. (2009). A Temperature and Abundance Retrieval Method for Exoplanet Atmospheres. *ApJ*, **707**, 24–39.

Madhusudhan, N., Nixon, M.C., Welbanks, L., Piette, A.A. & Booth, R.A. (2020). The interior and atmosphere of the habitable-zone exoplanet k2-18b. *The Astrophysical Journal*, **891**, L7.

Madronich, S., McKenzie, R.L., Björn, L.O. & Caldwell, M.M. (1998). Changes in biologically active ultraviolet radiation reaching the earth's surface. *Journal of Photochemistry and Photobiology B: Biology*, **46**, 5–19.

Margulis, L., Walker, J.C.G. & Rambler, M. (1976). Reassessment of roles of oxygen and ultraviolet light in Precambrian evolution. *Nature*, **264**, 620–624.

Marsh, D.R., Mills, M.J., Kinnison, D.E., Lamarque, J.F., Calvo, N. & Polvani, L.M. (2013). Climate Change from 1850 to 2005 Simulated in CESM1(WACCM). *Journal of Climate*, **26**, 7372–7391.

Marshall, J.E.A., Lakin, J., Troth, I. & Wallace-Johnson, S.M. (2020). UV-B radiation was the Devonian-Carboniferous boundary terrestrial extinction kill mechanism. *Science Advances*, **6**, eaba0768.

Marty, B., Zimmermann, L., Pujol, M., Burgess, R. & Philippot, P. (2013). Nitrogen Isotopic Composition and Density of the Archean Atmosphere. *Science*, **342**, 101–104.

Maruyama, T. (1994). 22Upward Transport of Westerly Momentum due to Disturbances of the Equatorial Lower Stratosphere in the Period Range of about 2 Days. *Journal of the Meteorological Society of Japan*, **72**, 423–432.

Matsuo, T., Greene, T.P., Johnson, R.R., Mcmurray, R.E., Roellig, T.L. & Ennico, K. (2019). Photometric Precision of a Si:As Impurity Band Conduction Mid-infrared Detector and Application to Transit Spectroscopy. *PASP*, **131**, 124502.

Matthes, K., Funke, B., Andersson, M.E., Barnard, L., Beer, J., Charbonneau, P., Clilverd, M.A., Dudok de Wit, T., Haberreiter, M., Hendry, A., Jackman, C.H., Kretzschmar, M., Kruschke, T., Kunze, M., Langematz, U., Marsh, D.R., Maycock, A.C., Misios, S., Rodger, C.J., Scaife, A.A., Seppälä, A., Shangguan, M., Sinnhuber, M., Tourpali, K., Usoskin, I., van de Kamp, M., Verronen, P.T. & Versick, S. (2017). Solar forcing for CMIP6 (v3.2). *Geoscientific Model Development*, **10**, 2247–2302.

Maurin, A.S., Selsis, F., Hersant, F. & Belu, A. (2012). Thermal phase curves of nontransiting terrestrial exoplanets. II. Characterizing airless planets. *A&A*, **538**, A95.

May, E.M., Taylor, J., Komacek, T.D., Line, M.R. & Parmentier, V. (2021). Water Ice Cloud Variability and Multi-epoch Transmission Spectra of TRAPPIST-1e. *ApJ*, **911**, L30.

Mayor, M. & Queloz, D. (1995). A Jupiter-mass companion to a solar-type star. *Nature*, **378**, 355–359.

Mayor, M., PEPE, F., QUELOZ, D. & BOUCHY22, F. (2003). Setting new standards with harps. *The Messenger*, **114**, 20.

Meadows, V.S. (2017). Reflections on O_2 as a Biosignature in Exoplanetary Atmospheres. *Astrobiology*, **17**, 1022–1052.

Meadows, V.S., Arney, G.N., Schwieterman, E.W., Lustig-Yaeger, J., Lincowski, A.P., Robinson, T., Domagal-Goldman, S.D., Deitrick, R., Barnes, R.K., Fleming, D.P., Luger, R., Driscoll, P.E., Quinn, T.R. & Crisp, D. (2018a). The Habitability of Proxima Centauri b: Environmental States and Observational Discriminants. *Astrobiology*, **18**, 133–189.

Meadows, V.S., Reinhard, C.T., Arney, G.N., Parenteau, M.N., Schwieterman, E.W., Domagal-Goldman, S.D., Lincowski, A.P., Stapelfeldt, K.R., Rauer, H., DasSarma, S., Hegde, S., Narita, N., Deitrick, R., Lustig-Yaeger, J., Lyons, T.W., Siegler, N. & Grenfell, J.L. (2018b). Exoplanet Biosignatures: Understanding Oxygen as a Biosignature in the Context of Its Environment. *Astrobiology*, **18**, 630–662.

Melott, A.L., Lieberman, B.S., Laird, C.M., Martin, L.D., Medvedev, M.V., Thomas, B.C., Cannizzo, J.K., Gehrels, N. & Jackman, C.H. (2004). Did a gamma-ray burst initiate the late Ordovician mass extinction? *International Journal of Astrobiology*, **3**, 55–61.

Mendonça, J.M., Grimm, S.L., Grosheintz, L. & Heng, K. (2016). THOR: A New and Flexible Global Circulation Model to Explore Planetary Atmospheres. *ApJ*, **829**, 115.

Mie, G. (1908). Beiträge zur Optik trüber Medien, speziell kolloidaler Metallösungen. *Annalen der Physik*, **330**, 377–445.

Miller-Ricci Kempton, E. & Rauscher, E. (2012). Constraining High-speed Winds in Exoplanet Atmospheres through Observations of Anomalous Doppler Shifts during Transit. *ApJ*, **751**, 117.

Mills, D.B. & Canfield, D.E. (2014). Oxygen and animal evolution: Did a rise of atmospheric oxygen "trigger" the origin of animals? *BioEssays*, **36**, 1145–1155.

Mills, D.B., Ward, L.M., Jones, C., Sweeten, B., Forth, M., Treusch, A.H. & Canfield, D.E. (2014). Oxygen requirements of the earliest animals. *Proceedings of the National Academy of Science*, **111**, 4168–4172.

Mitchell, J.F.B. (1989). The 'greenhouse" effect and climate change. *Reviews of Geophysics*, **27**, 115–139.

Mitchell, J.L. & Lora, J.M. (2016). The Climate of Titan. *Annual Review of Earth and Planetary Sciences*, **44**, 353–380.

Mitchell, R.N., Zhang, N., Salminen, J., Liu, Y., Spencer, C.J., Steinberger, B., Murphy, J.B. & Li, Z.X. (2021). The supercontinent cycle. *Nature Reviews Earth and Environment*, **2**, 358–374.

Mlawer, E.J., Taubman, S.J., Brown, P.D., Iacono, M.J. & Clough, S.A. (1997). Radiative transfer for inhomogeneous atmospheres: RRTM, a validated correlated-k model for the longwave. *J. Geophys. Res.*, **102**, 16,663–16,682.

Mloszewska, A.M., Cole, D.B., Planavsky, N.J., Kappler, A., Whitford, D.S., Owttrim, G.W. & Konhauser, K.O. (2018). UV radiation limited the expansion of cyanobacteria in early marine photic environments. *Nature Communications*, **9**, 3088.

Montañés-Rodríguez, P., Pallé, E., Goode, P.R. & Martín-Torres, F.J. (2006). Vegetation Signature in the Observed Globally Integrated Spectrum of Earth Considering Simultaneous Cloud Data: Applications for Extrasolar Planets. *ApJ*, **651**, 544–552.

Morel, T. (2018). The chemical composition of α Centauri AB revisited. *A&A*, **615**, A172.

Mote, P.W., Rosenlof, K.H., McIntyre, M.E., Carr, E.S., Gille, J.C., Holton, J.R., Kinnersley, J.S., Pumphrey, H.C., Russell, I., James M. & Waters, J.W. (1996). An atmospheric tape recorder: The imprint of tropical tropopause temperatures on stratospheric water vapor. *J. Geophys. Res.*, **101**, 3989–4006.

Murgatroyd, R.J. & Singleton, F. (1961). Possible meridional circulations in the stratosphere and mesosphere. *Quarterly Journal of the Royal Meteorological Society*, **87**, 125–135.

Murray, L.T. (2016). Lightning nox and impacts on air quality. *Current Pollution Reports*, **2**, 115–133.

Narbonne, G.M. (2005). THE EDIACARA BIOTA: Neoproterozoic Origin of Animals and Their Ecosystems. *Annual Review of Earth and Planetary Sciences*, **33**, 421–442.

National Academies of Sciences, E. & Medicine (2021). *Pathways to Discovery in Astronomy and Astrophysics for the 2020s*.

Nawkar, G.M., Maibam, P., Park, J.H., Sahi, V.P., Lee, S.Y. & Kang, C.H. (2013). Uv-induced cell death in plants. *International journal of molecular sciences*, **14**, 1608–1628.

Neale, R.B., Chen, C.C., Gettelman, A., Lauritzen, P.H., Park, S., Williamson, D.L., Conley, A.J., Garcia, R., Kinnison, D., Lamarque, J.F. *et al.* (2010). Description of the ncar community atmosphere model (cam 5.0). *NCAR Tech. Note NCAR/TN-486+ STR*, **1**, 1–12.

Nettersheim, B.J., Brocks, J.J., Schwelm, A., Hope, J.M., Not, F., Lomas, M., Schmidt, C., Schiebel, R., Nowack, E.C., De Deckker, P. *et al.* (2019). Putative sponge biomarkers in unicellular rhizaria question an early rise of animals. *Nature ecology & evolution*, **3**, 577–581.

Noda, S., Ishiwatari, M., Nakajima, K., Takahashi, Y.O., Takehiro, S., Onishi, M., Hashimoto, G.L., Kuramoto, K. & Hayashi, Y.Y. (2017). The circulation pattern and day-night heat transport in the atmosphere of a synchronously rotating aquaplanet: Dependence on planetary rotation rate. *Icarus*, **282**, 1–18.

North, G.R. & Erukhimova, T.L. (2009). *Atmospheric thermodynamics: elementary physics and chemistry*. Cambridge University Press.

North, G.R., Pyle, J.A. & Zhang, F. (2014). *Encyclopedia of atmospheric sciences*, vol. 1. Elsevier.

Núñez-Pons, L., Avila, C., Romano, G., Verde, C. & Giordano, D. (2018). Uv-protective compounds in marine organisms from the southern ocean. *Marine drugs*, **16**, 336.

Och, L.M. & Shields-Zhou, G.A. (2012). The Neoproterozoic oxygenation event: Environmental perturbations and biogeochemical cycling. *Earth Science Reviews*, **110**, 26–57.

Olson, S.L., Reinhard, C.T. & Lyons, T.W. (2016). Limited role for methane in the mid-Proterozoic greenhouse. *Proceedings of the National Academy of Science*, **113**, 11447–11452.

Olson, S.L., Schwieterman, E.W., Reinhard, C.T. & Lyons, T.W. (2018a). *Earth: Atmospheric Evolution of a Habitable Planet*, 189. Springer.

Olson, S.L., Schwieterman, E.W., Reinhard, C.T., Ridgwell, A., Kane, S.R., Meadows, V.S. & Lyons, T.W. (2018b). Atmospheric Seasonality as an Exoplanet Biosignature. *The Astrophysical Journal Letters*, **858**, L14.

Oreopoulos, L. & Barker, H.W. (1999). Accounting for subgrid-scale cloud variability in a multi-layer ID solar radiative transfer algorithm. *Quarterly Journal of the Royal Meteorological Society*, **125**, 301–330.

Otegi, J.F., Bouchy, F. & Helled, R. (2020). Revisited mass-radius relations for exoplanets below 120 $M_{\oplus}$. *A&A*, **634**, A43.

Owen, J.E. & Mohanty, S. (2016). Habitability of terrestrial-mass planets in the HZ of M Dwarfs - I. H/He-dominated atmospheres. *MNRAS*, **459**, 4088–4108.

Ozaki, K. & Reinhard, C.T. (2021). The future lifespan of Earth's oxygenated atmosphere. *Nature Geoscience*, **14**, 138–142.

Pack, A., Höweling, A., Hezel, D.C., Stefanak, M.T., Beck, A.K., Peters, S.T.M., Sengupta, S., Herwartz, D. & Folco, L. (2017). Tracing the oxygen isotope composition of the upper Earth's atmosphere using cosmic spherules. *Nature Communications*, **8**, 15702.

Paradise, A., Menou, K., Lee, C. & Fan, B.L. (2021). Fundamental Challenges to Remote Sensing of Exo-Earths. *arXiv e-prints*, arXiv:2106.00079.

Parmentier, V. & Crossfield, I.J.M. (2018). *Exoplanet Phase Curves: Observations and Theory*, 116.

Paul, N.D. & Gwynn-Jones, D. (2003). Ecological roles of solar uv radiation: towards an integrated approach. *Trends in Ecology & Evolution*, **18**, 48–55.

Pavlov, A.A. & Kasting, J.F. (2002). Mass-Independent Fractionation of Sulfur Isotopes in Archean Sediments: Strong Evidence for an Anoxic Archean Atmosphere. *Astrobiology*, **2**, 27–41.

Pavlov, A.A., Brown, L.L. & Kasting, J.F. (2001). UV shielding of NH_3 and O_2 by organic hazes in the Archean atmosphere. *Journal of Geophysical Research: Planets*, **106**, 23267–23288.

Pavlov, A.A., Hurtgen, M.T., Kasting, J.F. & Arthur, M.A. (2003). Methane-rich Proterozoic atmosphere? *Geology*, **31**, 87.

Payne, R.C., Brownlee, D. & Kasting, J.F. (2020). Oxidized micrometeorites suggest either high pCO2 or low pN2 during the Neoarchean. *Proceedings of the National Academy of Science*, **117**, 1360–1366.

Peacock, S., Barman, T., Shkolnik, E.L., Hauschildt, P.H. & Baron, E. (2019). Predicting the Extreme Ultraviolet Radiation Environment of Exoplanets around Low-mass Stars: The TRAPPIST-1 System. *ApJ*, **871**, 235.

Penn, J. & Vallis, G.K. (2017). The Thermal Phase Curve Offset on Tidally and Nontidally Locked Exoplanets: A Shallow Water Model. *ApJ*, **842**, 101.

Perryman, M., Hartman, J., Bakos, G. & Lindegren, L. (2014). Astrometric exoplanet detection with GAIA. *Astrophysical Journal*, **797**.

Petigura, E.A., Howard, A.W. & Marcy, G.W. (2013). Prevalence of Earth-size planets orbiting Sun-like stars. *Proceedings of the National Academy of Science*, **110**, 19273–19278.

Pettit, J., Randall, C.E., Marsh, D.R., Bardeen, C.G., Qian, L., Jackman, C.H., Woods, T.N., Coster, A. & Harvey, V.L. (2018). Effects of the September 2005 Solar Flares and Solar Proton Events on the Middle Atmosphere in WACCM. *Journal of Geophysical Research (Space Physics)*, **123**, 5747–5763.

Pham, D. & Kaltenegger, L. (2022). Follow the water: Finding water, snow and clouds on terrestrial exoplanets with photometry and machine learning. *MNRAS*.

Pierazzo, E., Garcia, R.R., Kinnison, D.E., Marsh, D.R., Lee-Taylor, J. & Crutzen, P.J. (2010). Ozone perturbation from medium-size asteroid impacts in the ocean. *Earth and Planetary Science Letters*, **299**, 263–272.

Pierrehumbert, R. & Gaidos, E. (2011). Hydrogen Greenhouse Planets Beyond the Habitable Zone. *ApJ*, **734**, L13.

Pierrehumbert, R.T. & Hammond, M. (2019). Atmospheric Circulation of Tide-Locked Exoplanets. *Annual Review of Fluid Mechanics*, **51**, 275–303.

Pikuta, E.V., Hoover, R.B. & Tang, J. (2007). Microbial extremophiles at the limits of life. *Critical reviews in microbiology*, **33**, 183–209.

Plougonven, R. & Zhang, F. (2014). Internal gravity waves from atmospheric jets and fronts. *Reviews of Geophysics*, **52**, 33–76.

Plumb, R.A. (2002). Stratospheric Transport. *Journal of the Meteorological Society of Japan*, **80**, 793–809.

Pollacco, D.L., Skillen, I., Cameron, A.C., Christian, D.J., Hellier, C., Irwin, J., Lister, T., Street, R., West, R.G., Anderson, D. *et al.* (2006). The wasp project and the superwasp cameras. *Publications of the Astronomical Society of the Pacific*, **118**, 1407.

Pope, E.C., Bird, D.K. & Rosing, M.T. (2012). Isotope composition and volume of Earth's early oceans. *Proceedings of the National Academy of Science*, **109**, 4371–4376.

Poulton, S.W., Bekker, A., Cumming, V.M., Zerkle, A.L., Canfield, D.E. & Johnston, D.T. (2021). A 200-million-year delay in permanent atmospheric oxygenation. *Nature*, 1–5.

Price, E., Mielikainen, J., Huang, M., Huang, B., Huang, H.L.A. & Lee, T. (2014). GPU-Accelerated Longwave Radiation Scheme of the Rapid Radiative Transfer Model for General Circulation Models (RRTMG). *IEEE Journal of Selected Topics in Applied Earth Observations and Remote Sensing*, **7**, 3660–3667.

Proedrou, E. & Hocke, K. (2016). Characterising the three-dimensional ozone distribution of a tidally locked Earth-like planet. *Earth, Planets and Space*, **68**, 96.

Proedrou, E., Hocke, K. & Wurz, P. (2016). The middle atmospheric circulation of a tidally locked Earth-like planet and the role of the sea surface temperature. *Progress in Earth and Planetary Science*, **3**, 22.

Quanz, S.P., Kammerer, J., Defrère, D., Absil, O., Glauser, A.M. & Kitzmann, D. (2018). Exoplanet science with a space-based mid-infrared nulling interferometer. In M.J. Creech-Eakman, P.G. Tuthill & A. Mérand, eds.,

Optical and Infrared Interferometry and Imaging VI, vol. 10701 of *Society of Photo-Optical Instrumentation Engineers (SPIE) Conference Series*, 107011I.

Quanz, S.P., Absil, O., Benz, W., Bonfils, X., Berger, J.P., Defrère, D., van Dishoeck, E., Ehrenreich, D., Fortney, J., Glauser, A., Grenfell, J.L., Janson, M., Kraus, S., Krause, O., Labadie, L., Lacour, S., Line, M., Linz, H., Loicq, J., Miguel, Y., Pallé, E., Queloz, D., Rauer, H., Ribas, I., Rugheimer, S., Selsis, F., Snellen, I., Sozzetti, A., Stapelfeldt, K.R., Udry, S. & Wyatt, M. (2021). Atmospheric characterization of terrestrial exoplanets in the mid-infrared: biosignatures, habitability, and diversity. *Experimental Astronomy*.

Quarles, B., Quintana, E.V., Lopez, E., Schlieder, J.E. & Barclay, T. (2017). Plausible Compositions of the Seven TRAPPIST-1 Planets Using Long-term Dynamical Simulations. *ApJ*, **842**, L5.

Rambler, M.B. & Margulis, L. (1980). Bacterial Resistance to Ultraviolet Irradiation under Anaerobiosis: Implications for Pre-Phanerozoic Evolution. *Science*, **210**, 638–640.

Ranjan, S. & Sasselov, D.D. (2016). Influence of the UV Environment on the Synthesis of Prebiotic Molecules. *Astrobiology*, **16**, 68–88.

Rasp, S., Pritchard, M.S. & Gentine, P. (2018). Deep learning to represent subgrid processes in climate models. *Proceedings of the National Academy of Science*, **115**, 9684–9689.

Ratner, M.I. & Walker, J.C.G. (1972). Atmospheric Ozone and the History of Life. *Journal of Atmospheric Sciences*, **29**, 803–808.

Rauer, H., Aerts, C., Cabrera, J. & PLATO Team (2016). The PLATO Mission. *Astronomische Nachrichten*, **337**, 961.

Rayleigh, L. (1899). Xxxiv. on the transmission of light through an atmosphere containing small particles in suspension, and on the origin of the blue of the sky. *The London, Edinburgh, and Dublin Philosophical Magazine and Journal of Science*, **47**, 375–384.

Read, P.L. (1986). Super-rotation and diffusion of axial angular momentum. II. A review of quasi-axisymmetric models of planetary atmospheres. *Quarterly Journal of the Royal Meteorological Society*, **112**, 253–272.

Read, P.L. & Lebonnois, S. (2018). Superrotation on Venus, on Titan, and Elsewhere. *Annual Review of Earth and Planetary Sciences*, **46**, 175–202.

Read, P.L., Lewis, S.R. & Vallis, G.K. (2018). Atmospheric Dynamics of Terrestrial Planets. In H.J. Deeg & J.A. Belmonte, eds., *Handbook of Exoplanets*, 50.

Rein, H., Fujii, Y. & Spiegel, D.S. (2014). Some inconvenient truths about biosignatures involving two chemical species on Earth-like exoplanets. *Proceedings of the National Academy of Science*, **111**, 6871–6875.

Reinhard, C., Schwieterman, E.W., Olson, S.L., Planavsky, N.J., Arney, G.N., Ozaki, K., Som, S., Robinson, T.D., Domagal-Goldman, S.D., Lisman, D., Mennesson, B., Meadows, V.S. & Lyons, T.W. (2019). The remote detectability of Earth's biosphere through time and the importance of UV capability for characterizing habitable exoplanets. *Bulletin of the American Astronomical Society*, **51**, 526.

Reinhard, C.T., Olson, S.L., Schwieterman, E.W. & Lyons, T.W. (2017). False Negatives for Remote Life Detection on Ocean-Bearing Planets: Lessons from the Early Earth. *Astrobiology*, **17**, 287–297.

Retallack, G.J., Krull, E.S., Thackray, G.D. & Parkinson, D. (2013). Problematic urn-shaped fossils from a Paleoproterozoic (2.2Ga) paleosol in South Africa. *Precambrian Research*, **235**, 71–87.

Rhines, P.B. (1975). Waves and turbulence on a beta-plane. *Journal of Fluid Mechanics*, **69**, 417–443.

Ribas, I., Bolmont, E., Selsis, F., Reiners, A., Leconte, J., Raymond, S.N., Engle, S.G., Guinan, E.F., Morin, J., Turbet, M., Forget, F. & Anglada-Escudé, G. (2016). The habitability of Proxima Centauri b. I. Irradiation, rotation and volatile inventory from formation to the present. *A&A*, **596**, A111.

Richter, J.H., Sassi, F. & Garcia, R.R. (2010). Toward a Physically Based Gravity Wave Source Parameterization in a General Circulation Model. *Journal of Atmospheric Sciences*, **67**, 136.

Ricker, G.R., Latham, D., Vanderspek, R., Ennico, K., Bakos, G., Brown, T., Burgasser, A., Charbonneau, D., Deming, L., Doty, J. *et al.* (2009). The transiting exoplanet survey satellite (tess). In *Bulletin of the American Astronomical Society*, vol. 41, 193.

Ridgway, R.J., Zamyatina, M., Mayne, N.J., Manners, J., Lambert, F.H., Braam, M., Drummond, B., Hébrard, E., Palmer, P.I. & Kohary, K. (2023). 3D modelling of the impact of stellar activity on tidally locked terrestrial exoplanets: atmospheric composition and habitability. *MNRAS*, **518**, 2472–2496.

Rimmer, P., Shorttle, O. & Rugheimer, S. (2019). Oxidised micrometeorites as evidence for low atmospheric pressure on the early earth. *Geochemical perspectives letters*, **9**, 38.

Rimmer, P.B., Xu, J., Thompson, S.J., Gillen, E., Sutherland, J.D. & Queloz, D. (2018). The origin of RNA precursors on exoplanets. *Science Advances*, **4**, eaar3302.

Roberson, A.L., Roadt, J., Halevy, I. & Kasting, J. (2011). Greenhouse warming by nitrous oxide and methane in the proterozoic eon. *Geobiology*, **9**, 313–320.

Robinson, T.D. (2017). A Theory of Exoplanet Transits with Light Scattering. *ApJ*, **836**, 236.

Rodler, F. & López-Morales, M. (2014). Feasibility Studies for the Detection of O_2 in an Earth-like Exoplanet. *The Astrophysical Journal*, **781**, 54.

Rodríguez-Mozos, J.M. & Moya, A. (2019). Erosion of an exoplanetary atmosphere caused by stellar winds. *A&A*, **630**, A52.

Rogers, L.A. (2015). Most 1.6 earth-radius planets are not rocky. *The Astrophysical Journal*, **801**, 41.

Rosenfeld, D. (2006). Aerosol-Cloud Interactions Control of Earth Radiation and Latent Heat Release Budgets. *Space Sci. Rev.*, **125**, 149–157.

Rothschild, L.J. (1999). The influence of uv radiation on protistan evolution. *Journal of Eukaryotic Microbiology*, **46**, 548–555.

Rugheimer, S. & Kaltenegger, L. (2018). Spectra of Earth-like Planets through Geological Evolution around FGKM Stars. *The Astrophysical Journal*, **854**, 19.

Rugheimer, S., Kaltenegger, L., Zsom, A., Segura, A. & Sasselov, D. (2013). Spectral Fingerprints of Earth-like Planets Around FGK Stars. *Astrobiology*, **13**, 251–269.

Rugheimer, S., Kaltenegger, L., Segura, A., Linsky, J. & Mohanty, S. (2015a). Effect of UV Radiation on the Spectral Fingerprints of Earth-like Planets Orbiting M Stars. *ApJ*, **809**, 57.

Rugheimer, S., Segura, A., Kaltenegger, L. & Sasselov, D. (2015b). UV Surface Environment of Earth-like Planets Orbiting FGKM Stars through Geological Evolution. *The Astrophysical Journal*, **806**, 137.

Rushby, A.J., Claire, M.W., Osborn, H. & Watson, A.J. (2013). Habitable zone lifetimes of exoplanets around main sequence stars. *Astrobiology*, **13**, 833–849.

Rustamkulov, Z., Sing, D.K., Liu, R. & Wang, A. (2022). Analysis of a JWST NIRSpec Lab Time Series: Characterizing Systematics, Recovering Exoplanet Transit Spectroscopy, and Constraining a Noise Floor. *ApJ*, **928**, L7.

Sagan, C. (1973). Ultraviolet selection pressure on the earliest organisms. *Journal of theoretical biology*, **39**, 195–200.

Sagan, C. & Mullen, G. (1972). Earth and Mars: Evolution of Atmospheres and Surface Temperatures. *Science*, **177**, 52–56.

Sagan, C., Thompson, W.R., Carlson, R., Gurnett, D. & Hord, C. (1993). A search for life on Earth from the Galileo spacecraft. *Nature*, **365**, 715–721.

Salazar, A.M., Olson, S.L., Komacek, T.D., Stephens, H. & Abbot, D.S. (2020). The Effect of Substellar Continent Size on Ocean Dynamics of Proxima Centauri b. *ApJ*, **896**, L16.

Sánchez-Baracaldo, P. & Cardona, T. (2020). On the origin of oxygenic photosynthesis and cyanobacteria. *New Phytologist*, **225**, 1440–1446.

Sandu, A., Verwer, J., Van Loon, M., Carmichael, G., Potra, F., Dabdub, D. & Seinfeld, J. (1997). Benchmarking stiff ode solvers for atmospheric chemistry problems-i. implicit vs explicit. *Atmospheric environment*, **31**, 3151–3166.

Sarkar, S., Argyriou, I., Vandenbussche, B., Papageorgiou, A. & Pascale, E. (2018). Stellar pulsation and granulation as noise sources in exoplanet transit spectroscopy in the ARIEL space mission. *MNRAS*, **481**, 2871–2877.

Schachat, S.R., Labandeira, C.C., Saltzman, M.R., Cramer, B.D., Payne, J.L. & Boyce, C.K. (2018). Phanerozoic p o2 and the early evolution of terrestrial animals. *Proceedings of the Royal Society B: Biological Sciences*, **285**, 20172631.

Scharf, C.A. (2006). The Potential for Tidally Heated Icy and Temperate Moons around Exoplanets. *ApJ*, **648**, 1196–1205.

Schlaufman, K.C. & Laughlin, G. (2010). A physically-motivated photometric calibration of M dwarf metallicity. *A&A*, **519**, A105.

Schlawin, E., Leisenring, J., Misselt, K., Greene, T.P., McElwain, M.W., Beatty, T. & Rieke, M. (2020). JWST Noise Floor. I. Random Error Sources in JWST NIRCam Time Series. *AJ*, **160**, 231.

Schlawin, E., Leisenring, J., McElwain, M.W., Misselt, K., Don, K., Greene, T.P., Beatty, T., Nikolov, N., Kelly, D. & Rieke, M. (2021). JWST Noise Floor. II. Systematic Error Sources in JWST NIRCam Time Series. *AJ*, **161**, 115.

Schneider, T. (2006). The General Circulation of the Atmosphere. *Annual Review of Earth and Planetary Sciences*, **34**, 655–688.

Schopf, J.W., Kitajima, K., Spicuzza, M.J., Kudryavtsev, A.B. & Valley, J.W. (2018). SIMS analyses of the oldest known assemblage of microfossils document their taxon-correlated carbon isotope compositions. *Proceedings of the National Academy of Science*, **115**, 53–58.

Schulze-Makuch, D., Méndez, A., Fairén, A.G., von Paris, P., Turse, C., Boyer, G., Davila, A.F., António, M.R.D.S., Catling, D. & Irwin, L.N. (2011). A Two-Tiered Approach to Assessing the Habitability of Exoplanets. *Astrobiology*, **11**, 1041–1052.

Schwartz, J.C., Sekowski, C., Haggard, H.M., Pallé, E. & Cowan, N.B. (2016). Inferring planetary obliquity using rotational and orbital photometry. *MNRAS*, **457**, 926–938.

Schwieterman, E., Reinhard, C., Olson, S. & Lyons, T. (2018a). The Importance of UV Capabilities for Identifying Inhabited Exoplanets with Next Generation Space Telescopes. *arXiv e-prints*, arXiv:1801.02744.

Schwieterman, E.W., Kiang, N.Y., Parenteau, M.N., Harman, C.E., DasSarma, S., Fisher, T.M., Arney, G.N., Hartnett, H.E., Reinhard, C.T., Olson, S.L., Meadows, V.S., Cockell, C.S., Walker, S.I., Grenfell, J.L., Hegde, S., Rugheimer, S., Hu, R. & Lyons, T.W. (2018b). Exoplanet Biosignatures: A Review of Remotely Detectable Signs of Life. *Astrobiology*, **18**, 663–708.

Scinocca, J.F. & McFarlane, N.A. (2000). The parametrization of drag induced by stratified flow over anisotropic orography. *Quarterly Journal of the Royal Meteorological Society*, **126**, 2353–2394.

Seager, S. & Deming, D. (2010). Exoplanet Atmospheres. *Annual Review of Astronomy and Astrophysics*, **48**, 631–672.

Seager, S., Turner, E.L., Schafer, J. & Ford, E.B. (2005). Vegetation's Red Edge: A Possible Spectroscopic Biosignature of Extraterrestrial Plants. *Astrobiology*, **5**, 372–390.

Seager, S., Bains, W. & Petkowski, J.J. (2016). Toward a List of Molecules as Potential Biosignature Gases for the Search for Life on Exoplanets and Applications to Terrestrial Biochemistry. *Astrobiology*, **16**, 465–485.

Segura, A., Krelove, K., Kasting, J.F., Sommerlatt, D., Meadows, V., Crisp, D., Cohen, M. & Mlawer, E. (2003). Ozone Concentrations and Ultraviolet Fluxes on Earth-Like Planets Around Other Stars. *Astrobiology*, **3**, 689–708.

Segura, A., Kasting, J.F., Meadows, V., Cohen, M., Scalo, J., Crisp, D., Butler, R.A.H. & Tinetti, G. (2005). Biosignatures from Earth-Like Planets Around M Dwarfs. *Astrobiology*, **5**, 706–725.

Segura, A., Walkowicz, L.M., Meadows, V., Kasting, J. & Hawley, S. (2010). The Effect of a Strong Stellar Flare on the Atmospheric Chemistry of an Earth-like Planet Orbiting an M Dwarf. *Astrobiology*, **10**, 751–771.

Selsis, F. (2000). Review: Physics of Planets I: Darwin and the Atmospheres of Terrestrial Planets. In B. Schürmann, ed., *Darwin and Astronomy : the Infrared Space Interferometer*, vol. 451 of *ESA Special Publication*, 133.

Selsis, F., Despois, D. & Parisot, J.P. (2002). Signature of life on exoplanets: Can Darwin produce false positive detections? *Astronomy and Astrophysics*, **388**, 985–1003.

Selsis, F., Wordsworth, R.D. & Forget, F. (2011). Thermal phase curves of nontransiting terrestrial exoplanets. I. Characterizing atmospheres. *A&A*, **532**, A1.

Sergeev, D.E., Lambert, F.H., Mayne, N.J., Boutle, I.A., Manners, J. & Kohary, K. (2020). Atmospheric Convection Plays a Key Role in the Climate of Tidally Locked Terrestrial Exoplanets: Insights from High-resolution Simulations. *ApJ*, **894**, 84.

Sergeev, D.E., Fauchez, T.J., Turbet, M., Boutle, I.A., Tsigaridis, K., Way, M.J., Wolf, E.T., Domagal-Goldman, S.D., Forget, F., Haqq-Misra, J., Kopparapu, R.K., Lambert, F.H., Manners, J. & Mayne, N.J. (2022a). The TRAPPIST-1 Habitable Atmosphere Intercomparison (THAI). II. Moist Cases-The Two Waterworlds. , **3**, 212.

Sergeev, D.E., Lewis, N.T., Lambert, F.H., Mayne, N.J., Boutle, I.A., Manners, J. & Kohary, K. (2022b). Bistability of the Atmospheric Circulation on TRAPPIST-1e. , **3**, 214.

Serindag, D.B. & Snellen, I.A.G. (2019). Testing the Detectability of Extraterrestrial O_2 with the Extremely Large Telescopes Using Real Data with Real Noise. *ApJ*, **871**, L7.

Shields, A.L. (2019). The Climates of Other Worlds: A Review of the Emerging Field of Exoplanet Climatology. *The Astrophysical Journals*, **243**, 30.

Showman, A.P. & Polvani, L.M. (2011). Equatorial Superrotation on Tidally Locked Exoplanets. *ApJ*, **738**, 71.

Showman, A.P., Wordsworth, R.D., Merlis, T.M. & Kaspi, Y. (2013). Atmospheric Circulation of Terrestrial Exoplanets. In S.J. Mackwell, A.A.

Simon-Miller, J.W. Harder & M.A. Bullock, eds., *Comparative Climatology of Terrestrial Planets*, 277–327.

Silva, R.A., West, J.J., Zhang, Y., Anenberg, S.C., Lamarque, J.F., Shindell, D.T., Collins, W.J., Dalsoren, S., Faluvegi, G., Folberth, G. *et al.* (2013). Global premature mortality due to anthropogenic outdoor air pollution and the contribution of past climate change. *Environmental Research Letters*, **8**, 034005.

Singh, S.P., Häder, D.P. & Sinha, R.P. (2010). Cyanobacteria and ultraviolet radiation (uvr) stress: mitigation strategies. *Ageing research reviews*, **9**, 79–90.

Sinha, R.P. & Häder, D.P. (2002). Uv-induced dna damage and repair: a review. *Photochemical & Photobiological Sciences*, **1**, 225–236.

Smith, R., Jones, P., Briegleb, B., Bryan, F., Danabasoglu, G., Dennis, J., Dukowicz, J., Eden, C., Fox-Kemper, B., Gent, P. *et al.* (2010). The parallel ocean program (pop) reference manual ocean component of the community climate system model (ccsm) and community earth system model (cesm). *LAUR-01853*, **141**, 1–140.

Smith, R.C., Prezelin, B.B., Baker, K.S., Bidigare, R.R., Boucher, N.P., Coley, T., Karentz, D., MacIntyre, S., Matlick, H.A., Menzies, D., Ondrusek, M., Wan, Z. & Waters, K.J. (1992). Ozone Depletion: Ultraviolet Radiation and Phytoplankton Biology in Antarctic Waters. *Science*, **255**, 952–959.

Snellen, I.A.G., de Kok, R.J., de Mooij, E.J.W. & Albrecht, S. (2010). The orbital motion, absolute mass and high-altitude winds of exoplanet HD209458b. *Nature*, **465**, 1049–1051.

Snellen, I.A.G., de Kok, R.J., le Poole, R., Brogi, M. & Birkby, J. (2013). Finding Extraterrestrial Life Using Ground-based High-dispersion Spectroscopy. *The Astrophysical Journal*, **764**, 182.

Socas-Navarro, H., Haqq-Misra, J., Wright, J.T., Kopparapu, R., Benford, J., Davis, R. & TechnoClimes 2020 workshop participants (2021). Concepts for future missions to search for technosignatures. *Acta Astronautica*, **182**, 446–453.

Som, S., Catling, D.C., Harnmeijer, J., Polivka, P. & Buick, R. (2012). Air density 2.7 billion years ago limited to less than twice modern levels by fossil raindrop imprints. In *AGU Fall Meeting Abstracts*, vol. 2012, P11G–04.

Som, S.M., Buick, R., Hagadorn, J.W., Blake, T.S., Perreault, J.M., Harnmeijer, J.P. & Catling, D.C. (2016). Earth's air pressure 2.7 billion years ago constrained to less than half of modern levels. *Nature Geoscience*, **9**, 448–451.

Song, Q., Yang, J., Luo, H., Li, C. & Fu, S. (2022). Idealized 2D Cloud-resolving Simulations for Tidally Locked Habitable Planets. *ApJ*, **934**, 149.

Souto, D., Unterborn, C.T., Smith, V.V., Cunha, K., Teske, J., Covey, K., Rojas-Ayala, B., García-Hernández, D., Stassun, K., Zamora, O. *et al.* (2018). Stellar and planetary characterization of the ross 128 exoplanetary system from apogee spectra. *The Astrophysical Journal Letters*, **860**, L15.

Sperling, E.A., Robinson, J., Pisani, D. & Peterson, K.J. (2010). Where's the glass? biomarkers, molecular clocks, and micrornas suggest a 200-

myr missing precambrian fossil record of siliceous sponge spicules. *Geobiology*, **8**, 24–36.

Sperling, E.A., Wolock, C.J., Morgan, A.S., Gill, B.C., Kunzmann, M., Halverson, G.P., MacDonald, F.A., Knoll, A.H. & Johnston, D.T. (2015). Statistical analysis of iron geochemical data suggests limited late Proterozoic oxygenation. *Nature*, **523**, 451–454.

Squire, O.J., Archibald, A.T., Abraham, N.L., Beerling, D.J., Hewitt, C.N., Lathière, J., Pike, R.C., Telford, P.J. & Pyle, J.A. (2014). Influence of future climate and cropland expansion on isoprene emissions and tropospheric ozone. *Atmospheric Chemistry & Physics*, **14**, 1011–1024.

Steadman, J.A., Large, R.R., Blamey, N.J., Mukherjee, I., Corkrey, R., Danyushevsky, L.V., Maslennikov, V., Hollings, P., Garven, G., Brand, U. & Lécuyer, C. (2020). Evidence for elevated and variable atmospheric oxygen in the Precambrian. *Precambrian Research*, **343**, 105722.

Stüeken, E.E., Som, S.M., Claire, M., Rugheimer, S., Scherf, M., Spross, L., Tosi, N., Ueno, Y. & Lammer, H. (2020). Mission to Planet Earth: The First Two Billion Years. *Space Science Reviews*, **216**, 31.

Tarter, J.C., Backus, P.R., Mancinelli, R.L., Aurnou, J.M., Backman, D.E., Basri, G.S., Boss, A.P., Clarke, A., Deming, D., Doyle, L.R., Feigelson, E.D., Freund, F., Grinspoon, D.H., Haberle, R.M., Hauck, I., Steven A., Heath, M.J., Henry, T.J., Hollingsworth, J.L., Joshi, M.M., Kilston, S., Liu, M.C., Meikle, E., Reid, I.N., Rothschild, L.J., Scalo, J., Segura, A., Tang, C.M., Tiedje, J.M., Turnbull, M.C., Walkowicz, L.M., Weber, A.L. &

Young, R.E. (2007). A Reappraisal of The Habitability of Planets around M Dwarf Stars. *Astrobiology*, **7**, 30–65.

Teal, D.J., Kempton, E.M.R., Bastelberger, S., Youngblood, A. & Arney, G. (2022). Effects of UV Stellar Spectral Uncertainty on the Chemistry of Terrestrial Atmospheres. *ApJ*, **927**, 90.

Tedetti, M. & Sempéré, R. (2006). Penetration of ultraviolet radiation in the marine environment. a review. *Photochemistry and photobiology*, **82**, 389–397.

Teinturier, L., Vieira, N., Jacquet, E., Geoffrion, J., Bestavros, Y., Keating, D. & Cowan, N.B. (2022). Mapping the surface of partially cloudy exoplanets is hard. *MNRAS*, **511**, 440–447.

Tennyson, J. & Yurchenko, S.N. (2012). ExoMol: molecular line lists for exoplanet and other atmospheres. *MNRAS*, **425**, 21–33.

Tennyson, J., Yurchenko, S.N., Al-Refaie, A.F., Clark, V.H.J., Chubb, K.L., Conway, E.K., Dewan, A., Gorman, M.N., Hill, C., Lynas-Gray, A.E., Mellor, T., McKemmish, L.K., Owens, A., Polyansky, O.L., Semenov, M., Somogyi, W., Tinetti, G., Upadhyay, A., Waldmann, I., Wang, Y., Wright, S. & Yurchenko, O.P. (2020). The 2020 release of the ExoMol database: Molecular line lists for exoplanet and other hot atmospheres. *J. Quant. Spec. Radiat. Transf.*, **255**, 107228.

The LUVOIR Team (2019). The LUVOIR Mission Concept Study Final Report. *arXiv e-prints*, arXiv:1912.06219.

Thompson, M.A., Krissansen-Totton, J., Wogan, N., Telus, M. & Fortney, J.J. (2022). The case and context for atmospheric methane as an

exoplanet biosignature. *Proceedings of the National Academy of Sciences*, **119**, e2117933119.

Tie, X., Madronich, S., Walters, S., Zhang, R., Rasch, P. & Collins, W. (2003). Effect of clouds on photolysis and oxidants in the troposphere. *Journal of Geophysical Research (Atmospheres)*, **108**, 4642.

Tilley, M.A., Segura, A., Meadows, V., Hawley, S. & Davenport, J. (2019). Modeling Repeated M Dwarf Flaring at an Earth-like Planet in the Habitable Zone: Atmospheric Effects for an Unmagnetized Planet. *Astrobiology*, **19**, 64–86.

Tinetti, G., Meadows, V.S., Crisp, D., Fong, W., Fishbein, E., Turnbull, M. & Bibring, J.P. (2006a). Detectability of Planetary Characteristics in Disk-Averaged Spectra. I: The Earth Model. *Astrobiology*, **6**, 34–47.

Tinetti, G., Meadows, V.S., Crisp, D., Kiang, N.Y., Kahn, B.H., Fishbein, E., Velusamy, T. & Turnbull, M. (2006b). Detectability of Planetary Characteristics in Disk-Averaged Spectra II: Synthetic Spectra and Light-Curves of Earth. *Astrobiology*, **6**, 881–900.

Tokano, T., McKay, C.P., Neubauer, F.M., Atreya, S.K., Ferri, F., Fulchignoni, M. & Niemann, H.B. (2006). Methane drizzle on Titan. *Nature*, **442**, 432–435.

Tomkins, A.G., Bowlt, L., Genge, M., Wilson, S.A., Brand, H.E.A. & Wykes, J.L. (2016). Ancient micrometeorites suggestive of an oxygen-rich Archaean upper atmosphere. *Nature*, **533**, 235–238.

Trainer, M.G., Pavlov, A.A., Dewitt, H.L., Jimenez, J.L., McKay, C.P., Toon, O.B. & Tolbert, M.A. (2006). Inaugural Article: Organic

haze on Titan and the early Earth. *Proceedings of the National Academy of Science*, **103**, 18035–18042.

Traub, W.A. (2012). Terrestrial, Habitable-zone Exoplanet Frequency from Kepler. *The Astrophysical Journal*, **745**, 20.

Tsai, S.M., Lyons, J.R., Grosheintz, L., Rimmer, P.B., Kitzmann, D. & Heng, K. (2017). VULCAN: An Open-source, Validated Chemical Kinetics Python Code for Exoplanetary Atmospheres. *ApJS*, **228**, 20.

Tsiaras, A., Waldmann, I.P., Tinetti, G., Tennyson, J. & Yurchenko, S.N. (2019). Water vapour in the atmosphere of the habitable-zone eight-earth-mass planet k2-18 b. *Nature Astronomy*, 1–6.

Turbet, M., Leconte, J., Selsis, F., Bolmont, E., Forget, F., Ribas, I., Raymond, S.N. & Anglada-Escudé, G. (2016). The habitability of Proxima Centauri b. II. Possible climates and observability. *A&A*, **596**, A112.

Turbet, M., Fauchez, T.J., Sergeev, D.E., Boutle, I.A., Tsigaridis, K., Way, M.J., Wolf, E.T., Domagal-Goldman, S.D., Forget, F., Haqq-Misra, J., Kopparapu, R.K., Lambert, F.H., Manners, J., Mayne, N.J. & Sohl, L. (2022). The TRAPPIST-1 Habitable Atmosphere Intercomparison (THAI). I. Dry Cases-The Fellowship of the GCMs. , **3**, 211.

Turyshev, S.G. & Toth, V.T. (2022). Resolved imaging of exoplanets with the solar gravitational lens. *MNRAS*, **515**, 6122–6132.

Uveges, B.T., Izon, G., Ono, S., Beukes, N.J. & Summons, R.E. (2023). Reconciling discrepant minor sulfur isotope records of the Great Oxidation Event. *Nature Communications*, **14**, 279.

Vida, K., Kővári, Z., Pál, A., Oláh, K. & Kriskovics, L. (2017). Frequent Flaring in the TRAPPIST-1 System—Unsuited for Life? *ApJ*, **841**, 124.

Vida, K., Oláh, K., Kővári, Z., van Driel-Gesztelyi, L., Moór, A. & Pál, A. (2019). Flaring Activity of Proxima Centauri from TESS Observations: Quasiperiodic Oscillations during Flare Decay and Inferences on the Habitability of Proxima b. *ApJ*, **884**, 160.

Vidotto, A.A., Jardine, M., Morin, J., Donati, J.F., Lang, P. & Russell, A.J.B. (2013). Effects of M dwarf magnetic fields on potentially habitable planets. *A&A*, **557**, A67.

Villanueva, G.L., Smith, M.D., Protopapa, S., Faggi, S. & Mandell, A.M. (2018). Planetary Spectrum Generator: An accurate online radiative transfer suite for atmospheres, comets, small bodies and exoplanets. *J. Quant. Spec. Radiat. Transf.*, **217**, 86–104.

Villanueva, G.L., Liuzzi, G., Faggi, S., Protopapa, S., Kofman, V., Fauchez, T., Stone, S.W. & Mandell, A.M. (2022). *Fundamentals of the Planetary Spectrum Generator*.

Villefranque, N., Blanco, S., Couvreux, F., Fournier, R., Gautrais, J., Hogan, R.J., Hourdin, F., Volodina, V. & Williamson, D. (2021). Process Based Climate Model Development Harnessing Machine Learning: III. The Representation of Cumulus Geometry and Their 3D Radiative Effects. *Journal of Advances in Modeling Earth Systems*, **13**, e2020MS002423.

Visconti, G. (2016). *Fundamentals of Physics and Chemistry of the Atmosphere*. Springer.

Wallace, M.W., Hood, A.v., Shuster, A., Greig, A., Planavsky, N.J. & Reed, C.P. (2017). Oxygenation history of the Neoproterozoic to early Phanerozoic and the rise of land plants. *Earth and Planetary Science Letters*, **466**, 12–19.

Wang, T. & Dessler, A.E. (2012). Analysis of cirrus in the tropical tropopause layer from CALIPSO and MLS data: A water perspective. *Journal of Geophysical Research (Atmospheres)*, **117**, D04211.

Wang, Y., Read, P.L., Tabataba-Vakili, F. & Young, R.M.B. (2018). Comparative terrestrial atmospheric circulation regimes in simplified global circulation models. Part I: From cyclostrophic super-rotation to geostrophic turbulence. *Quarterly Journal of the Royal Meteorological Society*, **144**, 2537–2557.

Warke, M.R., Di Rocco, T., Zerkle, A.L., Lepland, A., Prave, A.R., Martin, A.P., Ueno, Y., Condon, D.J. & Claire, M.W. (2020). The Great Oxidation Event preceded a Paleoproterozoic "snowball Earth". *Proceedings of the National Academy of Science*, **117**, 13314–13320.

Waugh, D.W., Sobel, A.H. & Polvani, L.M. (2017). What is the polar vortex and how does it influence weather? *Bulletin of the American Meteorological Society*, **98**, 37–44.

Way, M.J., Aleinov, I., Amundsen, D.S., Chandler, M.A., Clune, T.L., Del Genio, A.D., Fujii, Y., Kelley, M., Kiang, N.Y., Sohl, L. & Tsigaridis, K. (2017). Resolving Orbital and Climate Keys of Earth and Extraterrestrial Environments with Dynamics (ROCKE-3D) 1.0: A General Circulation Model for Simulating the Climates of Rocky Planets. *The Astrophysical Journal Supplement Series*, **231**, 12.

Wenger, M., Ochsenbein, F., Egret, D., Dubois, P., Bonnarel, F., Borde, S., Genova, F., Jasniewicz, G., Laloë, S., Lesteven, S. & Monier, R. (2000). The SIMBAD astronomical database. The CDS reference database for astronomical objects. *A&AS*, **143**, 9–22.

Wiedner, M.C., Aalto, S., Armus, L., Bergin, E., Birkby, J., Bradford, C.M., Burgarella, D., Caselli, P., Charmandaris, V., Cooray, A., De Beck, E., Desert, J.M., Gerin, M., Goicoechea, J., Griffin, M., Hartogh, P., Helmich, F., Hogerheijde, M., Hunt, L., Karska, A., Kral, Q., Leisawitz, D., Melnick, G., Meixner, M., Matsuura, M., Milam, S., Pearson, C., Pesce, D.W., Pontoppidan, K.M., Pope, A., Rigopoulou, D., Roellig, T., Sakon, I., Staguhn, J. & Stevenson, K. (2021). Origins space telescope: from first light to life. *Experimental Astronomy*, **51**, 595–624.

Williams, D.M. & Pollard, D. (2002). Earth-like worlds on eccentric orbits: excursions beyond the habitable zone. *International Journal of Astrobiology*, **1**, 61–69.

Williams, G.E. (1993). History of the earth's obliquity. *Earth Science Reviews*, **34**, 1–45.

Wilson, D.J., Froning, C.S., Duvvuri, G.M., France, K., Youngblood, A., Schneider, P.C., Berta-Thompson, Z., Brown, A., Buccino, A.P., Hawley, S., Irwin, J., Kaltenegger, L., Kowalski, A., Linsky, J., Parke Loyd, R.O., Miguel, Y., Pineda, J.S., Redfield, S., Roberge, A., Rugheimer, S., Tian, F. & Vieytes, M. (2021). The Mega-MUSCLES Spectral Energy Distribution of TRAPPIST-1. *ApJ*, **911**, 18.

Wogan, N., Krissansen-Totton, J. & Catling, D.C. (2020). Abundant Atmospheric Methane from Volcanism on Terrestrial Planets Is Unlikely and Strengthens the Case for Methane as a Biosignature. , **1**, 58.

Wolf, E.T. (2017). Assessing the Habitability of the TRAPPIST-1 System Using a 3D Climate Model. *ApJ*, **839**, L1.

Wolf, E.T. & Toon, O.B. (2014). Delayed onset of runaway and moist greenhouse climates for Earth. *Geophys. Res. Lett.*, **41**, 167–172.

Wolf, E.T., Shields, A.L., Kopparapu, R.K., Haqq-Misra, J. & Toon, O.B. (2017). Constraints on Climate and Habitability for Earth-like Exoplanets Determined from a General Circulation Model. *The Astrophysical Journal*, **837**, 107.

Wolf, E.T., Kopparapu, R., Haqq-Misra, J. & Fauchez, T.J. (2022). ExoCAM: A 3D Climate Model for Exoplanet Atmospheres. , **3**, 7.

Wolszczan, A. & Frail, D.A. (1992). A planetary system around the millisecond pulsar PSR1257 + 12. *Nature*, **355**, 145–147.

Wordsworth, R. & Kreidberg, L. (2022). Atmospheres of Rocky Exoplanets. *ARA&A*, **60**, 159–201.

Wordsworth, R. & Pierrehumbert, R. (2014). Abiotic Oxygen-dominated Atmospheres on Terrestrial Habitable Zone Planets. *The Astrophysical Journal Letters*, **785**, L20.

World Health Organization *et al.* (2000). *Air quality guidelines for Europe*. World Health Organization. Regional Office for Europe.

Wunderlich, F., Godolt, M., Grenfell, J.L., Städt, S., Smith, A.M.S., Gebauer, S., Schreier, F., Hedelt, P. & Rauer, H. (2019).

Detectability of atmospheric features of Earth-like planets in the habitable zone around M dwarfs. *A&A*, **624**, A49.

Yang, J., Cowan, N.B. & Abbot, D.S. (2013). Stabilizing Cloud Feedback Dramatically Expands the Habitable Zone of Tidally Locked Planets. *ApJ*, **771**, L45.

Yang, J., Abbot, D.S., Koll, D.D.B., Hu, Y. & Showman, A.P. (2019). Ocean Dynamics and the Inner Edge of the Habitable Zone for Tidally Locked Terrestrial Planets. *ApJ*, **871**, 29.

Yang, J., Ji, W. & Zeng, Y. (2020). Transition from eyeball to snowball driven by sea-ice drift on tidally locked terrestrial planets. *Nature Astronomy*, **4**, 58–66.

Yassin Jaziri, A., Charnay, B., Selsis, F., Leconte, J. & Lefèvre, F. (2022). Dynamics of the Great Oxidation Event from a 3D photochemical-climate model. *Climate of the Past*, **18**, 2421–2447.

Yates, J.S., Palmer, P.I., Manners, J., Boutle, I., Kohary, K., Mayne, N. & Abraham, L. (2020). Ozone chemistry on tidally locked M dwarf planets. *MNRAS*, **492**, 1691–1705.

Young, G.M. (2013). Precambrian supercontinents, glaciations, atmospheric oxygenation, metazoan evolution and an impact that may have changed the second half of earth history. *Geoscience Frontiers*, **4**, 247–261.

Youngblood, A., Drake, J., Mason, J., Osten, R., Jin, M., Kowalski, A., France, K., Fleming, B., Allred, J., Amerstorfer, U., Berta-Thompson, Z., Bourrier, V., Fossati, L., Froning, C., Garraffo, C., Gronoff, G., Koskinen, T. & Lichtenegger, H. (2019). EUV observations of cool dwarf stars. *BAAS*, **51**, 300.

Zahnle, K. & Walker, J.C.G. (1987). A constant daylength during the precambrian era? *Precambrian Research*, **37**, 95–105.

Zahnle, K.J., Catling, D.C. & Claire, M.W. (2013). The rise of oxygen and the hydrogen hourglass. *Chemical Geology*, **362**, 26–34.

Zahnle, K.J., Gacesa, M. & Catling, D.C. (2019). Strange messenger: A new history of hydrogen on Earth, as told by Xenon. *Geochimica Cosmochimica Acta*, **244**, 56–85.

Zedek, F. & Bureš, P. (2018). Holocentric chromosomes: from tolerance to fragmentation to colonization of the land. *Annals of botany*, **121**, 9–16.

Zedek, F., Veselỳ, P., Tichỳ, L., Elliott, T.L., Garbolino, E., de Ruffray, P. & Bureš, P. (2021). Holocentric plants are more competitive under higher uv-b doses. *New Phytologist*.

Zendejas, J., Segura, A. & Raga, A.C. (2010). Atmospheric mass loss by stellar wind from planets around main sequence M stars. *Icarus*, **210**, 539–544.

Zhang, G.J. & McFarlane, N.A. (1995). Sensitivity of climate simulations to the parameterization of cumulus convection in the canadian climate centre general circulation model. *Atmosphere-ocean*, **33**, 407–446.

Zhang, X. & Cui, L. (2016). Oxygen requirements for the cambrian explosion. *Journal of Earth Science*, **27**, 187–195.

Zhao, X., Wang, X., Shi, X., Tang, D. & Shi, Q. (2018). Stepwise oxygenation of early Cambrian ocean controls early metazoan diversification. *Palaeogeography Palaeoclimatology Palaeoecology*, **504**, 86–103.

Zhao, Z., Liu, Y., Li, W., Liu, H. & Man, K. (2021). Climate Change of over 20 °C Induced by Continental Movement on a Synchronously Rotating Exoplanet. *ApJ*, **910**, L8.

Zhu, Q., Jung, D.Y., Oganov, A.R., Glass, C.W., Gatti, C. & Lyakhov, A.O. (2013). Stability of xenon oxides at high pressures. *Nature Chemistry*, **5**, 61–65.

Zink, J.K. & Hansen, B.M.S. (2019). Accounting for multiplicity in calculating eta Earth. *Monthly Notices of the Royal Astronomical Society*, **487**, 246–252.

Zumberge, J.A., Love, G.D., Cárdenas, P., Sperling, E.A., Gunasekera, S., Rohrssen, M., Grosjean, E., Grotzinger, J.P. & Summons, R.E. (2018). Demosponge steroid biomarker 26-methylstigmastane provides evidence for neoproterozoic animals. *Nature ecology & evolution*, **2**, 1709–1714.